



**Peer Reviewed**

**Title:**

Charge Carrier Dynamics in Transition Metal Oxides Studied by Femtosecond Transient Extreme Ultraviolet Absorption Spectroscopy

**Author:**

[Jiang, Chang-Ming](#)

**Acceptance Date:**

2015

**Series:**

[UC Berkeley Electronic Theses and Dissertations](#)

**Degree:**

Ph.D., [Chemistry](#)[UC Berkeley](#)

**Advisor(s):**

[Leone, Stephen R](#)

**Committee:**

[Saykally, Richard J.](#) [Müller, Holger](#)

**Permalink:**

<http://escholarship.org/uc/item/7129618s>

**Abstract:**

**Copyright Information:**

All rights reserved unless otherwise indicated. Contact the author or original publisher for any necessary permissions. eScholarship is not the copyright owner for deposited works. Learn more at [http://www.escholarship.org/help\\_copyright.html#reuse](http://www.escholarship.org/help_copyright.html#reuse)



eScholarship  
University of California

---

eScholarship provides open access, scholarly publishing services to the University of California and delivers a dynamic research platform to scholars worldwide.

Charge Carrier Dynamics in Transition Metal Oxides Studied by  
Femtosecond Transient Extreme Ultraviolet Absorption Spectroscopy

By

Chang-Ming Jiang

A dissertation submitted in partial satisfaction of the

requirements for the degree of

Doctor of Philosophy

in

Chemistry

in the

Graduate Division

of the

University of California, Berkeley

Committee in charge:

Professor Stephen R. Leone, Chair

Professor Richard J. Saykally

Professor Holger Müller

Summer 2015

Charge Carrier Dynamics in Transition Metal Oxides Studied by  
Femtosecond Transient Extreme Ultraviolet Absorption Spectroscopy

Copyright 2015

by

Chang-Ming Jiang

## Abstract

Charge Carrier Dynamics in Transition Metal Oxides Studied by  
Femtosecond Transient Extreme Ultraviolet Absorption Spectroscopy

by

Chang-Ming Jiang

Doctor of Philosophy in Chemistry

University of California, Berkeley

Professor Stephen R. Leone, Chair

With the ability to disentangle electronic transitions that occur on different elements and local electronic structures, time-resolved extreme ultraviolet (XUV) spectroscopy has emerged as a powerful tool for studying ultrafast dynamics in condensed phase systems. In this dissertation, a visible-pump/XUV-probe transient absorption apparatus with femtosecond resolution was constructed to investigate the carrier relaxation dynamics in semiconductors after photo-excitation. This includes timescales for carrier thermalization by carrier-carrier and carrier-phonon scattering. The 30 – 72 eV photon energy coverage (17 – 40 nm wavelength) generated by a table-top XUV light source is suitable for probing the 3p-to-3d core level absorptions of various transition metal oxides (TMOs) with specificities to elements and oxidation states.

In Chapter 1, a brief introduction to charge carrier dynamics in semiconductor-based materials is given. In addition, fundamentals of core-level spectroscopy and the high harmonic generation (HHG) process are also addressed in this introductory chapter. Specifications of the experimental apparatus that was constructed are summarized in Chapter 2, including the design concepts and characterization of performance. Chapter 3 presents the spectral tunability of the XUV pulses generated from a semi-infinite gas cell (SIGC), as well as the data acquisition procedures. Charge carrier relaxation dynamics in  $\text{Co}_3\text{O}_4$  following the charge transfer excitation pathway at 400 nm are documented in Chapter 4. In Chapter 5, various visible pump wavelengths are used to excite  $\text{Co}_3\text{O}_4$  and the differences in the carrier dynamics versus excitation wavelength are considered. After selectively photoexciting a Si/TiO<sub>2</sub> heterojunction, the resulted electron transfer process is observed and reported in Chapter 6. The concluding remarks of the dissertation are made in Chapter 7, while several ongoing time-resolved experiments are addressed in the Appendix sections.



*To my parents*



# Contents

<b>Chapter 1</b>	<b>Introduction</b>	<b>1</b>
<b>1.1</b>	<b>Charge Carrier Dynamics in Semiconductor</b>	<b>1</b>
1.1.1	Electronic Structure of a Semiconductor	1
1.1.2	Carrier Relaxation Pathways	6
1.1.3	Interfacial Charge Transfer	10
<b>1.2</b>	<b>XUV and Core Level Spectroscopy</b>	<b>12</b>
1.2.1	Core Level Transitions	12
1.2.2	XUV Light Sources	15
1.2.3	X-ray Absorption Spectroscopy	15
1.2.4	Transient X-ray/XUV Absorption Spectroscopy	19
<b>1.3</b>	<b>High-Order Harmonic Generation</b>	<b>19</b>
1.3.1	Three-Step Model	20
1.3.2	Phase Matching	23
1.3.3	Semi-Infinite Gas Cell	26
1.3.4	Two-Color Gating and Even-Order Harmonics	29
<b>Chapter 2</b>	<b>Design and Construction of the Transient XUV Absorption Apparatus</b>	<b>33</b>
<b>2.1</b>	<b>Ultrafast Laser System</b>	<b>35</b>
2.1.1	Femtosecond Chirped Pulse Amplifier	35
2.1.2	Characterization of Pulse Duration	37
<b>2.2</b>	<b>Optical Layout</b>	<b>38</b>
2.2.1	Probe Beam Path	39
2.2.2	Pump Beam Path	39
<b>2.3</b>	<b>Optical Parametric Amplifiers</b>	<b>40</b>
2.3.1	Concepts	40
2.3.2	Home-built Noncollinear Optical Parametric Amplifier	42
2.3.3	TOPAS	44
<b>2.4</b>	<b>Vacuum Chamber Assembly</b>	<b>48</b>
2.4.1	High Harmonic Generation Chamber	48
2.4.2	Refocusing Chamber	51
2.4.3	Sample Chamber	54
2.4.4	XUV Spectrometer Chamber	56
<b>2.5</b>	<b>Future Improvements</b>	<b>60</b>
<b>Chapter 3</b>	<b>Characterization of High-Order Harmonics and Experimental Principles</b>	<b>63</b>
<b>3.1</b>	<b>Effect of Laser Focus Position</b>	<b>63</b>
3.1.1	Harmonic Flux	64
3.1.2	Spectral Broadening and Blueshift	65
3.1.3	XUV Focus Size	67
3.1.4	Effects on Ar Harmonics	68
<b>3.2</b>	<b>Variation in the Gas Pressure</b>	<b>70</b>
3.2.1	Harmonic Flux	70
3.2.2	Spectral Blueshift	71
3.2.3	XUV Focus Size	73
3.2.4	Effects on Ar Harmonics	74
<b>3.3</b>	<b>Generation of Even-Order Harmonics</b>	<b>75</b>

<b>3.4 Chirp Dependence of High Harmonic Spectra</b>	<b>76</b>
<b>3.5 Data Acquisition Procedures</b>	<b>78</b>
3.5.1 Daily Check List for System Performance	78
3.5.2 Static XUV Absorption Spectrum	80
3.5.3 Transmission Map	81
3.5.4 Overlap of Pump and Probe Beams	82
3.5.5 Transient XUV Absorbance Measurements	84
<b>Chapter 4 Characterization of Photo-Induced Charge Transfer and Hot Carrier Relaxation Pathways in Spinel Cobalt Oxide (<math>\text{Co}_3\text{O}_4</math>)</b>	<b>87</b>
4.1 <i>Introduction</i>	88
4.2 <i>Experimental Methods</i>	91
4.3 <i>Results and Discussion</i>	94
4.3.1 Static XUV Absorption Spectrum and Fitting Results	94
4.3.2 Photo-Induced XUV Absorbance Changes at Cobalt M-edge	96
4.3.3 Femtosecond Charge Carrier Dynamics in $\text{Co}_3\text{O}_4$	101
4.4 <i>Conclusions</i>	105
<b>Chapter 5 Pump Wavelength Resolved Excited-State Dynamics in Spinel Cobalt Oxide (<math>\text{Co}_3\text{O}_4</math>)</b>	<b>107</b>
5.1 <i>Experimental Methods</i>	107
5.2 <i>Results and Discussion</i>	108
5.2.1 Initial Excited-State Spectra	110
5.2.2 Effect of Carrier Thermalization	111
5.2.3 Difference in Excited-State Dynamics	112
5.3 <i>Conclusions</i>	114
<b>Chapter 6 Observing Photo-Induced Electron Transfer Dynamics in a Type II Si/TiO<sub>2</sub> Heterojunction</b>	<b>115</b>
6.1 <i>Introduction</i>	115
6.1.1 Semiconductor Doping	116
6.1.2 Heterojunction	118
6.2 <i>Experimental Methods</i>	120
6.2.1 Sample Preparation and Characterization	120
6.2.2 Valence Photoemission	122
6.2.3 Transient XUV Absorbance at the Ti M <sub>2,3</sub> -edge	123
6.3 <i>Results and Discussion</i>	124
6.3.1 Alignment of Energy Bands	124
6.3.2 Electron Transfer from p-Si to n-TiO <sub>2</sub>	126
6.4 <i>Conclusions and Perspectives</i>	128
<b>Chapter 7 Outlook and Conclusion</b>	<b>131</b>
<b>Appendix</b>	<b>129</b>
A. <i>Excited-State Dynamics of Iron Pyrite</i>	133
B. <i>Pump-Probe Measurement on Fe<sub>2</sub>O<sub>3</sub> Nanoparticles</i>	137
C. <i>Pump-Probe Measurement on Co<sub>3</sub>O<sub>4</sub> Nanocubes</i>	139
<b>Bibliography</b>	<b>143</b>

# List of Figures

1-1	Interpretation of energy band by the tight-binding model. (a) Discrete energy levels in an atomic potential. (b) In a periodic lattice, interactions between atoms broaden atomic energy level to energy bands.	4
1-2	Energy band alignment of the first-row transition metal oxides in the case of (a) Mott-Hubbard semiconductor, and (b) charge transfer semiconductor.	5
1-3	Examples of relaxation mechanisms of a photo-excited carrier from the creation to the recombination.	6
1-4	Schematic of Auger relaxation processes in addition to the (middle) carrier-phonon scattering channel. (left) Excess energy can be transferred from electron to hole prior to the phonon relaxation. (right) Carrier multiplication splits a high-energy exciton into two excitons, while the reverse Auger recombination process reduces the density of charge carriers.	9
1-5	(a) The Marcus model for non-adiabatic electron transfer ( $H_{DA} \ll \lambda$ ) for a homogenous donor-acceptor (D-A) pair. (b) Modified Marcus model when the conduction band of a semiconductor is accepting an electron from the donor (excited chromophore $S^*$ ). (c) Schematic of corresponding energy levels in the electron injection process.	11
1-6	Schematic comparison of core level transitions that are excited by X-ray or XUV radiations, with electronic transitions within the valence levels that are excited by photon frequencies in the infrared to ultraviolet range.	13
1-7	(a) Static $M_{2,3}$ -edge X-ray absorption spectra of selected first-row transition metal oxides. (b) $M_{2,3}$ -edge X-ray absorption spectra of spinel $Co_3O_4$ , amorphous $CoS_x$ and cubic pyrite $CoS_2$ .	14
1-8	An X-ray absorption process excites a core electron into the empty density of states in the semiconductor conduction band. In the final state $\Phi_f$ the conduction band contains one extra electron, while a core hole is created in the core level.	16
1-9	X-ray absorption process in the laboratory scale. An X-ray absorption spectrum can be acquired either by measuring the ratio between $I$ to $I_0$ at each specific photon energy, or by measuring the yield of electrons (TEY), ions (TIY) and photons (TFY).	18
1-10	The three-step model for high harmonics generation describes the sequential interactions between a noble gas atom and an intense electric field.	21
1-11	Selected classical electron trajectories plotted in the position-velocity plane. Adapted from [46].	22
1-12	The same phase velocities between the laser field and the XUV emission allow coherent addition among individual noble gas atoms, so that the high harmonic intensity grows with distance.	24
1-13	The schematic design of a semi-infinite gas cell (SIGC) as an XUV light source.	27

1-14	The influence of varying the laser focus position $z_f$ relative to the end of semi-infinite gas cell.	29
1-15	HHG processes at (a) without, (b) intermediate and (c) full two-color gating conditions.	30
2-1	Schematic of the table-top transient XUV absorption apparatus.	34
2-2	Output infrared spectra of (a) the prism-based Ti:Sapphire oscillator, and (b) the chirped pulse Ti:Sapphire amplifier.	35
2-3	The operating principle of chirped pulse amplification.	36
2-4	Scanning knife-edge traces on the (a) horizontal and (b) vertical directions for the chirped pulse amplifier output.	36
2-5	(a) Illustration and (b) image of the home-built intensity autocorrelator.	37
2-6	(a) Second-order harmonic spectra acquired at various time delays $\tau$ in the autocorrelator. (b) Plot of the integrated second-order harmonic intensity to time delay $\tau$ . The red line gives a fit of $35.8$ fs $\text{sech}^2$ -shaped peak. (c) Retrieved spectrum and spectral phase using the FROG analysis technique. (d) Retrieved laser pulse electric field and the associated phase by the same FROG analysis scheme.	38
2-7	The optical layout for (a) SHG and (b) THG processes. (c) The spectra of second and third harmonic of the 800 nm infrared light (red).	40
2-8	(a) Conceptual scheme of the optical parametric amplification process. (b) Phase matching in a noncollinear OPA interaction geometry.	41
2-9	Optical layout of the home-built noncollinear OPA.	42
2-10	(a) Selected tunable output spectra of the home-built NOPA. (b) Intensity autocorrelation trace for 530 nm NOPA output wavelength.	43
2-11	Detailed layout of TOPAS, a two-stage OPA system that converts femtosecond infrared input to tunable wavelength visible output. Courtesy of Light Conversion Ltd.	45
2-12	Tunable output spectra of TOPAS. (a) SFS: Sum frequency of the signal beam and the 800 nm pump beam. (b) SFI: Sum frequency of the idler beam and the 800 nm pump beam. (c) SHS: Second harmonic of the signal beam. (d) SHI: Second harmonic of the idler beam.	46
2-13	The TOPAS output power at various wavelengths at 1kHz repetition rate.	47
2-14	(a) Second-harmonic FROG trace of the 520 nm TOPAS output. (b) Retrieved electric field and temporal phase by the FROG analysis.	48
2-15	Design of the semi-infinite gas cell in the high harmonic generation chamber. The optical layout for two-color gating technique is also drawn in the same scale.	49
2-16	(a) The purple-colored argon plasma observed during the high harmonic generation process and (b) the resulted high-order harmonic spectrum. (c) The orange-colored neon plasma and (d) the corresponding neon high-order harmonics.	50

2-17	(a) Reflectivity of a gold surface for 60 eV XUV photons at different incidence angles. (b) Reflectivity vs. photon energy curve at 86° incidence angle for a gold surface with 10Å root mean square roughness.	52
2-18	XUV beam path from the SIGC exit to the X-ray CCD detector.	52
2-19	Nominal profile of the infrared fundamental beam focused by the toroidal mirror, the image is acquired with a beam profiler placed in the sample chamber.	53
2-20	Knife-edge scan traces for integrated high-order harmonics produced with (a) 20 Torr of Ar and (b) 80 Torr of Ne at 1.8 mJ fundamental infrared energy.	54
2-21	Top view of the interaction geometry between the solid-state sample and pump and probe beams. The sample is supported on either a 100 nm Si <sub>3</sub> N <sub>4</sub> window, or a 250 nm Si membrane.	55
2-22	(a) Front view of the solid-state sample mounting system. The supporting substrate can be either a Si <sub>3</sub> N <sub>4</sub> window (left) or a Si membrane (middle). A 300 µm diameter pinhole (Right) is used to find the spatial overlap between the visible pump beam and the XUV probe beam. The arrows indicate the sample raster directions. (b) XUV transmission curves of 100 nm Si <sub>3</sub> N <sub>4</sub> window and 250 nm Si membrane.	55
2-23	Design of the liquid flow cell module (top view).	56
2-24	Configuration of the XUV spectrometer.	57
2-25	(a) Transmitted XUV spectra of a sample gas cell that is either (red) filled with xenon or (black) empty detected by the X-ray CCD camera in the spectrometer. (b) Raw absorption spectrum of xenon in the CCD camera pixel space.	58
2-26	(a) Reference points and the fit curve for wavelength calibration of the XUV spectrometer. (b) The xenon static absorption spectrum in the wavelength (photon energy) space.	59
2-27	The Voigt function fitting results for the (a) 4d <sup>-1</sup> ( <sup>2</sup> D <sub>5/2</sub> )6p( <sup>2</sup> P <sub>3/2</sub> ), (b) 4d <sup>-1</sup> ( <sup>2</sup> D <sub>5/2</sub> )7p( <sup>2</sup> P <sub>3/2</sub> ) and (c) 4d <sup>-1</sup> ( <sup>2</sup> D <sub>3/2</sub> )7p( <sup>2</sup> P <sub>1/2</sub> ) states.	60
2-28	Transmission of XUV of 200 nm thick Al and Zr.	61
3-1	High harmonic spectra generated from a semi-infinite gas cell filled with 80 Torr, recorded at different laser focus position $z_f$ .	64
3-2	Plot of the intensities of individual Ne harmonics with respect to the laser focus position $z_f$ . (a) Intensities of lower-order harmonics (H29 - H37). (b) Intensity of higher-order harmonics (H39 – H47).	65
3-3	(a) The 45 <sup>th</sup> -order Ne harmonic exhibits significant spectral broadening and ~150 meV energy blueshift as the laser focus is translated into the XUV-generating gas cell. (b) Evolution of the Ne harmonic spectra with decreasing $z_f$ positions.	66
3-4	(a) Center photon energies of the H33, H39, and H45 generated in 80 Torr Ne at 1.8 × 10 <sup>15</sup> W/cm <sup>2</sup> electric field intensity. (b) The linear energy blueshifting rate shows a linearly increasing relation with the harmonic order $q$ .	67

3-5	(a) XUV beam sizes measured at the sample location by the scanning knife-edge method. (b) The vertical beam sizes (FWHM) for individual harmonic orders.	68
3-6	(a) High harmonic spectra generated from a semi-infinite gas cell filled with 35 Torr Ar using ~45 fs pulses with 1.5 mJ energy at 800 nm center wavelength, recorded at different laser focus position $z_f$ . (b) H27 and H29 exhibit spectral broadening and blueshifting as $z_f$ value becoming more negative, while H33 shows the opposite, a spectral redshifting. (c) Intensities of individual harmonics versus the laser focus position $z_f$ . Quadratic fits for H21 – H29 are also plotted as solid curves.	69
3-7	Spectra of Ne harmonics with 40, 60, 80 and 100 Torr gas pressure, respectively.	70
3-8	(a) Intensities of different harmonic orders to the Ne gas pressure in the SIGC, illustrated on a logarithmic scale. (b) Pressure-dependent intensities of Ne H45, measured at three different laser focus positions.	71
3-9	The variation of harmonic energies of H45, H39, and H33 to the Ne pressures.	72
3-10	(a) XUV focus size (vertical FWHM) measured in the sample chamber by scanning knife-edge method, as a function of Ne pressures used for generating high-order harmonics. (b) The vertical beam sizes (FWHM) for individual harmonic orders.	73
3-11	(a) Evolution of the Ar harmonic spectrum with respect to the gas pressure. (b) and (c) Pressure dependence of intensities of different Ar harmonic orders.	74
3-12	(a) Spectral blueshift of Ar harmonics caused by increasing pressure. Linear correlations are found between the harmonic energy and the Ar pressure. (b) The spectral blueshifting rates of different harmonic orders.	75
3-13	Effects of two-color gating on the Ne harmonic spectrum. About 30 $\mu$ J of 400 nm pulses are superimposed with the fundamental field in the semi-infinite gas cell. The zero time delay is defined as when the even-order harmonics are most intense.	76
3-14	(a) Images of Ne harmonics directly detected on the X-ray CCD camera. The corresponding integrated high harmonic spectra for the five images are shown in (b) separately on the same logarithmic scale.	77
3-15	Influence of chirping the infrared pulses to the Ar harmonic spectrum that is generated from a 35 Torr gas cell, with two-color gating technique employed.	78
3-16	Optical components that are critical to the infrared alignment through the SIGC.	79
3-17	Nominal beam profiles of (a) the 800 nm fundamental field and (b) the 400 nm symmetry-breaking field, detected by a CCD beam profiler.	80
3-18	(a) The XUV spectra transmitted through a 100 nm bare $\text{Si}_3\text{N}_4$ substrate (black dotted line) and a $\text{Fe}_2\text{O}_3$ thin-film supported on a $\text{Si}_3\text{N}_4$ substrate (red solid line). (b) The $\text{Fe}_2\text{O}_3$ absorption spectrum after averaging 32 sets of transmitted spectra through the sample and the substrate.	81
3-19	XUV transmission maps of (a) a thin-film $\text{TiO}_2$ on a 250 nm Si substrate, (b) a $\text{CoS}_x$ thin-film on a 250 nm Si substrate prepared by electrodeposition, and (c) a dispersion of $\text{Co}_3\text{O}_4$ nanocubes on a 100 nm $\text{Si}_3\text{N}_4$ substrate.	82

3-20	Procedure for spatial overlap between the visible pump and the XUV probe beam under a high vacuum condition.	83
3-21	(a) Cross-correlation between the 800 nm beam that follows the XUV beam path and the 400 nm pump beam. (b) The Co M-edge response to the 800 nm optical excitation. The signal rise is fit with a $39.5 \pm 10.8$ fs error function.	83
3-22	The LabVIEW data acquisition program for time-resolved experiments, the circled numbers indicate the sequence of command/trigger for acquiring one set of pump on/off XUV transmission spectra.	84
3-23	Plot of 46 set time delay values (x-coordinate) to the recorded actual values (black dots, y-coordinate).	85
4-1	(a) Illustration of the crystal structure of spinel $\text{Co}_3\text{O}_4$ . Red: oxygen <i>fcc</i> sublattice. Blue: $\text{Co}^{2+}$ ions occupying tetrahedral sites. Green: $\text{Co}^{3+}$ ions occupying octahedral sites. (b) Six possible optical excitation pathways in $\text{Co}_3\text{O}_4$ .	88
4-2	UV/Vis absorption spectrum of thin-film $\text{Co}_3\text{O}_4$ on a quartz substrate prepared by the same procedure as described in the section 4-2.	89
4-3	Layout of the transient XUV absorption instrument.	91
4-4	(a) Selected area electron diffraction (SAED) pattern of spinel $\text{Co}_3\text{O}_4$ thin-film. (b) Electron diffractogram of spinel $\text{Co}_3\text{O}_4$ thin-film measured before and after pump-probe experiment.	92
4-5	Raman spectrum of fresh (black) and illuminated (red) spinel $\text{Co}_3\text{O}_4$ thin-film measured by micro-Raman technique.	92
4-6	Red line: Spectrum of near-infrared (NIR) pulses used for high harmonics generation in a semi-infinite gas cell. Blue line: Second-order harmonics of near-infrared generated by frequency-doubling in a 100 $\mu\text{m}$ thick type-I $\beta\text{-BaB}_2\text{O}_4$ (BBO).	93
4-7	Static M-edge absorption spectrum of $\text{Co}_3\text{O}_4$ in the extreme ultraviolet region. Black line: experimental spectrum. Red line: spectrum calculated by charge transfer multiplet model. Blue sticks and dashed line: tetrahedrally coordinated $\text{Co}^{2+}$ absorption contribution. Green sticks and dashed line: octahedrally coordinated $\text{Co}^{3+}$ absorption contribution. The 1:2 $\text{Co}^{2+}/\text{Co}^{3+}$ stoichiometric ratio has been accounted for.	94
4-8	(a) Transient extreme ultraviolet (XUV) spectra near the cobalt M-edge. Optical excitation is by 2.33 $\mu\text{J}$ pump energy at 400 nm wavelength. (b) Transient absorbance traces at 55.7, 60.4, 62.4, 65.0, and 72.4 eV.	96
4-9	(a) Experimental contour plot in the first 2 ps after the pump beam excitation. (b) Reconstructed contour plot from global fit results using a two-component sequential model.	97
4-10	Retrieved evolutional spectra by a two-component sequential model global fit. Black solid line: the excited state A immediately after 400 nm photoexcitation. Red solid line: the long-lived state B that the initial excited state A decays into. Red dotted line: state B spectrum after being normalized to the same peak amplitude as state A. Inset: Populations	

of state A and B versus time. It identifies a  $190 \pm 10$  fs decay time constant ( $1/k$ ) convoluted with a 45 fs Gaussian instrumental response function. 97

- 4-11 Differential XUV absorption spectra between ground state and calculated (a) LMCT excited states, (b) MMCT excited states and (c) *d-d* excited states. Spectra in blue lines indicate  $\text{Co}^{2+}$  in tetrahedral site receives an electron from oxygen or  $\text{Co}^{3+}$ . Spectra in green lines indicate  $\text{Co}^{3+}$  in octahedral site receives an electron from oxygen or  $\text{Co}^{2+}$ . Experimentally obtained transient spectra of the initial excited state A (black dashed line) and the long-lived state B (red dotted line) have been normalized and overlaid with calculated spectra. 100
- 4-12 (a) The differential XUV absorption spectra between ground state  $\text{Co}^{2+}$  (high-spin,  $^4\text{A}_2$ ) and calculated *d-d* excited states. (b) The differential XUV absorption spectra between ground state  $\text{Co}^{3+}$  (low-spin,  $^1\text{A}_1$ ) and calculated *d-d* excited states. 103
- 4-13 (a) Kinetics traces at 62.40 eV (maximum amplitude of the enhanced absorbance) as 400 nm pump beam energy varies from 0.86 to 2.70  $\mu\text{J}$ . (b) Decay time constants by global fit based on a two-component sequential model. 103
- 4-14 Top: Transient absorbance traces at 61.2, 62.0 and 64.0 eV at 2.33  $\mu\text{J}$  400 nm pump energy. Bottom: Processed traces after normalizing the maximum amplitude of every transient spectrum after the pump-probe temporal overlap. Solid lines are fitted by a two-component sequential model global fit with a 535 fs time constant. 104
- 5-1 UV/visible absorption spectrum of  $\text{Co}_3\text{O}_4$  (black line) and spectral profiles of the pump beam at 400 (blue), 480 (cyan), 520 (green), 595 (orange) and 800 (red) nm wavelengths. 108
- 5-2 Experimental contour plots of transient absorbance signals with respect to the pump-probe time delay (x-axis) and the XUV photon energy (y-axis). Each plot corresponds to a different pump wavelength: (a) 400 nm, (b) 480 nm, (c) 520 nm, (d) 595 nm, and (e) 800 nm. 109
- 5-3 Transient absorbance spectra of the initial excited states created by optical excitations at various wavelengths. 110
- 5-4 Transient absorbance changes at early pump-probe delays using (a) 400 nm, (b) 520 nm, (c) 595 nm, and (d) 800 nm as the pump wavelength. 112
- 5-5 Comparison of transient absorbance traces at 62.4 eV using three different pump wavelengths. 113
- 5-6 Retrieved spectra evolution assuming a sequential three-component model global fit at (a) 520 nm, (b) 595 nm, and (c) 800 nm pump wavelengths. Insets: population evolution curves for the three spectral components. 114
- 6-1 Dopant in a semiconductor alters charge carrier concentration by introducing new energy levels in the band gap. 117
- 6-2 In an anatase  $\text{TiO}_2$  crystal, each  $\text{Ti}^{4+}$  ion (blue) is 6-fold coordinated while each  $\text{O}^{2-}$  ion (red) is 3-fold coordinated. An oxygen vacancy (pink) would make the three surrounding  $\text{Ti}$  ions (dark blue) partially reduced. In addition, extra  $\text{Ti}^{3+}$  ions can diffuse into interstitial sites. 117

6-3	Energy band alignments for each type of semiconductor heterojunction.	118
6-4	Band diagram of the <i>p</i> -Si/ <i>n</i> -TiO <sub>2</sub> heterojunction. (a) Each semiconductor has a characteristic Fermi energy $E_F$ and a band gap $E_g$ separating the conduction band minimum $E_c$ and the valence band maximum $E_v$ . (b) Energy bands of two semiconductors are aligned with respect to the same vacuum level, which has energy $\chi$ above $E_c$ . Note that the charge carriers are not at a thermal equilibrium yet. (c) Charge carrier diffusion causes the band bending and the depletion region near the <i>p</i> - <i>n</i> junction. An electric field is also induced by the charged regions near the interface.	119
6-5	Schematic of the experimental setup used for sample preparation and characterization. The chamber on the left is responsible for cleaning of Si (100) substrate, evaporation of Ti and generation of TiO <sub>2</sub> , and Auger electron spectroscopy (AES). Optical layout on the right denotes where the Ar high harmonic emission is generated, energetically dispersed, and then refocused into the sample chamber for valence photoemission spectroscopy (PES) studies. Courtesy of Dr. Mihai E. Vaida.	121
6-6	(a) Auger electron spectrum of the as-prepared clean Si(100) surface (black line), and the spectra taken after deposition of metallic Ti metal (red line) or an oxidized TiO <sub>2</sub> thin-film (blue line). (b) Ti/Si Auger electron signal ratio with respect to the Ti evaporation time.	122
6-7	Static XUV absorption spectrum of a <i>n</i> -TiO <sub>2</sub> film prepared on a <i>p</i> -Si(100) substrate.	122
6-8	Experimental configuration for the 520 nm-pump/XUV-probe measurement of the Si/TiO <sub>2</sub> heterojunction.	123
6-9	(a) Energy spectrum of the 520 nm pump pulses. The spectral bandwidth is 9 nm / 10.3 THz. (b) Intensity autocorrelation trace of the pump pulses by a 50 μm thick BBO (type I, θ = 48°).	124
6-10	Photoemission spectra of 5 ML Ti evaporated on Si(100) substrates at different oxygen partial pressures. The 27 <sup>th</sup> -order Ar harmonic emission ( $E_{ph} = 40.8$ eV) is used to ionize the electrons in the valence levels.	125
6-11	Schematic of the pump-probe experiment on the Si/TiO <sub>2</sub> system and the relevant band diagram. Energy band alignment between two semiconductor forms a type II heterojunction, and additional defect states caused by the oxygen vacancies are ~1.0 eV below the TiO <sub>2</sub> conduction band.	126
6-12	(a) Contour plot of the XUV absorbance change ΔmOD between 31 – 49 eV energy region (x-axis) with respect to the pump-probe time delay (y-axis). (b) Transient absorbance spectra measured on the Si/TiO <sub>2</sub> heterostructure at different times after the 520 nm photo-excitation. In the top panel, the static XUV absorption spectrum of TiO <sub>2</sub> is overlaid for comparison.	127
6-13	(a) Transient absorbance traces at 34.5 (black) and 43.6 eV (red). The fit curve for 34.5 eV is a 60 fs wide Gaussian instrument response function convoluted with a $75 \pm 37$ fs exponential decay. The fit curve for 43.6 eV is a $54 \pm 38$ fs exponential rise convoluted with a $79 \pm 32$ fs exponential decay. (b) Transient absorbance trace at 38.9 eV, fit by the instrument response function and an exponential raise with $254 \pm 95$ fs time constant.	128

A-1	Simplified band structure of FeS <sub>2</sub> . The Fe 3d orbitals are split into <i>e<sub>g</sub></i> and <i>t<sub>2g</sub></i> levels by the local <i>O<sub>h</sub></i> symmetry, and the S 3p orbitals in the S <sub>2</sub> <sup>2-</sup> dimer form bonding and anti-bonding orbitals. The conduction band of FeS <sub>2</sub> is strongly hybridized between the Fe <i>e<sub>g</sub></i> and S 3p orbitals, while the top of the valence band is contributed solely by the Fe <i>t<sub>2g</sub></i> orbitals.	133
A-2	Static XUV absorption spectrum of FeS <sub>2</sub> and Fe <sub>2</sub> O <sub>3</sub> at the Fe M-edge.	134
A-3	(a) Contour plot of the excited-state XUV absorbance changes after the 800 nm excitation with respect to pump-probe time delays. (b) Lineouts at 55.6 and 66.8 eV show, respectively, an enhanced absorbance and a bleaching signal; both appear faster than the 40 fs instrument response function. A $118 \pm 28$ fs exponential decay leads to a long-lived state.	134
A-4	Retrieved spectral evolution by a two-component sequential model global fit. Black solid line is the transient absorption spectrum of the initially created excited state A, which then undergoes a $118 \pm 28$ fs decay into state B (red solid line). The thin red line in the state B spectrum normalized at the same maximum amplitude as state A. Inset: Population of state A and B at different pump-probe time delays.	135
A-5	(a) The optical microscope image shows damaged spots on a FeS <sub>2</sub> thin-film after illumination by a 400 nm pump beam. Spacing between adjacent spots matches the 100 $\mu\text{m}$ step size used for the raster scan. (b) Change of static FeS <sub>2</sub> XUV absorption spectrum after 400 nm illumination.	136
B-1	Static XUV absorption spectra at the Fe M-edge of thin-film Fe <sub>2</sub> O <sub>3</sub> (grey line) and Fe <sub>2</sub> O <sub>3</sub> nanoparticles (blue line), respectively.	137
B-2	(a) Transient XUV absorption spectra of Fe <sub>2</sub> O <sub>3</sub> nanoparticles after the 400 nm photoexcitation. (b) Kinetic traces at 55.0, 56.4, and 57.7 eV.	138
B-3	Transient XUV absorbance spectra obtained 100 fs after 3.0 $\mu\text{J}$ 400 nm photoexcitation. The spectrum measured from a thin-film sample (red) has three times signal amplitude when compared to the nanoparticle assembly.	138
C-1	(a) XUV transmission map of a $2 \times 2 \text{ mm}^2$ Si <sub>3</sub> N <sub>4</sub> substrate that is drop-cast with 5 nm Co <sub>3</sub> O <sub>4</sub> nanocubes. The static absorption spectra at the Co M-edge taken at locations c-f are compared in (b).	139
C-2	Raman spectra of thin-film and nanocube Co <sub>3</sub> O <sub>4</sub> , taken with 1.28 mW of 528 nm excitation in a 5 $\mu\text{m}$ diameter spot.	140
C-3	(a) Transient XUV absorption spectra of Co <sub>3</sub> O <sub>4</sub> nanocubes with 400 nm optical excitation. (b) Transient absorbance traces at 58.4 and 64.6 eV. (c) Transmission map of the same sample as in Fig. C-1(a), but taken after the pump-probe experiment. (d) Static XUV absorption spectra at location c and d labeled in Fig. C-1(a), after the pump-probe experiment the non-resonant absorption level exhibit a significant drop with the Co M-edge redshifted by $\sim 2$ eV.	141
C-4	Schematic of the proposed Co <sub>3</sub> O <sub>4</sub> degrading mechanism under light illumination. The pump pulses heat up the sample and facilitate the oxidation of the organic ligands surrounding the nanocubes. Since this process happens in a vacuum environment, Co atoms are reduced to lower oxidation states.	141

# List of Tables

2-1	Wavelength tuning range and available pulse energies for different TOPAS output modes. The pump wavelength is 800 nm with horizontal polarization. Pulse energies are obtained by dividing the output power by the 1 kHz repetition rate. <sup>a</sup> SH: second-order harmonic generation. <sup>b</sup> V: vertically polarized. H: horizontally polarized.	44
2-2	List of the reference points used for wavelength calibration of the XUV spectrometer, including the Al L <sub>3</sub> -edge cutoff on the neon harmonics, and several xenon $4d \rightarrow np$ resonant absorption lines.	59
4-1	Calculation and broadening parameters used for fitting of Co <sub>3</sub> O <sub>4</sub> ground state M-edge absorption spectrum. <sup>a</sup> Ratio relative to atomic parameters. <sup>b</sup> The variable Lorentzian linewidth $\Gamma$ is approximated by the formula $\Gamma = L_{\min} + dL^*(E - E_{\text{onset}})$ .	95
4-2	Cobalt oxidation states and electronic symmetries at tetrahedral and octahedral lattice sites at each possible excited states. <sup>a</sup> Numbers indicating excitation pathways can be referred to Figure 4-1(b).	98
5-1	Result of the global fit analysis for the transient absorption traces acquired with 400, 595, and 800 nm pump wavelengths. <sup>a</sup> Since the longest pump-probe time delay is usually much shorter than the fitting results, the values are only set as the lower limit of the lifetime. <sup>b</sup> Only up to 2.8 ps pump-probe time delay have been measured.	113



# Acknowledgements

First and foremost, I have to express appreciation to my research advisor Prof. Stephen Leone; this dissertation would never have been accomplished without his encouragement and financial support. During this six-year period of Ph.D study, Steve not only provided his scientific wisdoms whenever I encountered problems with research, but also constantly challenged me to become a better scientist. Thank you for providing me with such a great opportunity to work in this top-notch research environment. I would also like to thank the rest of my committee: Prof. Richard Saykally and Prof. Holger Müller, for their insightful comments in my qualifying exam up until the completion of this dissertation.

Since I found my passion towards chemistry in high school, I have been inspired by many great minds among classmates, teachers, and senior instructors. In particular, I am grateful to I-Chi Lee for showing me the door to the wonderful chemistry world. My sincere thanks also go to Prof. Jim-Min Fang and Prof. Tien-Yau Luh, who allowed me to join their synthetic research groups at the National Taiwan University. I am also immensely appreciative of Prof. Pi-Tai Chou, who was at first my quantum chemistry instructor then became my scientific advisor when I decided to step into the ultrafast spectroscopy. It was his encouragement and intrepid character that motivated me to pursue a graduate degree in this research field.

At Berkeley, I am blessed for having the pleasure of working with so many outstanding colleagues from around the world. Among whom Dr. Josh Vura-Weis and Dr. Robert Baker also contributed significantly to the instrument construction and the establishment of the data analysis scheme. I also thank Mihai Vaida, Hiroki Mashiko, Jim Prell, Martin Schultze, Andrey Gandman and Christian Ott for sharing their invaluable knowledge and experiences with me. I was also fortunate to join a research group that had many selfless senior graduate students: Erik Hosler, Allison Pymer, Ming-Fu Lin, Amy Cordones-Hahn, Christine Koh, and Andy Caughey, who were all willing to help me survive the depressing moments in graduate school.

Thanks are also extended to other fellow members of the Leone group for the summer softball experiences and innumerable discussions on science, culture, sports and movies, the list includes (but is not limited to) Amir Golan, Hsiang-An Chen, Terefe Habteyes, Teresa Bixby, Shirley Liu, Zephy Leung, Jordy Bouwman, Lorena Piticco, Adrian Pfeiffer, Scott Sayres, Birgitta Bernhardt, Desiré Whitmore, Jessica Lockyear, Krupa Ramasesha, Jeremy Axelrod, Denisia Popolan-Vaida, Nour Nijem, Theodora Nah, Annelise Beck, Aditi Bhattacharjee, Mazyar Sabbar and Henry Timmers. I also feel proud that Lucas Carneiro will be taking the reins of this research project that I have been working on for six years. He and other younger generations of graduate students, such as Andrew Attar, Lauren Borja, Marieke Jager, Natalie Gibson, Marina Yang and Chris Kaplan, will surely expand the current accomplishments in the Leone group to the next level. I would also like to express gratitude to officers and members of the Berkeley Association of Taiwanese Students. It is your organized events that helped me overcome the nostalgia. In particular, I was constantly motivated by Li-Chiang Lin's positive (sometimes mixed with a little obsessive) life attitude, as well as his devotion to research.

Special thanks are due to the facility supports from the College of Chemistry: Eric Grunland of the machine shop, Emanuel "Manny" Druga of the electrical shop, and Mike and his wood shop army. Administrative supports from Kathleen Fowler, Adam Bradford, Mary

Holloway and Patricia Jung have always bridged my needs to the Chemistry Department and LBNL. Lynn Keithlin and Aileen Harris of the Graduate Student Affairs Office also have helped tremendously since my first day at Cal.

Last but not least, I am deeply indebted to my family, especially my parents. They have sacrificed a lot in raising me from a baby to an individual, and allowed me to pursue my dream on the other side of the Pacific Ocean. I will always aim to be a person of benevolence and decency as you are.

# Chapter 1

## Introduction

Semiconductors have made tremendous impacts on human society over the last decades. Not only existing in integrated circuits that are used in virtually all electronic equipment, the ability of semiconductor materials to convert solar energy into electricity or chemical energy also makes them a promising solution for long term sustainable energy. Numerous efforts have been devoted to the manufacturing of innovative semiconductor-based devices, and the results are reflected by soaring device performances. The advance of nanotechnology also benefits the development of photovoltaic and photocatalytic devices; sophisticated control of the growth and morphology during nanomaterial synthesis provides more strategies for tailoring the electronic properties of semiconductors. In order to push the performance of these devices to the next level, it is crucial to gain a better understanding of how semiconductors respond to photoexcitation, and how do excited charge carriers relax before being extracted and stored as electrical or chemical energies. In this dissertation, a new spectroscopic approach is developed to observe and measure the charge carrier dynamics in semiconductors, mainly transition metal oxides (TMOs), in the femtosecond to picosecond timescales. The frequency of extreme ultraviolet (XUV) radiation, which is generated from femtosecond infrared pulses via the high harmonic generation (HHG) process, is high enough to probe the electronic transitions from atomic core levels to outer valence levels, thus possessing the ability to acquire invaluable element-specific information that is otherwise challenging for traditional spectroscopic methods. In this chapter, the current understanding of electronic structure and charge carrier dynamics in semiconductor materials is briefly summarized, as well as introductions to core level spectroscopy and the HHG technique.

### 1.1 Charge Carrier Dynamics in Semiconductor

#### 1.1.1 Electronic Structure of a Semiconductor

In an extended solid-state system that possesses crystallinity, i.e. the arrangement of atoms perfectly follows a periodic manner; the electronic structure is determined by both the properties of individual atoms and the crystal structure. When solving the Schrödinger equation for a single electron in such a crystalline solid, the effective potential demonstrates a periodicity  $U(\vec{r} + \vec{R}) = U(\vec{r})$  that corresponds to every Bravais lattice vector  $\vec{R}$ .

$$\left[ -\frac{\hbar^2}{2m_e} \nabla^2 + U(\vec{r}) \right] \psi = \varepsilon \psi \quad (1.1)$$

Eigenstates  $\psi$  of Eq. (1.1) may be represented in the form of a Bloch function<sup>1</sup> which is written as the product of a plane wave times a function  $u_{n\vec{k}}(\vec{r})$  with the same periodicity of the crystal lattice  $u_{n\vec{k}}(\vec{r}) = u_{n\vec{k}}(\vec{r} + \vec{R})$

$$\psi_{n\vec{k}}(\vec{r}) = e^{i\vec{k}\cdot\vec{r}} u_{n\vec{k}}(\vec{r}) \quad (1.2)$$

For a given crystal wave vector  $\vec{k}$  there are many solutions to the Schrödinger equation that are labeled by the band index  $n$ . Since the number of allowed  $\vec{k}$  is equal to the number of primitive cells, in an extended crystalline system  $\vec{k}$  varies almost continuously; the corresponding eigenvalues  $\varepsilon_n(\vec{k})$  thus also form a continuous distribution with an upper and lower bound, which is the so-called energy band. Different energy bands in a solid may overlap, but there also exist energy gaps that are forbidden to any electron. The electronic properties of a crystal is usually determined by how valence electrons fill the allowed energy bands, and these can be roughly categorized into three types: in an insulator energy bands are either entirely filled or entirely empty, and the band gap  $E_g$  that separates the highest occupied band (valence band) from the lowest unoccupied band (conduction band) is too large to be overcome by thermal excitations. As a result, the electrical resistivities of insulators are extremely high ( $\rho > 10^9 \Omega\text{-cm}$ ). On the other hand, the crystal behaves as a conductor if at least one partially occupied band exists, so that the electrons can respond to an electric field and conduct current ( $\rho < 10^{-8} \Omega\text{-cm}$ ). The third type, semiconductor, has moderate band gaps and electrical conductivities falling between conductors and insulators. Therefore some electrons can be thermally promoted to the conduction band and move freely, and the vacancies left in the valence band can also be filled by other electrons and act like positive charge carriers.

In a semiconductor, the electrons in the conduction band and the vacancies (holes) in the valence band move in opposite directions under an applied electric field. For an intrinsic semiconductor the electron and hole concentrations are equal ( $n_e = n_h = n_i$ ) and determined by both the band gap  $E_g$  and the temperature  $T$ :

$$n_i = \sqrt{N_c N_v} \exp\left(-\frac{E_g}{2k_B T}\right) \quad (1.3)$$

where  $k_B$  is the Boltzmann's constant,  $T$  is the absolute temperature, and  $N_c$  and  $N_v$  are the effective density of states in the conduction and valence band, respectively. For example, the carrier concentration in pure silicon is  $\sim 1.45 \times 10^{10} \text{ cm}^{-3}$  at 300 K. Other than the intrinsic electrons and holes, the charge carrier densities in a semiconductor can be manipulated by purposely adding defects or impurities (dopants) to the crystal in the case of an extrinsic semiconductor. The materials can either have very large electron concentrations ( $n$ -type semiconductor) or very large hole concentrations ( $p$ -type semiconductor), but the product of the concentrations of electrons and holes is still a temperature-dependent constant:

$$n_e \times n_h = n_i^2 = N_c N_v \exp\left(-\frac{E_g}{k_B T}\right) \quad (1.4)$$

The non-equal carrier concentrations caused by dopants may be explained by the introduction of allowed energy levels located within the original forbidden band gap. In  $n$ -type

semiconductors, these dopant states (donor levels) are near the conduction band minimum and provide extra electron concentrations by thermal excitations. These donor levels also shift the energy bands lower in energy such that the Fermi level is closer to the conduction band. Conversely, *p*-type semiconductors have empty dopant states (acceptor levels) right above the valence band maximum, and the Fermi level is shifted closer to the valence band. Dopant states in extrinsic semiconductors can make the majority carrier concentration several orders of magnitude greater than that of an intrinsic semiconductor, thus providing a sophisticated way to design devices such like diodes and transistors.

The Schrödinger equation (1.1) may be solved by two different approaches that each corresponds to an extreme scenario: either a collection of nearly free conducting electrons, or a collection of weakly interacting atoms. The first approach (nearly free electron model) views the solid as a free electron gas weakly perturbed by a periodic potential from the lattice consisting of cations, which is most suitable for describing the conducting electrons in metals and covalent semiconductors consisting of *s* and *p* electrons outside of a closed-shell noble gas electronic configuration. However, it is somewhat unrealistic to use the nearly free electron model on the core energy levels or more ionic crystals, where the electrons perceive a significant atomic potential. The second approach, the tight-binding model, treats the interactions between atoms as a modification to the localized atomic wavefunctions. As depicted in Fig. 1-1, the energy levels in an arbitrary lattice with very large interatomic distance are essentially the *N*-fold degeneracy version of the atomic levels, where *N* denotes the number of primitive cells in the crystal. But as the distance between neighboring atoms decreases, individual atomic orbitals start to overlap and discrete energy levels broaden into energy bands. The bandwidth of each energy band is proportional to the orbital overlap integral, thus at small interatomic spacing all the bands become wider. In the tight-binding model, the Bloch states  $\psi_{\vec{k}}(\vec{r})$  in (1.2) can be transformed to a set of Wannier functions  $\phi_{\vec{R}}(\vec{r})$  that are mutually orthogonal and maximally localized at each Bravais lattice vector  $\vec{R}$ :

$$\phi_{\vec{R}}(\vec{r}) = \frac{1}{\sqrt{N}} \sum_{\vec{k}} e^{-i\vec{k} \cdot \vec{R}} \psi_{\vec{k}}(\vec{r}) \quad (1.5)$$

Using Wannier functions as an alternative basis to describe a periodic one-electron Hamiltonian provides insights into localized phenomena in a material, such like chemical bonding and impurity states. Since the core level atomic wavefunctions (e.g. *1s* levels) are very confined and centered around the atom nuclei, their overlap integral with the nearest neighbor is negligible. Not only is a very narrow band formed in the solid state by these atomic wavefunctions, their distributions are very similar to the corresponding Wannier functions. On the other hand, the valence atomic wavefunctions range further from the nucleus and thus overlap extensively in a lattice. This leads to a larger energy spread in the energy band, and the Wannier functions would bear little resemblance to the isolated atomic orbitals.

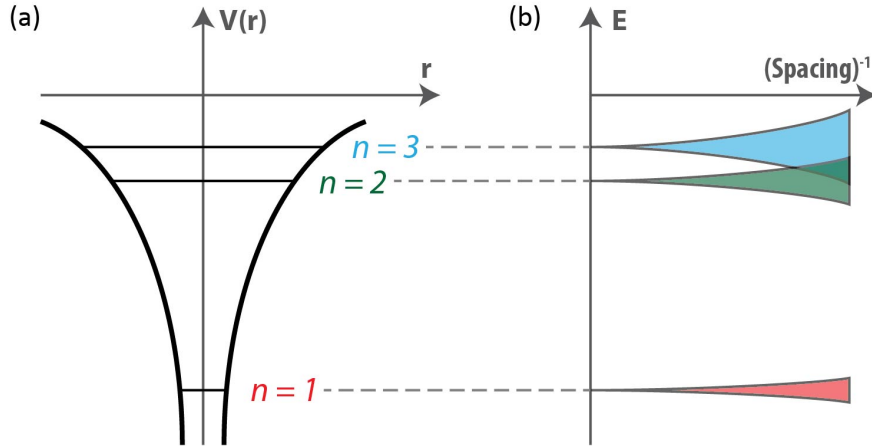


Figure 1-1: Interpretation of energy band by the tight-binding model. (a) Discrete energy levels in an atomic potential. (b) In a periodic lattice, interactions between atoms broaden atomic energy level to energy bands. Energy bands with higher energy tend to spread wider and in each band the bandwidth increases with decreasing interatomic spacing.

Both the nearly free electron model and the tight-binding model rely on the independent electron approximation, which either totally neglects the interaction between electrons or purposely oversimplifies it as part of the periodic potential perceived by a single electron. Nevertheless, the independent electron approximation fails to address crucial electron correlation effects, e.g. electrons with parallel spins would prefer to stay away from each other, which is usually non-periodic. This break down of the independent electron approximation is especially apparent when discussing materials with a partially filled  $d$ -shell, such as transition metals. Computational methods like the Hartree-Fock formalism or density functional theory are dedicated to the exact solution of interacting electron wavefunctions in a many-body system.

It should be noted that the compounds of transition metal oxides (TMOs), which are extensively investigated in this dissertation, tend to be predicted as conducting metals by one-electron theories due to the partially filled  $d$ -orbitals on the metal cations. Factually most TMOs have significant band gaps, e.g. 3.2, 2.1 and 1.6 eV for  $\text{TiO}_2$ ,  $\text{Fe}_2\text{O}_3$ , and  $\text{Cu}_2\text{O}$ , respectively; this suggests the correlation effects among  $d$  electrons play an important role in the electronic structure and the charge transport properties of these semiconducting materials. The Hubbard theory, which was initially proposed to explain the metal-insulator transition (“Mott transitions”) in some magnetic materials,<sup>2,3</sup> specify the four possible configurations on each ion site: either empty, occupied by one electron with either of two spins, or occupied by two electrons with opposite spins. The Hamiltonian of the Hubbard model is written as:

$$H = H_{\text{hop}} + H_{\text{int}} \quad (1.6)$$

in which the first component  $H_{\text{hop}}$  consists of the hopping integral describing the quantum mechanical probability that an electron hops between sites, while the interaction Hamiltonian  $H_{\text{int}}$  defines the short-ranged Coulomb repulsion energy if two electrons with opposite spins occupying the same site. It is the ratio between the matrix elements (called  $t$  and  $U$  for hopping and interaction Hamiltonian, respectively) that determines the magnetic properties and the electrical conductivity. In the limit of large on-site repulsion ( $U \gg t$ ) the  $d$ -band would be split

into the lower (filled) and higher Hubbard bands (unfilled) and the material acts like an insulator (or a semiconductor). In this scenario, charge fluctuations between adjacent  $d$ -orbitals

$$d_i^n d_j^n \rightarrow d_i^{n-1} d_j^{n+1} \quad (1.7)$$

require energy to overcome a band gap, which is dominated by the Coulomb repulsive interactions  $U_{dd}$ . Nevertheless, the transition metal cation is not the only species that can provide charge in a TMO compound. The charge transport in an ionic metal oxide can also happen via charge transfer from an oxygen  $2p$  level to a metal  $d$  level

$$d_i^n \rightarrow d_i^{n-1} \underline{L} \quad (1.8)$$

which leaves a positive charge on the oxygen ligand  $\underline{L}$ . The energy required for this charge transfer excitation is denoted as  $\Delta_{CT}$ , and the band gap property of transition metal compounds depends largely on the relation between  $U_{dd}$  and  $\Delta_{CT}$ .<sup>4</sup> Fig. 1-2 illustrates the two simplified cases: TMO can be either a Mott-Hubbard semiconductor ( $U_{dd} < \Delta_{CT}$ ), in which the band gap represents the Coulomb repulsion energy between the  $d$  electrons, or a charge transfer semiconductor ( $U_{dd} > \Delta_{CT}$ ) in which the charge transfer energy  $\Delta_{CT}$  determines the band gap. Although in reality both the lower Hubbard band and the oxygen  $2p$  band would each have a broad distribution of energies and thus overlap significantly in the valence band. The electronic structures of TMOs have inspired some debate in the last three decades between theory and experiments, although no consensus is yet to be made. Part of the works presented in this dissertation try to solve this mystery of TMO energies and excitation by means of core level spectroscopy, which will be introduced in the latter sections.

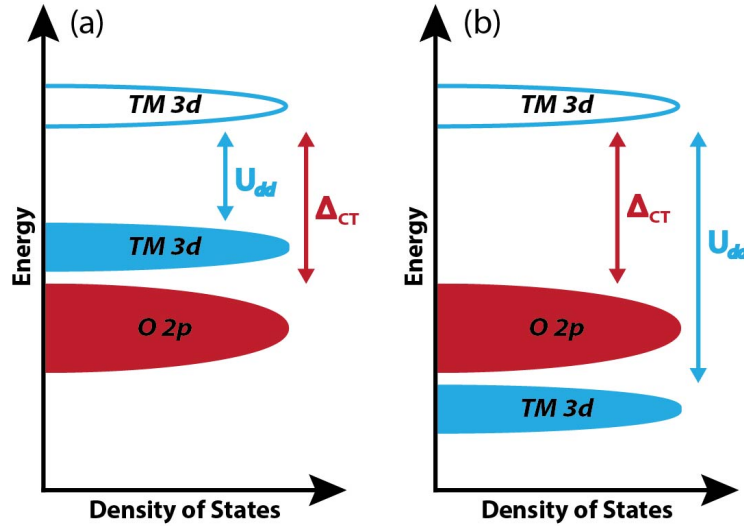


Figure 1-2: Energy band alignment of the first-row transition metal oxides in the case of (a) Mott-Hubbard semiconductor, and (b) charge transfer semiconductor. The Coulomb interaction and exchange energy  $U_{dd}$  indicates the separation between the upper (unfilled) and lower (filled) Hubbard bands in an open  $d$ -shell material. Charge transfer energy  $\Delta_{CT}$  represents the energy required to move an electron from oxygen  $2p$  levels into the upper Hubbard band.

### 1.1.2 Carrier Relaxation Pathways

Instead of being thermally excited, charge carriers in semiconductors can also be created by light absorption if the photon energy is larger than the band gap ( $\hbar\omega > E_g$ ). Like the electronic transitions in molecular systems, the photo-excitation of a valence electron into the conduction band occurs instantaneously and interrupts the thermodynamic equilibrium in the semiconductor. The excited charge carriers (both electrons and holes) will undergo various relaxation mechanisms over a wide range of time scales and eventually re-establish the thermodynamic equilibrium. Fig. 1-3 summarizes several characteristic stages in a “life cycle” of charge carriers: starting from the creation of excitonic states, to the thermalization among carriers, followed by cooling of hot carriers to the band edges, and lastly the recombination of electrons and holes.

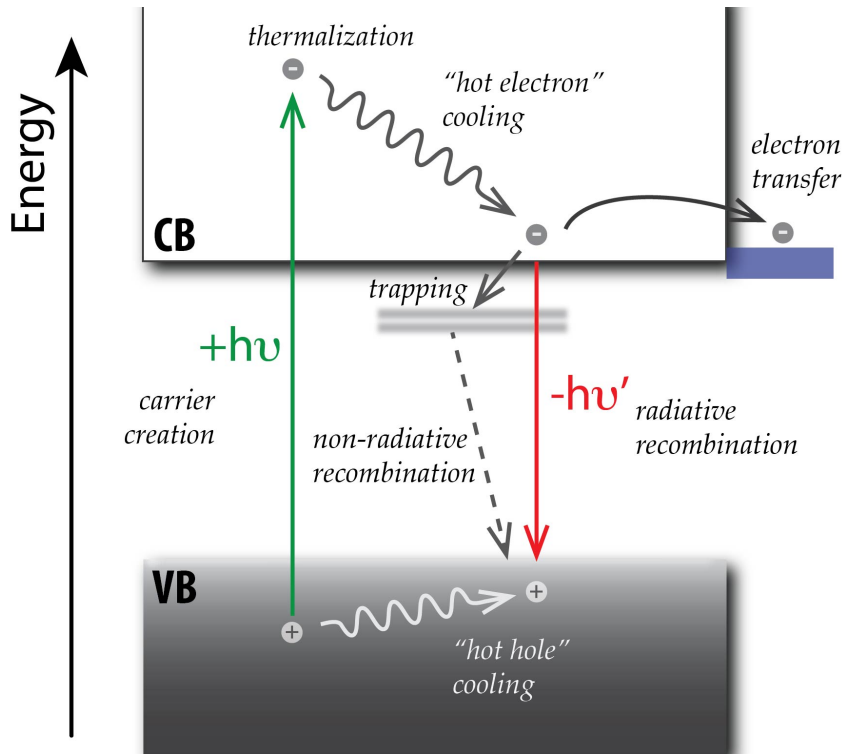


Figure 1-3: Examples of relaxation mechanisms of a photo-excited carrier from the creation to the recombination. Thermalization of carriers takes place shortly after the excitation, and then is followed by the carrier-phonon scattering that relaxes the hot carriers (both electrons and holes) to the band edges. Trapping of carriers can occur in the presence of defect and/or impurity states, which would also facilitate non-radiative recombination to the static state. Extraction of carriers prior to the recombination plays an important role in photovoltaic and photocatalytic applications.

Right after the photo-excitation the charge carriers are in a non-thermal regime, i.e. the carrier energy distribution in an ensemble does not follow Fermi-Dirac statistics. These excited carriers can exchange energy by scattering with each other in few-fs timescales and eventually are thermalized to a quasi-equilibrium state. Carrier thermalization is one of the fastest dynamics in a semiconductor, usually accomplished in less than 100 fs after the photo-excitation; thus the

related spectroscopic studies are largely limited by the laser pulse durations. Because the thermalization process is mediated by the Coulomb interaction between electrons, its rate is expected to be faster at a higher carrier density. Due to the variation in effective masses, electrons and holes may be thermalized at different rates. The carrier-carrier scattering times in both the bulk GaAs and the GaAs-GaAlAs quantum-well structures have been studied by the femtosecond photon echo technique and exhibit an  $n^{-1/D}$ -dependence for carrier density  $n$  and dimensionality  $D$ .<sup>5</sup> Besides thermalization, excitons can also be formed in parallel during the carrier-carrier scattering events, i.e. the Coulomb force between an electron-hole pair results in a bound excitonic state. In materials with small dielectric constants, the averaged distance between electron and hole (exciton radius) is comparable to the interatomic spacings, and the strongly bound excitons (binding energy > 100 meV) are referred as the Frenkel excitons. Conversely, Wannier excitons with small binding energy (1 – 10 meV) are more delocalized, and are often found in a highly dielectric material.

After the thermalization, carriers may have reached an energy distribution that can be characterized by a temperature in the Fermi-Dirac function, but this equilibrium temperature is still higher than the lattice temperature. The “cooling” of “hot carriers” represents the energy dissipation from carriers to the surrounding lattice and usually takes place in time scales ranging from 100 fs to 100 ps, depending on the material and the type of lattice vibrational mode involved. The periodicity of the lattice allows quantized collective vibrational modes that can be excited in the unit of a phonon. If a unit cell contains more than one atom, the lattice would exhibit two types of phonons: acoustic phonons and optical phonons. According to whether the displacements of atoms are perpendicular or parallel to the phonon propagation direction, each type of phonon can be further divided into transverse or longitudinal modes. Among all types of phonon modes the longitudinal optical (LO) phonons are most likely to interact with charge carriers in a polar semiconductor. This scattering phenomena is not only important for charge transport, also plays a crucial role in the relaxation of photoexcited carriers. The energy loss rate from an electron to a LO phonon mode with vibrational frequency  $\omega_{LO}$  can be described through the Fröhlich interaction:<sup>6</sup>

$$W(E) = 2\alpha\omega_{LO}\sqrt{\frac{\hbar\omega_{LO}}{E}} \left\{ \langle n \rangle_{LO} \sinh^{-1} \left( \frac{E}{\hbar\omega_{LO}} \right) + (\langle n \rangle_{LO} + 1) \sinh^{-1} \left[ \left( \frac{E}{\hbar\omega_{LO}} \right) - 1 \right] \right\} \quad (1.9)$$

where  $\langle n \rangle_{LO}$  is the phonon occupation number given by Bose-Einstein statistics

$$\langle n \rangle_{LO} = \frac{1}{\exp \left[ \frac{\hbar\omega_{LO}}{k_B T} \right] - 1} \quad (1.10)$$

With a large amount of excess energy ( $E \gg \hbar\omega_{LO}$ ), the scattering rate expression (1.9) would approximate to  $2\alpha\omega_{LO}$ , where  $\alpha$  is called the Fröhlich coupling coefficient:<sup>7</sup>

$$\alpha = \frac{e^2}{\hbar c} \sqrt{\frac{m_e c^2}{2\hbar\omega_{LO}}} \left( \frac{1}{\epsilon_\infty} - \frac{1}{\epsilon_0} \right) \quad (1.11)$$

where  $m_e$  is the electron mass, and  $\epsilon_\infty$  and  $\epsilon_0$  are the optical and static dielectric permittivities, respectively. Based on Eq. (1.9) to (1.11), it can be seen that the electron-phonon scattering rate is largely affected by both the phonon frequency and the lattice temperature. The hot carrier cooling process can thus create a significant amount of phonon population, and the associated lattice vibrational motions have been experimentally observed.<sup>8,9</sup> In a lattice the presence of a photoexcited electron can also shift the surrounding atoms out of the equilibrium in order to screen the charge of the electron. This deformation of the lattice would follow the electron when it is moving, and can be viewed as a fermionic quasi-particle called a polaron. Formation of a polaron can locally stabilize the lattice, but meanwhile decrease the electron mobility. At the weak coupling limit the self-energy of a polaron  $\Delta E$  can be approximated as<sup>7</sup>

$$\frac{\Delta E}{\hbar\omega_{LO}} \approx -\alpha - 0.0123\alpha^2 \quad (1.12)$$

and the effective mass  $m^*$  of a polaron can be represented by

$$m^* \approx m_e \left( 1 + \frac{\alpha}{6} + 0.025\alpha^2 \right) \quad (1.13)$$

The carrier-phonon scattering forms a main channel of energetic relaxation in the 100 fs – 100 ps time span after the photoexcitation, but several other relaxation mechanisms can also happen in parallel to assist both electrons and holes to reach the band edges (Fig. 1-4). If a high excitation density is employed, or the charge carriers are spatially confined (e.g. quantum dots), then Auger relaxation pathways would start to participate. The simplest Auger process is the energy transfer from electron to hole, which due to its larger effective mass is easier to be relaxed by phonon scattering. In some material when the excitation photon frequency is high enough ( $\hbar\omega > 2E_g$ ), the created hot exciton can split into two lower energy excitons. This exciton multiplication phenomenon is of scientific interest because each photon absorbed would produce two or more excitons, which can help increase the quantum efficiency of solar cells. In some other cases the opposite of exciton multiplication, i.e. Auger recombination/ionization, can happen and reduce the charge carrier density.

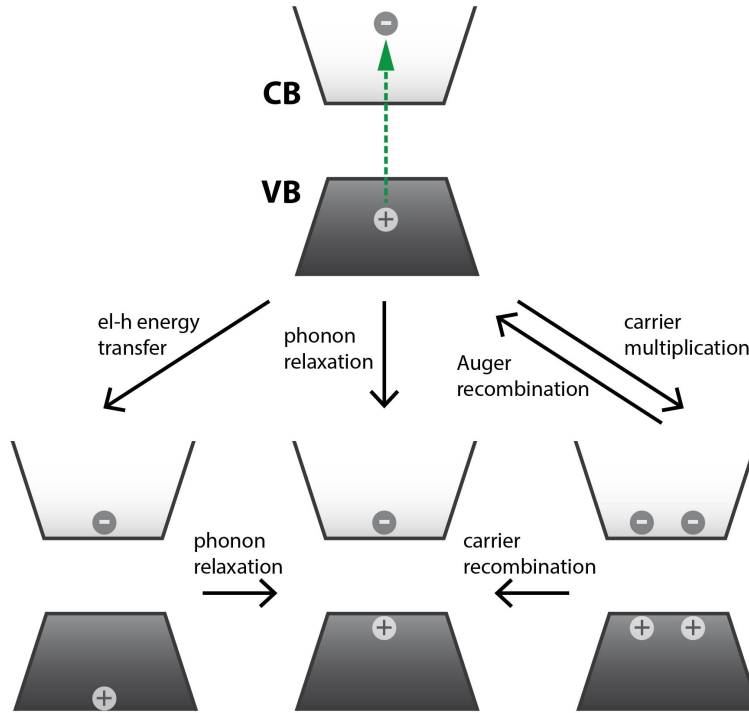


Figure 1-4: Schematic of Auger relaxation processes in addition to the (middle) carrier-phonon scattering channel. (left) Excess energy can be transferred from electron to hole prior to the phonon relaxation. (right) Carrier multiplication splits a high-energy exciton into two excitons, while the reverse Auger recombination process reduces the density of charge carriers.

At the end of the phonon relaxation regime, all types of carriers would share the same temperature with the lattice, however there is still an excess amount of carriers at the edge of both the conduction and valence bands. The re-establishment of thermodynamic equilibrium can take place by the emission of one photon, and this radiative recombination time for a semiconductor ranges from nanoseconds to microseconds. In a non-perfect crystal (which is mostly the case) there exist different types of defects, e.g. atom vacancies, dangling bonds, and impurities; these defects not only alter the transport properties of the semiconductor, but also contribute additional energy levels in the band gap. These mid-gap defect states are likely to trap carriers and lead to non-radiative recombination, which would decrease the quantum efficiency of emission. For applications like quantum dot light emitting diodes (QLEDs), the surface defects of the semiconductor are often passivated with ligands or another material, so that nearly-unity emission quantum yield can be achieved. In photovoltaic and photocatalytic applications, the excited carriers need to be extracted out prior to recombination so that the band gap can be exploited to drive current or chemical reactions. Therefore the device efficiencies are strongly influenced by the interplay between carrier cooling, recombination, trapping, and extraction; a large portion of this dissertation will aim for a better understanding of carrier dynamics in the condensed phase systems.

### 1.1.3 Interfacial Charge Transfer

Other than the carrier relaxation pathways in a single component semiconductor, charge transfer to and from an inorganic semiconductor are also important to both fundamental science and industrial applications. These nanoscale and ultrafast charge transfer processes have been extensively investigated by both theoretical modeling and experimental spectroscopies.<sup>10-12</sup> Charge carrier migration can occur either between two semiconductors with different band gaps, which is often referred as a heterojunction system, or between a semiconductor and a electron donor/acceptor at the interface or in the solution. The later case can be further separated into four categories based on the direction of current flow and the type of charge carrier involved: (a) electron transfer from conduction band of a semiconductor to an electrolyte/chromophore, (b) electron injection from an excited chromophore to the conduction band, (c) hole transfer from the valence band to an electrolyte/chromophore, and (d) hole injection from a chromophore to a semiconductor. The most well-known application for type (a) and (c) charge transfers is the water splitting reaction, in which the hydrogen evolution reactions (HER) and the oxygen evolution reactions (OER) take place near the conduction and valence bands, respectively.<sup>13</sup> The type (b) electron injection is a crucial step in dye-sensitized solar cells (DSSCs) when an *n*-type semiconductor is used as the electron acceptor;<sup>11</sup> while type (d) hole injection, although not frequently investigated, has been reported on sensitized *p*-type semiconductor electrodes.<sup>14</sup>

In 1985, Marcus proposed a model to address the nonadiabatic electron transfer process in a homogeneous donor-acceptor system.<sup>15</sup> The total energy of a donor-acceptor (D-A) pair is largely affected by the surrounding dielectric environment, and the potential can be approximated as a parabola with respect to solvent reorganization (Fig. 1-5(a)). The separation in the reaction coordinate between the initial (D-A) and final ( $D^+$ - $A^-$ ) states is reflected by an energy  $\lambda$  that defines the extent of reorganization required for the electron transfer to take place, and in the non-adiabatic limit the electronic coupling between donor and acceptor  $H_{DA}$  is weak compared to the reorganization energy  $\lambda$ . The electron transfer rate constant can thus be represented by Fermi's Golden Rule as follows:

$$k_{ET} = \frac{2\pi}{\hbar} |H_{DA}|^2 \frac{1}{\sqrt{4\pi\lambda k_B T}} \exp\left[-\frac{(\lambda + \Delta G)^2}{4\lambda k_B T}\right] \quad (1.14)$$

where  $k_B$  is the Boltzmann's constant,  $T$  is the absolute temperature, and  $\Delta G$  is the total change of Gibbs free energy. Eq. (1.14) predicts that the maximum rate would be achieved when the reaction free energy cancels out the reorganization energy ( $\Delta G = -\lambda$ ), so that the electron transfer process becomes barrier-less. At more negative  $\Delta G$ , which is the so-called Marcus inverted region, electron transfer would be slowed down despite the reaction being more thermodynamically favorable.

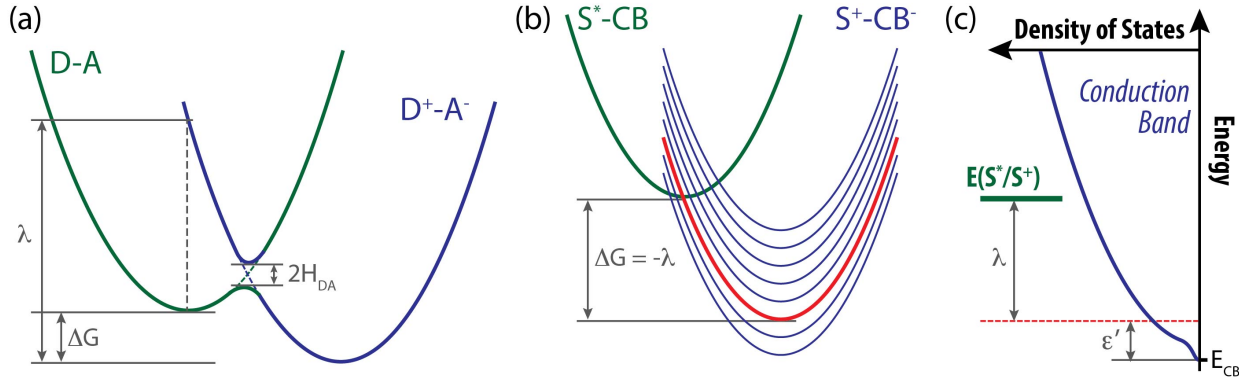


Figure 1-5: (a) The Marcus model for non-adiabatic electron transfer ( $H_{DA} \ll \lambda$ ) for a homogenous donor-acceptor (D-A) pair. (b) Modified Marcus model when the conduction band of a semiconductor is accepting an electron from the donor (excited chromophore  $S^*$ ). The red parabola denotes the barrierless electron transfer, where the reaction free energy equals to the reorganization energy  $\lambda$ . (c) Schematic of corresponding energy levels in the electron injection process. The conduction band consists of a continuous distribution of empty states that is each  $\varepsilon'$  higher than the band edge  $E_{CB}$ .

In the case of electron injection from an excited chromophore  $S^*$  into a semiconductor, one major deviation from the original Marcus theory is the continuous distribution of acceptor levels in the conduction band. In Fig. 1-5(b) this is visualized by using a series of parabolas to represent all the possible  $S^+ \text{-} \text{CB}^-$  states. The density of states  $\rho(\varepsilon')$  defines the number of accessible levels in a semiconductor with energy  $\varepsilon'$  higher than the conduction band minimum  $E_{CB}$ , and each level is electronically coupled to the chromophore by a coupling parameter  $H(\varepsilon')$ . The total electron transfer rate is the sum of individual rate constants and can be written as follows:<sup>16</sup>

$$k_{ET}^{total} = \frac{2\pi}{\hbar} \frac{1}{\sqrt{4\pi\lambda k_B T}} \int_0^\infty d\varepsilon' \rho(\varepsilon') |H(\varepsilon')|^2 \exp\left\{-\frac{[\lambda + E_{CB} + \varepsilon' - E(S^*/S^+)]^2}{4\lambda k_B T}\right\} \quad (1.15)$$

The barrier-less electron transfer, similar to its molecular equivalent, happens to the electron accepting level at  $\lambda$  below the chromophore level, as depicted in the red parabola and dashed line in Fig. 1-5(b) and 1-5(c), respectively. However, the Marcus inverted region is not expected for the electron injection process due to the presence of continuous empty states in the conduction band. Instead the electron transfer rate obtained with Eq. (1.15) would keep increasing at larger driving forces (more separation between  $E(S^*/S^+)$  and  $E_{CB}$ ), but the rate variation becomes less dramatic in the region that the driving force is greater than the reorganization energy.

Electron flow from a semiconductor to a chromophore can be similarly modeled by the modified Marcus theory.<sup>17</sup> In this scenario, the electron transfer rate  $k_{ET}(\vec{k}, \vec{r})$  would have a dependence on both the wave vector  $\vec{k}$  of the donor electronic state in the conduction band, and the position of the chromophore  $\vec{r}$  relative to the interface. The first order electron transfer rate constant, which is independent of the chromophore concentration, can thus be represented as

$$k_{ET}^{total} = \frac{1}{\sigma} \int_{\vec{r}} k_{ET}(\vec{r}) d^3\vec{r} = \frac{1}{\sigma} \int_{\vec{r}} \left( \sum_{\vec{k}} k_{ET}(\vec{k}, \vec{r}) \right) d^3\vec{r} \quad (1.16)$$

where  $\sigma$  is the surface area of the interface. Assuming the electron density in the conduction band is low enough, the transfers of each electron are independent events; in the non-adiabatic limit the summation of Eq. (1.16) can be carried out as follows

$$k_{ET}^{total} = \frac{2\pi}{\hbar} \frac{1}{\sqrt{4\pi\lambda k_B T}} \int_0^\infty d\varepsilon' \rho(\varepsilon') \langle |\bar{H}(\varepsilon')| \rangle \times \exp \left[ -\frac{(\lambda + \Delta G^0 - \varepsilon')}{4\lambda k_B T} \right] \quad (1.17)$$

where  $\Delta G^0$  is the energy difference from the conduction band edge to the chromophore state, and  $\rho(\varepsilon')$  and  $\langle |\bar{H}(\varepsilon')| \rangle$  are the density of states and electronic coupling normalized in an unit cell, respectively.

## 1.2 XUV and Core Level Spectroscopy

### 1.2.1 Core Level Transitions

Since femtosecond lasers were first developed in the 1980s,<sup>18</sup> ultrafast pump-probe spectroscopy has become an important tool for studying fast chemical processes that cannot be captured by either mechanical or electronic shutters. Photo-induced processes, especially, are the main focus of femtosecond spectroscopy. Since the interaction between the atom and photon occurs extremely fast, the temporal resolution is usually limited by how short a single light pulse can be prepared. Examples include photo-dissociation of molecules,<sup>19</sup> photo-induced energy and electron transfer,<sup>20</sup> vibrational wavepackets<sup>21</sup> and photocatalytic reactions.<sup>22</sup> In pump-probe spectroscopy, the studied system would interact with the first ultrashort laser pulse (“pump pulse”), and after a controlled time delay a second pulse (“probe pulse”) detects how the system responds to the initial interaction with photon. Various types of information can be obtained by using different electromagnetic frequencies as the probe. For example, the energy separation between the highest-occupied molecular orbital (HOMO) and the lowest-unoccupied molecular orbital (LUMO) can usually be excited by absorbing an ultraviolet or visible photon, thus using UV/Vis pulses as the probe is sensitive to the electronic structure change in a molecule (Fig. 1-6). The vibrational levels of each electronic state, on the other hand, need to be excited by infrared radiation, so that transient infrared spectroscopy is able to detect the light-induced structure changes.

As semiconductors started being utilized for manufacturing photovoltaic and photocatalytic devices, more ultrafast spectroscopic research has been directed toward photo-induced charge carrier dynamics, which has been briefly introduced in the previous section. The traditional UV/visible or IR transient absorption spectroscopy, however, encounters a huge challenge when studying solid-state systems: the discrete energy levels in the molecular systems become continuous energy bands in condensed phases, such that the electronic transitions between energy bands exhibit larger linewidths when compared to their molecular analogues. This makes the assignment and interpretation of the observed absorbance changes in the excited states an extremely nontrivial and challenging task.

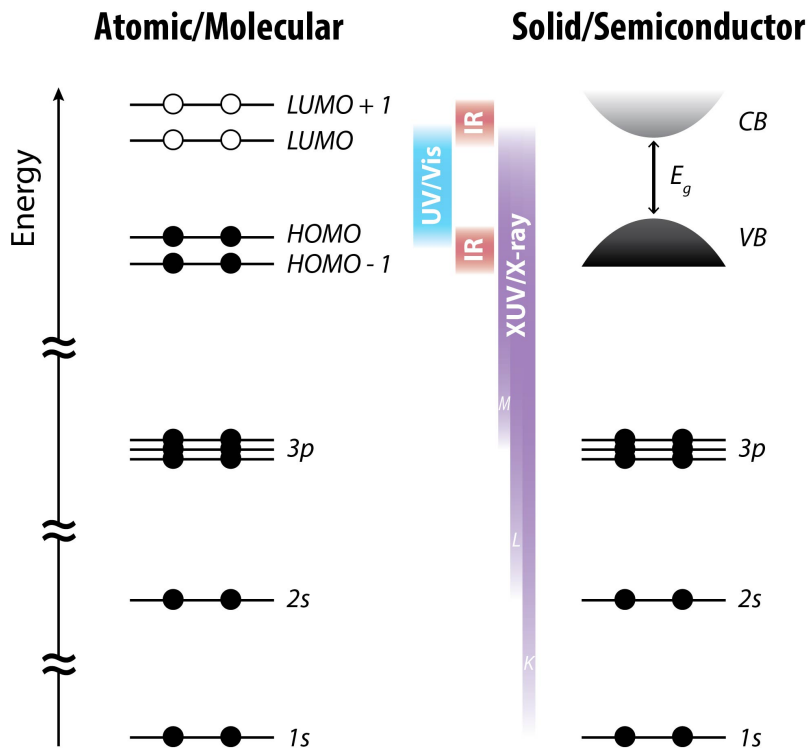


Figure 1-6: Schematic comparison of core level transitions that are excited by X-ray or XUV radiations, with electronic transitions within the valence levels that are excited by photon frequencies in the infrared to ultraviolet range. The solid-state effect broadens the valence levels to energy bands, while the core levels remain discrete energetically.

Since the electronic wavefunctions of core levels are more confined, in an extended lattice the overlap between neighboring atomic orbitals is negligible, and therefore the core levels stay spatially localized and energetically discrete (Fig. 1-6). Nomenclature for core level transitions is based on the principal quantum numbers of core levels: K-edge for  $1s$  orbitals, L-edges for  $2s$  and  $2p$  orbitals, and M-edges for  $3s$  and  $3p$  orbitals. In order to excite an electron from core levels to valence levels, electromagnetic radiation in the extreme ultraviolet (XUV) and X-ray range is required. For example, K-edge transitions of first-row transition metals need several kilo-electronvolts (keV) to excite, while the binding energies for L-edge are in the 400 – 1000 eV range. The  $M_{2,3}$ -edge transitions from  $3p$  orbitals, which are the main focus of this dissertation, are excited by photons with 40 – 100 eV energy, which corresponds to XUV radiation.

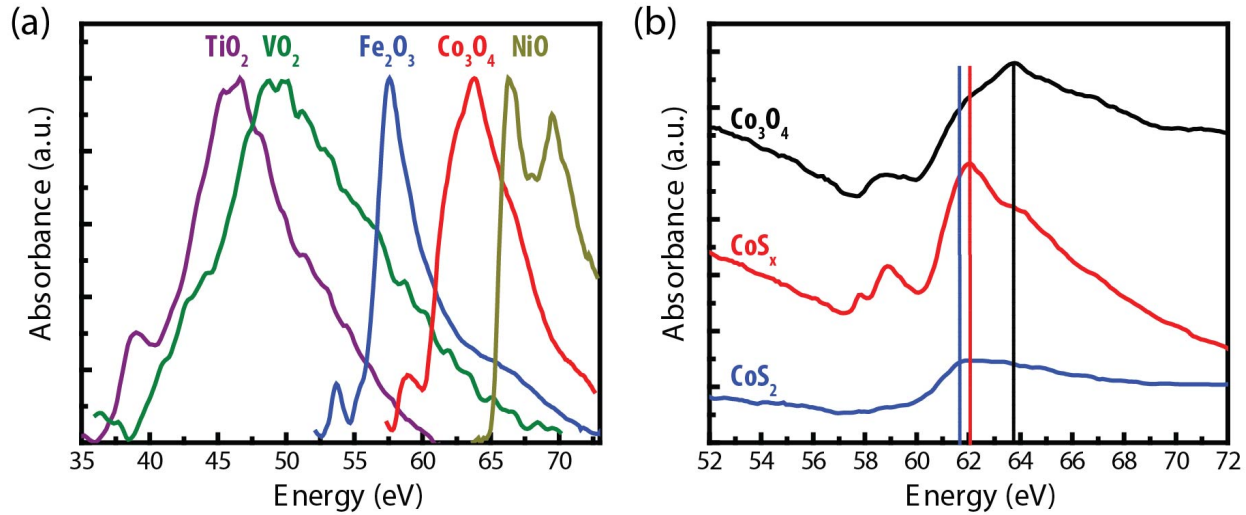


Figure 1-7: (a) Static  $M_{2,3}$ -edge X-ray absorption spectra of selected first-row transition metal oxides. (b)  $M_{2,3}$ -edge X-ray absorption spectra of spinel  $Co_3O_4$ , amorphous  $CoS_x$  and cubic pyrite  $CoS_2$ .

Using core level transitions as the probe in ultrafast spectroscopy could be advantageous in several aspects. First, since core levels retain significant atomic character, their binding energies are element-specific.  $M_{2,3}$ -edge absorption spectra of several first-row TMOs are shown in Fig. 1-7(a), which clearly exhibits an increasing  $3p$  electron binding energy with atomic number, starting from 47 eV for  $TiO_2$ , 49 eV for  $VO_2$ , to 58 eV, 64 eV and 67 eV for  $Fe_2O_3$ ,  $Co_3O_4$  and  $NiO$ , respectively. Moreover, for the same element, variation in oxidation states would also affect the core level binding energies. Empirically the L-edge absorption of transition metals exhibits an  $\sim 1.5$  eV blue-shift for each oxidation state increase.<sup>23</sup> In the M-edge, the Co  $3p$  binding energy of spinel cobalt oxide ( $Co_3O_4$ ) is about 1 eV higher than that of amorphous cobalt sulfide and cubic cobalt disulfide (Fig. 1-7(b)), which matches well with the difference in average oxidation states. The specificities to elements and chemical valence suggest that when a semiconductor heterojunction is photoexcited, local electronic structure changes induced by the newly-created charge carriers would also affect the core level transitions; therefore monitoring all the element-specific energy regions provides a way to “track” the carrier location in a complicated heterojunction system at different time delays after the excitation. If two compounds contain the same element with the same oxidation state, only differ in the detailed arrangement of electronic spins, their individual spectroscopic features are also distinguishable by the core level transitions. This has been demonstrated on the Fe L<sub>3</sub>-edge absorption between the low-spin ( $^1A_{1g}$ ;  $(t_{2g})^6$ ) and high-spin ( $^5T_{2g}$ ;  $(t_{2g})^4(e_g)^2$ ) configurations of the  $[Fe(tren(py)_3)]^{2+}$  complex.<sup>24</sup> The covalence of chemical bonding may also be probed by core level transitions, as the L-edge absorption of ionic  $MnF_2$  shows sharper features comparing to the more covalent  $MnO$ .<sup>23</sup> In summary, core level transitions provide systematic information on elements, chemical valence, spin multiplicities, and bonding character. This information is complementary to what can be acquired with ultraviolet, visible, and infrared spectroscopic techniques, and it is especially useful for studying electronic structures of condense phase systems.

### 1.2.2 XUV Light Sources

With the ability to provide unambiguous information, core level transitions have been utilized as an important research tool in various fields of chemistry, biology, geography and astronomy. Related core level techniques include X-ray absorption spectroscopy (XAS), X-ray photoemission spectroscopy (XPS), X-ray emission spectroscopy (XES), electron energy loss spectroscopy (EELS) and coherent X-ray diffraction imaging (CXDI). The majority of these works has been carried out at synchrotron facilities, which provide coherent electromagnetic radiation by accelerating electrons through magnetic fields. Beamlines in the third-generation synchrotron light sources use bending magnets and undulators to generate a smooth continuous range of photon energies (10 – 10,000 eV) with extremely high photon flux that is one billion times brighter than the sun. Temporal profile of synchrotron radiations is typically quasi-continuous, i.e. emitted as a train of  $\sim$ 100 ps bunches at a several hundred MHz repetition rate, depending on how fast the electrons make round trips in the storage ring and how many electron bunches are injected. In order to detect ultrafast dynamics, additional pulse-slicing techniques<sup>25</sup> can be exploited to reduce the pulse duration to  $\sim$ 100 fs. Several fourth-generation light sources, X-ray free electron lasers (FELs), are able to provide peak brightnesses that are several orders of magnitude greater than the third-generation sources, as well as highly coherent pulses with 100 fs or shorter duration.

Alternatively, XUV pulses can be generated by converting femtosecond infrared pulses to high-order harmonics, which is a highly nonlinear process called high harmonic generation (HHG). The maximum achievable photon only exceeds 1000 eV, and the photon flux is at least ten orders of magnitude lower than synchrotron light sources. The availability of commercial Ti:Sapphire laser amplifiers, however, is much greater than that of the synchrotron facilities. XUV radiation generated by HHG are already in the form of attosecond pulse trains enclosed in an envelope function with a temporal width that is no more than the duration of fundamental pulses (<100 fs). These ultrashort XUV pulses are used as the probe beam in the pump-probe spectroscopy in this dissertation. The theory describing the HHG process will be described later in Sec. 1.3.

### 1.2.3 X-ray Absorption Spectroscopy

Like other types of absorption spectroscopy, X-ray absorption spectroscopy (XAS) measures the sample's absorption of X-ray radiation as a function of photon energy. The “absorption edge” is named after the core electron that is excited: *K*-, *L*-, and *M*-edges corresponding to the principle quantum numbers  $n = 1, 2$ , and  $3$ , respectively. Both the filled valence band and the empty conduction band of a semiconductor are drawn in Fig. 1-8, together with an arbitrary and filled core level with a relatively discrete energy distribution. Because of the Pauli exclusion principle, excitation of core electrons to the valence band is forbidden, thus the lowest possible core level transition goes to the bottom of the conduction band. Comparing to the initial state  $\Phi_i$  prior to X-ray absorption, the final state  $\Phi_f$  has an electron vacancy in the core level (“core hole”) and an extra electron in the conduction band. Fermi’s Golden Rule states that the transition probability  $W_{fi}$  from  $\Phi_i$  to  $\Phi_f$  is given by:

$$W_{fi} = \frac{2\pi}{\hbar} \left| \langle \Phi_f | \hat{T} | \Phi_i \rangle \right|^2 \delta(\hbar\omega - \varepsilon' + \varepsilon_c) \quad (1.18)$$

where  $\hat{T}$  is the transition operator. For a one-photon XAS process that is dominated by the electric dipole transition (electric quadrupole is neglected), Eq. (1.18) can be written as<sup>26</sup>

$$W_{fi} = \frac{e^2}{\hbar c} \frac{4\omega^3}{3c^2} n \sum_q \left| \langle \Phi_f | \vec{e}_q \cdot \vec{r} | \Phi_i \rangle \right|^2 \delta(\hbar\omega - \epsilon' + \epsilon_c) \quad (1.19)$$

where  $n$  is the number of photons and  $\vec{e}_q$  is the polarization vector of a photon. This can be further simplified by assuming the absorption process does not affect all other electrons (not really a valid assumption and will be addressed in a later section), so that the initial state is reduced to the core level wavefunction  $c$ , while the final state is a free electron wavefunction  $\epsilon$ :

$$\left| \langle \Phi_f | \vec{e}_q \cdot \vec{r} | \Phi_i \rangle \right|^2 \approx \left| \langle \Phi_i | \epsilon | \vec{e}_q \cdot \vec{r} | \Phi_i \rangle \right|^2 = \left| \langle \epsilon | \vec{e}_q \cdot \vec{r} | c \rangle \right|^2 = M^2 \quad (1.20)$$

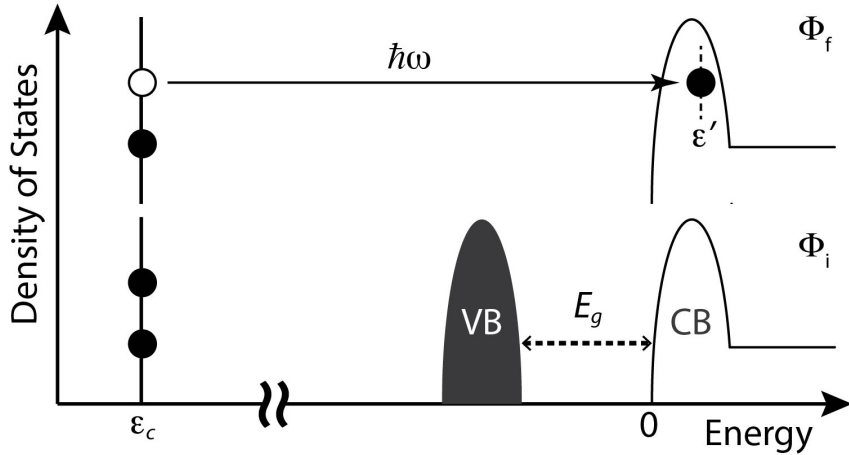


Figure 1-8:  $\Phi_i$  and  $\Phi_f$  denote the initial and final states for an X-ray absorption process, respectively. The absorption excites a core electron into the empty density of states in the semiconductor conduction band. The photon energy  $\hbar\omega$  needs to match the energy difference from the core level to the conduction band. In the final state  $\Phi_f$  the conduction band contains one extra electron, while a core hole is created in the core level.

Since the core level resembles the discrete atomic character, the  $\delta$  function in Eq. (1.19) gives the density of empty states in the conduction band  $\rho$ , and therefore the XAS cross section  $\sigma_{XAS}$  is a measure of  $\rho$  weighted by the squared matrix element between the core level and the conduction band:

$$\sigma_{XAS} \propto M^2 \rho \quad (1.21)$$

Eq. (1.21) provides an explanation for the XAS selection rules, given that the dipole matrix element  $M$  is nonzero only if the azimuthal quantum number of the final state differs by one from the initial state ( $\Delta L = \pm 1$ ) and the electronic spin is conserved ( $\Delta S = 0$ ). Therefore for transition metals that have empty  $d$  states, only the  $p \rightarrow d$  excitations (e.g. L<sub>2,3</sub>- and M<sub>2,3</sub>-edges) can take place, while the  $s \rightarrow d$  excitations (e.g. L<sub>1</sub>- and M<sub>1</sub>-edges) are basically dipole forbidden. Nevertheless, the transition metal K-edge that corresponds to a  $1s \rightarrow 3d$  transition, requires a

photon energy of more than 5 keV to excite and the governing electric quadrupole contribution is more apparent at higher frequency. Eq. (1.21) also suggests that the XAS cross section is proportional to the overlap integral between the core level and the valence level, which thus explains why the M-edge absorption section ( $\sim 10^{-17} \text{ cm}^2/\text{atom}$ ) is higher than that of L-edge and K-edge by one and two orders of magnitude, respectively.<sup>27</sup> From the wave propagation point of view, when an X-ray is traveling through a medium of uniform density, the absorption cross section of the medium is written as:<sup>28</sup>

$$\sigma_{\text{XAS}} = \frac{4\pi r_e c}{\omega} f_2^0(\omega) \quad (1.22)$$

where  $r_e$  is the classical electron radius,  $\omega$  is the angular frequency of the X-ray electric field, and  $f_2^0(\omega)$  is the imaginary part of the atomic scattering factor. While  $f_2^0$  scales slowly with the atomic number  $Z$  and decreases slightly at higher  $\omega$ , it is also the  $\omega^{-1}$ -dependence of  $\sigma_{\text{XAS}}$  that causes the dramatic drop from M-edge to L- and K-edges. It is worth noting that the 30 - 70 eV XUV photon energy used in this work matches the transition metal M-edge absorption, and the associated penetration depth  $\Lambda_p$

$$\Lambda_p = \frac{1}{\rho_N \sigma_{\text{XAS}}} \quad (1.23)$$

where  $\rho_N$  is the number density, ranges from 5 to 20 nm. Even in air the XUV intensity would be attenuated to  $1/e$  of its value by traveling  $\sim 100 \mu\text{m}$  distance. Therefore, not only does the sample need to be thin enough, but the spectroscopic measurement has to be operated in a high vacuum environment.

In Fig. 1-8, it can be seen that X-ray absorption process creates a core hole, which is highly unstable. Decay of a core hole can happen via two mechanisms: in the fluorescence channel, an electron from a higher level fills the core hole and the energy difference is released as electromagnetic radiation; in the Auger decay channel, the filling of a core hole by a higher energy electron excites another electron, thus splitting a deep core hole into two shallow core holes. With either core hole decay mechanism, many photons or electrons are emitted in sequential steps until the atom is relaxed to its ground state. The lifetime  $\Delta\tau$  of a core hole is on the order of one femtosecond; thus according to the Heisenberg uncertainty principle

$$\Delta\tau \times \Delta E \approx \hbar = 10^{-16} \text{ eV} \cdot \text{sec} \quad (1.24)$$

the lifetime broadening would contribute  $\sim 100 \text{ meV}$  Lorentzian linewidth to the XAS spectra.

Because of the continuous spectra provided by the light sources, synchrotron-based XAS studies often use monochromators for selecting and tuning the photon energy to illuminate the sample. The absorption cross section at a specific energy  $E$  can be acquired by measuring the transmission of X-rays through the sample (Fig. 1-9) and using the Beer-Lambert law:

$$\frac{I(E)}{I_0(E)} = \exp(-\rho_N \cdot \sigma_{\text{abs}} \cdot x) \quad (1.25)$$

where  $x$  is the distance the X-ray travels through the sample. Alternatively, lots of synchrotron beamline XAS experiments quantify the sample absorption by detecting the fluorescence decay of the core hole. This is sometimes referred as a total fluorescence yield (TFY) measurement,

which is largely based on the fact that the fluorescence decay channel is proportional to the absorption cross section. The same approach can instead measure the yields of photoelectrons or ions produced by the Auger decay channel, which are called total electron yield (TEY) and total ion yield (TIY) measurements, respectively. It should be noted that neither of these methods directly detects the absolute absorption cross section; therefore, the X-ray/XUV absorption spectroscopy work in this dissertation stays with the transmission measurement method.

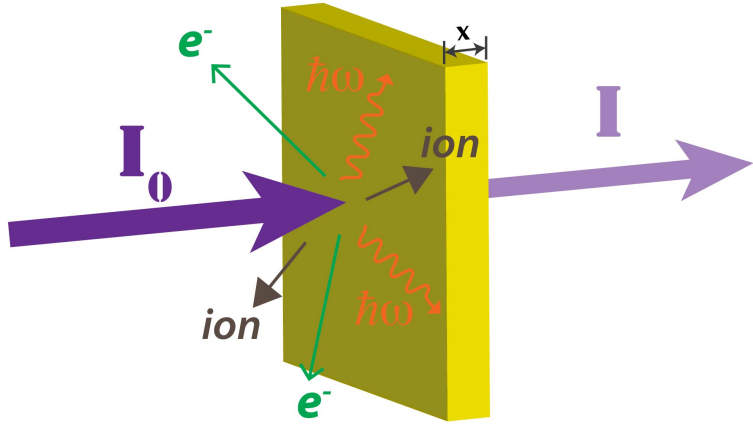


Figure 1-9: X-ray absorption process in the laboratory scale. Not only does the X-ray intensity gets attenuated by the sample ( $I < I_0$ ) with a thickness  $x$ , the decay of core holes would emit electrons, ions, and photons. An X-ray absorption spectrum can be acquired either by measuring the ratio between  $I$  to  $I_0$  at each specific photon energy, or by measuring the yield of electrons (TEY), ions (TIY) and photons (TFY).

The XAS data can be divided into two energy regions: First, the X-ray absorption near edge structure (XANES) focuses on an energy region 50 – 100 eV above the core electron binding energy. XAS spectra of this region give information on the photoabsorption cross section from a core level to the lowest unoccupied valence levels. The second energy region is located 150 eV above the absorption edge and is called extended X-ray absorption fine structure (EXAFS). Since the X-ray photon energy is much larger than the core electron binding energy in the region, photoelectrons are generated with high kinetic energies

$$\varepsilon_k = \hbar\omega - \phi = \frac{2\pi^2\hbar^2}{m_e\lambda_e^2} \quad (1.26)$$

where  $\phi$  is the work function of the material. Since the photoelectron wavelength  $\lambda_e$  is shorter than the interatomic distance, in the EXAFS region the scattering of the excited photoelectrons with neighboring atoms can be approximated in the single-scattering regime, as opposed to the multiple-scattering regime in the XANES region. The interference between scattered photoelectrons causes oscillations in the EXAFS spectra, which can provide information on the coordination environment around the absorbing atom. Limited by the spectral bandwidth of the XUV probe beam, this work mainly studies the XANES energy region of the  $M_{2,3}$ -edge of transition metals. Instead of using a monochromator to select a certain XUV frequency to illuminate the sample, the entire range of photon energies is transmitted through the sample before being energetically dispersed by a XUV spectrometer and detected by an array detector.

This design enables efficient spectral acquisition since all photon energies are being detected at the same time, which is advantageous for operating time-resolved XAS experiments.

#### 1.2.4 Transient X-ray/XUV Absorption Spectroscopy

With transient X-ray/XUV absorption spectroscopy, the sample interacts with a visible pulse (the pump beam) first, either by electronic excitation or strong field ionization, and then after a controlled time delay  $\Delta t$  a second pulse (the probe beam) detects the evolution of the created excited states. The experimentally acquired optical density can be related to the right side of Eq. (1.25) by adding a convolution with the energy resolution  $\Delta$  of the XUV spectrometer:

$$OD(E) = -\log_{10} \left[ e^{-\rho_N \sigma(E)x} \cdot \sqrt{\frac{4 \cdot \ln(2)}{\pi \Delta^2}} \cdot e^{-\frac{4 \cdot \ln(2) E^2}{\Delta^2}} \right] \quad (1.27)$$

The method combines the short temporal resolution provided by femtosecond lasers<sup>29</sup> or synchrotron light sources,<sup>30</sup> with the abundance of information provided by core level spectroscopy, and thus has become a powerful technique for studying electron dynamics in atoms and molecules.<sup>24,31,32</sup> The same technique also has been applied to more complicated condensed phase systems, starting from observing ultrafast structural changes,<sup>33,34</sup> to probing the optical phonon excitation,<sup>35</sup> mapping the electronic structure in excited states,<sup>36</sup> and carrier-carrier and carrier-phonon scattering processes.<sup>37</sup>

As mentioned earlier, typical pulse durations of synchrotron radiation is approximately 100 ps, which is not sufficient for studying faster electron dynamics. The temporal resolution can be improved by either implementing the pulse-slicing technique<sup>25</sup> or using fast X-ray detectors like streak cameras.<sup>38</sup> The temporal resolution of the table-top apparatus described here, which generates subfemtosecond XUV pulses via the high harmonic generation process, is superior to that of the synchrotron-based methods. The differential absorbance in the excited state at a specific XUV frequency is measured by dividing the transmitted intensity in the presence of the pump beam  $I_{on}(E, \Delta t)$  with that in the absence of the pump beam  $I_{off}(E, \Delta t)$ :

$$\Delta OD(E, \Delta t) = -\log_{10} \left[ \frac{I_{on}(E, \Delta t) + I_b}{I_{off}(E, \Delta t)} \right] \quad (1.28)$$

where  $I_b$  accounts for the scattering background of the pump beam. The data acquisition procedures for pump-probe experiments will be described in detail in Chapter 3.

### 1.3 High-Order Harmonic Generation

When an electric field  $\vec{E}$  is applied to a dielectric medium, a polarization density  $\vec{P}$  is induced:

$$\vec{P} = \epsilon_0 \chi \vec{E} \quad (1.29)$$

where  $\epsilon_0$  is the permittivity of free space and  $\chi$  is the electric susceptibility of the medium. In an anisotropic medium there could exist a nonlinear dielectric response, such that the electric field and the induced polarization do not have to follow the same direction. In which case the electric

susceptibility becomes a second-rank tensor with a given order  $n$ , and the polarization density may be expanded into a Taylor series:

$$\vec{P} = \epsilon_0 \sum_n \chi^{(n)} \vec{E}^n \quad (1.30)$$

The resulting polarization density in the medium may exhibit contributions at a frequency different from the original electric field. One of the most well-known nonlinear optical processes is second-harmonic generation (SHG), which was first observed in 1961 by Franken et al. by focusing the ruby laser onto a quartz plate.<sup>39</sup> In this case the induced polarization density consists of twice the incident frequency and can be written as

$$\vec{P}^{(2)}(2\omega) = \epsilon_0 \chi^{(2)} \vec{E}^2(\omega) \quad (1.31)$$

Nonlinear polarizations at higher orders can also be generated in a similar manner but with lower efficiency. Besides converting commercially available laser outputs to desired frequencies, these nonlinear processes can also be utilized as sensitive spectroscopic techniques, such as surface sum-frequency generation and four-wave mixing spectroscopy. With advances of femtosecond laser technology, investigating the highly nonlinear interactions between a dielectric medium and intense electric field has become possible. In 1987, McPherson et al. observed the existence of harmonics up to 17<sup>th</sup> order by ionizing neon gas with intense femtosecond pulses,<sup>40</sup> and this inspired both theoretical and experimental studies of the high harmonic generation (HHG) process. After nearly 30 years, high harmonic spectroscopy has emerged as an invaluable tool for probing atomic wavefunctions<sup>41</sup>, electron dynamics<sup>42</sup> and chemical reactions.<sup>43</sup> Moreover, the wavelengths of these high-order harmonics fall into the XUV and soft X-ray ranges, at which the short optical cycles are essential for generating attosecond pulses. Current knowledge of HHG can be divided into two aspects: The microscopic non-perturbative treatment of the single-atom response to an intense electric field, and the macroscopic phase matching among an ensemble of emitters; both aspects will be discussed in the following sections.

### 1.3.1 Three-Step Model

An intuitive way to understand the generation of high-order harmonics is the semi-classical three-state model proposed by Corkum<sup>44</sup> as illustrated in Fig. 1-10. Consider a noble gas atom being illuminated by a laser pulse in which the electric field is represented by

$$E(t) = E_0 \cos(\omega_L t + \rho) \quad (1.32)$$

where  $\omega_L$  and  $\rho$  are the frequency and phase of the electric field, respectively. Other than the atomic Coulomb potential  $V_{Coulomb}(\vec{r})$ , the valence electron in the noble gas atom also perceives an instantaneous potential  $V_{EF}(\vec{r}, t)$  caused by the electric field, such that the effective potential becomes

$$V_{eff}(\vec{r}, t) = V_{EF}(\vec{r}, t) + V_{Coulomb}(\vec{r}) = e\vec{E}(t)\vec{r} - \frac{e^2}{4\pi\epsilon_0 r} \quad (1.33)$$

where  $e$  is the charge of an electron and  $\epsilon_0$  is the electric permittivity of vacuum. As the electric field intensity is greater than  $10^{14}$  W/cm<sup>2</sup>, the valence electron may be removed from the atom

through tunnel ionization near the peak electric field (step 1). The electron tunneling probability  $T$  can be solved using the Ammosov-Delone-Krainov ionization model<sup>45</sup> as

$$T = \left| \exp\left(-\int_a^b k_e dr\right) \right|^2 = \left| \exp\left(-\int_a^b \frac{\sqrt{2m_e[I_p - V_{eff}(r)]}}{\hbar} dr\right) \right|^2 \quad (1.34)$$

where  $k_e$  and  $m_e$  are the wave vector and the mass of the tunneling electron,  $a$  and  $b$  are, respectively, the inner and outer edges of the energy barrier,  $I_p$  is the atomic ionization potential, and  $V_{eff}(r)$  is the distorted atomic potential.

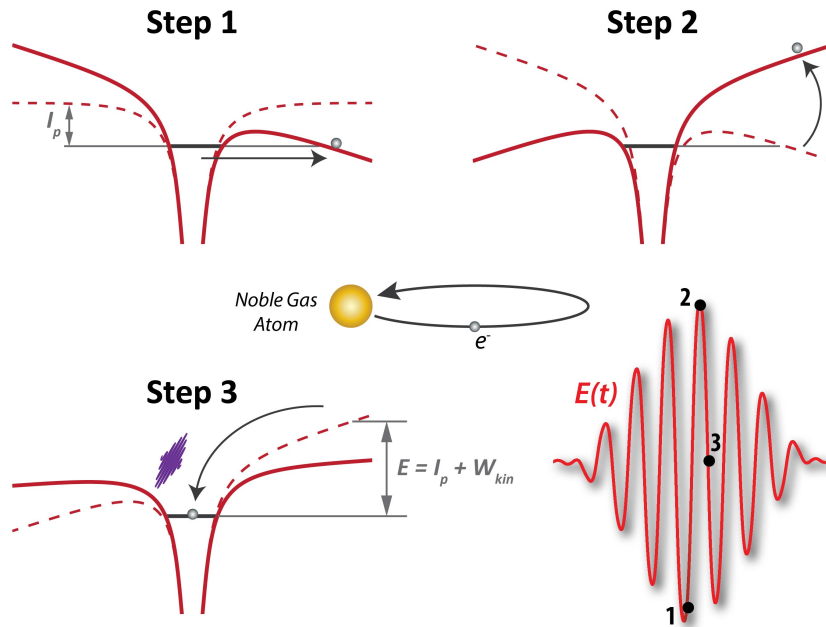


Figure 1-10: The three-step model for high harmonics generation describes the sequential interactions between a noble gas atom and an intense electric field. (1) The atomic potential is deformed by the electric field so that valence electrons can be tunnel ionized. (2) The electron is accelerated and gains momentum as the electric field switches sign. (3) Recollision of the electron with the parent ion emits an XUV photon with energy equal to the sum of electron kinetic energy  $W_{kin}$  and the atomic ionization potential  $I_p$ .

After ionization the electron is accelerated away from the parent ion by the same laser field, and, as the electric field switches its sign, the electron is decelerated and then accelerated back toward the parent ion (step 2). When the “smashing”, or the encounter of the electron and the parent ion happens, there is a certain recollision probability that leads to the emission of a photon (step 3). The frequency  $\omega$  of the emitted photon is determined by the sum of the atomic ionization potential  $I_p$  and the electron’s momentary kinetic energy  $W_{kin}$  prior to recollision:

$$\hbar\omega = I_p + W_{kin}(\rho) \quad (1.35)$$

Since the tunnel ionization can take place at different phases  $\rho$  (relative to the maximum electric field) as long as the intensity of electric field is sufficiently high, the electron could

follow a range of trajectories that may be determined by solving Newtonian equations of motion. As a result, the kinetic energy  $W_{kin}$  is also a function of  $\rho$ , and the average kinetic energy gained by an electron is denoted as the ponderomotive energy,  $U_p$ , which is proportional to the driving laser field intensity  $I_L$

$$U_p = \overline{W_{kin}} = \frac{e^2 E_0^2}{4m_e \omega_L^2} = 9.3 \times 10^{-14} I_L \left( \frac{W}{cm^2} \right) \lambda_L^2 (\mu m^2) \quad (1.36)$$

where  $e$  and  $m_e$  are the charge and the mass of an electron, respectively. Fig. 1-11 plots several electron trajectories corresponding to different phases  $\rho$  in the position-velocity plane, where the position axis represents the distance between the electron and the parent ion. It can be seen that some trajectories would return to the parent ion at position 0 after propagation, and the electron kinetic energy at the moment of recollision is determined by the intersection with the velocity axis. The highest kinetic energy of  $3.17U_p$  is obtained when the ionization happens at  $\rho = 17^\circ$  (trajectory b), and it explains the maximum photon energy (cutoff energy) of the experimentally generated XUV radiation:

$$E_{cutoff} = I_p + 3.17U_p \quad (1.37)$$

Electrons following trajectories a ( $\rho = 45^\circ$ ) and c ( $\rho = 3^\circ$ ) return to the parent ion with the same kinetic energy  $W_{kin}$ , despite spending different amounts of time propagating in the continuum, thus referred to as the “short” and “long” trajectories accordingly. Electrons are most likely to be ionized at the peak of the electric field (trajectory d,  $\rho = 0^\circ$ ) however after propagation these electrons would return to the parent ion with zero kinetic energy. It should be noted that most of the ionization events take place at unfavorable phases, like trajectory e ( $\rho = -45^\circ$ ), such that the electrons cannot be decelerated when the electric field reverses sign. These electrons never return to the parent ion and have no contribution to the emission of XUV radiation.

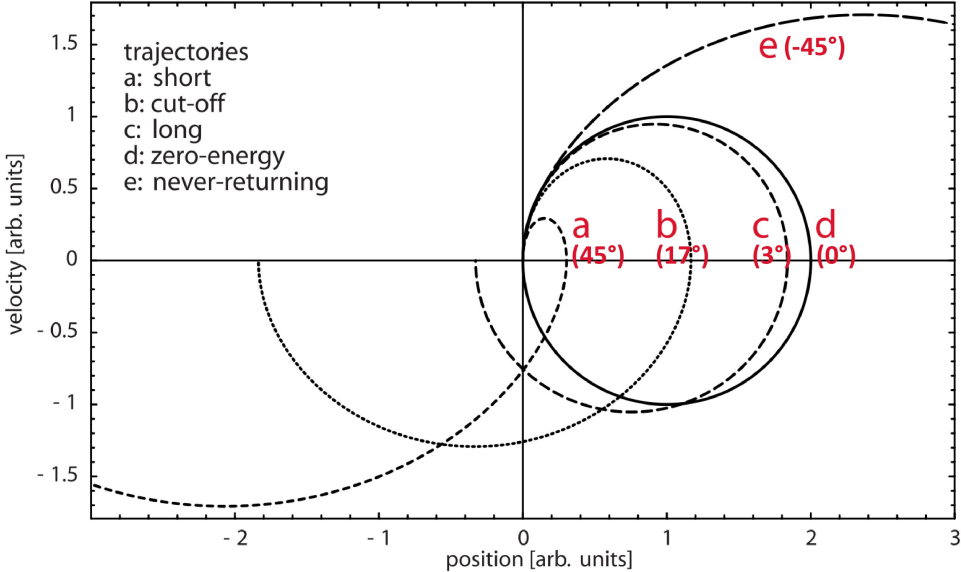


Figure 1-11: Selected classical electron trajectories plotted in the position-velocity plane. Each trajectory is related to a different phase  $\rho$  where the tunnel ionization occurs. The phase  $\rho$  is defined relatively to the maximum electric field. Adapted from [46].

According to the three-step model, interaction between a many-cycle linearly polarized laser pulse and a noble gas atom, which is a centrosymmetric medium, would produce an XUV burst for every half-cycle of the electric field, thus resulting in a pulse train with a periodicity of half a laser period ( $T = \pi / \omega_L$ ). The interference among pulses in the train leads to the  $2\hbar\omega_L$  photon energy spacing in the frequency space, which can be understood from the reciprocity of the Fourier transform. Moreover, consecutive recollisions between the electron and the parent ion take place in opposite directions, so that the corresponding XUV bursts would have different spectral signs. The destructive interference of the pulse train explains only the odd-order harmonics [ $\omega_{XUV} = (2n+1)\omega_L$ ] that are observed experimentally.

Besides the aforementioned semi-classical model, the high harmonic generation process can also be described with a quantum mechanical approach. This was firstly done by Lewenstein et al.<sup>47</sup> by numerically simulating the time-dependent Schrödinger equation. The solved time-dependent electron wavefunction gives an accelerating dipole that emits XUV radiation with certain temporal structures. The Lewenstein model successfully rephrases the classical interpretations done by Corkum's three-step model, including the discrete harmonic spectra and the existence of cutoff energy, and it provides more insights into the quantum phases of XUV radiation. For example, it has been shown that the long trajectory emission possesses greater angular divergence and shorter coherence time than the short trajectory emission.<sup>48</sup> The spectral width of individual harmonics is strongly affected by the quantum path interference between the aforementioned two trajectories, and the dominating long trajectory would lead to substantial spectral broadening. The contribution ratio between short and long trajectories can be controlled by adjusting the laser field intensity.<sup>49</sup>

Eq. (1.37) suggests that the XUV cutoff energy can be extended, i.e. generating higher order harmonics, by increasing either the ionization potential  $I_p$  or the ponderomotive energy  $U_p$ . The first approach can be done by choosing a different medium; among the noble gas group, the ionization potential increases with the following order: Xe (12.13 eV) < Kr (14.00 eV) < Ar (15.76 eV) < Ne (21.56 eV) < He (23.59 eV). Although there is no dramatic difference between these ionization potentials, using a medium with higher  $I_p$  also requires more intense laser fields to facilitate the tunnel ionization step, which leads to a substantial increase in  $U_p$ . However, at higher  $I_p$  the recollision cross section is compromised, thus the overall HHG conversion efficiency becomes significantly lower. Because of its  $\lambda_L^2$  dependence, the ponderomotive energy  $U_p$  can also be increased by using longer wavelength lasers for the driver pulses. Although most HHG experiments use femtosecond Ti:Sapphire amplifiers that operate at  $\sim 0.8$   $\mu\text{m}$  wavelength, the development of ultrafast mid-infrared lasers such as optical parametric chirped pulse amplifiers (OPCPAs) has had some success over the past decade. Using helium as the generating medium and 2.0  $\mu\text{m}$  driver wavelength, coherent high-order harmonics with photon energy up to 1.6 keV has been reported.<sup>50</sup> The spectrum covers the so-called soft X-ray “water window”, which lies in between the K-edge of carbon (280 eV) and oxygen (530 eV), therefore opening up numerous potential applications for ultrafast high harmonic spectroscopy.

### 1.3.2 Phase Matching

Although high-harmonic generation can be well modeled by both the semi-classical and the quantum-mechanical points of view, there are still some characteristics, e.g. total photon flux and center wavelength of the harmonic spectrum, that cannot be explained without considering

the macroscopic XUV propagation in the gaseous medium. As depicted in Fig. 1-12, when a femtosecond laser pulse is focused into an ensemble of noble gas atoms, high harmonic emissions can be generated at different locations along the propagation direction, as long as the electric field intensity is sufficient. The phase velocities of the fundamental laser frequency and the high harmonics must be equal

$$v_p^{laser} = v_p^{XUV} \quad (1.38)$$

so that high harmonic emission from individual emitters add up coherently. Since phase velocity is determined by the frequency  $\omega$  and the wave vector  $k$  ( $v_p = \omega/k$ ), a discrepancy between phase velocities can be attributed to the phase mismatch factor  $\Delta k_q$

$$\Delta k_q = qk_L - k_{XUV}(q) \quad (1.39)$$

where  $k_L$  and  $k_{XUV}(q)$  are the wave vectors of the fundamental laser field and the  $q$ th order harmonic, respectively. Note that the dependence on the harmonic order  $q$  suggests that it is challenging to achieve perfect phase matching conditions ( $\Delta k_q = 0$ ) over a wide energy range. The coherence length  $L_{coh}$ , which is defined as the longest distance that the high harmonic emission can build up without destructive interference

$$L_{coh}(q) = \frac{\pi}{\Delta k_q} \quad (1.40)$$

would decrease significantly with any non-zero  $\Delta k_q$ .

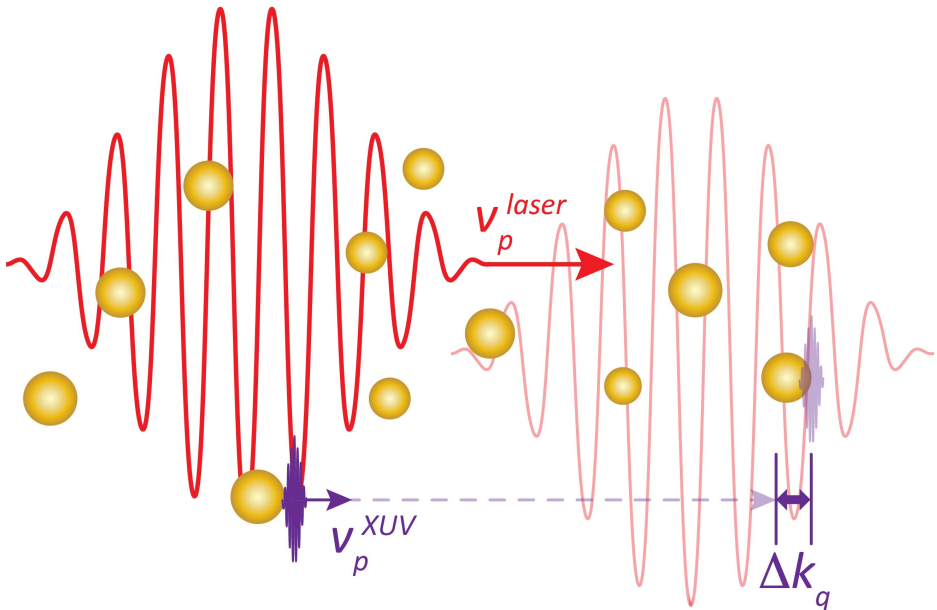


Figure 1-12: The same phase velocities between the laser field and the XUV emission allow coherent addition among individual noble gas atoms, so that the high harmonic intensity grows with distance. The phase mismatch at the  $q$ th order harmonic over a certain length is defined as  $\Delta k_q$ .

In the early HHG experiments, the laser field had to be tightly focused into a gas jet of noble gas medium, and, as a result, the Gouy phase of the Gaussian beam

$$\eta(z) = \tan^{-1}\left(\frac{2z}{b}\right) \quad (1.41)$$

where  $b$  is the confocal parameter and  $z = 0$  corresponds to the position of the beam waist, had a substantial geometrical contribution to the wave vector

$$k_{Gouy} = \frac{d}{dz}\eta(z) \approx \frac{2}{b} \quad (1.42)$$

near the focus ( $z \ll b$ ). The phase mismatch associated with the Gouy phase shift of a focused Gaussian beam is given as

$$\Delta k_{Gouy}(q) = (q - 1)\frac{2}{b} \quad (1.43)$$

It should be noted that this geometrical phase mismatch becomes more apparent for higher order harmonics and a tighter focus, and the coherence length is usually much shorter than the confocal parameter. Experimentally the influence of Gouy phase can be overcome by placing the laser focus before the gas jet that contains the generating medium, so that a decreasing electric field intensity compensates the Gouy-induced phase mismatch.<sup>51</sup>

As the femtosecond lasers with millijoule pulse energy become more accessible, HHG can be operated using confined gas cells at loose focusing conditions.<sup>52</sup> Not only is the Gouy phase shift minimized, but the electric field can interact with the generating medium at higher gas density  $N_{at}$  and longer interaction length  $L_{med}$ , which generally leads to brighter harmonic emissions (assuming  $L_{med} < L_{coh}$ ). The same advantages are also shared by performing HHG in a gas-filled hollow waveguide: the driving laser field propagates as a non-diverging plane-wave, thus the Gouy phase can be neglected, and the well-controlled gas pressure stays constant over the length of the waveguide. The number of emitted photons  $I_q$  for the  $q$ th order harmonic is given as<sup>53</sup>

$$I_q \propto N_{at}^2 \frac{4L_{abs}^2}{1 + 4\pi^2(L_{abs}/L_{coh})^2} \left[ 1 + \exp\left(-\frac{L_{med}}{L_{abs}}\right) - 2 \exp\left(-\frac{L_{med}}{2L_{abs}}\right) \cos\left(\frac{\pi L_{med}}{L_{coh}}\right) \right] \quad (1.44)$$

where  $L_{abs}$  is the density-dependent absorption length of the noble gas. When  $L_{abs}$  is large the gas absorption effect can be neglected and Eq. (1.44) is approximated as

$$I_q \propto N_{at}^2 \frac{\sin^2(L_{med}\Delta k_q / 2)}{\Delta k_q^2} \quad (1.45)$$

Eq. (1.45) indicates that the output harmonic intensity is strongly related to gas density  $N_{at}$ , interaction length  $L_{med}$ , and the phase mismatch  $\Delta k_q$ . Without considering the Gouy phase shift, the major source of phase mismatch  $\Delta k_q$  in a confined gas cell or a hollow waveguide is the pressure-dependent dispersion. For a light wave transversing a partially ionized gaseous medium, both the neutral atoms and the plasma modify the wave vector as follows:

$$k = \left[ \frac{2\pi}{\lambda} \right]_{vacuum} + \left[ \frac{2\pi}{\lambda} N_a n(\lambda) \right]_{neutral} + \left[ N_e r_e \lambda \right]_{plasma} \quad (1.46)$$

where  $N_a$  and  $N_e$  are the densities of neutral atoms and free electrons, respectively,  $n(\lambda)$  is the refractive index per unit neutral atom density at a given wavelength  $\lambda$ , and  $r_e$  is the classical electron radius. Both  $N_a$  and  $N_e$  are related to the gas pressure  $P$  (in atm) and the ionization fraction  $\eta(t)$ , which can be calculated by the Ammosov-Delone-Krainov model. Therefore Eq. (1.46) can be written as

$$k = \frac{2\pi}{\lambda} [1 + P(1 - \eta)N_{atm}] + P\eta N_{atm}r_e \lambda \quad (1.47)$$

where  $N_{atm}$  is the atomic number density at atmosphere pressure. By substituting (1.47) into (1.39) and using  $\lambda_{XUV}(q) = \lambda_L / q$ , the dynamic phase mismatch between the laser field and the  $q$ th order harmonic emission is represented as

$$\Delta k_q = \frac{2\pi q}{\lambda_L} P(1 - \eta) \Delta n - P\eta N_{atm} r_e \lambda_L \left[ \frac{q^2 - 1}{q} \right] \quad (1.48)$$

where  $\Delta n$  stands for the difference between refractive indices at atmosphere ( $\Delta n = n_{laser}^{atm} - n_{XUV}^{atm}$ ).

Besides the output harmonic flux, there are other details of HHG that can be explained by phase matching. For instance, the energy profile of high-order harmonics is usually more asymmetric and blue-shifted at higher laser intensity; The underlying reason is that the phases of long trajectory emissions possess a strong dependence on laser intensity, which translates into a blue-broadening and blue-shifting on the rising edge of the pulse.<sup>54</sup> A better understanding of phase matching would enable tailoring the HHG process experimentally. Many studies have been devoted to the optimization and shaping of high-order harmonics, including increasing conversion efficiency and suppressing or enhancing a certain order harmonic by shaping the driver laser pulses with a spatial light modulator coupled to a feedback-control loop.<sup>46</sup>

### 1.3.3 Semi-Infinite Gas Cell

Since the generation of high-order harmonics was first observed in 1987, several interaction geometries between electric field and noble gas medium have been tested and exploited. As mentioned in the previous section, early experiments used a pulsed valve to produce gas jets as the source of high harmonics. Although the Gouy phase shift contributes solely to the phase mismatch and can be compensated by controlling the relative position of the laser focus and the gas jet, the pulsed valve does not provide very high gas density, i.e. the maximum on-axis pressure is  $\sim 10$  Torr over 1 to 2 mm interaction length  $L_{med}$ . Due to the quadratic dependence of harmonic yield on the gas density, the HHG conversion efficiency with pulsed valves is highly limited. In comparison, finite gas cells confine the gas medium in space and thus are able to provide a static high-density environment that can interact with the laser field, which enters and leaves the gas cell through separate pinholes. Optimal lengths of the finite gas cells vary with the laser focusing parameters, which range from a few millimeters to several centimeters. In the high gas density regime, not only the phase mismatch is mainly contributed by the medium and plasma dispersion, but re-absorption by the gas medium also becomes apparent. The highest reported conversion efficiency is  $1.5 \times 10^{-5}$  for the generation of the 27<sup>th</sup>

order harmonic in an argon-filled cell.<sup>55</sup> Similarly, using capillaries as hollow waveguides also prepares the generating medium in a static and homogeneous distribution, and this results in bright and highly coherent harmonic emission. The travelling laser electric field is restricted by Fresnel reflections at the inner wall, and therefore the effective interaction length is independent of the confocal parameter and can be as long as several centimeters. In addition to the dispersion caused by neutral atoms and plasma, an additional capillary dispersion term needs to be included. An XUV supercontinuum has been demonstrated by employing a quasi-phase-matching scheme, either by using periodically modulated hollow waveguides or by superimposing several light fields in the gas medium.<sup>56</sup> However, the positioning of the capillary needs to be precise in order to couple the laser field to the correct capillary mode, and the energy lost accompanying the coupling limits the pulse energy that is available for the HHG process.

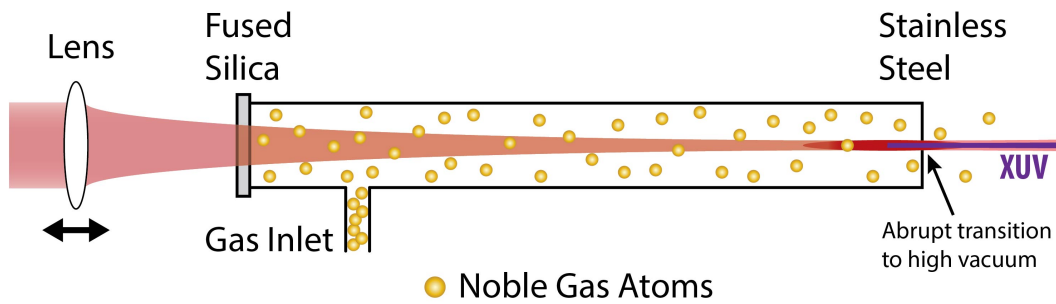


Figure 1-13: The schematic design of a semi-infinite gas cell (SIGC) as an XUV light source. The harmonic emission is generated near the driver laser focus that is located close to the exit foil of the gas cell. The intense laser field ablates a pinhole on the stainless steel foil separating the gas cell from a high vacuum chamber.

In 2004, a semi-infinite gas cell (SIGC)<sup>57</sup> was utilized as an alternative HHG source. Initially inspired by the self-guiding effect in an argon-filled gas cell<sup>58</sup> that compresses many-cycle pulses to few-cycle pulses, the SIGC also shares the advantage of the long interaction region characteristic of a hollow waveguide. While the finite gas cells are typically several millimeters long and have a pair of pinholes for the laser to travel through, in a SIGC the generating medium fills most of the region from the focusing lens to the laser focus (Fig. 1-13). The entrance side of the SIGC is made of a fused silica window, while a stainless steel foil is placed near the laser focus at the exit end of the cell. The high electric field intensity can ablate a pinhole that connects the SIGC to a high vacuum chamber, which acts as a differential pumping stage to evacuate the noble gas medium. The fundamental laser field is focused loosely into the SIGC and generates a single filamentation that is longer than the confocal parameter. The balance between the Kerr lensing effect (“self-focusing”) and the plasma defocusing resulting from multiple-photon ionization of a gaseous medium makes the laser electric field propagate without angular dispersion in the filamentation. A systematic study that compares different HHG geometries demonstrates that the conversion efficiency of a SIGC is at least one order of magnitude higher than the finite gas cells, and two orders of magnitude more than the pulsed valves.<sup>59</sup> Similar to the gas-filled capillaries, the SIGC has the ability to fulfill the phase matching condition over an extended propagation distance that results in bright high harmonic output with excellent spatial and temporal coherence. The difference is that the SIGC relies on

the self-guiding of laser pulses rather than the physical confinement of the electric field in a waveguide, and it is therefore advantageous for its simplicity of design and daily alignment procedures.

When operating a SIGC, several parameters can be adjusted to optimize the harmonic output in terms of the photon flux, the average photon energy, or the wavelength of an individual harmonic. First, it has been reported that partially closing an aperture before the focusing lens can enhance the harmonic flux by at least 10 times.<sup>60</sup> This apertured-beam effect can be explained as the interplay between the atomic dipole response (which favors high electric field intensity at larger apertures) and the focusing geometry and ionization fraction (favors smaller apertures). The second “control knob” is the gas pressure that fills the SIGC. Like finite gas cells and capillaries, the XUV flux from a SIGC source would increase with gas pressure with a nearly quadric dependence until the gas absorption effect starts to factor in. Since the absorption cross sections of noble gases are larger at lower photon energies, the lower order harmonic would reach the maximum flux at lower gas pressure than higher order harmonics. This explains why the peak of the high harmonic spectrum would shift to higher energy (or shorter wavelength) at a higher gas pressure. The wavelength of an individual harmonic generated from a SIGC can be tuned to shorter values by increasing the gas pressure, as has been demonstrated in other interaction geometries. This is due to the blue-shifting of the fundamental laser frequency caused by the plasma in the interaction region, which can be described by the following equation:<sup>61</sup>

$$\delta E_f = \frac{h^2 N_{at}}{2\pi m_e c} \frac{1}{E_f} \frac{df_e}{dt} L_{med} \quad (1.49)$$

where  $h$  is Planck’s constant,  $N_{at}$  is the total gas density,  $E_f$  is the photon energy of laser,  $m_e$  is the mass of an electron,  $c$  is the speed of light in vacuum,  $df_e/dt$  is the increasing rate of ionization fraction, and  $L_{med}$  is the interaction length. This wavelength tuning effect with gas pressure is especially apparent in a medium with lower ionization potential because the ionization fraction would be higher. Eq. (1.49) also suggests that at a fixed gas pressure, tuning the wavelength of high harmonics is accessible by chirping the fundamental pulses, which would affect the plasma density as well. Chirping the fundamental laser field, essentially modulating the ratio of short- and long-trajectory emissions, can also lead to broadening of the spectra width of individual harmonics, which translates to the overlap of neighboring harmonics.

The last control parameter for the SIGC is the relative position of the laser focus to the exit foil. The focusing lens for the fundamental laser pulses is mounted on a translational stage and can be moved along the direction of propagation, thus the focus position can be varied. As sketched in Fig. 1-14, moving the focus position  $z_f$  into the gas cell brings more overlap volume between the generating medium and the laser confocal range. Since both the gas density  $N_{at}$  and the interaction length  $L_{med}$  are increased, according to Eq. (1.45) brighter and higher-order harmonic emission is expected. The influence of variation in the focus position has been experimentally studied, and the harmonic intensity scales quadratically with decreasing values of  $z_f$ .<sup>62</sup> When the laser focus is placed deeper into the gas cell, nonetheless, reabsorption by the generating medium becomes crucial and is reflected by an exponential decay in the harmonic intensity. It should be noted that the ionization cross-sections of the noble gases are usually larger at lower photon energy; therefore lower-order harmonics are more likely to be affected by

the reabsorption. For example, in a SIGC filled with 70 mbar helium, the intensity of the 19<sup>th</sup> harmonic is maximized when the focus is placed right after the exit foil ( $z_f \sim 1$  mm).<sup>63</sup> In comparison, the 39<sup>th</sup> harmonic peaks its intensity at  $z_f = -2$  mm; while the 59<sup>th</sup> harmonic is most optimal at  $z_f = -9$  mm.

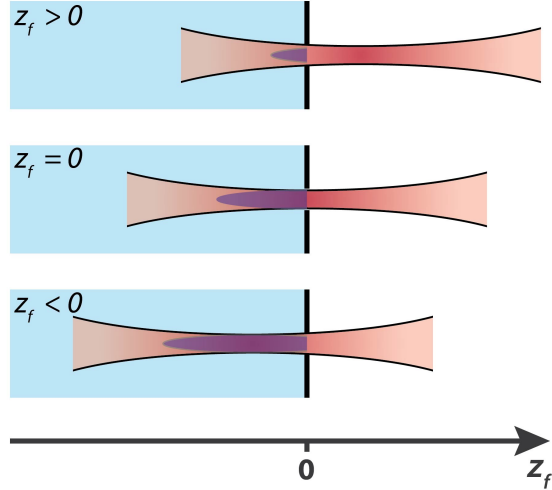


Figure 1-14: The influence of varying the laser focus position  $z_f$  relative to the end of semi-infinite gas cell. When the focus is placed after the exit foil ( $z_f > 0$ ), only the end of the confocal range has enough electric field intensity to produce high harmonic emission. In comparison, at  $z_f = 0$  a longer interaction length is created inside the gas cell. If the laser focus is deep into the gas cell ( $z_f < 0$ ), the entire confocal range can interact with the generating medium, thus resulting in a brighter harmonic flux.

Combining the simplicity of design and high flux output, it is not surprising that the SIGC is now commonly used as a XUV light source in high harmonic spectroscopy. It has shown potential for the generation of isolated attosecond pulses,<sup>64</sup> and the highest cutoff energy has reached the water window.<sup>65</sup> Although translating the laser focus provides an easy control for the harmonic wavelength, intensity, and distribution, if any refocusing mirror is placed after the light source the corresponding focal plane is also shifted, thus a careful characterization of the XUV output is necessary. The design of the SIGC used for this dissertation and the detailed study of HHG with various parameters will be presented and summarized in the corresponding sections in Chapter 2 and 3.

#### 1.3.4 Two-Color Gating and Even-Order Harmonics

As has been stated in Sec. 1.3.1, the three-step model predicts that many-cycle pulses would generate a train of XUV bursts with a periodicity of half the laser period ( $T = \pi / \omega_L$ ). Efforts are devoted to the generation of single attosecond XUV pulses from few-cycle driving laser pulses, and several gating techniques, such as amplitude gating, ionization gating, and double optical gating, have been developed for isolating a single attosecond pulse from the attosecond pulse train (APT) by suppressing all but one of the pulses.<sup>66</sup> One characteristic of having an isolated attosecond pulse is the broadband continuum spectrum instead of modulated peaks with  $2\hbar\omega_L$  energy spacings [ $\omega_{XUV} = (2n+1)\omega_L$ ], which is caused by interference among pulses in the pulse train. Although the time-resolved experiments in this dissertation do not aim

for attosecond resolution, a more even spectral coverage can cover the broad core level transitions in solids, thus increasing the signal-to-noise ratio in the region between neighboring harmonics. Therefore, a simple two-color gating scheme (Fig. 1-15) is implemented for the generation of both the odd- and even-order harmonics [ $\omega_{XUV} = n\omega_L$  ].

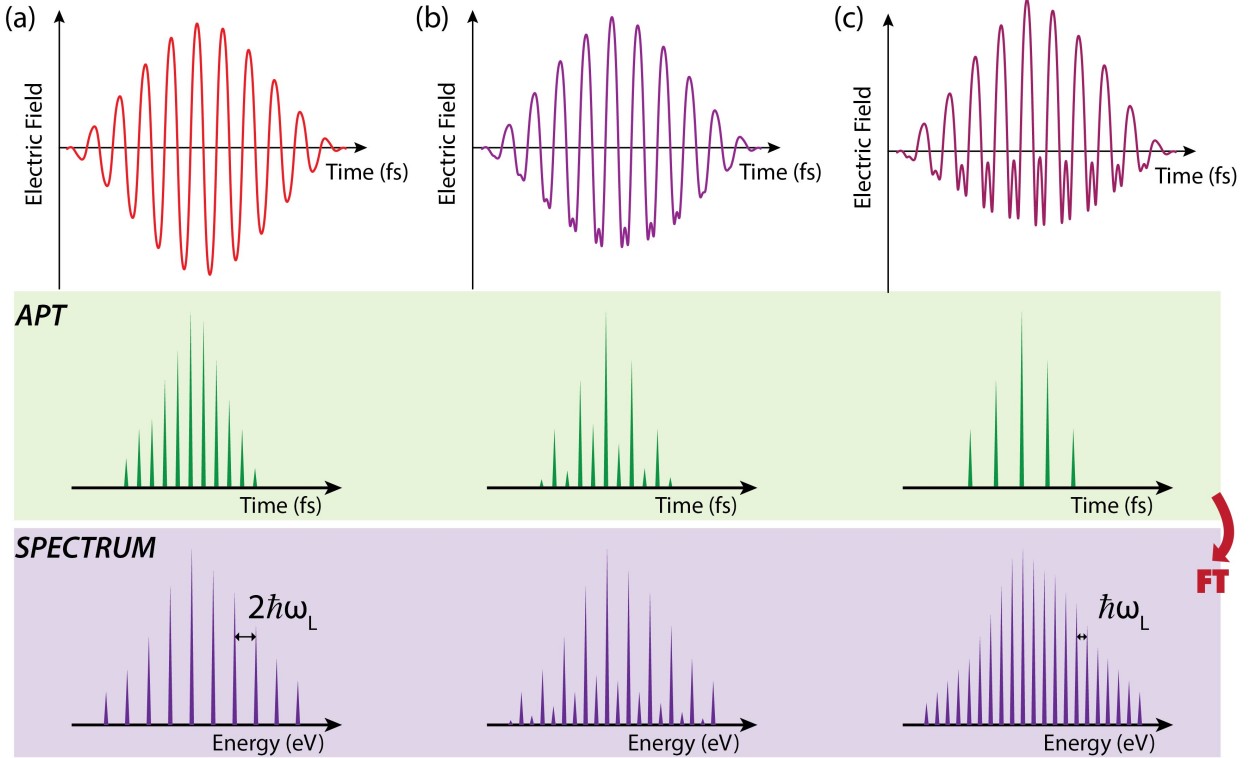


Figure 1-15: HHG processes at (a) without, (b) intermediate and (c) full two-color gating conditions. Mixing in the second-order harmonic of the fundamental field breaks the inversion symmetry of the electric field, so that an XUV burst is emitted for every optical cycle instead of every half optical cycle. The high harmonic spectra in the energy (frequency) domain can be obtained by Fourier transforming the temporal structure of the attosecond pulse train (APT).

In the two-color gating method, a small portion of the laser driver pulses is frequency-doubled to the second-order harmonic by a  $\beta$ -barium borate (BBO) crystal and then recombined with the fundamental field. The fundamental and the second harmonic field propagate collinearly and are both focused into the noble gas medium. The presence of the second harmonic lifts the inversion symmetry of the fundamental field near the laser focus, essentially a means to control the electric field on a subcycle scale, so that half of the electric field maxima can no longer facilitate the tunnel ionization of noble gas atoms. After the recollision step, the timing difference between adjacent XUV bursts becomes a full fundamental laser cycle ( $T = 2\pi/\omega_L$ ). Because the modulated harmonic spectrum is the result of destructive interference among the APT, reducing the number of pulses in an APT would decrease the energy spacing between neighboring harmonics to  $\hbar\omega_L$  in the far-field spectrum. When using the  $0.8 \mu\text{m}$  wavelength of Ti:Sapphire laser as the driver pulses and the second harmonic ( $0.4 \mu\text{m}$ ) as the symmetry-breaking field, the spacing between harmonics is about  $1.5 \text{ eV}$  and both the odd- and even-order

harmonics are observed. The two-color gating technique not only enhances the HHG conversion efficiency by generating more harmonics, but it also decreases the energy spacing and increases the existence of more XUV continuum underneath the modulated harmonic peak structure. The two-color gating has been carried out both theoretically and experimentally,<sup>41,67,68</sup> when the polarization of the fundamental field and the second harmonic field are parallel and perpendicular to each other. Even-order harmonics are obtained by using both polarization directions of the second harmonic field, although the generating mechanisms could be very different. When the intensity of the second harmonic is less than 10% of the fundamental pulse energy, the role of the second harmonic field is to perturb the fundamental field symmetry as stated earlier, and the polarizations of the two fields have to be parallel. While the second harmonic possesses comparable pulse energy as the fundamental field, even-order harmonics are generated by four-wave mixing processes, e.g.  $\omega_{20} = \omega_{17} + \omega_1 + \omega_2$  or  $\omega_{20} = \omega_{21} + \omega_1 - \omega_2$ ; where  $\omega_n$  is the angular frequency of the  $n$ th-order harmonic of the fundamental laser field. In this case the polarization of the second harmonic field may be perpendicular to the fundamental field. Recently a phase-matched, circularly-polarized high harmonic light source has also been developed by focusing the fundamental and second harmonic beams that are with opposing helicities into a gas-filled hollow waveguide.<sup>69</sup>

The contents of the rest of the dissertation are organized as follows: Chapter 2 gives an overview of the transient XUV absorption apparatus, including the femtosecond laser system, vacuum chamber assembly, and the XUV spectrometer. Chapter 3 describes both the characterization of high-order harmonics and the operation procedures for various types of experiments. The charge transfer excitation pathway in spinel cobalt oxide ( $\text{Co}_3\text{O}_4$ ) at 400 nm pump wavelength and the following carrier relaxation dynamics are presented in Chapter 4. The pump wavelength dependence study of cobalt oxide will be shown in Chapter 5. Preliminary results of electron transfer in Si/TiO<sub>2</sub> type-II heterojunctions are given in Chapter 6. Concluding remarks will be addressed in Chapter 7, along with an overview of the research project.



# Chapter 2

## Design and Construction of the Transient XUV Absorption Apparatus

A table-top transient XUV absorption apparatus is built for studying the charge carrier dynamics in semiconductor materials. As most of the early XUV pump-probe experiments are dedicated to study atoms and molecules, this instrument is one of the first table-top experiments to apply the advantages of core level absorption to condensed matter systems. The apparatus consists of several major components as illustrated in Fig. 2-1: a femtosecond XUV light source that generates high-order harmonics of the infrared fundamental pulses, which are provided by a commercially available Ti:Sapphire laser system; the same laser system is also responsible for a tunable wavelength optical pump source that can match the band gap of various semiconductors; due to the low attenuation length of XUV in air, a high vacuum chamber assembly is necessary for generating, operating, and detecting XUV; a sample stage that enables raster scanning and an XUV spectrometer comprising a concave grating and a charge-coupled device (CCD) detector. The detailed descriptions of each component will be presented in this chapter: Sec. 2-1 introduces the femtosecond Ti:Sapphire chirped pulse amplifier system, while Sec. 2-2 addresses the optical layout of the experiment, including both the visible pump beam and the XUV probe beam; The optical parametric amplifier, which provides femtosecond visible pulses with tunable wavelength, is described in Sec. 2.3; the functions of each high vacuum chamber for XUV propagation are listed in Sec. 2.4; and in Sec. 2.5, the last of this section, possible improvements and upgrades for the current apparatus are proposed.

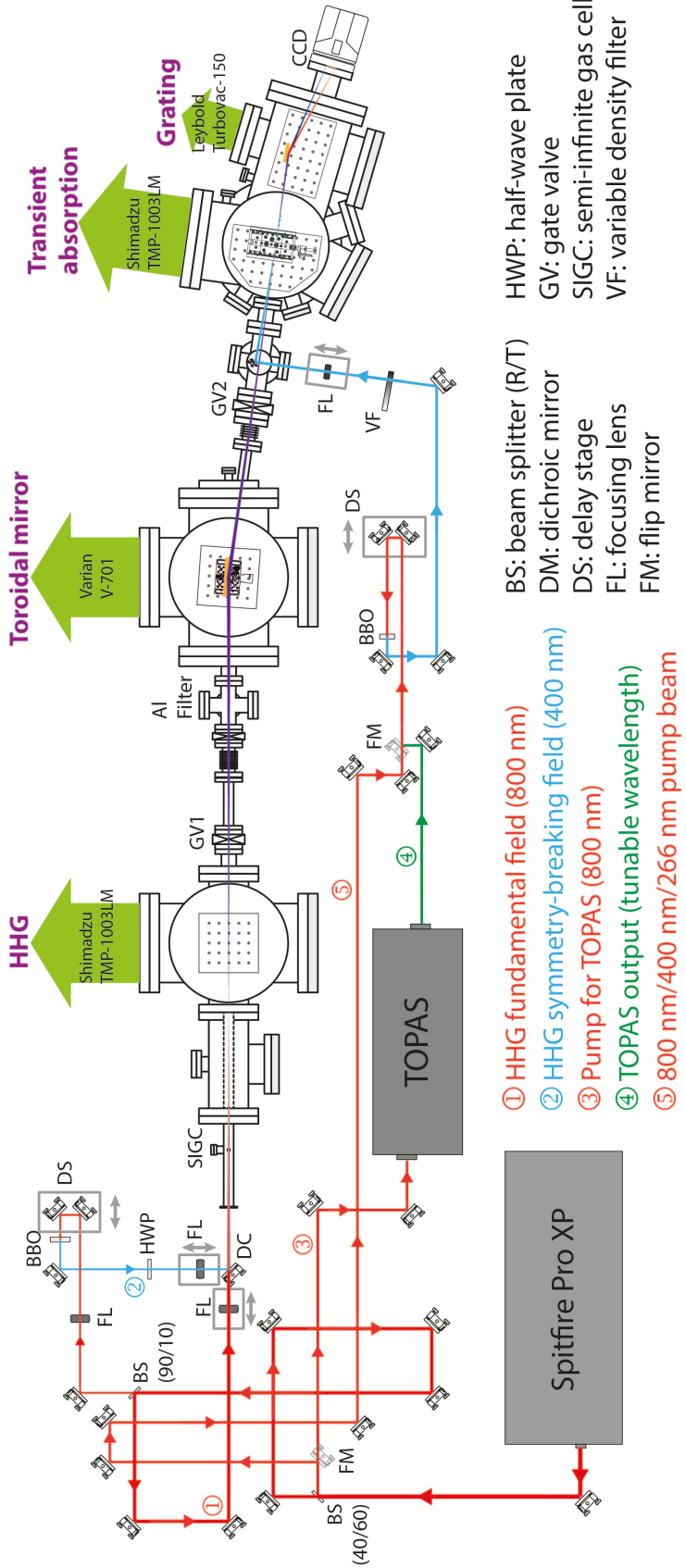


Figure 2-1: Schematic of the table-top transient XUV absorption apparatus. For clarity, beam paths are categorized into the probe arm (1 and 2, used to generated XUV pulses) and the pump arm (3-5, varying in wavelengths). Translational stages used for controlled temporal delay and focus adjustment are shown as gray double arrows next to rectangular boxes. Propagation and detection of XUV are done in a high vacuum chamber assembly, which is labeled in purple color.

## 2.1 Ultrafast Laser System

### 2.1.1 Femtosecond Chirped Pulse Amplifier

A stable infrared laser source guarantees high quality pump and probe beams, which are crucial for transient absorption spectroscopy. In this apparatus a commercial chirped pulse amplifier (Spitfire Pro XP, Spectra Physics) is seeded by a prism-based Ti:Sapphire oscillator (Tsunami, Spectra Physics) and pumped by a Q-switched Nd:YLF laser (Empower 30, Spectra Physics), which is able to produce 3.5 mJ, 35 fs, 800 nm pulses at a 1kHz repetition rate. The oscillator is pumped by a 3.9 W continuous wave (CW) 532 nm diode laser (Millennia, Spectra Physics), which generates 3 nJ, 35 fs pulses at 80 MHz repetition rate through active mode-locking by a acousto-optic modulator. While mode-locked properly, the typical oscillator spectrum has  $\sim$ 75 nm FWHM (Fig. 2-2(a)). Polarization directions of the oscillator and amplifier output are vertical and horizontal, respectively.

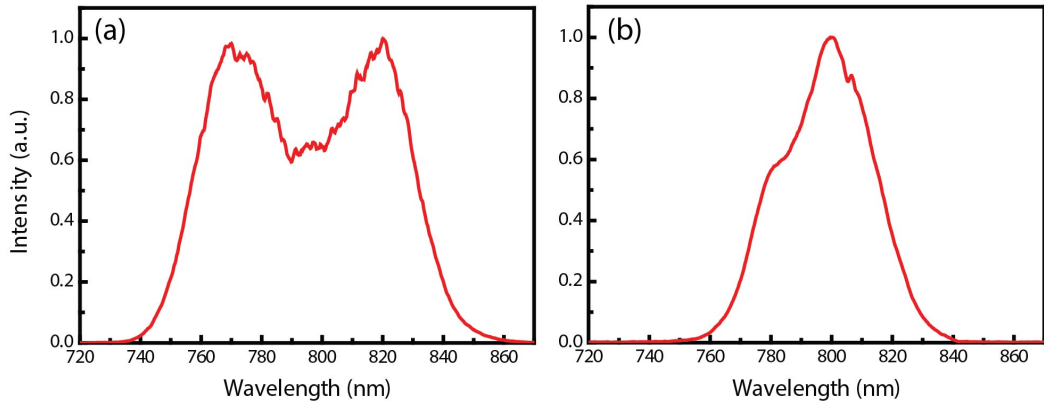


Figure 2-2: Output infrared spectra of (a) the prism-based Ti:Sapphire oscillator, and (b) the chirped pulse Ti:Sapphire amplifier.

In the Ti:Sapphire amplifier, the oscillator pulse retains its spectral characteristic but gains  $10^6$  times more energy from a pump laser. However, the intense pulse energy tends to self-focus the beam in the Ti:Sapphire crystal and would result in damage. A three-stage chirp pulse amplification concept allows the crystal to operate at a power density lower than the damage threshold (Fig. 2-3): a grating stretcher prior to the amplification stage deliberately adds a positive chirp to the seed pulse, meaning that the short wavelength components are delayed with respect to the long wavelength components, and the pulse duration is stretched to  $\sim$ 100 ps. By doing so the peak power density in the regenerative amplifier is effectively reduced. A Pockels cell selectively injects the 80 MHz seed pulses into an optical resonator at 1 kHz frequency, matching the repetition rate of the Q-switched pump laser. The  $\sim$ 18 mJ pulses at 527 nm provided by the pump laser are used to create population inversion in the amplifier Ti:Sapphire crystal. The relative humidity around the Ti:Sapphire crystal is controlled below 10% during the operation, while the temperature is modulated by a thermoelectric circuit. The seed pulse is amplified to a higher energy level after several round trips in the resonator, and eventually

released by a second Pockels cell. After the amplification stage a grating-based compressor reverses the temporal chirp and compresses the pulses to nearly transform-limited, and the distance between a retro-reflector to the grating can be finely controlled to achieve the most optimal pulse compression. The pulse energy before and after the compressor is 4.5 and 3.5 mJ, respectively. The output spectrum of the chirped pulse amplifier usually has 40 nm spectral FWHM centered at 800 nm (Fig. 2-2(b)).

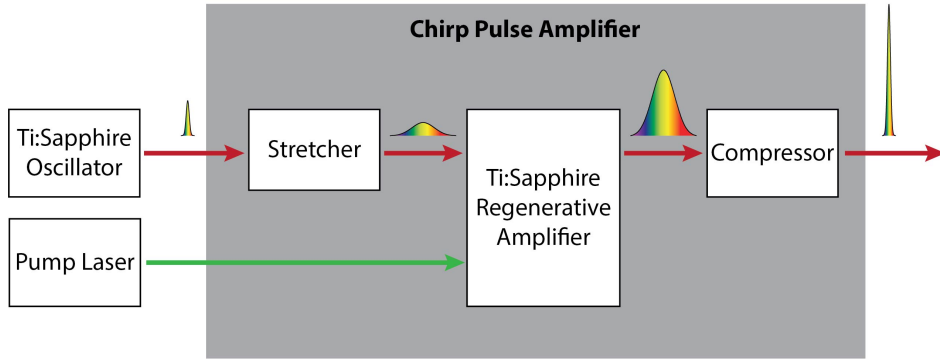


Figure 2-3: The operating principle of chirped pulse amplification. The seed pulses are purposely stretched to  $\sim$ 100 picosecond duration before being sent into the Ti:Sapphire amplification crystal where the seed pulses gain energy from the pump laser. The amplified pulses are then compressed to a temporal profile that is nearly Fourier transform-limited.

The beam profile of the amplifier pulse output is characterized by the scanning knife-edge method (Fig. 2-4). Right at the output port of the amplifier, the measured  $1/e^2$  beam waists  $2\omega_0$  for the horizontal and vertical directions are 7.57 mm and 7.97 mm, respectively. The beam waists are also measured further away on the pump beam path, about 4.5 meters away from the amplifier output port, and the angular dispersion is found to be less than 2%.

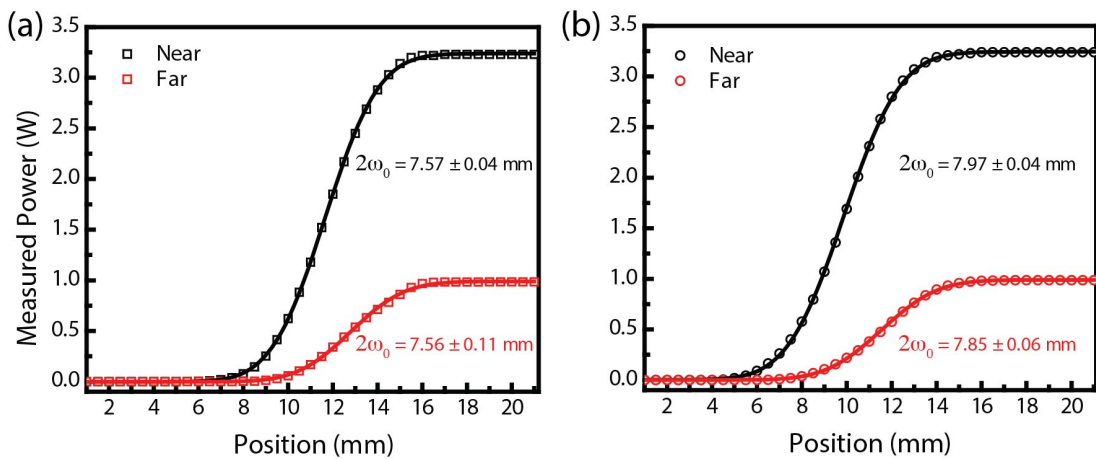


Figure 2-4: Scanning knife-edge traces on the (a) horizontal and (b) vertical directions for the chirped pulse amplifier output. The traces in black color are measured at the output port of the amplifier, while the red traces are obtained  $\sim$ 4.5 meters further away.

### 2.1.2 Characterization of Pulse Duration

The temporal profile of the infrared pulsed can be characterized by autocorrelation. Fig. 2-5 shows the home-built intensity autocorrelator for both infrared and visible wavelengths. A 50% reflectivity beamsplitter splits the sample beam into two copies, which are superimposed in a  $\beta$ -barium borate crystal with a  $\chi^{(2)}$  nonlinearity. When the temporal delay induced by the path length difference is minimized, sum-frequency generation at type-I phase matching condition can lead to the second-order harmonic output, which is detected by a spectrometer (USB-2000+, Ocean Optics). Since the two sample beams overlap at the BBO crystal with  $\sim 2^\circ$  crossing angle, the second harmonic signal can be separated from the sample beams by an iris diaphragm.

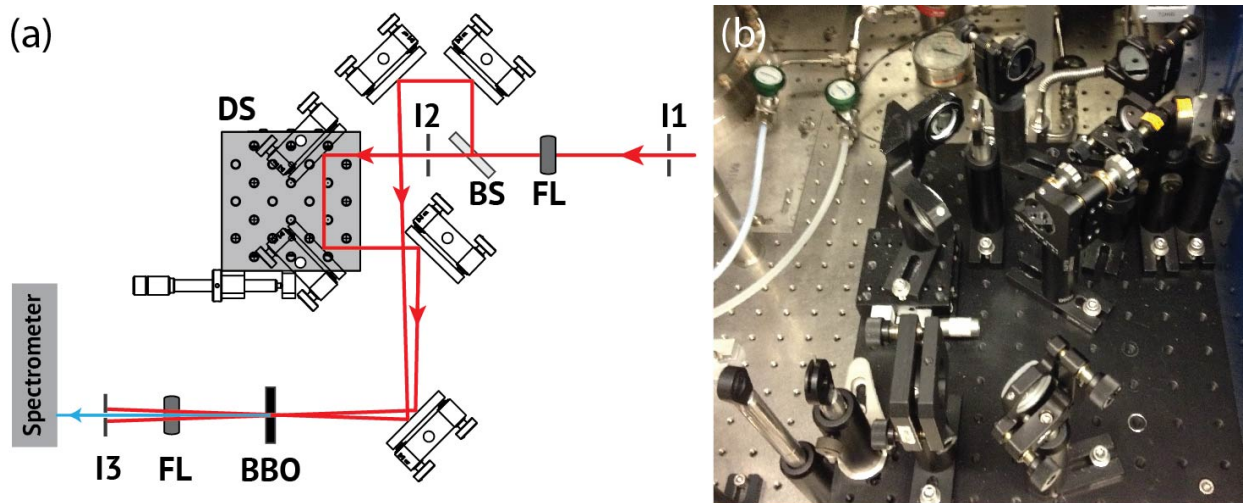


Figure 2-5: (a) Illustration and (b) image of the home-built intensity autocorrelator. I: iris; FL: focusing lens; BS: beam splitter; DS: delay stage.

Using a motorized translational stage to vary the time difference between the two sample beams, a spectrogram can be recorded as shown in Fig. 2-6(a). Since in the intensity autocorrelation the beam is gated by itself, the spectrogram should be symmetric with respect to the zero time delay. The dependence of the autocorrelation signal  $I_{ac}$ , which is the integrated second harmonic output, on the time delay  $\tau$  is defined by

$$I_{ac}(\tau) = \int_{-\infty}^{+\infty} I(t)I(t-\tau)dt \quad (2.1)$$

where  $I(t)$  is the temporal profile of the sample beam. If the measured pulses have a Gaussian temporal profile, the width of the pulse is  $\sim 0.71$  times the width of the autocorrelation signal. For  $\text{sech}^2$ -shaped pulses, the ratio between the sample pulse width and the autocorrelation signal width becomes 0.65. Fig. 2-6(b) shows an autocorrelation trace taken right before the semi-infinite gas cell, which can be fit well by a  $35.8 \pm 0.2$  fs  $\text{sech}^2$  function. This result indicates that the infrared pulses have  $40.9 \pm 0.2$  fs full width at half-maximum (FWHM), which matches the laser specification. Alternatively, the spectral information in the acquired spectrogram can be used for frequency-resolved optical gating (FROG) analysis. Intensity of the second harmonic signal at frequency  $\omega$  is determined by<sup>70</sup>

$$I_{FROG}(\omega, \tau) = \int_{-\infty}^{+\infty} E(t)E(t-\tau)\exp(-i\omega t)dt \quad (2.2)$$

Therefore in the time-frequency domain, a proper algorithm can give both electric field and temporal phase, or their Fourier-transform equivalent, energy spectrum and the spectral phase. The retrieved spectrum and electric field by doing the FROG analysis on the spectrogram in Fig. 2-6(a) are given in Fig. 2-6(c) and Fig. 2-6(d), respectively. The FWHM of the electric field is about 45.0 fs, which is comparable to the value obtained by fitting the autocorrelation trace.

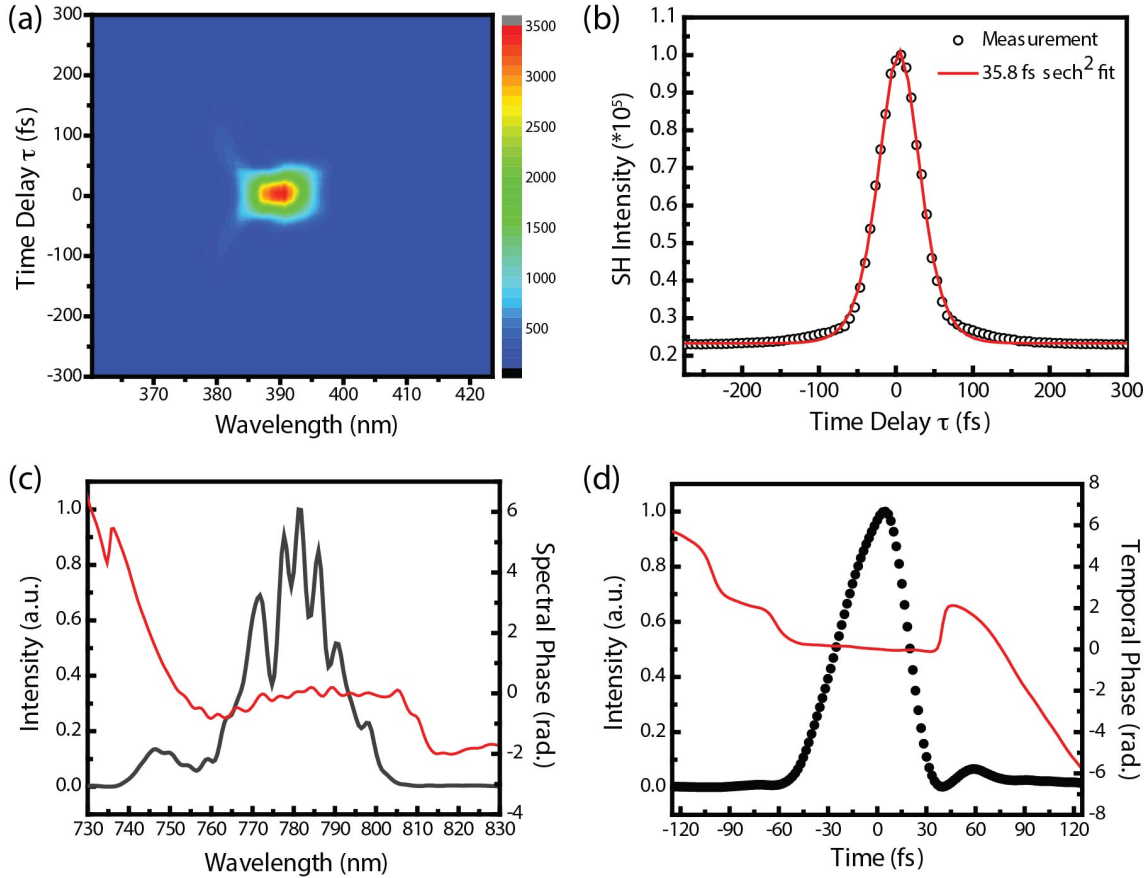


Figure 2-6: (a) Second-order harmonic spectra acquired at various time delays  $\tau$  in the autocorrelator. (b) Plot of the integrated second-order harmonic intensity to time delay  $\tau$ . The red line gives a fit of 35.8 fs  $\text{sech}^2$ -shaped peak. (c) Retrieved spectrum and spectral phase using the FROG analysis technique. (d) Retrieved laser pulse electric field and the associated phase by the same FROG analysis scheme.

## 2.2 Optical Layout

The optical layout from the femtosecond amplifier laser system to the vacuum chamber assembly is illustrated in Fig. 2-1. A 1 mm thick 40% reflectivity beamsplitter (BS1-800-40-1004-45P, CVI) divides the 3.5 mJ pulse energy into two portions: The transmitted part ( $\sim 2$  mJ) is directed to the semi-infinite gas cell for generating high-order harmonics as the probe beam,

while the reflected part ( $\sim 1.5$  mJ) can be converted to various pump beam wavelengths based on the need of experiments.

### 2.2.1 Probe Beam Path

After transiting the first beamsplitter, the  $\sim 2$  mJ 800 nm pulses are further divided by a 90% reflectivity beamsplitter (BS1-800-90-1004-45P, CVI). The  $\sim 1.8$  mJ reflected beam (beam path 1 in Fig. 2-1) is used as the fundamental driver for HHG, which is focused into the semi-infinite gas cell (SIGC) by a 700 mm focal length UV-grade fused silica spherical lens (PLCX-25.4-360.6-UV-670-1064, CVI). The focusing lens mounted on a 1" travel translational stage allows the control of infrared focus position in the SIGC. For the purpose of two-color gating, the  $\sim 200$   $\mu$ J beam transmitted through the 90% reflectivity beamsplitter (beam path 2) is focused onto a 200  $\mu$ m thick type-I BBO ( $\theta = 29.2^\circ$ ) by a 500 mm focal length spherical lens. The generated 400 nm second harmonic has  $\sim 30$   $\mu$ J pulse energy, and its polarization is rotated to the horizontal direction by a zero-order half-waveplate (QWPO-400-08-2-R10, CVI). Then a 1 mm thick dichroic mirror (BSR-48-1004, CVI) recombines the 400 nm symmetry-breaking field collinearly with the fundamental infrared pulses, and their relative arrival time at the SIGC end plate can be manually controlled by a delay line in the 400 nm beam path.

### 2.2.2 Pump Beam Path

From the first beamsplitter that separates the pump and probe beams, the  $\sim 1.5$  mJ reflected infrared pulses can be directly used for optically exciting small band gap samples (beam path 5 in Fig. 2-1). After focusing by a 500 mm focal length spherical lens (PLCX-25.4-257.5-UV-670-1064, CVI), the pump beam enters the sample chamber through a 1 mm thick UV-graded fused silica window (W2-PW1-1004-UV-425-675-0, CVI) and is then directed to the sample by an aluminum mirror (PAUV-SQM-1025-C). The crossing angle between pump and probe beams at the sample is  $\sim 1^\circ$ . Considering the pump beam focus size (80  $\mu$ m FWHM), less than 10 fs temporal broadening is induced by this crossing angle. The path length of the pump beam is designed and calculated to match that of the XUV probe, so that the infrared/visible pump beam and the XUV probe beam arrive at the sample at roughly the same time. The relative timing between pump and probe beams can be finely controlled by an encoded stage with DC-servo motor (M-511, Physik Instrumente) in the pump beam path.

If the semiconductor sample has a band gap greater than 1.55 eV, the second-harmonic generation (SHG) or the third-harmonic generation (THG) processes can convert the 800 nm pulses to visible or ultraviolet wavelengths, respectively. For the SHG purpose, a 100  $\mu$ m thick type-I BBO crystal ( $\theta = 29.2^\circ$ ) is placed after the delay stage with its optical axis perpendicular to the 800 nm polarization (Fig. 2-7), and the residual 800 nm is filtered out by a couple of 400 nm dielectric mirrors (TLM1-400-UNP-1037, CVI). The contrast between 400 nm and 800 nm is greater than 1000, and typically 80  $\mu$ J of 400 nm light can be obtained without focusing the infrared pulses into the BBO crystal. When the third-order harmonic of 800 nm is desired, both the residual 800 nm (horizontally polarized) and the second harmonic (vertically polarized) are sent through a calcite plate (225-2110, Eksma), so that the group velocity delay between two wavelengths is compensated. A zero order dual waveplate ( $\lambda/2@800$  nm +  $\lambda@400$  nm, Eksma) rotates the 800 nm polarization by  $90^\circ$  so that it is parallel to the 400 nm polarization. Sum-frequency generation between 800 nm and 400 nm occurs in a 20  $\mu$ m thick THG BBO ( $\theta = 44.3^\circ$ ) of type-I phase matching. Similarly the generated 266 nm is separated from other

harmonics by a pair of dielectric mirrors with  $\sim 4 \mu\text{J}$  pulse energy and the contrast between 266 nm and 800 nm is greater than 100. The second- and third- order harmonic spectra are shown in Fig. 2-7(c), with 62 meV and 27 meV spectral FWHM, respectively.

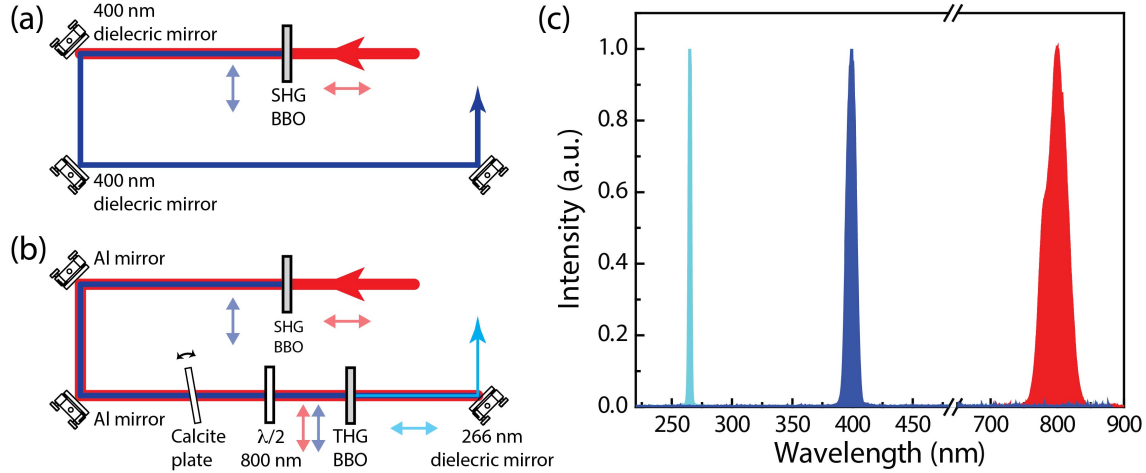


Figure 2-7: The optical layout for (a) SHG and (b) THG processes. Double arrows indicate the polarization directions of each wavelength. (c) The spectra of second harmonic (400 nm, blue) and third harmonic (266 nm, cyan) of the 800 nm infrared light (red). Spectral FWHMs are 27 meV and 62 meV at 266 nm and 400 nm, respectively.

## 2.3 Optical Parametric Amplifiers

Other than the aforementioned second- and third-order harmonics of the 800 nm pulses, a tunable pump wavelength in the visible region is very valuable for studying semiconductor heterojunctions for selectively exciting only one material. Optical parametric amplification is a nonlinear process that can effectively convert the widely available femtosecond infrared pulses from Ti:Sapphire amplifiers into wavelength-tunable visible pulses. Initially in this work a home made noncollinear optical parametric amplifier (NOPA) is constructed, however the poor energy output and the non-ideal spatial profile prohibited using this NOPA for pump-probe experiments. A commercial two-stage optical parametric amplifier (TOPAS-Prime, Light Conversion) now provides reliable femtosecond pulses over a continuous wavelength region from mid-infrared to visible. The concepts and designs of these two OPAs are introduced in the following sections.

### 2.3.1 Concepts

Optical parametric amplification is a second-order nonlinear effect that can exchange energy between photons of different frequencies, as illustrated in Fig. 2-8. In a suitable nonlinear crystal, a high intensity beam (the pump beam) with high photon frequency  $\omega_p$  (wavelength  $\lambda_p = 2\pi c / \omega_p$ ) transfers its energy to another weaker beam (the signal beam) with lower photon frequency  $\omega_s$ , and with this interaction a third beam (the idler beam with frequency  $\omega_i$ ) is emitted from the nonlinear crystal. Overall the photon energy has to be conserved during the interaction:

$$\omega_p = \omega_s + \omega_i \quad (2.3)$$

thus the frequency of idler beam  $\omega_i$  is the difference of the fixed pump frequency  $\omega_p$  and the tunable signal frequency  $\omega_s$ . When an 800 nm beam is used as the pump beam, the wavelength of signal beam is tunable from 800 nm to the 1.6  $\mu\text{m}$  degeneracy point, where  $\lambda_s = \lambda_i = 2\lambda_p$ , while the idler extends from 1.6  $\mu\text{m}$  to longer wavelength. Alternatively the pump beam can be the frequency-doubled 400 nm pulses, in which case the signal is tunable between the 400 – 800 nm visible wavelength while the idler is in the near-infrared region. In this respect, the nonlinear process is similar to difference frequency generation (DFG), except in the case of optical parametric amplification the pump beam is more intense than the signal beam, such that the pump energy depletion can be neglected.

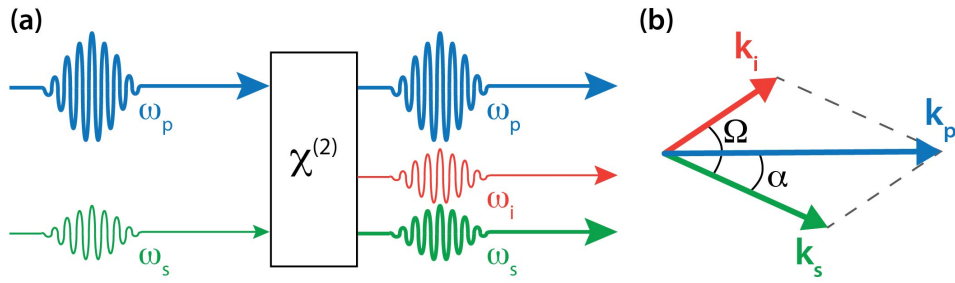


Figure 2-8: (a) Conceptual scheme of the optical parametric amplification process. (b) Phase matching in a noncollinear OPA interaction geometry.

Additionally, the phase matching condition

$$\vec{k}_p = \vec{k}_s + \vec{k}_i \quad (2.4)$$

requires the momentum of all involved photons to be conserved, in which  $\vec{k}_p$ ,  $\vec{k}_s$ , and  $\vec{k}_i$  are the wave vectors of pump, signal, and idler beams, respectively. Efficient energy transfer from the pump beam to a broadband signal beam can be achieved by choosing an interaction angle  $\alpha$  when superimposing two beams on the nonlinear crystal (Fig. 2-8(b)). Comparing to the signal beam, the idler has a longer wavelength and the refractive index is smaller, such that it travels faster than the signal in the nonlinear crystal. The angle  $\Omega$  between signal and idler varies with signal wavelength at a fixed  $\alpha$  angle, and the most efficient energy transfer happens when the group velocity mismatch is compensated:

$$v_g^s = v_g^i \cos \Omega \quad (2.5)$$

so that the signal and idler beams can stay overlapped while travelling through the nonlinear crystal and keep amplifying each other. Combining Eq. (2.4) and (2.5), the optimal angle  $\alpha$  for broadband phase matching is given as<sup>71</sup>

$$\alpha = \sin^{-1} \sqrt{\frac{1 - (v_g^s / v_g^i)^2}{1 + 2v_g^s n_s \omega_s / v_g^i n_i \omega_i + n_s^2 \omega_s^2 / n_i^2 \omega_i^2}} \quad (2.6)$$

where  $n$  is the refractive index in the nonlinear crystal.

### 2.3.2 Home-built Noncollinear Optical Parametric Amplifier

A single-stage, noncollinear optical parametric amplifier (NOPA) is built and its optical layout is illustrated in Fig. 2-9. About 1 mJ of horizontally polarized, 35 fs, 800 nm pulses is frequency-doubled to 400 nm by a 200  $\mu\text{m}$  thick type-I BBO ( $\theta = 29.2^\circ$ ) as the pump beam of NOPA. A small fraction of infrared is split off by a 2% reflectivity beamsplitter and focused into a 1 mm thick sapphire window by a concave mirror, and a variable neutral density filter is used to adjust the energy of the infrared. At suitable field intensity, self-phase modulation and self-guiding effects in the sapphire window would generate a stable single-filament white-light continuum (WLC) with high spatial coherence (Fig. 2-9(b)). A 750 nm short-wave pass edge filter is used to cut out the residual 800 nm light, and the measured WLC spectrum extends to as short as 470 nm with  $\sim 50$  nJ pulse energy (Fig. 2-9(c)). A second curved mirror refocuses the WLC signal beam to  $\sim 120 \mu\text{m}$  diameter at a second BBO (1 mm thick,  $\theta = 32^\circ$ ), which is used as the nonlinear mixing crystal. The 400 nm pump beam and the WLC signal beam are superimposed at the mixing crystal with an  $\sim 6.5^\circ$  crossing angle. Polarizations of the signal and pump beams are respectively horizontal and vertical directions, and the cut angle of the wave-mixing BBO is chosen for type-II ( $o_s + e_i \rightarrow e_p$ ) phase matching. This means the amplified signal beam remains horizontally polarized while the emitted idler beam is vertically polarized.

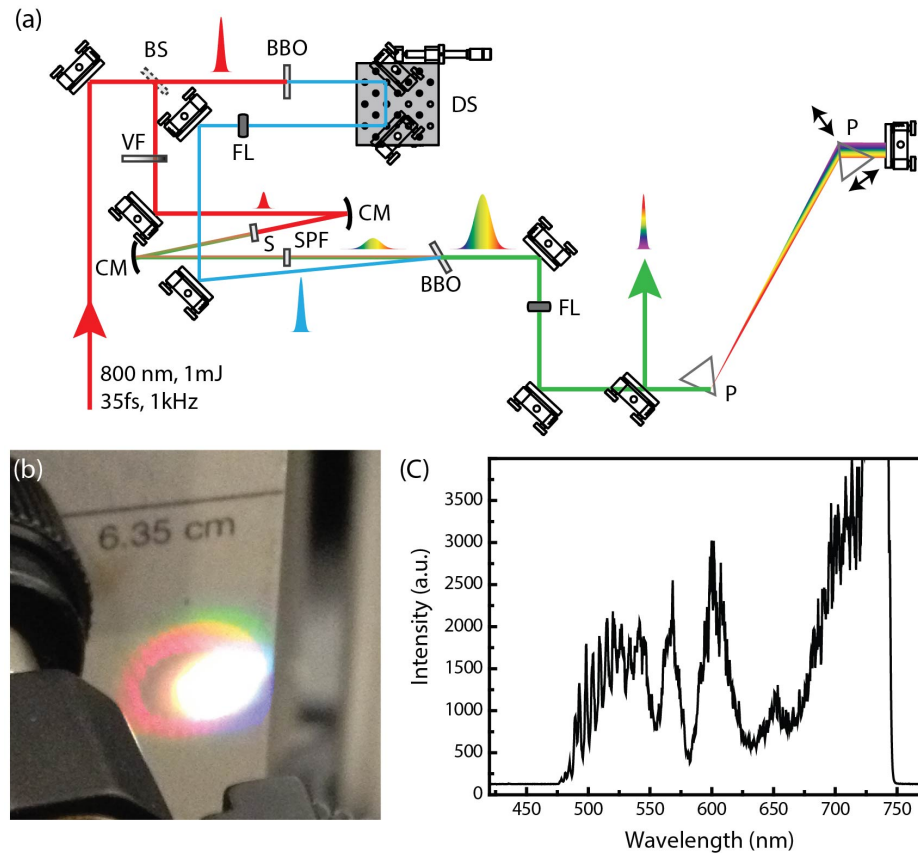


Figure 2-9: Optical layout of the home-built noncollinear OPA. BS: beamsplitter; DS: delay stage; FL: focusing lens; VF: variable density filter; CM: concave focusing mirror; S: sapphire plate; SPF: short-pass filter; P: prism.

Since the WLC is highly chirped, the pump beam can only temporally overlap and transfer energy to a small portion of the WLC spectrum. A delay stage in the pump beam path can be used to select the spectral component in the WLC to be amplified, thus the NOPA output wavelength is tunable in the 490 – 650 nm range as shown in Fig. 2-10(a). Several parameters need to be optimized in order to maximize the output power at each wavelength: the spatial overlap between pump and signal beams at the wave-mixing BBO, the crossing angle between pump and signal beams, and BBO angle relative to the incident beams. The averaged NOPA output power is 18 mW at 1 kHz repetition rate, corresponding to a parametric gain of 360 in a single pass through the crystal and ~12% energy conversion efficiency from the pump beam. The amplified signal pulses can be compressed by implementing a folded 2-prism compressor (Fig. 2-9(a)): after collimation by a spherical lens, the NOPA output signal beam is sent through near the tip of a BK7 equilateral dispersing prism that is placed at the angle of minimum deviation. The second prism is also placed at the angle of minimum deviation in order to compensate the angular dispersion, and then an aluminum mirror reflects the beam back through the same path but tilted downwardly by a small angle. The second prism is mounted on a linear translation stage and can be moved in and out of the beam, such that the best pulse compression can be achieved by varying the traveling distance in the prism. The optimal distance between two prisms (~ 35 cm) also needs to be adjusted slightly according to the wavelength. After the beam passes through the prism four times (two times through each prism), the returning beam would be ~ 3 mm lower than the input beam and can be sent out with a pick-off mirror. The same intensity autocorrelator that is described in Sec. 2.1.2 can also be used to measure the temporal pulse profile of the NOPA output by replacing the original type-I BBO with another that is cut at 48° angle. In Fig. 2-10(b), the pulse duration at 530 nm output wavelength is measured to be a  $77.0 \pm 3.4$  fs Gaussian function. The time-bandwidth product  $\Delta t \times \Delta\omega$  is 0.697, which slightly deviates from 0.44 for a Fourier transform-limited pulse.

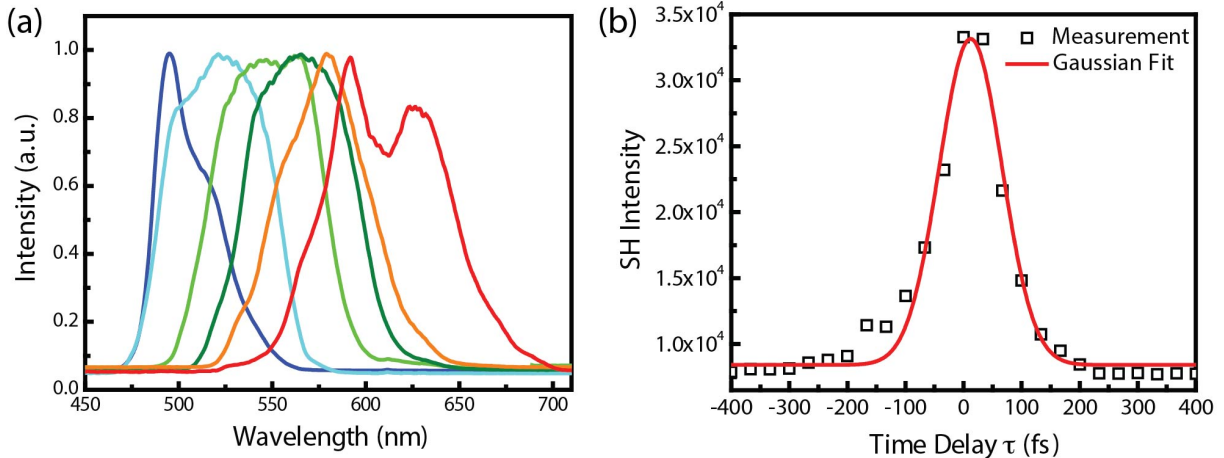


Figure 2-10: (a) Selected tunable output spectra of the home-built NOPA. (b) Intensity autocorrelation trace for 530 nm NOPA output wavelength. The Gaussian fit gives a  $77.0 \pm 3.4$  fs pulse duration.

Although the home-built NOPA is able to provide tunable wavelength output in the visible region, there have been some problems prohibiting using it as the pump light source for transient XUV absorption experiments: first of all, a significant portion of the output energy was lost before arriving at the sample chamber. Some of the energy lost can be attributed to the reflectivity of metal-coated mirrors, but most of the loss happens in the prism compressor. Even

at the maximum 18 mW output that is measured right after the wave-mixing crystal, only 4 mW was left prior entering the sample chamber. This means that it is especially crucial to maintain the NOPA at its best performance on a daily basis in order to have sufficient energy to excite the solid-state sample. Secondly, the signal beam output from NOPA cannot be focused down to a spot with size comparable to the XUV probe beam focus ( $\sim 80 \mu\text{m}$  diameter). Several combinations of collimation and focusing lens have been tested but the smallest focus spot ever obtained is  $\sim 250 \mu\text{m}$  in diameter. The poor spatial mode may be attributed to the distorted 400 nm beam profile during the parametric amplification stage, *i.e.* the self-focusing caused by the intense electric field near the focus would give a donut-shaped beam profile. By placing the pump beam focus after the wave-mixing crystal, spatial beam quality of the amplified signal can be improved, however the output power would be compromised. Overall, insufficient pulse energy combined with large focal spot size means it would be difficult to use the home-built NOPA for creating enough excited charge carrier density in the semiconductor samples. Alternatively, a commercial two-stage OPA (TOPAS, Light Conversion) will be used to generate femtosecond visible pulses with higher power and superior beam quality. The working concepts and characterization of TOPAS will be stated in Sec. 2.3.3.

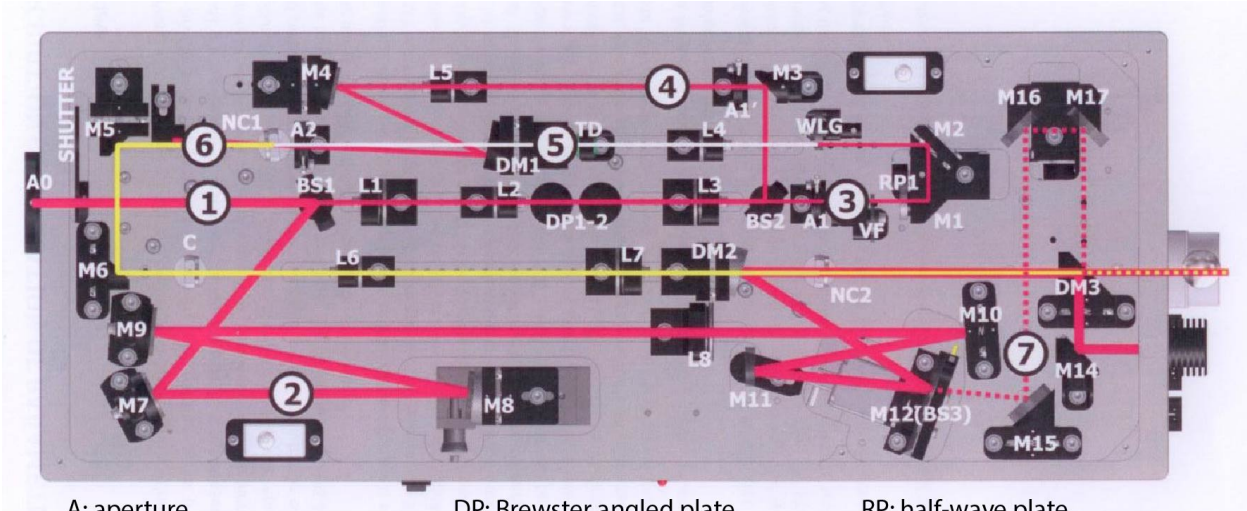
### 2.3.3 TOPAS

The TOPAS amplifier used in this work is customized to be pumped with 1.4 mJ, 800 nm, and 35 fs infrared pulses at 1 kHz repetition rate. It consists of two stages of amplification: the first stage amplifier (pre-amp) is seeded by a WLC and is responsible for providing a high quality signal beam in a noncollinear interaction geometry; the second stage (power amplifier) amplifies the pre-amp output with higher gain in a collinear geometry. The wavelength of the TOPAS signal beam output is tunable from 1.16  $\mu\text{m}$  to the 1.60  $\mu\text{m}$  degeneracy point, while the idler ranges from 1.60 to 2.60  $\mu\text{m}$ . An extra frequency-doubling or sum-frequency crystal converts these near-infrared outputs to the visible light region. Table 2-1 summarizes the tunable wavelength ranges for each operation mode, as well as the pulse energies and polarizations. It can be seen that TOPAS is able to deliver reliable femtosecond pulses that cover most of the visible and near-IR region. Since in TOPAS all the optical elements are motorized and enclosed, it is also an advantage over the home-built NOPA in terms of the ease of operation and maintenance.

Output Variety	Wavelength ( $\mu\text{m}$ )	Pulse Energy ( $\mu\text{J}$ )	Polarization <sup>b</sup>
<b>Signal</b>	1.14 – 1.60	190 – 300	V
<b>Idler</b>	1.60 – 2.80	70 – 220	H
<b>SH<sup>a</sup> of Signal</b>	0.57 – 0.80	10 – 60	H
<b>SH of Idler</b>	0.80 – 1.15	2 – 20	V
<b>Signal + Pump</b>	0.47 – 0.53	80 – 160	V
<b>Idler + Pump</b>	0.53 – 0.62	35 - 70	V

Table 2-1: Wavelength tuning range and available pulse energies for different TOPAS output modes. The pump wavelength is 800 nm with horizontal polarization. Pulse energies are obtained by dividing the output power by the 1 kHz repetition rate. <sup>a</sup> SH: second-order harmonic generation. <sup>b</sup> V: vertically polarized. H: horizontally polarized.

The optical layout of the TOPAS is illustrated in Fig. 2-11 and discussed as follows: The majority of the 1.4 mJ input energy (beam path 1) is reflected by a 96% beam splitter (BS1) to be used as the pump beam (beam path 2) for the second-stage power amplifier. The transmitted beam through BS1 is telescopically down and further divided by an 80% reflectivity beam splitter (BS2). The transmitted beam (beam path 3) has its polarization rotated to the vertical direction before being focused into a 2 mm thick sapphire plate for the generation of a single filament WLC. Similar to the home-built NOPA, a variable density filter is used for smooth adjustment of the 800 nm intensity in the sapphire plate. The generated WLC (beam path 5) goes through a dispersive plate, which is used to stretch out the WLC pulse temporally, and then focused onto the pre-amplifier nonlinear crystal (NC1). The reflected part off BS2 is used as the pump beam (beam path 4) for the pre-amplifier, and its intensity should be high enough to generate parametric super-fluorescence in NC1 but not exceed the threshold for generating white-light continuum. Since the pre-amplifier is operated in a noncollinear geometry, the amplified signal beam can be easily separated from the residual pump and the emitted idler. Wavelength tuning of the signal beam can be achieved by changing the delay of the WLC with respect to the 800 nm pump beam, while rotating the pre-amp crystal can optimize phase-matching and thus increase the amplification gain.



A: aperture  
BS: beam splitter  
C: compensator  
DM: dichroic mirror

DP: Brewster angled plate  
L: spherical lens  
M: mirror  
NC: nonlinear crystal

RP: half-wave plate  
TD: dispersive plate  
VF: variable density filter  
WLG: sapphire plate

Figure 2-11: Detailed layout of TOPAS, a two-stage OPA system that converts femtosecond infrared input to tunable wavelength visible output. Courtesy of Light Conversion Ltd.

The highly divergent pre-amplifier signal output (beam path 6) is collimated and directed through the second nonlinear crystal (NC2) in the power amplifier. This second-stage amplifier is pumped by the bulk of the incoming 800 nm energy (beam path 2), and the high pump intensity can lead to saturated amplification. Both pump and signal beams go collinearly through the nonlinear crystal, which is mounted on a computer controlled rotation stage. The delay between signal and pump in the power amplifier is modulated by a pair of Brewster angled plate (DP1 & DP2) in the pre-amplifier beam path: these two plates can be rotated in opposite directions in order to change the path length and the delay with respect to the pump beam. Changing the angle of the pre-amp crystal would introduce a lateral displacement to its signal

output, which eventually affects the spatial overlap at the power amplifier crystal. This displacement can be eliminated by rotating a compensator plate in the beam path 6 to the opposite direction. The signal and idler generated from the second-stage power amplifier propagate collinearly and are separated from the residual pump beam by a dichroic mirror (DM3). The maximum combined energy of signal and idler is about 500  $\mu$ J, corresponding to  $\sim 36\%$  energy conversion efficiency from the 1.4 mJ 800 nm pump energy.

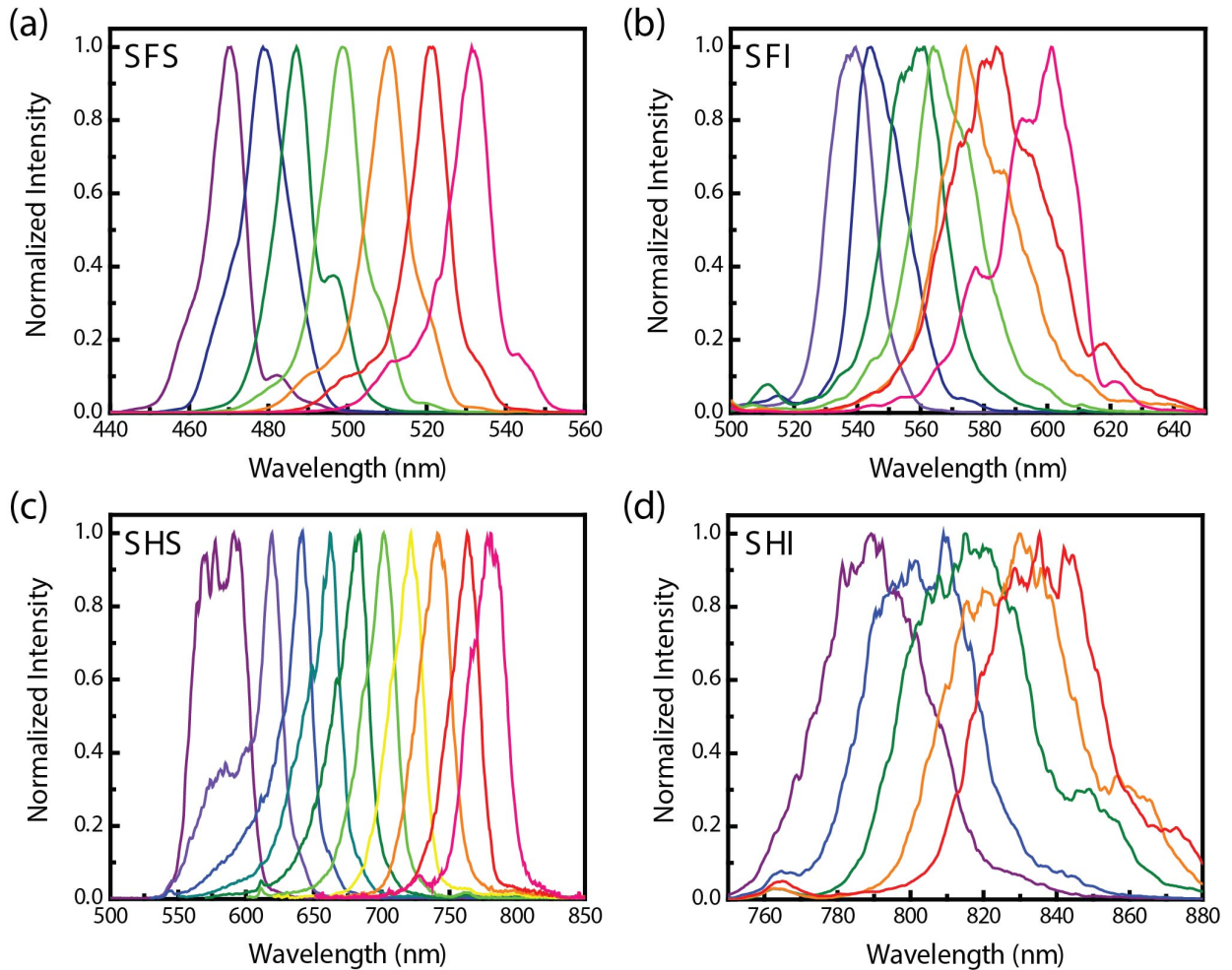


Figure 2-12: Tunable output spectra of TOPAS. (a) SFS: Sum frequency of the signal beam and the 800 nm pump beam. (b) SFI: Sum frequency of the idler beam and the 800 nm pump beam. (c) SHS: Second harmonic of the signal beam. (d) SHI: Second harmonic of the idler beam.

In order to deliver output in the visible wavelength range, a third BBO crystal of type-I phase matching is placed after the main module of TOPAS. This BBO is used for generating the second-order harmonic of either signal or idler beams (SHS and SHI, respectively). Since the signal beam is vertically polarized, when operating at the SHS mode the BBO crystal needs to be rotated  $90^\circ$  accordingly such that the extraordinary axis is perpendicular to signal beam polarization. The SHS/SHI wavelength can be tuned by changing the signal/idler output wavelength and rotating the last BBO accordingly, and the residual signal/idler is filtered out by

a pair of dichroic mirrors. Several output spectra are shown in Fig. 2-12, and the FWHM of each spectrum ranges from 20 to 40 nm. In addition, dichroic mirror DM3 in the TOPAS can be removed so that both the idler and the residual 800 nm pump beam are sent to the third BBO for sum frequency generation of type-I phase matching (SFI). Because the pump frequency is higher than the idler, the SFI mode produces a shorter wavelength output than the SHI mode, ranging from 530 nm to 620 nm. Sum frequency generation between the signal and the pump beam (SFS) can also be done. But since these two beams have perpendicular polarizations, this mode needs to be operated using another BBO of type-II phase matching. This extends the output wavelength down to 470 nm, the shortest wavelength of all operating modes (Fig. 2-12(a)). The output power and the tunable wavelength range of each TOPAS output mode are summarized in Fig. 2-13.

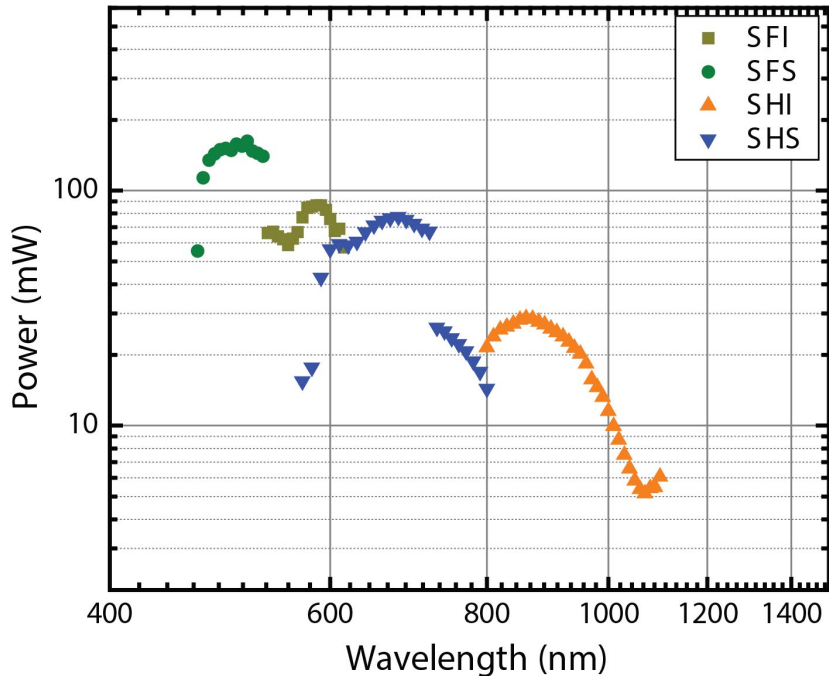


Figure 2-13: The TOPAS output power at various wavelengths at 1kHz repetition rate. The discontinuity of measured power at 720 nm is not a real performance drop, but rather caused by the different wavelength settings of the power meter.

Temporal profile of the 530 nm SFS output is measured by the intensity autocorrelation technique. A type-I BBO that is cut at  $\theta = 48^\circ$  allows phase matching for second-harmonic generation at this wavelength. The SH FROG trace and analysis results are shown in Fig. 2-14. Not only the retrieved 55 fs pulse duration is shorter than the home-built NOPA, the available power is also 10 times higher. Moreover, the TOPAS outputs exhibit better beam qualities than that of home-built NOPA and is thus more suitable as the optical pump light source for transient absorption experiments on a daily basis. Excited-state charge carrier dynamics in spinel cobalt oxide ( $\text{Co}_3\text{O}_4$ ) are investigated at multiple pump wavelengths generated from the TOPAS, and the results will be presented in Chapter 5.

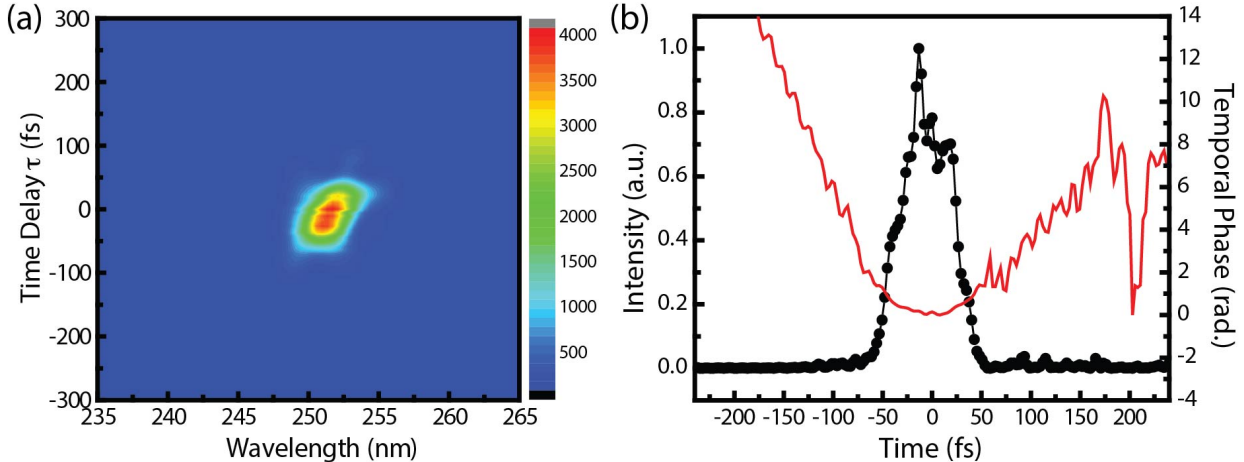


Figure 2-14: (a) Second-harmonic FROG trace of the 520 nm TOPAS output. (b) Retrieved electric field and temporal phase by the FROG analysis. The temporal FWHM is  $\sim 55$  fs.

## 2.4 Vacuum Chamber Assembly

Since XUV photons have very short attenuation lengths in air, a high vacuum environment is necessary once infrared pulses are converted to XUV via high harmonic generation in the semi-infinite gas cell. The instrument comprises three high vacuum chambers, in which XUV pulses are generated, focused, interact with samples, spectrally dispersed, and detected (Fig. 2-1). These chambers are separated by two pneumatic gate valves, so each can be vented to atmosphere without affecting the vacuum environments in other chambers. The first chamber (HHG chamber) is pumped by a 1000 L/sec turbo molecular pump (TMP-1003LM, Shimazu), which is backed by a 40 m<sup>3</sup>/hour rotary vane pump (Trivac D40B, Oerlikon Leybold). The chamber pressure remains below  $4 \times 10^{-5}$  Torr ( $5.3 \times 10^{-3}$  Pa) if the SIGC is filled by noble gas during HHG, however in the case of an empty SIGC the base pressure in the HHG chamber is lower than  $8 \times 10^{-9}$  Torr ( $1.1 \times 10^{-6}$  Pa). The second chamber (refocusing chamber) houses a toroidal mirror that focuses the XUV pulses and is pumped by a 700 L/sec turbo molecular pump (Turbo-V 701, Varian), which is backed by a 25 m<sup>3</sup>/hour rotary vane pump (Trivac D25B, Oerlikon Leybold). The pressure in the refocusing chamber remains about  $4 \times 10^{-8}$  Torr ( $5.3 \times 10^{-6}$  Pa) during the experiments. The third and last chamber (sample and XUV spectrometer chamber) is divided into two sections that are pumped separately: a 1000 L/sec turbo molecular pump (TMP-1003LM, Shimazu) is used to evacuate the front section that contains sample-mounting stages, and a 150 L/sec turbo molecular pump (Turbovac-150, Oerlikon Leybold) is used for the rear spectrometer section. Both turbo molecular pumps are backed by the same 25 m<sup>3</sup>/hour rotary vane pump, and the base pressure in the spectrometer section is about  $2 \times 10^{-8}$  Torr ( $2.7 \times 10^{-6}$  Pa). The functions of each individual chamber are described as follow.

### 2.4.1 High Harmonic Generation Chamber

In this apparatus a semi-infinite gas cell (SIGC) is chosen as the XUV source over other HHG interaction geometries, such as pulsed valves or hollow waveguides, for the combination of high conversion efficiency and simplicity of design. The main function of the high harmonic generation chamber is to bridge the SIGC, which is filled with tens of Torr of noble gas medium,

to the high vacuum environment ( $<10^{-6}$  Torr). The design of the SIGC is illustrated in Fig. 2-15: A 40 cm long 1" outside diameter stainless steel tube acts as the gas cell that bridges from atmosphere to a high vacuum chamber. A 1 mm thick UV-grade fused silica substrate (W2-PW-1004-UV-670-1064-0, CVI) with broadband 633 - 1064 nm antireflection coating on both surfaces is used as the laser entrance window of the gas cell, while the exit side of the cell is an exchangeable 250  $\mu$ m thick stainless steel plate. Infrared pulses are focused into the SIGC by a 700 mm focal length spherical lens, and the focus position is placed near the stainless steel plate. Near the focus the peak intensity of the fundamental field (40 fs, 1.8 mJ at 800 nm center wavelength) is equivalent to  $\sim 1.8 \times 10^{15}$  W/cm<sup>2</sup> in vacuum, which would ablate an  $\sim 80$   $\mu$ m diameter pinhole on the stainless steel plate. It is also near this region that the intense electric field interacts with the noble gas atoms and facilitates an efficient HHG process. A 1000 L/sec turbo molecular pump (TMP-1003LM, Shimadzu) evacuates the noble gas atoms that diffuse through the pinhole. Considering the conductance of the pinhole in the viscous-flow regime:

$$C \approx 20A = 1 \times 10^{-3} \text{ L} \cdot \text{sec}^{-1} \quad (2.7)$$

where  $A$  is the area of the pinhole in cm<sup>2</sup>. The pressure  $P_2$  in the vacuum chamber when the SIGC is filled with 80 Torr of neon (denoted as  $P_1$ ) can be estimated via the master equation:

$$\frac{P_2}{S_p} = \frac{Q}{S_p} = \frac{(P_1 - P_2) \cdot C}{S_p} \sim 8 \times 10^{-5} \text{ Torr} \quad (2.8)$$

where  $Q$  stands for the gas throughput and  $S_p$  is the pumping speed. This estimated value is of the same order of magnitude to the actual pressure ( $4 \times 10^{-5}$  Torr) that is measured by an inverted magnetron gauge (IMG-100, Varian), and the reabsorption of XUV photons in the vacuum chamber can be neglected at this low pressure.

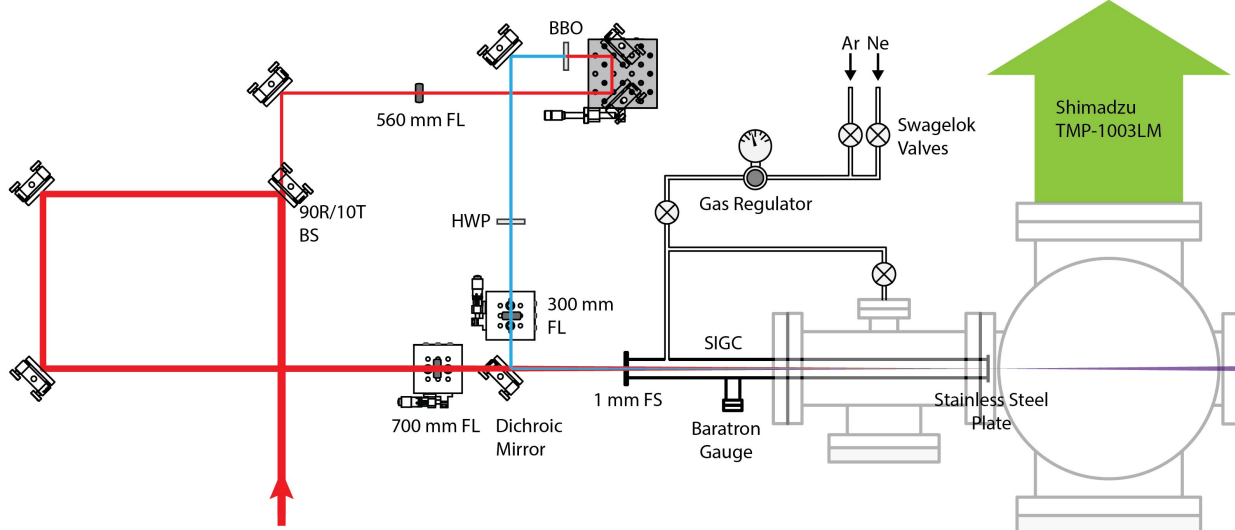


Figure 2-15: Design of the semi-infinite gas cell in the high harmonic generation chamber. The optical layout for two-color gating technique is also drawn in the same scale.

A gas regulator and Swagelok valves can be used to fill the SIGC with different noble gas mediums or to evacuate the gas cell by connection to the high vacuum chamber, and the gas pressure in the SIGC is measured by a Baratron pressure gauge located near the gas inlet. Both

100  $\mu\text{m}$  and 250  $\mu\text{m}$  thick stainless steel plates have been tested as the SIGC end plate, and it is discovered that the laser-drilled pinhole is smaller in the thicker plate. This not only preserves the noble gas usage by making the gas cell more confined, it also lowers the pressure in the high vacuum chamber under HHG conditions. The spectral profiles of the generated XUV pulses can be controlled by varying the gas pressure in the SIGC, the chirp of the infrared fundamental pulses, and the infrared focus position relative to the end plate of SIGC. The optimal operating pressures in the SIGC for argon and neon have been found to be 35 and 85 Torr, respectively. A purple-colored plasma can be observed near the SIGC exit when making high-order harmonics from argon, while neon produces an orange-colored plasma (Fig. 2-16).

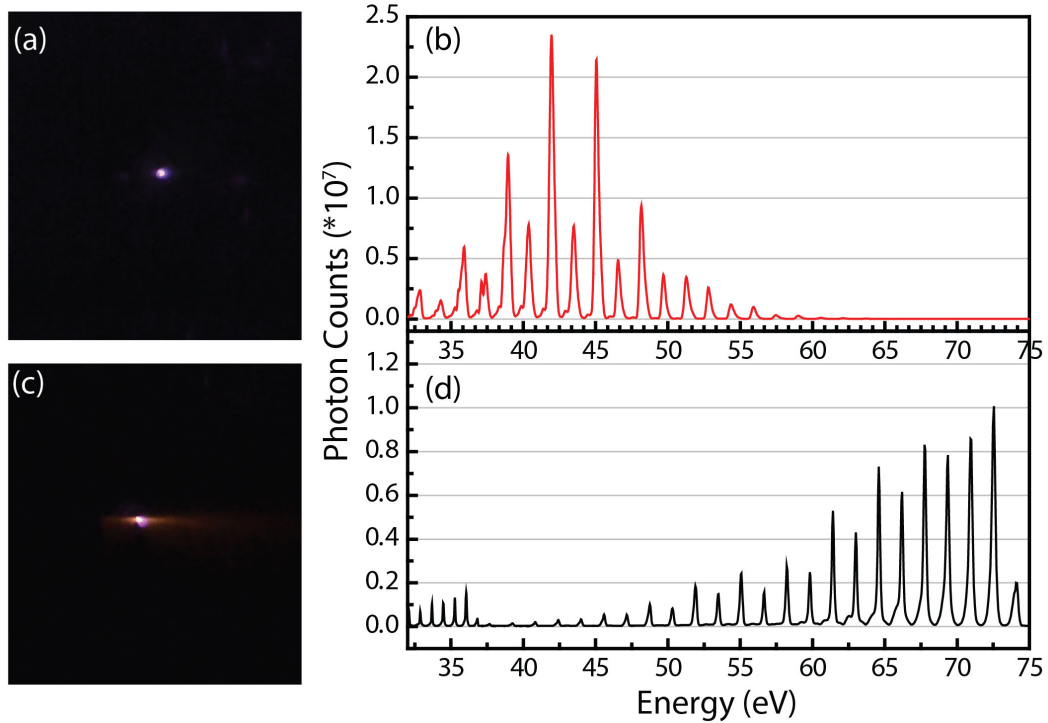


Figure 2-16: (a) The purple-colored argon plasma observed during the high harmonic generation process and (b) the resulted high-order harmonic spectrum. (c) The orange-colored neon plasma and (d) the corresponding neon high-order harmonics.

As has been introduced in Sec. 1.3.4, the two-color gating technique can break the inversion symmetry of the electric field and leads to the generation of both the odd- and even-order harmonics. This is practically done by mixing  $\sim 30 \mu\text{J}$  of 400 nm light into the fundamental 800 nm, so both beams propagate collinearly in the SIGC (Fig. 2-15). The high-order harmonic spectra generated with argon and neon gases with the two-color gating technique are shown in Fig. 2-16(b) and 2-16(d), respectively. The argon harmonics distribute strongly from 35 to 50 eV, while the neon harmonics range from 50 to 72 eV with less photon flux than argon. The difference in the energy range of high-order harmonics between argon and neon can be explained in terms of their ionization potentials, according to the relation between the cut-off energy  $E_{\text{cutoff}}$  and the ionization potential  $I_p$ :

$$E_{\text{cutoff}} \approx I_p + 3.17U_p \quad (2.9)$$

However tunnel ionization of neon is more difficult than the same process for argon, therefore the neon harmonics flux is about one order of magnitude lower. It worth noting that the highest observed neon harmonic (the 47<sup>th</sup> order) is cut off by the L-edge absorption of aluminum that is used as filters to separate the XUV from the residual fundamental field. From the shape of the spectrum, higher order harmonics are expected to exist in the 72 – 90 eV energy range.

The absolute XUV photon flux at the SIGC source can be estimated from the measured intensity at the X-ray CCD detector: the detected electron counts  $N_c$  on each CCD pixel are related to the number of photons illuminated  $N_{ph}$  on that pixel by the following equation

$$N_{ph}(E) = \frac{N_c(E) \cdot G}{QE(E)} \frac{3.65\text{eV}}{E} \quad (2.10)$$

where  $E$  is the photon energy in eV,  $G$  is the gain setting of the detector,  $QE$  is the energy-dependent quantum efficiency, which is fairly consistent at 41% over the energy range of 30 – 80 eV. Both the reflectivity off the gold-coated toroidal mirror and the transmittance of the aluminum filters for the XUV radiation can be estimated by the CXRO database,<sup>72</sup> and the efficiency of the grating is assumed to be ~5% for the first order diffraction. Combining Eq. (2-10) and the knowledge of every optical element in the apparatus, the HHG conversion efficiency from the 1.8 mJ, 800 nm fundamental pulses are calculated to be  $1 \times 10^{-6}$  and  $5 \times 10^{-8}$  for argon and neon gases, respectively. These values are comparable to what is obtained from hollow waveguides, and are at least two orders of magnitudes higher than the reported values by using pulsed valves and finite gas cells as the XUV sources. This can be attributed to the long interaction length caused by the laser filamentation. Moreover, SIGC also features an easier and more straightforward alignment procedure comparing to other HHG methods: there is no need for aligning the fundamental beam through the pinholes of a finite gas cell or a hollow waveguide; instead one iris diaphragm is located before the SIGC entrance window, and another one is placed before the toroidal mirror and used as the near and far alignment targets, respectively.

#### 2.4.2 Refocusing Chamber

After being generated in the high harmonic generation chamber, the XUV radiation diverges while propagating in the same direction of the residual fundamental field. A 0.65  $\mu\text{m}$  thick Al foil (Lebow Company) is used to block residual fundamental infrared pulses but allows 20-40% transmittance for XUV photons with 30-80 eV energies. Due to the low attenuation length in solid materials, XUV radiation needs to be focused by a reflective optical element instead of a transmissive lens. However, the reflectivity of XUV on a polished surface is also extremely low except for using a large incidence angle, as indicated in Fig. 2-17(a), thus a focusing mirror at grazing incidence is preferred for refocusing the dispersed XUV beam. A gold-coated focusing mirror is used at 86° incidence angle in the apparatus, which has 84 - 88% reflectivity over a photon energy range of 35-80 eV (Fig. 2-17(b)).<sup>72</sup>

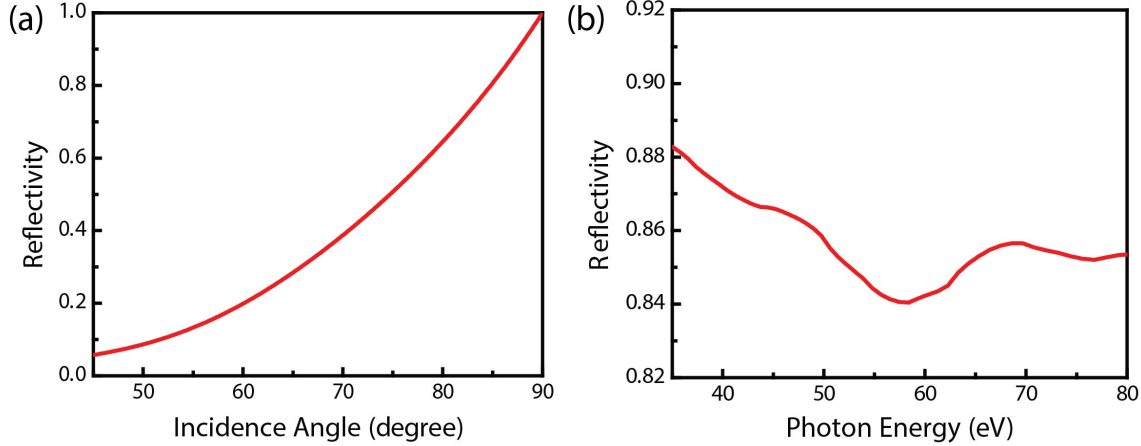


Figure 2-17: (a) Reflectivity of a gold surface for 60 eV XUV photons at different incidence angles. (b) Reflectivity vs. photon energy curve at 86° incidence angle for a gold surface with 10 Å root mean square roughness. These calculation results are obtained from the Center for X-ray Optics (CXRO) website, [www.cxro.lbl.gov](http://www.cxro.lbl.gov).

In order to minimize the astigmatism in the off axis optical system, a toroidal mirror (ARW Optical Corp.) is used instead of a spherical mirror. The relation between the focal length of the focusing mirror and the sagittal ( $R_s$ ) and tangential ( $R_t$ ) radii of curvature of a toroidal surface is as follows:

$$\frac{R_s}{R_t} = \cos^2 \theta \quad (2.11)$$

$$\frac{2 \cos \theta}{R_s} = \frac{1}{D_1} + \frac{1}{D_2} \quad (2.12)$$

where  $\theta$  is the incidence angle, and  $D_1$  and  $D_2$  are distances from the toroidal mirror to the object (XUV source near the SIGC end plate) and image (XUV focus at the sample), respectively. The design of the apparatus has  $D_1 = 110$  cm and  $D_2 = 85$  cm (Fig. 2-18), and by solving Eq. (2.11) and (2.12)  $R_s$  and  $R_t$  are given to be 6.689 cm and 1374.7 cm, respectively.

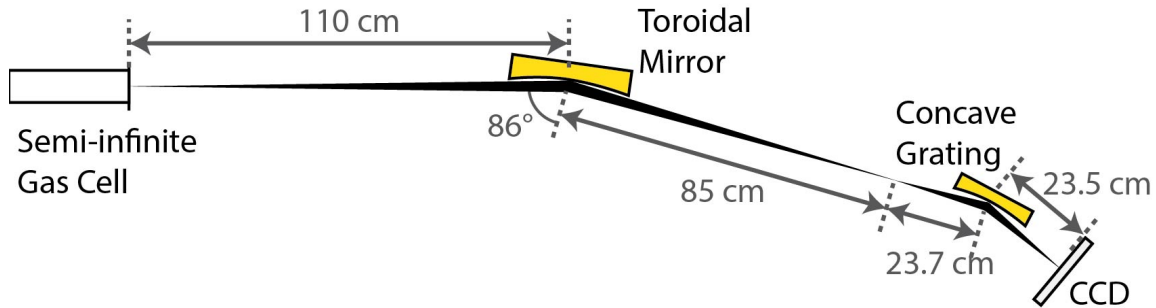


Figure 2-18: XUV beam path from the SIGC exit to the X-ray CCD detector.

The gold-coated toroidal mirror is mounted on a gimbaled three-axis tilt mount (UGP-1, Newport) and has a clear aperture of 10 cm ( $h$ )  $\times$  1 cm ( $v$ ). The size of the XUV beam when arriving at the toroidal mirror can be estimated from its  $1/e^2$  angular width at the source

$$\Theta = \frac{2\lambda}{\pi\omega} \quad (2.13)$$

where  $\lambda$  is the wavelength and  $\omega$  is the beam radius. Since high-order harmonics are emitted from the most intense part of the electric field, it is assumed that the XUV source is half the size of the infrared focus at the SIGC. According to Eq. (2.13), the full-angle divergence of a 60 eV photon from a 40  $\mu\text{m}$  diameter source is calculated to be 0.66 mrad. The small angular divergence means that the XUV beam size would still fit the toroidal mirror after propagation for the 110 cm distance. Alignment of the toroidal mirror is challenging due to the grazing incidence angle, but can be done by using a CCD beam profiler to detect the nominal profile of the infrared fundamental beam that is focused by the same toroidal mirror, since the fundamental infrared and the XUV should propagate collinearly. The gimbaled mount simplifies the alignment procedures to three rotational degrees of freedom: the short-axis tilting of the mirror changes the beam height in the far field, the long-axis tilting can be optimized by monitoring the astigmatism at the focus, and the correct incidence angle should give a Gaussian-shaped focus with nearly 1:1 aspect ratio. Additionally, the relative position of the center of the toroidal mirror to the incoming beam can be adjusted by a translational stage underneath the gimbaled mount. At the optimal toroidal alignment the focused infrared beam profile is shown in Fig. 2-19, and Gaussian fits give x- and y-axis FWHM of 139 and 140  $\mu\text{m}$ , respectively.

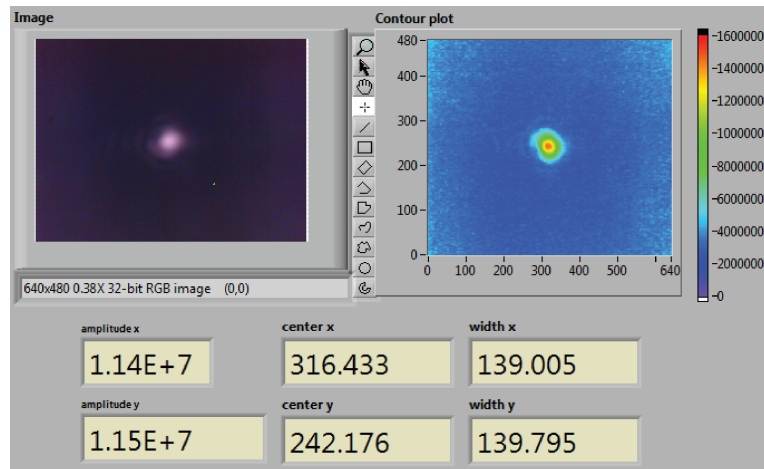


Figure 2-19: Nominal profile of the infrared fundamental beam focused by the toroidal mirror, the image is acquired with a beam profiler placed in the sample chamber.

The size of the XUV focus can also be measured by the scanning knife-edge method *in vacuo*. Fig. 2-20 shows typical knife-edge scan traces for the integrated high-order harmonics produced with 20 Torr of argon and 80 Torr of neon, respectively. The FWHM of the argon high harmonics at the focus is measured, respectively, to be  $111 \pm 1 \mu\text{m}$  ( $h$ ) and  $85 \pm 1 \mu\text{m}$  ( $v$ ), while the neon harmonics have FWHM of  $79 \pm 3 \mu\text{m}$  ( $h$ ) and  $39 \pm 1 \mu\text{m}$  ( $v$ ). It should be noted that although a decent circular infrared beam profile is obtained at the toroidal mirror focus, the XUV

beam always elongates along the horizontal direction no matter which gas is used for generating high-order harmonics. This suggests that the actual XUV source position is affected by the self-guiding of fundamental pulses in the SIGC, therefore the actual XUV focus deviates from the measuring position. This minor problem still needs to be addressed; nevertheless by carefully making the pump beam slightly larger than the XUV beam at the sample position, the apparatus is still capable of performing pump-probe experiments.

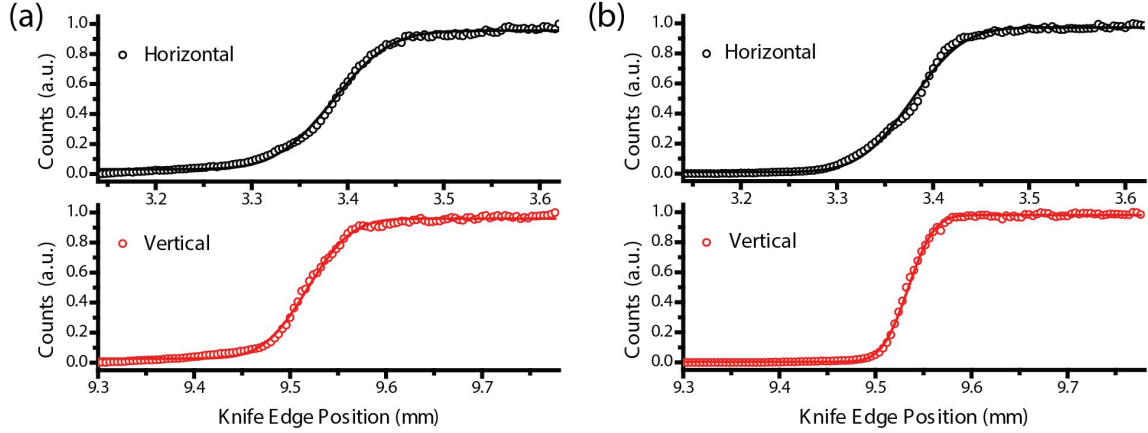


Figure 2-20: Knife-edge scan traces for integrated high-order harmonics produced with (a) 20 Torr of Ar and (b) 80 Torr of Ne at 1.8 mJ fundamental infrared energy. The traces are fitted by an Error function. The measured FWHMs are  $111 \pm 1$  (*h*) and  $85 \pm 1$  (*v*)  $\mu\text{m}$  for Ar harmonics, and  $79 \pm 3$  (*h*) and  $39 \pm 1$  (*v*)  $\mu\text{m}$  for Ne harmonics.

#### 2.4.3 Sample Chamber

The last chamber in the assembly is physically divided into two parts that are connected by a  $\sim 1 \text{ cm}^2$  size opening. The front part is where the semiconductor samples interact with the pump and probe beams, while the rear part hosts an XUV spectrometer consisting of a grating and an X-ray CCD detector. An UV-enhanced aluminum mirror in the sample chamber placed  $\sim 35 \text{ cm}$  before the XUV focus directs the pump beam to the samples, and the crossing angle between the visible pump and the XUV probe beams is  $\sim 1^\circ$  (Fig. 2-21). The barrier that separates the XUV spectrometer from the sample chamber blocks the pump beam while allowing the XUV beam to pass through, and an additional  $0.6 \mu\text{m}$  thick aluminum filter is used to prevent any indirect scatterings entering the spectrometer.

As mentioned in Sec. 1.2.3, the penetration length of XUV with  $30 - 80 \text{ eV}$  photon energy is less than  $20 \text{ nm}$  in a solid. Therefore all the solid-state samples, regardless whether they are thin-films or nanomaterials, are prepared on  $\text{Si}_3\text{N}_4$  or Si substrates (Fig. 2-22). These two substrates are used for supporting samples because of their relatively high transmittance of XUV. A  $100 \text{ nm}$  thick polycrystalline  $\text{Si}_3\text{N}_4$  is robust enough as a flat window and exhibits about 2% and 30% transmission for  $30 \text{ eV}$  and  $80 \text{ eV}$  photon energies, respectively. A  $250 \text{ nm}$  Si substrate, although much thicker than the aforementioned  $\text{Si}_3\text{N}_4$ , is more transparent to XUV, averaging  $\sim 45\%$  in the same energy range. However the Si substrate is soft and appears as a wrinkled membrane. It worth noting that although the XUV transmission is smaller at lower photon energies for both kinds of substrate, it is usually compensated by the higher available photon flux of the argon high harmonics.

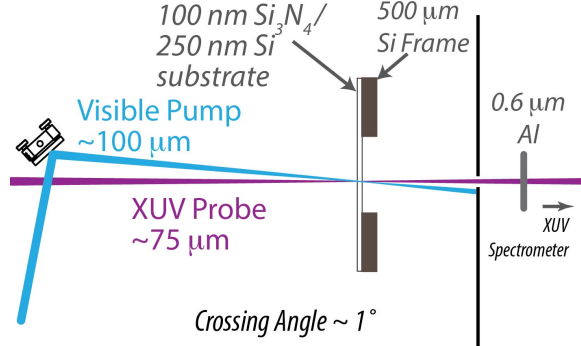


Figure 2-21: Top view of the interaction geometry between the solid-state sample and pump and probe beams. The sample is supported on either a 100 nm  $\text{Si}_3\text{N}_4$  window, or a 250 nm Si membrane.

The sample mounting system is capable of holding six solid-state samples at the same time, and a two-dimensional translational stage (MFA-CCV6, Newport) can be used to move different samples into the beam path *in vacuo*. It has been discovered that the pump beam would heat the sample and cause long-term degradation and damage. This can be avoided, or at least slowed down, by raster scanning the sample during a pump-probe experiment, *i.e.* the translational stage is synchronized with the data acquisition program such that the sample is moved 100  $\mu\text{m}$  (identical to the pump beam FWHM) away after 500 – 2000 pulses illuminated on the same spot. The raster scanning can be performed in both directions that are perpendicular to the probe beam propagation (red arrows in Fig. 2-22(a)), therefore for a sample with  $2 \times 2$  or  $3 \times 3 \text{ mm}^2$  window area there are hundreds of spots that can be used for data acquisition. This means the solid-state samples have to be spatially homogeneous in terms of composition and thickness over the entire window area. For thin-film samples this is easy to achieve by sputtering or atomic layer deposition technique to prepare the samples. For nanowires or quantum dots, nevertheless, care has to be taken when dispersing these nanoscale materials on the substrates.

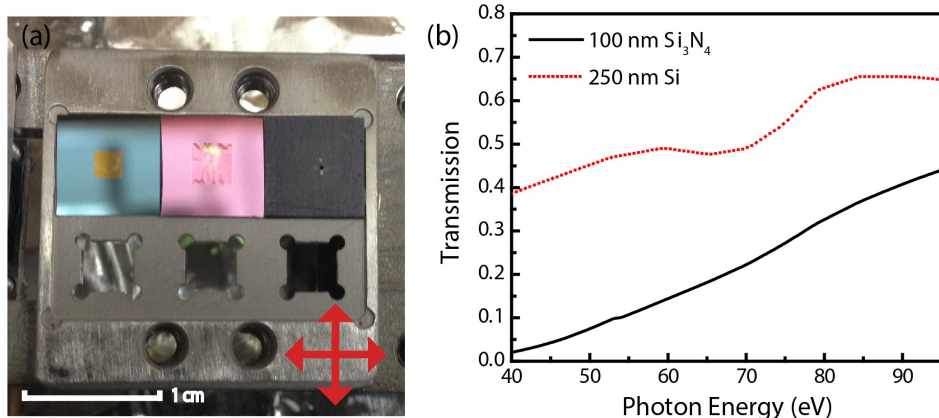


Figure 2-22: (a) Front view of the solid-state sample mounting system. The supporting substrate can be either a  $\text{Si}_3\text{N}_4$  window (left) or a Si membrane (middle). A 300  $\mu\text{m}$  diameter pinhole (Right) is used to find the spatial overlap between the visible pump beam and the XUV probe beam. The arrows indicate the sample raster directions. (b) XUV transmission curves of 100 nm  $\text{Si}_3\text{N}_4$  window and 250 nm Si membrane. These calculation results are obtained from the Center for X-ray Optics (CXRO) website, [www.cxro.lbl.gov](http://www.cxro.lbl.gov).

Additionally, a liquid flow cell module has also been developed. This kind of spectroscopic research is usually only performed in the synchrotron facilities at higher photon energy range, due to the short penetration length of XUV in liquids. As illustrated in Fig. 2-23, the liquid cell consists of two 100 nm Si<sub>3</sub>N<sub>4</sub> substrates that are separated by a 500 nm thick polymer spacer layer. In order to better hold the pressure difference between the interior liquid and the high vacuum environment, the window area on each Si<sub>3</sub>N<sub>4</sub> substrate is reduced to 1 × 1 mm<sup>2</sup>. The liquid inlet and outlet are sealed by rubber O-rings, and the pressure in the sample chamber during an experiment is  $\sim 2 \times 10^{-6}$  Torr ( $2.7 \times 10^{-4}$  Pa). The development of this liquid flow cell opens up many research directions, and it becomes possible to apply the transient XUV absorption spectroscopy for studying dynamics in the liquid phase or at the solid-liquid interface. The hole transfer process from the valence band of a photoexcited Co<sub>3</sub>O<sub>4</sub> thin-film to methanol molecules has been studied by this flow cell module in the current apparatus.<sup>73</sup>

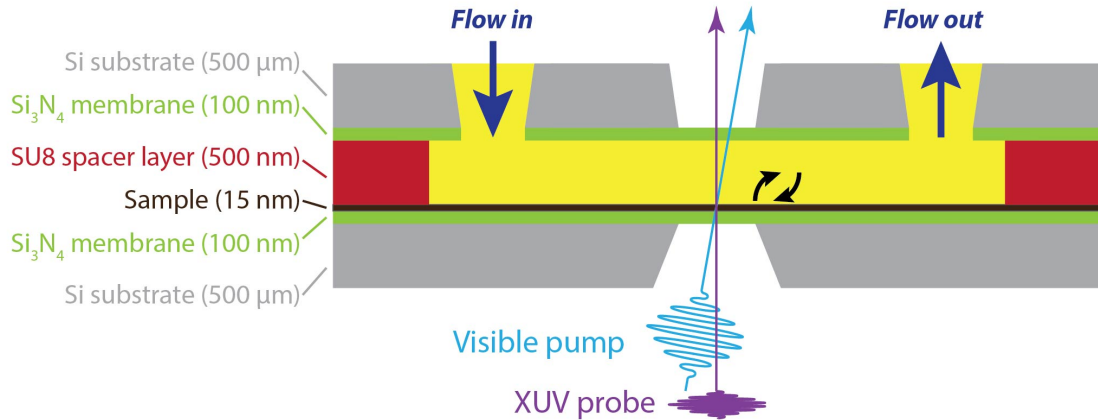


Figure 2-23: Design of the liquid flow cell module (top view). The liquid channel is confined between a pair of 100 nm thick Si<sub>3</sub>N<sub>4</sub> substrates, and the optical path length in the liquid channel can be controlled by the thickness of the spacer layer.

#### 2.4.4 XUV Spectrometer Chamber

After transmission through the sample, the XUV probe is energetically dispersed and detected by a charge-coupled device (CCD) camera. This post-sample spectrometer design enables concurrent counting of photons with different energies, making the data acquisition much more efficient than the pre-sample monochromator configuration. Design of the XUV spectrometer is as shown in Fig. 2-24: a gold-coated diffraction grating (Hitachi High Technologies) is positioned 237 mm away from the sample position, where is assumed to be the focus of the toroidal mirror. Similarly, a grazing incidence angle  $\alpha = 87^\circ$  onto the grating is used in order to have sufficient XUV reflectivity. The average ruling density of the grating is 1200 grooves/mm, and the diffraction angle  $\beta$  for a specific wavelength  $\lambda$  is given by the grating equation:

$$m\lambda = d(\sin \alpha + \sin \beta) \quad (2.14)$$

where  $m$  denotes the diffraction order and  $d$  is the spacing between grooves. According to Eq. (2.14), the first order diffraction ( $m = 1$ ) of the 32 – 77 eV photon energies would spread

between  $\beta = 72.20^\circ$  and  $78.32^\circ$ , respectively. The focal plane of the concave grating (radius of curvature  $R = 5649$  mm) is 235.3 mm from the center of the grating, and here a back-illuminated X-ray CCD camera (PIXIS-XO 400B, Princeton Instrument) is used for detection of the energetically dispersed XUV radiations. The CCD camera has  $1340 \times 400$  pixels and the size of each pixel is  $20 \times 20 \mu\text{m}^2$ , therefore the horizontal dimension of the sensor  $L = 26.8$  mm can be fit with the aforementioned first order diffraction of the 32 – 77 eV energy spread.

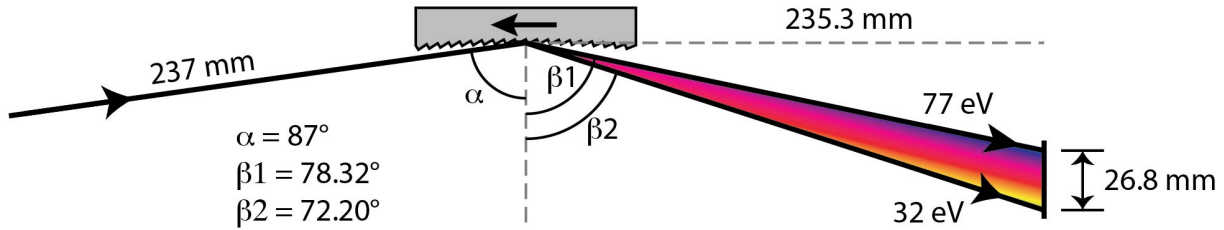


Figure 2-24: Configuration of the XUV spectrometer. The arrow on the grating specifies the blazing direction.  $\alpha$  denotes the incidence angle, and  $\beta_1/\beta_2$  indicate the first order diffraction of the energy spread 32 – 77 eV. The width of this energy range at the focal plane would match the width of the X-ray CCD array (26.8 mm).

A concave grating can energetically disperse and focus the XUV beam simultaneously, therefore it exhibits a higher photon throughput compared to the combination of a toroidal mirror and a plane grating. However, the focus positions at different wavelengths would form an arc that does not overlap well with the planar CCD detector. A flat-field focus can be achieved by using a variable line-spacing grating, *i.e.* the spacing  $\sigma$  between adjacent grooves on the grating is designed to follow the equation<sup>74</sup>

$$\sigma = \sigma_0 / \left( 1 + \frac{2b_2}{R}\omega + \frac{3b_3}{R^2}\omega^2 + \frac{4b_4}{R^3}\omega^3 \right) \quad (2.15)$$

where  $\sigma_0$  is the nominal groove spacing ( $1200 \text{ mm}^{-1}$ ),  $R$  is the radius of curvature of the grating,  $\omega$  is the horizontal distance from the center of the grating, and  $b_2, b_3, b_4$  are the variable-spacing ruling parameters.

Alignment of the spectrometer is done by the following procedures: The  $30 (h) \times 50 (v) \text{ mm}^2$  concave variable line-spacing grating with a blaze angle of  $3.2^\circ$  is placed in the rear compartment of the sample chamber, 237 mm away from the sample mounting system. The grating is mounted on a rotational stage (AG-PR100, Newport) that allows fine control of incidence angle. Initially the height of the grating is adjusted so that its center matches the location of an attenuated infrared fundamental beam. When the high order harmonics are generated with neon in the SIGC *in vacuo* and the residual fundamental light is blocked by aluminum filters, the grating is rotated until a bright spot corresponding to the 0<sup>th</sup>-order diffraction appears on the X-ray CCD camera. When the incidence angle is increased, the first-order diffraction of neon harmonics would appear on the detector with a characteristic energy cut-off caused by the aluminum L<sub>3</sub>-edge at 72.64 eV. Using the actual spectrometer dimension and the grating equation (2.15), the estimated position of the Al L<sub>3</sub>-edge on the X-ray CCD camera can be calculated. At the correct incidence angle, the second-order diffraction ( $m = 2$ ) of

the Al L<sub>3</sub>-edge, which is equivalent to 36.32 eV for the first-order diffraction, would also appear on the right-hand-side (corresponds to lower energy) of the CCD array.

For the wavelength calibration purpose, a sample gas cell filled with xenon can be translated into the XUV focus in the sample chamber, such that the static xenon absorption spectrum is acquired by dividing the transmitted XUV spectrum by another spectrum taken with an empty gas cell (Fig. 2-25(a)). In both spectra the first- and second-order diffractions of the Al L<sub>3</sub>-edge are visible and labeled by purple lines, and the energy region where the xenon electronic transitions take place is labeled by green. Using the Beer-Lambert law the xenon absorption spectrum can be calculated in the CCD camera pixel space (Fig. 2-25(b)). Other than a broad and featureless nonresonant absorption contribution, several peaks that correspond to the  $4d \rightarrow np$  core level absorption are found.

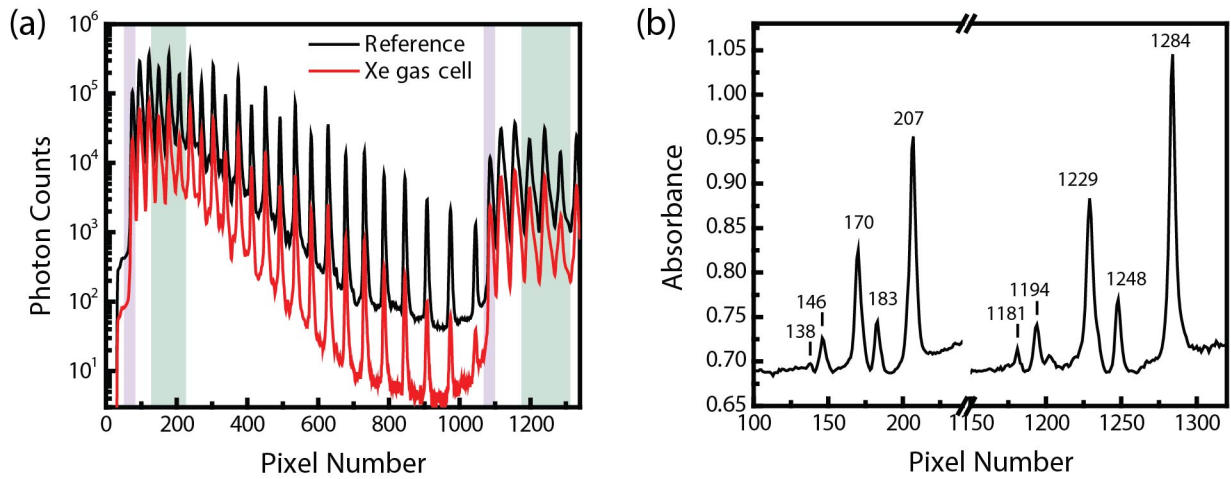


Figure 2-25: (a) Transmitted XUV spectra of a sample gas cell that is either (red) filled with xenon or (black) empty detected by the X-ray CCD camera in the spectrometer. The green shaded area indicates where the resonant absorptions of xenon occur, and the purple line labels the 72.64 eV cut-off on the neon harmonics caused by the Al absorption L<sub>3</sub>-edge. (b) Raw absorption spectrum of xenon in the CCD camera pixel space. For each of the first- and second-order diffractions, five resonant absorption peaks are resolved.

The spectrum in Fig. 2-25 (b) can be compared to the reported xenon photoabsorption data,<sup>75</sup> and the energies associated with these transitions are listed in Table 2-2. For example, the  $4d \rightarrow 6p$  electronic transition in xenon leaves a  $4d$  core hole, and the spin-orbit coupling splits this transition into two absorption peaks: the  $4d^1(^2D_{5/2})6p(^2P_{3/2})$  and  $4d^1(^2D_{3/2})6p(^2P_{1/2})$  states that require 65.11 and 67.04 eV photon energies to excite and appear at pixel #207 and #170, respectively.

Sample	Transition	n	Energy (eV)
Al	$L_3$ edge ( $2p \rightarrow nd$ )	3	72.64
Xe	$^1S_0 \rightarrow 4d^1(^2D_{5/2}) np(^2P_{3/2})$	6	65.11
		7	66.37
	$^1S_0 \rightarrow 4d^1(^2D_{3/2}) np(^2P_{1/2})$	6	67.04
		7	68.34
		8	68.82

Table 2-2: List of the reference points used for wavelength calibration of the XUV spectrometer, including the Al  $L_3$ -edge cutoff on the neon harmonics, and several xenon  $4d \rightarrow np$  resonant absorption lines.

It worth noting that since the neon harmonics have significant flux in the 60 – 70 eV range, the second-order diffraction of these wavelengths also appear on the detector in the high pixel number end, and so does the second-order diffraction of the xenon resonant absorption peaks. These reference points are plotted in Fig. 2-26(a) and can be fit well with Eq. (2-14). The fit function covers the acquired spectrum from the pixel space to the photon energy space, such as the xenon absorption spectrum shown in Fig. 2-26(b).

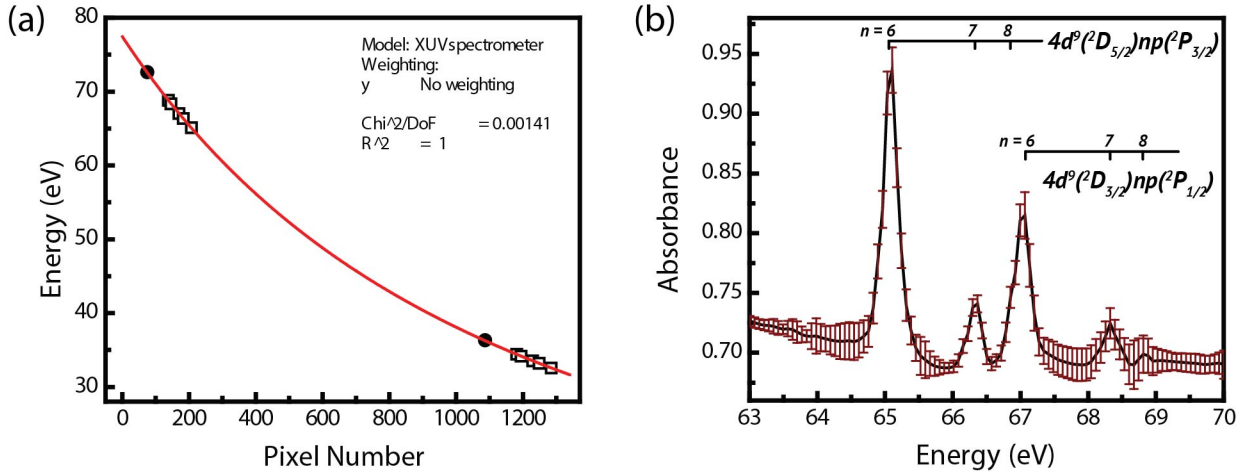


Figure 2-26: (a) Reference points and the fit curve for wavelength calibration of the XUV spectrometer. The solid circles stand for the first- (smaller pixel number) and second-order (larger pixel number) diffractions of the Al  $L_3$ -absorption edge. Open squares are the first- and second-order diffractions of the xenon  $4d \rightarrow np$  transitions in Table 2-2. (b) The xenon static absorption spectrum in the wavelength (photon energy) space. Error bars are calculated by averaging 64 different spectra that is each integrated over 300 pulses.

The energy resolution of the XUV spectrometer is obtained by fitting the Xe absorption peak in Fig. 2-26(b) by a Voigt function, which is a convolution of a Lorentzian peak function and a Gaussian function. The widths of the Lorentzian functions are determined by the core hole lifetimes and can be found in the literature,<sup>75</sup> while the Gaussian function represents the

instrumental broadening of the absorption lines. Figure 2-27 shows the fit results for the  $4d^1(^2D_{5/2})6p(^2P_{3/2})$ ,  $4d^1(^2D_{5/2})7p(^2P_{3/2})$ , and  $4d^1(^2D_{3/2})7p(^2P_{1/2})$  states, and the energy resolution is found to be 203, 175, and 227 meV, respectively. Moreover, the energies of these three absorption peaks after wavelength calibration are at  $65.09 \pm 0.01$ ,  $66.34 \pm 0.02$ , and  $68.33 \pm 0.04$  eV, respectively, which agree well with the literature values of 65.11, 66.37, and 68.34 eV. It should be noted that the absorption peak at 67.02 eV is not fit because the  $4d^1(^2D_{3/2})6p(^2P_{1/2})$  transition overlaps with the  $4d^1(^2D_{5/2})8p(^2P_{3/2})$  peak on its low-energy side, which appears as a shoulder near 66.8 eV in Fig. 2-26(b) but cannot be resolved as two peaks with this XUV spectrometer. In summary, the current spectrometer setup is able to detect XUV with photon energies from 32 to 77 eV with  $\sim 200$  meV spectral resolution (resolution power  $E / \Delta E \sim 350$ ). These specifications are more than capable of studying the changes of transition metal M-edge absorptions in the excited states.

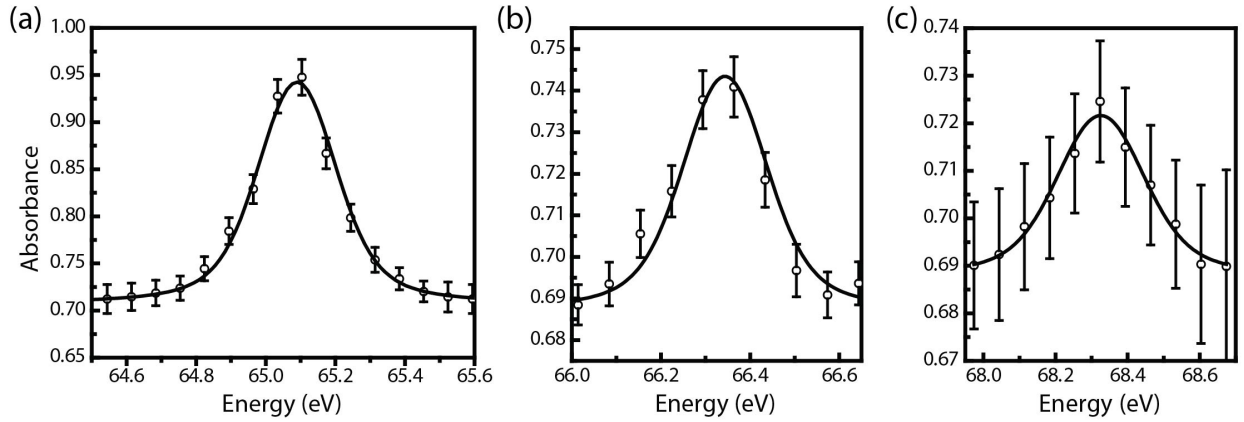


Figure 2-27: The Voigt function fitting results for the (a)  $4d^1(^2D_{5/2})6p(^2P_{3/2})$ , (b)  $4d^1(^2D_{5/2})7p(^2P_{3/2})$  and (c)  $4d^1(^2D_{3/2})7p(^2P_{1/2})$  states. The central energy (energy resolution) of each peak is found to be  $65.090 \pm 0.006$  eV (0.203 eV),  $66.344 \pm 0.027$  eV (0.175 eV) and  $68.326 \pm 0.024$  eV (0.227 eV), respectively.

## 2.5 Future Improvements

The table-top transient XUV absorption apparatus constructed during this work can be a powerful tool for studying charge carrier dynamics in various semiconductor materials, as its abilities have been demonstrated in this chapter. Several components have been upgraded over the past six years, however some improvements that would potentially enhance the instrument performance could still be done. For example, the noise levels of the acquired transient XUV absorption spectra are largely based on the fluctuations of the high-order harmonics. Although the stability has been improved significantly by carefully maintaining the femtosecond laser system and using robust mirror mounts and 1" diameter stainless steel pedestal posts in the beam path, it can benefit from implementing an active beam stabilization system to the beam path of infrared fundamental pulses. The beam stabilization system is already purchased, but hasn't been successfully integrated with the instrument. In order to reduce the XUV flux fluctuations, the beam stabilization system has to be placed as closed to the SIGC as possible, however the routine SIGC alignment procedure needs to be done with an attenuated infrared beam, which would interrupt the algorithm for the active beam path stabilization.

Secondly, Fig. 2-16(d) and 2-25(a) suggest that the neon harmonics possibly extend up to 90 eV but are limited by the L<sub>3</sub>-edge absorption by the Al filters. By replacing all the Al foils in the apparatus by Zr foils, XUV photons with 70 – 200 eV energy should be available (Fig. 2-28). This would reach absorption edges at higher energies, *e.g.* the copper M<sub>3</sub>-edge at 75.1 eV and the silicon L<sub>3</sub>-edge at 99.2 eV, thus expands the element groups that can be studied. The grating in the XUV spectrometer is actually designed to achieve flat-field focus for 60 – 200 eV photon energy, therefore only the position of the X-ray CCD camera needs to be moved.

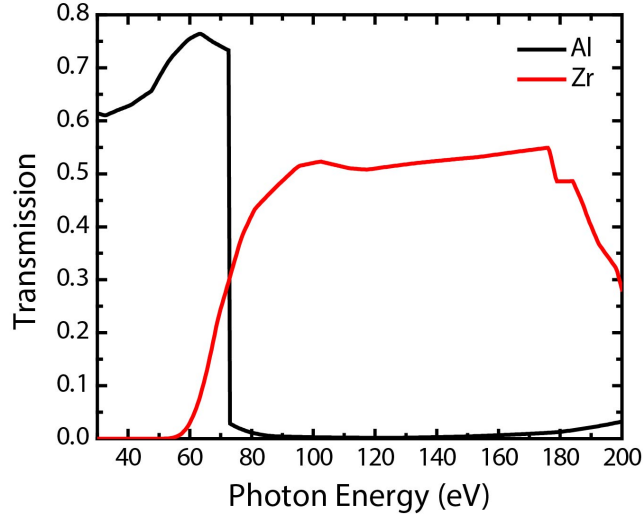


Figure 2-28: Transmission of XUV of 200 nm thick Al and Zr.

The tunable wavelength range and high pulse energy in the visible region provided by the optical parametric amplifier TOPAS has been shown in Sec. 2.3.3. During the pump-probe experiments, it has been found that the SFS (sum frequency between the signal and pump) mode delivers better beam qualities than the SFI mode. After contacting with the manufacturer, this issue is known to be caused by using the depleted 800 nm pump beam for sum-frequency generation. A fresh pump modification is recommended and has been ordered, which would split a portion of the 800 nm pump energy for the second-stage power amplifier for the wave-mixing with the signal and idler beams. Another wave-mixing crystal has also been purchased to extend the TOPAS output wavelength down to 189 nm, which would increase the instrument's ability to investigate hot carrier relaxation dynamics.

Lastly, so far all the solid-state samples are prepared separately by collaborators. In order to study materials that are sensitive to oxygen, it is necessary to have the ability for *in situ* sample preparation so that the measurement can be done without possible sample degradation/oxidation in the atmosphere. This will require major upgrades of the current sample/spectrometer chamber, including metal sputtering sources, characterization tools, and an ultra-high vacuum environment ( $< 10^{-9}$  Torr) for the preparation of clean sample interfaces.



# Chapter 3

## Characterization of High-Order Harmonics and Experimental Principles

In the last chapter the design and construction of a transient XUV absorption apparatus have been described, however various kinds of information are still needed in order to successfully perform a pump-probe experiment, such as: what noble gas pressure should be used in the SIGC to get a desired high harmonic spectrum; what kind of high harmonic spectrum is preferred to serve as the probe beam; how to check the spatial homogeneity of a solid-state sample; how can one synchronize different parts of the instrument to efficiently acquire a large dataset, etc. Invaluable experience has been gained through trouble-shooting and attempting to upgrade the apparatus, and several sets of operating procedures have been established. Further work might bring additional useful knowledge about the instrument, but this chapter is dedicated to presenting the up-to-date understanding in terms of generating high-order harmonics as the XUV probe beam and the experimental procedures for several common experiments. The tunability of high harmonic spectra by varying the laser focus position and the gas pressure are demonstrated in Sec. 3.1 and 3.2, respectively. Generation of even-order harmonics via two-color gating is given in Sec. 3.3, and Sec. 3.4 discusses the influence of frequency chirp in the fundamental pulses on the high harmonic spectra. In Sec. 3.5, operating procedures from the daily instrument checklist to the acquisition of time-resolved XUV absorbance spectra are summarized.

### 3.1 Effect of Laser Focus Position

In this section, Ne high harmonics are generated in a 80 Torr gas cell using 41 fs pulses with 1.8 mJ energy at 800 nm center wavelength, which achieves a peak intensity of  $1.8 \times 10^{15}$  W/cm<sup>2</sup> at the focus. The laser focus position  $z_f$  relative to the SIGC end plate can be adjusted by translating the focusing lens, and a positive  $z_f$  value means the infrared pulses are focused outside (or after) the gas cell. Several high harmonic spectra taken at different  $z_f$  values are given in Fig. 3-1. It can be clearly seen that the most intense harmonic order is largely affected by the laser focus position: At  $z_f = 10.9$  mm the 37<sup>th</sup> harmonic (H37) has the brightest emission among all the detected harmonics, but higher order harmonics gain intensity as the laser focus is moved closer to the SIGC. When the focus is placed right at the pinhole that connects the SIGC to the HHG chamber ( $z_f \approx 0$ ), H45 becomes the brightest output. It is also possible that H47 or higher-order harmonics are actually brighter, but are blocked by the Al foils that acts as low-frequency pass filter. This shift of the brightest harmonic order can be explained by the interaction between the laser electric field and the noble gas medium: the Rayleigh range near the laser focus has the most intense electric field; therefore after tunnel ionization the electron can be accelerated to a

higher kinetic energy, and the following recombination between the electron and the parent ion would emit a higher energy photon.

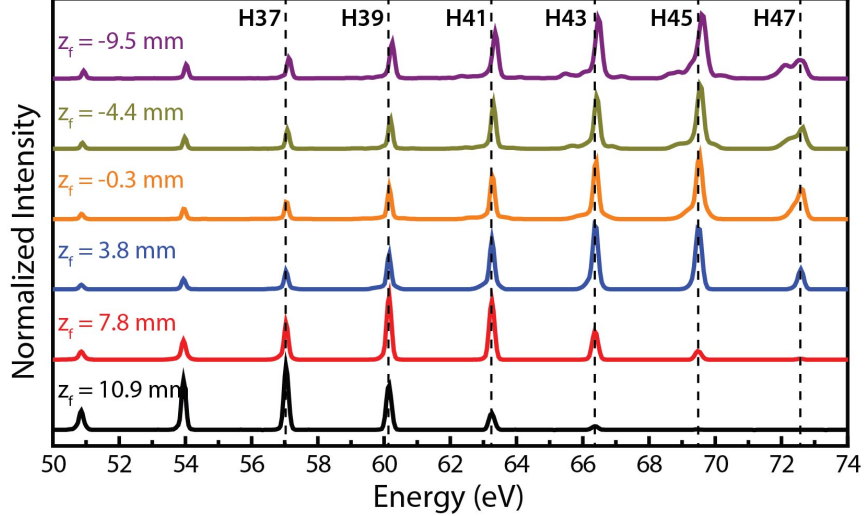


Figure 3-1: High harmonic spectra generated from a semi-infinite gas cell filled with 80 Torr, recorded at different laser focus position  $z_f$ . The highest intensities of individual spectra have been normalized for comparison.

### 3.1.1 Harmonic Flux

Decreasing the focus position  $z_f$  not only enhances the electric field interaction with noble gas atoms, but the length of the interaction region is also increased. More overlap between the Rayleigh range and the SIGC means the interaction volume is expanded. It has been discussed in Sec. 1.3.2 that under a proper phase-matched condition, the intensity of the  $q$ th-order harmonic emission is approximated by:

$$I_q \propto N_{at}^2 \frac{\sin^2(L_{med}\Delta k_q / 2)}{\Delta k_q^2} \quad (3.1)$$

where  $N_{at}$  is the gas density,  $L_{med}$  is the length of the interaction region, and  $\Delta k_q$  is the phase mismatch between the fundamental and XUV pulses. At a fixed Ne pressure (80 Torr in this scenario),  $I_q$  would exhibit a quadratic dependence on  $L_{med}$ , which is observed for harmonics lower than H39 (Fig. 3-2(a)). It should be noted that a more intense electric field is required for generating a harmonic of higher order, therefore the effective interaction volume is smaller than that of a lower-order harmonic. As a result, the intensity of higher-order emission shows a larger enhancement with the increasing interaction volume in this regime. This also justifies the observation in Fig. 3-1 that higher-order harmonics become brighter when the laser focus is moved toward the SIGC. When the laser focus is placed deeper than 5 mm inside the gas cell, the increasing flux of Ne harmonics versus focus position slows down and eventually turns into a decreasing flux. This indicates the reabsorption of XUV by the generating medium is no longer negligible, and an exponential decay of intensity with respect to the interaction length should be expected.

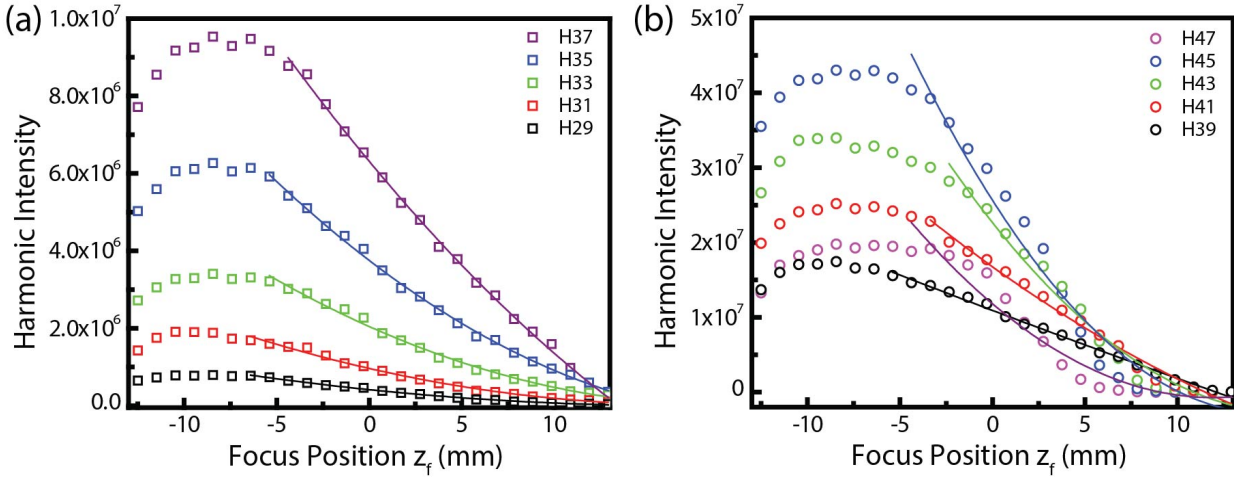


Figure 3-2: Plot of the intensities of individual Ne harmonics with respect to the laser focus position  $z_f$ . (a) Intensities of lower-order harmonics (H29 - H37) show a quadratic dependence (solid curves) on  $z_f$ , which correlates to the interaction length between laser and Ne atoms. (b) The intensity of higher-order harmonics (H39 – H47) rises faster than the quadratic functions, and therefore cannot be fit well.

Ne harmonics higher than the 39<sup>th</sup>-order (photon energy > 62 eV) also gain intensity as the interaction volume increases, however the increasing rates start to deviate from the quadratic relation (Fig. 3-2(b)). Compared to H29 – H37, these higher-order harmonics are enhanced more dramatically with a decreasing  $z_f$ , but are similarly dominated by the reabsorption effect when the laser focus is too deep in the gas cell. It is still unclear why the emission flux of higher-order harmonics are so sensitive to the focus position changes, but it could be possibly explained by the self-guiding effect of laser pulses in the gas cell.

### 3.1.2 Spectral Broadening and Blueshift

Another significant spectral evolution in Fig. 3-1 is each harmonic peak becomes broader in energy as the laser focus is moved toward the SIGC. In addition, each peak is shifted to higher photon energy as  $z_f$  decreases. Taking H45 as an example, the spectral broadening and blueshift phenomena are better visualized in Fig. 3-3(a). In addition, when the harmonic spectra are plotted on a logarithmic scale, as is done in Fig. 3-3(b), it can be clearly seen that not only are individual peaks broadened by decreasing the  $z_f$ , the underlying continuum part also shows at least a 20 times enhancement in intensity. The XUV continuum in the harmonic spectrum plays a crucial role in pump-probe experiments: since in a modulated harmonic spectrum the noise level is higher in the low flux regions, a higher XUV continuum level will connect adjacent harmonics and reduce the flux fluctuations. The causes of the XUV continuum and spectral broadening have been widely discussed, and the long-trajectory emission in the HHG process may be responsible for these phenomena. Comparing to the short-trajectory emission, of which the spectral width is independent of the electric field intensity, recollisions between the long-trajectory electron and the parent ion results in emission with larger angular divergence and shorter coherence time.<sup>48</sup> By translating the laser focus into the gas cell, the more intense electric field would make the long-trajectory emission more dominant, which therefore explains the observed broadening of individual harmonic peaks and the rise of XUV continuum level.

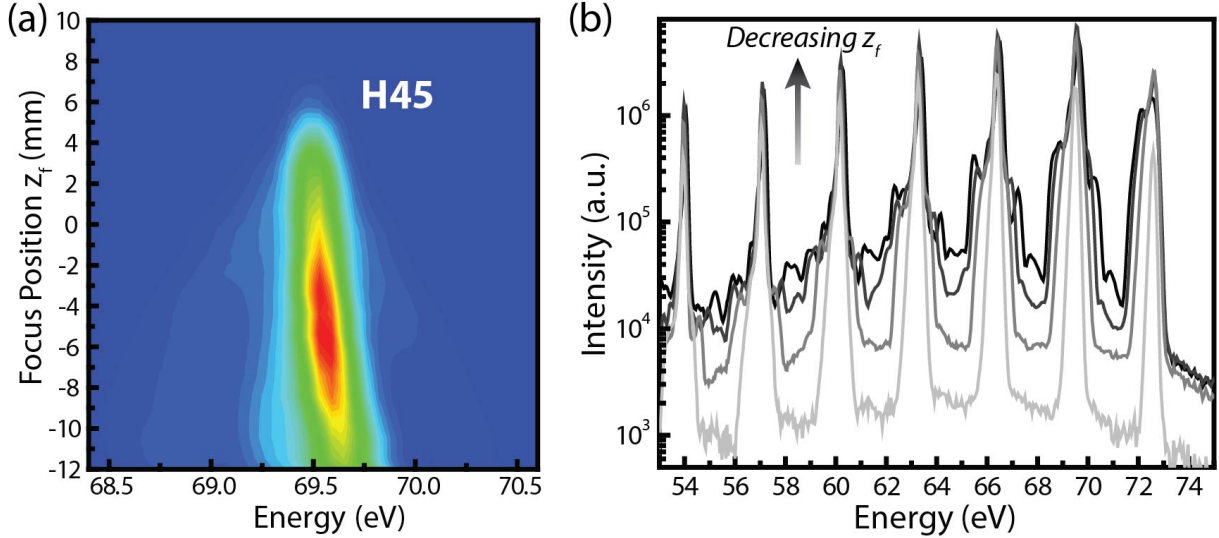


Figure 3-3: (a) The 45<sup>th</sup>-order Ne harmonic exhibits significant spectral broadening and  $\sim 150$  meV energy blueshift as the laser focus is translated into the XUV-generating gas cell. (b) Evolution of the Ne harmonic spectra with decreasing  $z_f$  positions. Each spectrum is integrated over 1000 pulses by the X-ray CCD camera.

Variation of the harmonic emission wavelength can be related to the blueshifting of the fundamental laser pulses caused by free electrons. The HHG process requires a strong electric field to facilitate tunnel ionization of the noble gas atoms, and a portion of the gas medium is constantly ionized by the laser pulses. The extent of photon energy shift caused by the plasma medium is given by<sup>61</sup>

$$\delta E = \frac{h^2 N_{at}}{2\pi m_e c} \frac{1}{E} \frac{df_e}{dt} L_{med} \quad (3.2)$$

where  $h$  is Planck's constant,  $N_{at}$  is the total gas density,  $E$  is the original photon energy,  $m_e$  is the mass of an electron,  $c$  is the speed of light in vacuum, and  $df_e/dt$  is the increasing rate of ionization fraction. If the frequency of the fundamental laser pulses were affected first by the plasma medium and then used to drive the HHG process, the spectral blueshift of the  $q$ -th order harmonic would be  $q$  times greater ( $\delta E_q = q\delta E_f$ ). On the other hand, if the XUV photons were emitted first and then influenced by the plasma medium later, the associated spectral blueshift would exhibit a  $q^{-1}$  dependence to the harmonic order.

In Fig. 3-4(a), the center energies of H33, H39, and H45 that are emitted from Ne gas and their variation with respect to the laser focus position are compared. All three harmonic orders show spectral blueshift at more negative  $z_f$  values, and the blueshifting rates become faster when the laser focus is deeper inside the SIGC. Every photon energy vs.  $z_f$  plot can be fit well with a second-order polynomial, which can be justified by the fact that both the ionization rate  $df_e/dt$  and the interaction length  $L_{med}$  in Eq. (3.2) are increased as the laser focus is brought into the noble gas medium. If the spectral blueshifts at three harmonic orders are compared, the highest order harmonic (H45) seems to have the largest change over the same range of  $z_f$  values. The linear energy blueshifting rates, i.e. the first-order coefficients obtained from the polynomial fit, show an approximately linear increasing trend with the harmonic order  $q$ , as shown in Fig. 3-

4(b). This suggests that the observed harmonic energy blueshifts are caused by the plasma-induced energy shift to the fundamental laser pulses, rather than the energy shift to XUV photons.

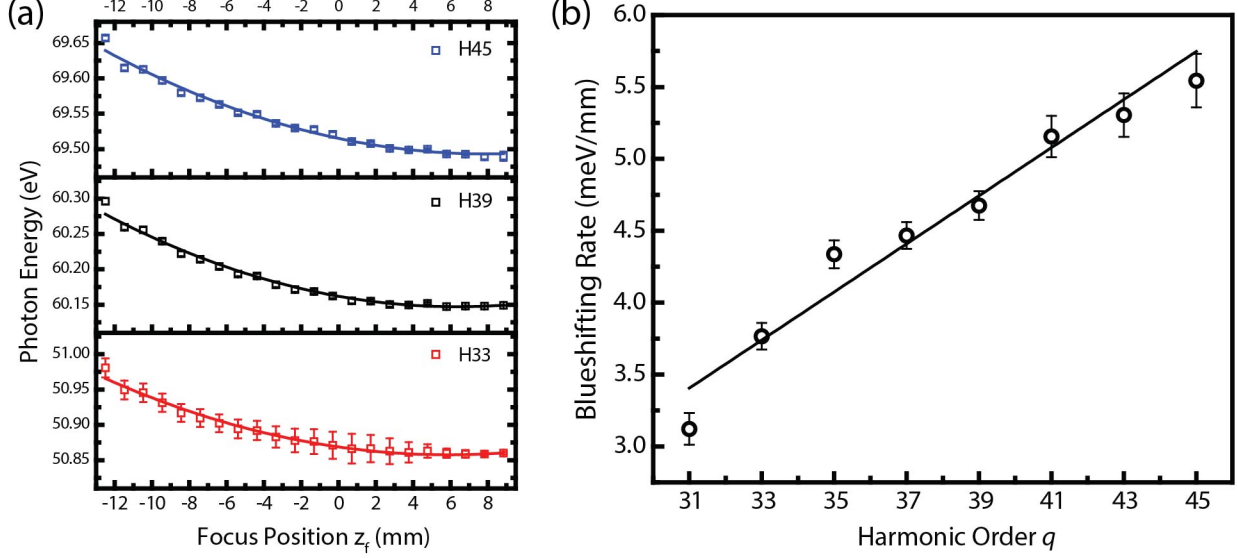


Figure 3-4: (a) Center photon energies of the H33, H39, and H45 generated in 80 Torr Ne at  $1.8 \times 10^{15}$  W/cm<sup>2</sup> electric field intensity. The fit functions are second-order polynomials of the focus position  $z_f$ . (b) The linear energy blueshifting rate shows a linearly increasing relation with the harmonic order  $q$ .

### 3.1.3 XUV Focus Size

Although various types of tunability of the higher-order harmonic emission generated from a semi-infinite gas cell have been demonstrated, it should be noted that varying the laser focus position would also change the distance from the XUV source to the refocusing toroidal mirror, therefore the location of the XUV focus in the sample chamber could also be affected. In Sec. 2.4.2, it has been mentioned that the focused XUV beam profile at the sample location has  $79 \pm 3$  and  $39 \pm 1$  μm FWHM along the horizontal and vertical directions, respectively. The same scanning knife-edge method is utilized again for studying the influence of laser focus position on the spatial profile of the focused XUV beam measured at the sample location. The measured beam sizes of five different Ne high harmonic spectra, each generated at a different laser focus position  $z_f$ , are shown in Fig. 3-5(a), among which is the  $z_f = -2.5$  mm data point has been mentioned in Sec. 2.4.2. Interestingly, the once elongated XUV focus profile transforms toward a 1:1 aspect ratio when the  $z_f$  value is increased, i.e. when the laser focus is placed after the SIGC. The XUV focus profile can be also analyzed for individual harmonics separately: When laser pulses interact with the harmonic generating medium, the highest order harmonic is only emitted from the center region of the beam, while the lower order harmonic emissions are generated from a region that is comparable to the laser focus. The XUV size variation of different harmonic orders at the source (SIGC) are transformed to the XUV focus, where the higher order harmonics generally have smaller beam sizes, as shown in Fig. 3-5(b). The size variation between different harmonic orders becomes less apparent when the laser pulses are focused inside the SIGC, since the entire Rayleigh range is interacting with the generating medium.

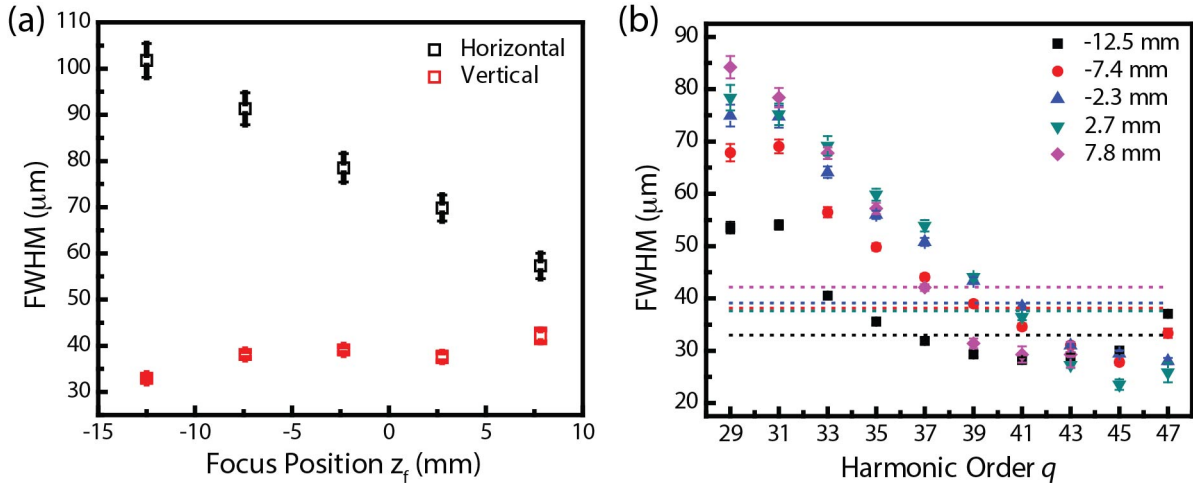


Figure 3-5: (a) XUV beam sizes measured at the sample location by the scanning knife-edge method. 80 Torr neon gas are used for generating high-order harmonics at different laser focus position  $z_f$  relative to the end plate of the SIGC. (b) The vertical beam sizes (FWHM) for individual harmonic orders. Dashed lines indicate the beam size measured for the integrated harmonic spectrum.

Compared to the spectral characteristics of an XUV spectrum, which are controlled by the distance between the laser focus and the end of the SIGC, e.g. intensity of a specific harmonic order and broadening/blueshifting of a harmonic peak, the XUV focus profile should be determined only by the distance from the laser focus to the toroidal mirror. Based on the trend observed in Fig. 3-5(a), it would be interesting to test a new semi-infinite gas cell that is  $\sim 15$  mm longer than the current one: by pushing both the gas cell and the laser focus closer to the toroidal mirror for the same distance, an XUV beam with similar spectral characteristics should be generated with a more rounded focus profile at the sample location.

### 3.1.4 Effects on Ar Harmonics

The effect of laser focus position also has been investigated on harmonics that are generated from 35 Torr Ar gas interacting with  $\sim 1.5 \times 10^{15}$  W/cm<sup>2</sup> electric field, and several XUV spectra are listed in Fig. 3-6(a). Similar to the Ne harmonics, the spectral profile shifts toward higher-order harmonics as the laser focus moves into the SIGC. A significant spectral broadening effect is also observed, however the energy blueshift only occurs for lower order harmonics (H27 and H29). At higher harmonic orders, e.g. H33 to H37, there is instead an energy redshift that is observed. The photon fluxes of individual Ar harmonics also rise sharply as the laser focus is translated into the gas cell (Fig. 3-6(c)). Similarly, the increasing rate of photon flux follows a quadratic relation for lower harmonic orders (H21 to H29), but becomes more dramatic for higher-order harmonics. The flux of the Ar harmonics saturates at roughly  $z_f = 2$  mm before reabsorption takes place, and this position is about 7 mm further than the saturation point of the Ne harmonics ( $z_f = -5$  mm). This can be justified by two explanations as follows: (1) the ionization potential of Ar (15.76 eV) is smaller than that of Ne (21.56 eV), therefore Ar atoms can be used for HHG at a much lower electric field intensity. The electric field used in the experiment ( $\sim 1.5 \times 10^{15}$  W/cm<sup>2</sup>) is more than enough, such that the high harmonic emissions reach their maximum fluxes even when the Rayleigh range only partially overlaps with the gas

cell. A large fraction of the Ar atoms would be ionized when the laser focus is brought further into the gas medium, and the depletion of neutral atoms would diminish the harmonic emission flux. (2) The photoabsorption cross section of Ar is much greater than Ne in the 20 – 40 eV energy range,<sup>76</sup> therefore the Ar harmonics are more likely to be reabsorbed by the generating medium even though a lower pressure is used in the gas cell (35 Torr Ar vs. 80 Torr Ne). In fact when one looks closely at Fig. 3-6(c), harmonics higher than H27 (~42 eV) are less affected by the gas reabsorption, and instead increase in emission flux at  $z_f$  values more negative than -6 mm.

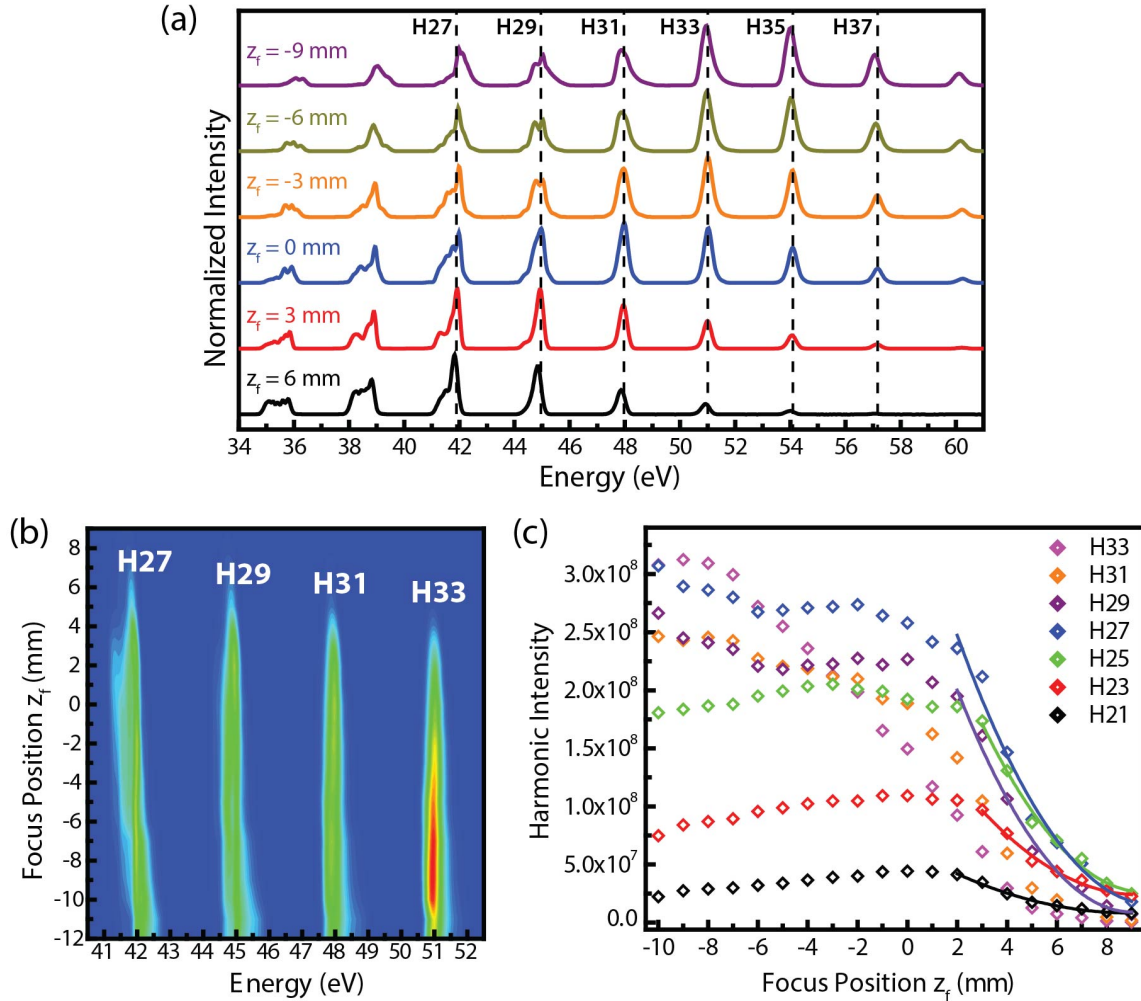


Figure 3-6: (a) High harmonic spectra generated from a semi-infinite gas cell filled with 35 Torr Ar using ~45 fs pulses with 1.5 mJ energy at 800 nm center wavelength, recorded at different laser focus position  $z_f$ . (b) H27 and H29 exhibit spectral broadening and blueshifting as  $z_f$  value becoming more negative, while H33 shows the opposite, a spectral redshifting. (c) Intensities of individual harmonics versus the laser focus position  $z_f$ . Quadratic fits for H21 – H29 are also plotted as solid curves.

## 3.2 Variation in the Gas Pressure

Other than the position of the laser focus, varying the gas pressure in the semi-infinite gas cell also provides an easy control of the XUV spectra. In this section, Ne harmonics are generated at different gas pressures measured at the SIGC inlet, with the same infrared pulses as used in Sec. 3.1, and the laser focus is fixed at  $z_f = -2.5$  mm. The influence of Ne pressure on the harmonic spectra are shown in Fig. 3-7: First, the intensity of each harmonic rises quickly with the increasing pressure, and also the XUV continuum enhances by almost 10 times. Nevertheless, the spectral broadening and blueshifting phenomena, although still occurring, are not as obvious as that shown in Sec. 3-1, which was induced by varying the laser focus with respect to the gas cell. Moreover, the brightest harmonic order does not change as much as that caused by moving the laser focus. Detailed discussions on how varying the gas pressure affects the detected harmonic spectra are given in the following sections.

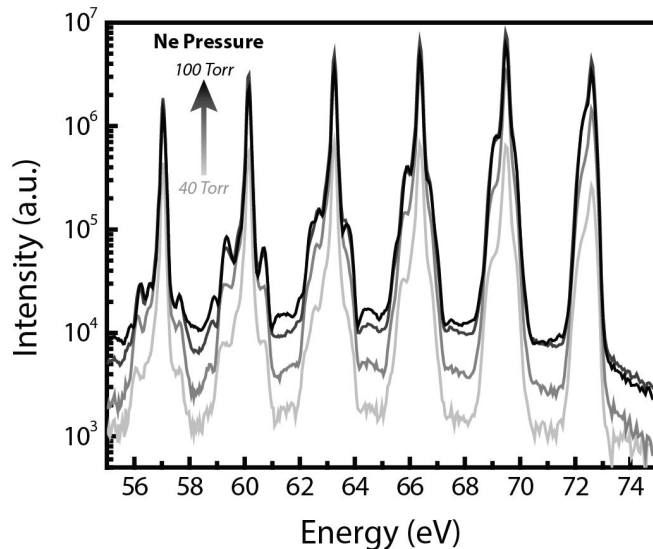


Figure 3-7: Spectra of Ne harmonics with 40, 60, 80 and 100 Torr gas pressure, respectively. The infrared laser pulses are focused 2.5 mm inside the semi-infinite gas cell. Each harmonic peak shows slight spectral broadening and blueshift with increasing Ne pressure, and the XUV continuum enhances by almost 10 times.

### 3.2.1 Harmonic Flux

Fig. 3-8(a) shows how the emission intensities of different Ne harmonic orders vary with gas pressure, with the laser focus 2.5 mm inside the gas cell ( $z_f = -2.5$  mm). According to Eq. (3.1), emission intensity should initially exhibit a  $p^2$ -dependence, as has been reported in He- and Xe-filled semi-infinite gas cells.<sup>63</sup> Above a certain pressure, absorption by noble gas atoms would diminish the harmonic intensities. This predicted behavior is in qualitative agreement with the measured intensities in Fig. 3-8(a), and the reabsorption effect starts to takes place at  $\sim 70$  Torr pressure for H31. For higher-order harmonics, reabsorption occurs at higher Ne pressure, for example, H45 does not see its intensity decreasing until 85 Torr. This can be explained by the slightly decreasing Ne photoabsorption cross sections in the 40 – 70 eV energy range.<sup>76</sup> A major

deviation from Eq. (3.1), though, is that the measured intensities rise much faster than a quadratic relation, and fitting with a power law ( $I_q \propto p^n$ ) gives a  $n \approx 4$  result for nearly every harmonic order. The cause of such a  $p^4$ -dependence is still unclear, but could be attributed to the phase mismatch factor  $\Delta k_q$  in Eq. (3.1): Varying the gas pressure not only controls the atomic gas density  $N_{at}$ , but also changes the amount of plasma in the medium, such that the dispersion to both the fundamental pulses and the XUV pulses are slightly modified. Another possible explanation is that the self-guiding effect of intense infrared pulses might be affected by changing the Ne pressure in the SIGC; therefore even if the focusing lens is not moved, the effective interaction length between the generating medium and the electric field would be different. The pressure dependence of Ne H45 emission intensity is also measured at laser focus positions that are either deeper into the gas cell ( $z_f = -7.5$  mm) or after the gas cell ( $z_f = 2.5$  mm). The intensity rise that is proportional to  $p^4$  remains consistent, but the reabsorption effect occurs at lower Ne pressure when the laser focus is positioned inside the gas cell (Fig. 3-8(b)). In addition, at more negative  $z_f$  values the intensity decay due to the gas absorption is more dramatic. These observations make sense because the XUV photons generated inside the gas cell are more likely to be absorbed by the generating medium.

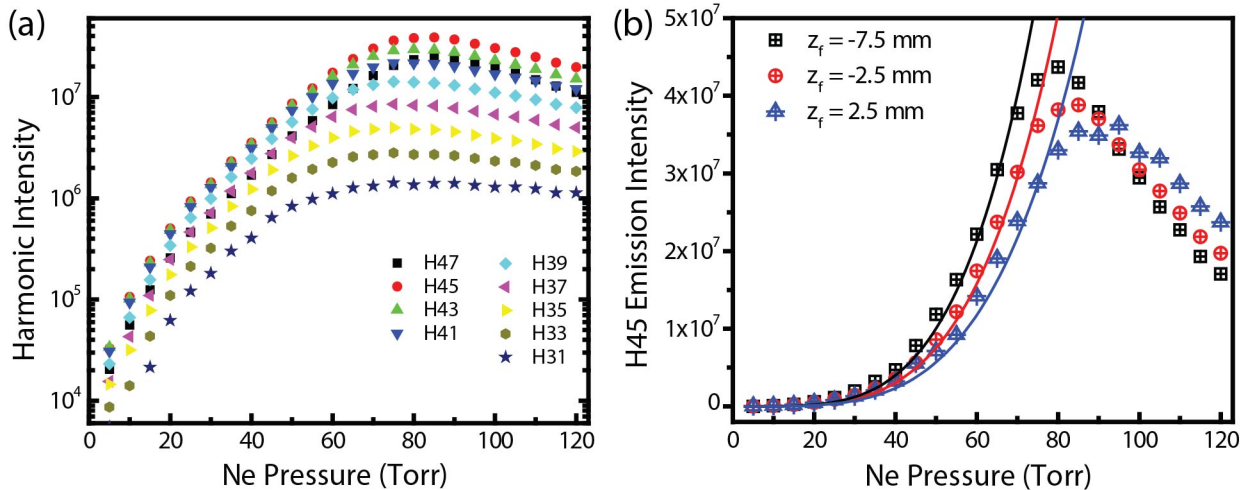


Figure 3-8: (a) Intensities of different harmonic orders to the Ne gas pressure in the SIGC, illustrated on a logarithmic scale. The laser focus position  $z_f$  is at -2.5 mm. (b) Pressure-dependent intensities of Ne H45, measured at three different laser focus positions. Curves represent the  $p^4$  power law fit results.

### 3.2.2 Spectral Blueshift

Each peak in a Ne harmonic spectrum is fitted by a Gaussian function, and the center energies of each harmonic order are plotted with respect to the Ne pressure in the gas cell. In the case that the laser is focused after the gas cell ( $z_f = 2.5$  mm), spectral shifts at all harmonic orders exhibit an approximately linear relation (Fig. 3-9(a)), and the degree of energy blueshift per unit pressure exhibits some dependence on the harmonic order  $q$  (Fig. 3-9(b)). From H37 to H45, the linearly increasing relationship between the blueshifting rate and the harmonic order  $q$  is similar to what is shown in Sec. 3.1.2, which can thus be attributed to the fundamental frequency shift caused by the plasma medium. The same spectral blueshift of Ne harmonics by varying gas

pressure has been reported earlier when using a hollow waveguide as the HHG interacting geometry.<sup>77</sup> It should be noted that the blueshifting rate measured in the semi-infinite gas cell is about two orders of magnitude smaller than in a waveguide. Take H43 as an example, the  $\sim 0.16$  meV/Torr energy blueshift in the SIGC is almost negligible compared to the 40 meV/Torr rate reported for the hollow waveguide.

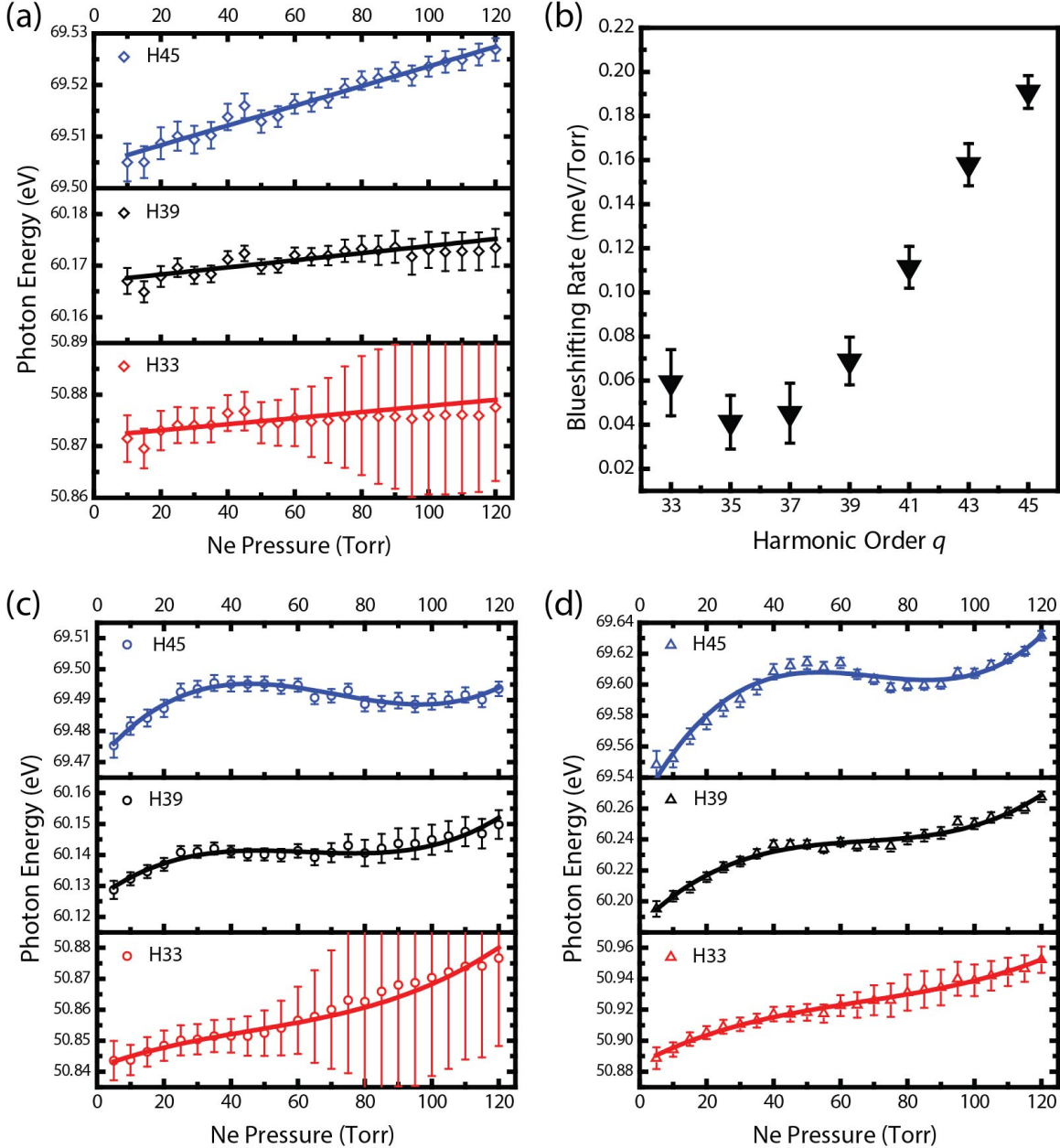


Figure 3-9: The variation of harmonic energies of H45, H39, and H33 to the Ne pressures. The measurements are done at  $z_f$  = (a) 2.5 mm, (c) -2.5 mm, and (d) -7.5 mm, respectively. (b) The plot of the linear spectral blueshifting rate at different harmonic order  $q$ , measured at the laser focus position  $z_f$  = 2.5 mm.

If the laser focus is moved inside the gas cell, nevertheless, the spectral blueshift phenomenon becomes more complicated. Fig. 3-9(c) and 3-9(d) present the cases of  $z_f$  at -2.5 and -7.5 mm, respectively. The correlation between the harmonic energy and the Ne gas pressure starts to deviate from linear correlation, especially at higher harmonic orders. The harmonic energy would increase with the gas pressure initially, then stay constant or even decrease a little over a certain pressure range, and then start increasing again. Plots of harmonic energy vs. Ne pressure can be fit well by cubic polynomial functions, although it is still unclear what experimental parameter besides the formation of a plasma would also modify the photon energy of emitted harmonics. Meanwhile, the extent of energy blueshift becomes greater if the laser focus is placed deeper in the gas cell. For example, at  $z_f = -7.5$  mm an  $\sim 100$  meV spectral shift is observed for H45, which is more than the  $< 25$  meV spectral shift that occurs for the same harmonic at  $z_f = 2.5$  mm.

### 3.2.3 XUV Focus Size

The spatial profile of the XUV beam is measured in the sample chamber by the scanning knife-edge technique at several different Ne pressures. Although photon flux varies a lot when the pressure is changed from 60 to 100 Torr, the vertical beam diameter of the XUV focus stays close to  $\sim 37$   $\mu\text{m}$  FWHM (Fig. 3-10(a)). At a much higher (120 Torr) or much lower (40 Torr) Ne pressure the variation of beam diameter is still less than 20%, which suggests that the gas pressure used for generating high-order harmonics does not affect the XUV beam size by much. By analyzing the size of individual harmonics, the increase in beam diameter at 40 Torr Ne pressure is largely related to the enlargement of lower-order harmonics (H31 – H37), while at 120 Torr Ne pressure it is the higher-order harmonics (H41- H47) that contribute to the expanded beam profile at the XUV focus (Fig. 3-10(b)).

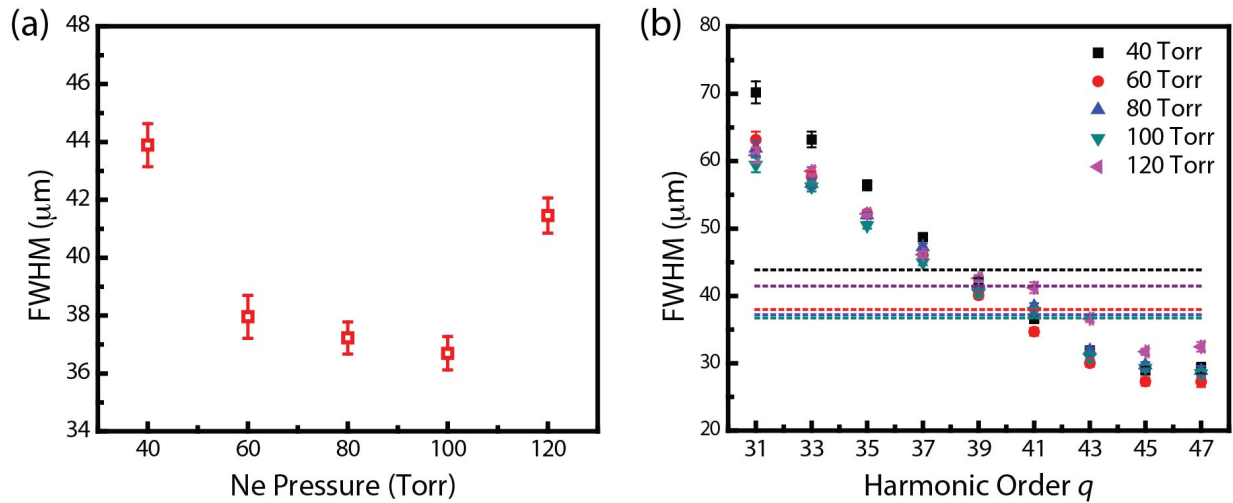


Figure 3-10: (a) XUV focus size (vertical FWHM) measured in the sample chamber by scanning knife-edge method, as a function of Ne pressures used for generating high-order harmonics. (b) The vertical beam sizes (FWHM) for individual harmonic orders. Dashed lines indicate the beam size measured for the integrated harmonic spectrum.

### 3.2.4 Effects on Ar Harmonics

With the same experimental approaches, the pressure dependence of high harmonic emission from Ar is analyzed. The contour plot Fig. 3-11(a) shows how the Ar harmonic spectrum evolves when the pressure in the gas cell is increased: not only does the relative intensity between different harmonic orders vary with the pressure, but a significant spectral blueshift is also observed for every harmonic. In terms of the pressure dependence of individual harmonic emission intensity, more complicated behaviors than the case of Ne harmonics are observed: H21 and H23 are very similar to the Ne harmonics that rise dramatically at low pressure but start to decrease in intensity above 25 Torr; H25 – H31 appear not to be affected by the gas reabsorption even at 50 Torr pressure; emission intensities of H33 – H39 remain very low until the Ar pressure is above 25 Torr, but after a sharp rising region these harmonic orders show a quick intensity decay after 35 Torr. Since the electric field used for generating these Ar harmonics is very intense ( $\sim 1.5 \times 10^{15} \text{ W/cm}^2$ ), the phase matching conditions might be largely perturbed. Therefore each harmonic order could respond very differently to the increasing gas pressure. In addition, the photoionization spectrum of Ar atoms has a Cooper minimum region from 50 to 56 eV, which correlates to the atomic electronic structure of Ar. The same low intensity region has also been observed in the Ar high harmonic spectrum.<sup>78</sup> For better understanding of the high harmonic generation process in Ar at such high electric field intensity, more theoretical modeling work would be required.

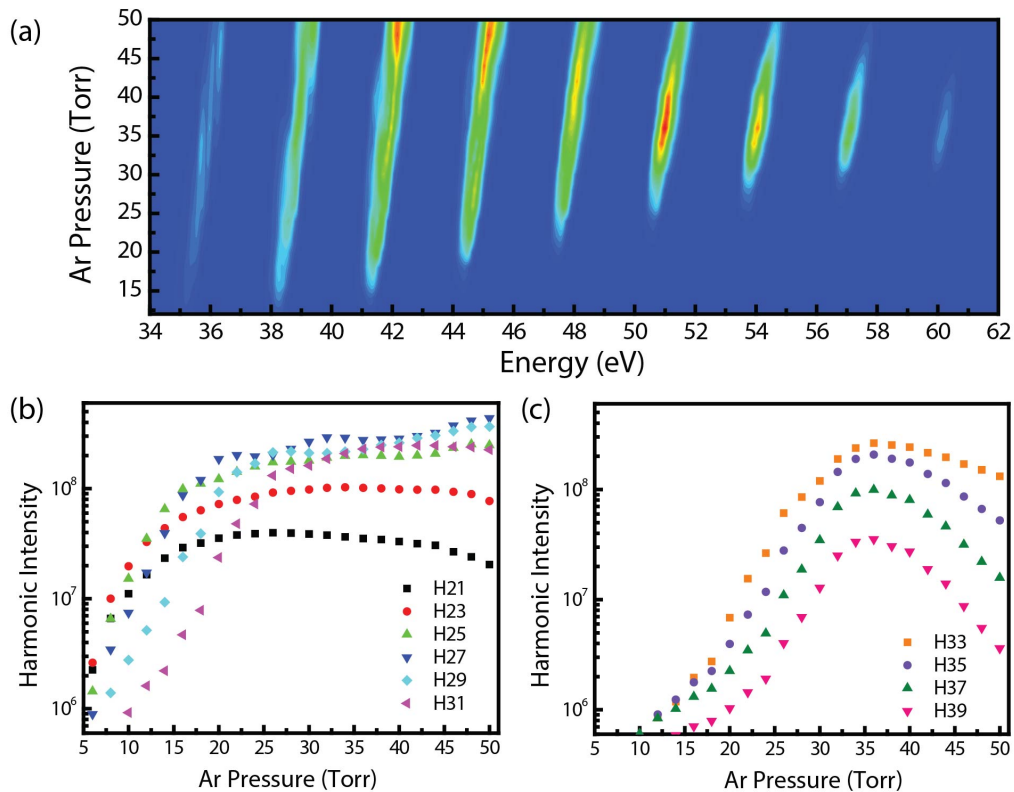


Figure 3-11: (a) Evolution of the Ar harmonic spectrum with respect to the gas pressure. The laser focus is placed 4 mm inside the gas cell ( $z_f = -4 \text{ mm}$ ). (b) and (c) Pressure dependence of intensities of different Ar harmonic orders.

Since Ar is easier to be ionized than Ne, given the experimental parameters a high ionization fraction should be achieved. According to Eq. (3.2), the extent of energy shift is proportional to the gas density, which directly translates to the plasma density. Fig. 3-12(a) demonstrates such a trend for nearly every Ar harmonic order in the pressure range of 20 – 50 Torr. The spectral blueshift caused per unit Ar pressure is plotted in Fig. 3-12(b) for different harmonic orders, and the  $q'$ -dependence between H27 and H37 indicates the frequency shift occurs in the fundamental pulses. Interestingly, the slightly decreasing blueshifting rate from H21 to H27 might have a  $q'^{-1}$ -dependence, which suggests it is the XUV photons emitted by the HHG process that are directly blueshifted by the plasma medium.

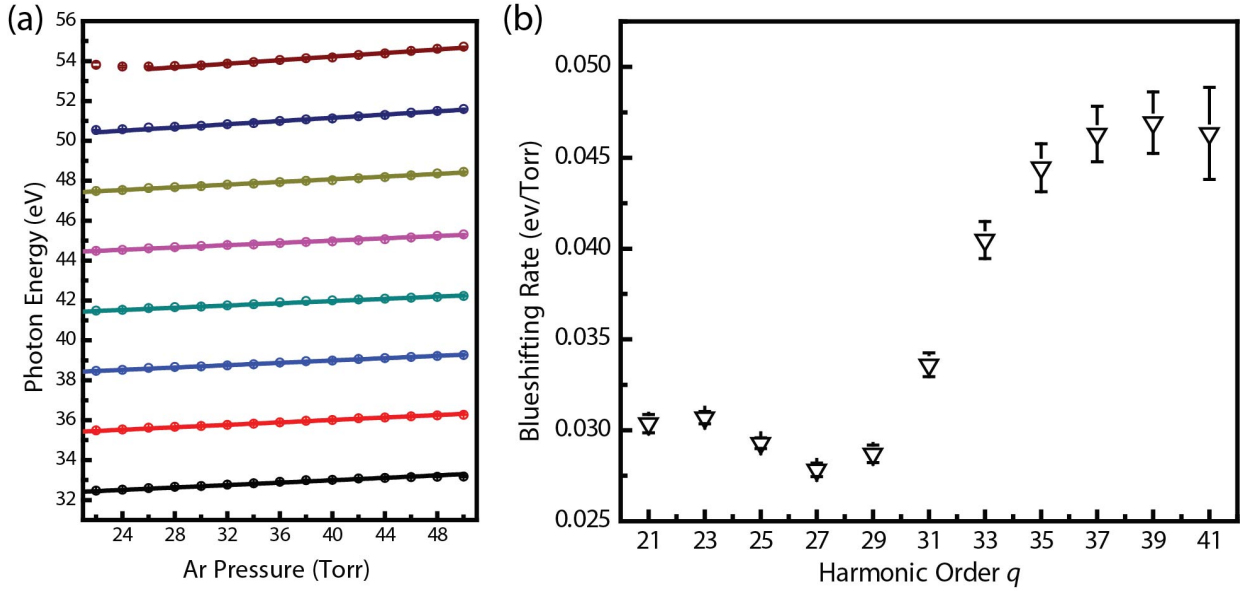


Figure 3-12: (a) Spectral blueshift of Ar harmonics caused by increasing pressure. Linear correlations are found between the harmonic energy and the Ar pressure. (b) The spectral blueshifting rates of different harmonic orders.

### 3.3 Generation of Even-Order Harmonics

So far the investigations of high harmonic spectra, either generated by Ne or Ar gases, use only the 800 nm light as the fundamental HHG driver pulses, therefore only the odd-order harmonics are observed. In order to use these XUV spectra for probing core level transitions in a transient absorption experiment, even more photon energy coverage is preferred. Sec. 1.3.4 introduced the two-color gating technique, which is capable of generating both the odd- and even-order harmonics from noble gas medium. Experimentally this is carried out by mixing  $\sim 30 \mu\text{J}$  of 400 nm light into the laser electric field to break the inversion symmetry, and the even-order harmonics appear when both the spatial and temporal overlap between 400 nm and 800 nm beams is achieved. Fig. 3-13 shows how the Ne harmonic spectrum evolves with respect to the delay of the 400 nm symmetry-breaking field. It can be seen that the odd-order harmonics diminish a little when the even-order harmonics start to grow up at partial overlap between the fundamental and symmetry-breaking fields. Within a  $\sim 40 \text{ fs}$  time window, even-order harmonics

can be generated at intensities that are comparable to the adjacent odd-order harmonics. Although the HHG conversion efficiency is slightly compromised when the two-color gating scheme is employed, the presence of even-order harmonics has proved beneficial for pump-probe experiments.

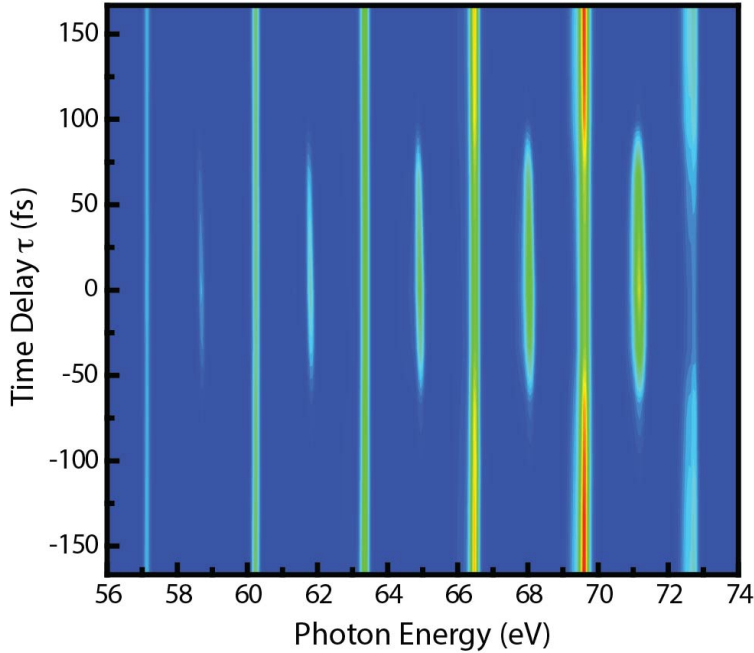


Figure 3-13: Effects of two-color gating on the Ne harmonic spectrum. About 30  $\mu\text{J}$  of 400 nm pulses are superimposed with the fundamental field in the semi-infinite gas cell. The zero time delay is defined as when the even-order harmonics are most intense.

### 3.4 Chirp Dependence of High Harmonic Spectra

Compared to other control parameters, chirping the fundamental infrared pulses is able to provide the most dramatic variation to the high harmonic spectrum. The chirped pulse amplifier utilizes a folded grating module for compressing the amplified seed pulses. When the distance from the motorized retroreflector to the compressor grating is reduced, positive chirp is induced, i.e. the high frequency components are delayed with respect to the low frequency components. Conversely, negatively chirped pulses are prepared by increasing the distance between the retroreflector and the compressor grating, such that the high frequency components are leading in a pulse. Fig. 3-14(a) shows the influence of chirped infrared pulses on the Ne harmonic spectrum. These images are the detected diffraction patterns from the XUV spectrometer grating on the X-ray CCD camera, and both odd- and even-order harmonics are present. Every harmonic order is at the highest intensity when the infrared pulse compression is optimized. Spectral redshift and peak broadening are clearly observed as the infrared pulses are positively chirped. Not only are the modulated spectra profiles becoming more discrete, but the top of each harmonic peak turns flatter and shows signs of finer splitting. This phenomenon has been explained by theoretical studies as the interference between the short- and long-trajectory emissions in the HHG process.<sup>49,54</sup> If the fundamental pulses are chirped negatively, the center of

each harmonic is shifted to higher photon energy, accompanied with more asymmetric peak shapes. The most important effect made by negatively chirped pulses is the enhancement of the XUV continuum, which is  $\sim 10$  times higher than the harmonics spectra generated by well-compressed or positively chirped pulses (Fig. 3-14(b)). The high XUV continuum level forms a broad connection underneath all the modulating peaks, and is especially effective when the even-order harmonics are also generated. The Ne harmonic spectrum in the lowest panel of Fig. 3-14(b) exhibits a good coverage from 50 eV to the 72.6 eV aluminum cut-off energy, which is excellent for studying samples containing late transition metals such like Fe, Co, and Ni.

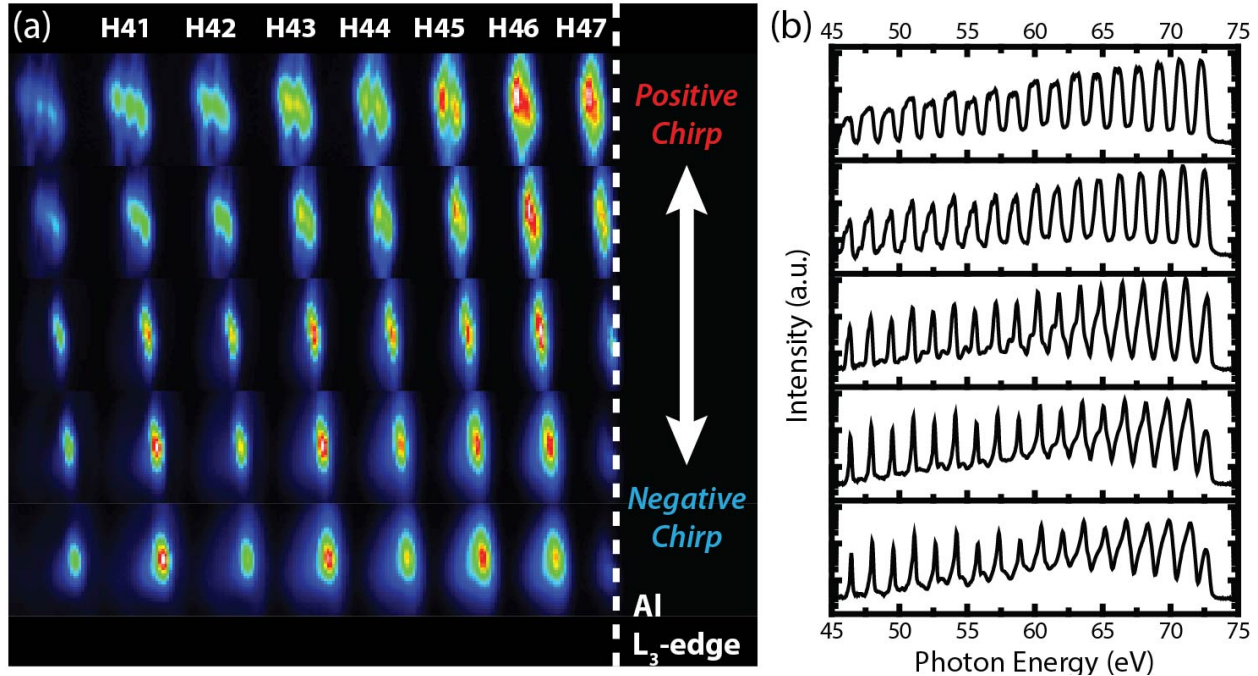


Figure 3-14: (a) Images of Ne harmonics directly detected on the X-ray CCD camera. Harmonic energy shift and peak broadening caused by either positively or negatively chirping the fundamental infrared pulses are clearly visible. The corresponding integrated high harmonic spectra for the five images are shown in (b) separately on the same logarithmic scale.

The chirp of the fundamental infrared pulses also affects the Ar harmonic spectrum in a similar manner. As Fig. 3-15 demonstrates, adding negative chirp to the infrared pulses significantly blueshifts and broadens every single harmonic peak. This type of harmonic spectrum is ideal for studying materials that contain Ti or V.

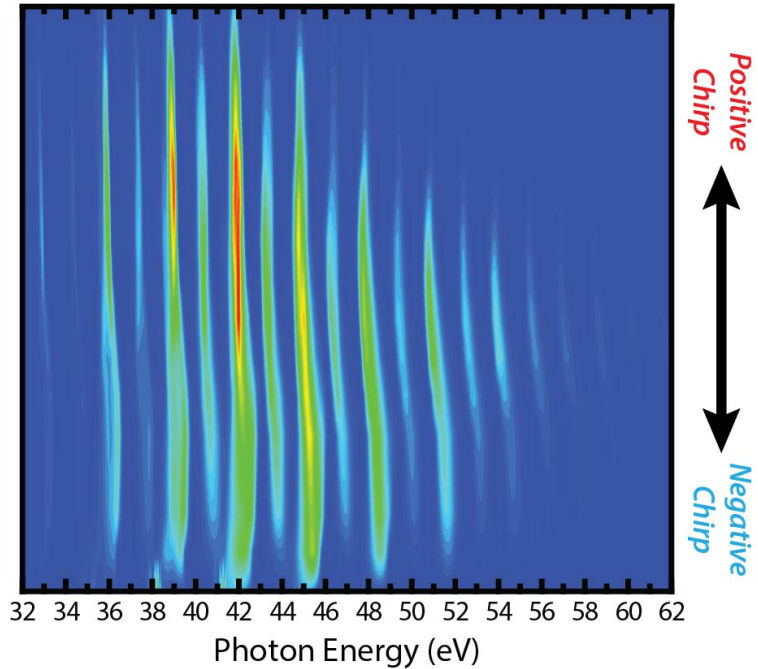


Figure 3-15: Influence of chirping the infrared pulses to the Ar harmonic spectrum that is generated from a 35 Torr gas cell, with two-color gating technique employed.

## 3.5 Data Acquisition Procedures

### 3.5.1 Daily Check List for System Performance

The experimental apparatus is capable of performing pump-probe measurements on a daily basis. In order to repeat the quality of data, several aspects of the instrument need to be monitored constantly. Since the warm-up times for the Ti:Sapphire oscillator and its diode pump laser could range from several days to several weeks, these lasers are typically left on all the time. Before engaging the chirped pulse amplifier, it is crucial to assure the oscillator is mode-locked properly and has sufficient spectral bandwidth ( $\text{FWHM} > 72 \text{ nm}$ ). The Nd:YLF pump laser for the amplifier is turned on daily and given at least 30 minutes warm-up time until the regenerative cavity reaches thermal equilibrium. The high-speed drivers of the Pockels cells then can be activated; by doing so the oscillator pulses are selectively injected into the regenerative cavity and then ejected after amplification. An oscilloscope connected to a fast photodiode detecting the leakage of the regenerative cavity can be used to determine whether the build-up time is correct. Another 30 minutes is required for the intra-cavity pulse train and the compressor assembly to reach a steady-state equilibrium. If the amplifier power output is lower than 3.20 W, or the spectral FWHM is narrower than 38 nm, then the cavity alignment needs to be optimized. Empirically once properly aligned, the amplifier can stay at a decent to good performance for at least two weeks without further adjustment.

The infrared output is directed along the designed beam path by the installed alignment targets. Among all, the two targets used for aligning an attenuated infrared beam into the SIGC are the most important ones, which are respectively (1) an iris diaphragm placed in front of the

SIGC entrance window and (2) an alignment target specifically manufactured at  $45^\circ$  passing angle placed right before the toroidal mirror (Fig. 3-16). The rear half of the SIGC has to be removed during the alignment, and so does the Al foil that is used for blocking the residual fundamental beam. A CCD webcam positioned outside the refocusing chamber is used to detect the infrared scattering on the alignment target, so that the entire alignment procedure can be done *in vacuo*. A ring-shaped scattering pattern (Fig. 3-16) should be observed before placing the Al foil and the SIGC back into the beam path. Now the full infrared power (1.70 - 1.80 W) may be let into the SIGC and ablate the stainless steel end plate that separates the SIGC and the HHG chamber. Because the gimbaled mount that hosts the toroidal mirror is locked after the initial alignment, the optimal XUV focus beam profile can be reproduced if the infrared fundamental beam is properly aligned into the SIGC following the abovementioned procedures.

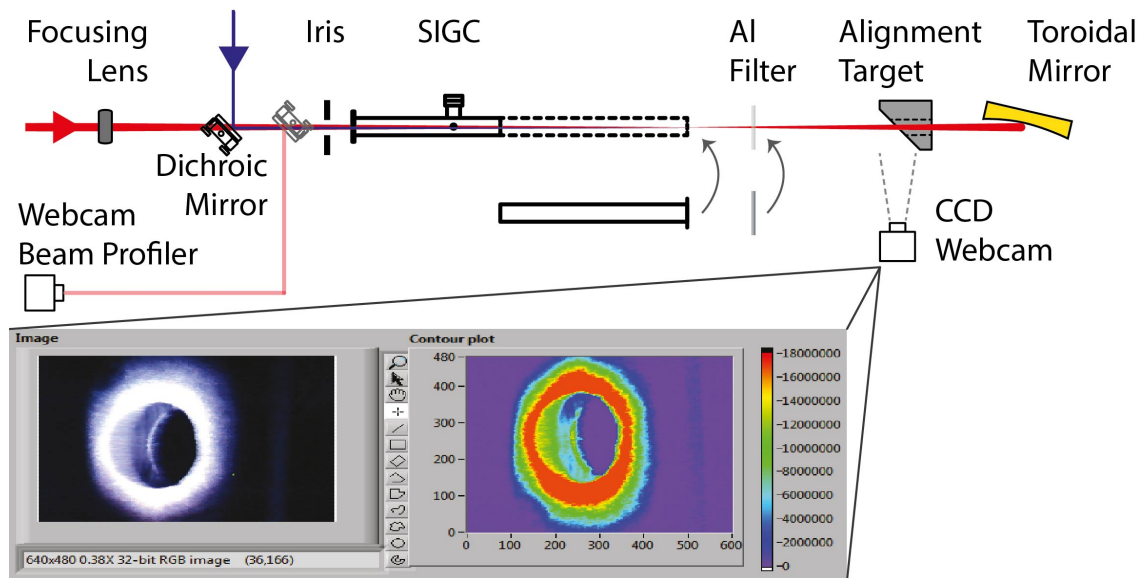


Figure 3-16: Optical components that are critical to the infrared alignment through the SIGC: both the rear half of the SIGC and the Al foil need to be removed when centering the infrared beam on both the iris and the alignment target. A flip mirror in front of the SIGC directs both 800 nm and 400 nm beams to a CCD beam profiler, where the focuses of both beams are overlapped.

The 400 nm symmetry-breaking field can also be aligned in the same manner, and the precise spatial overlap between 800 nm and 400 nm beams is carried out by rerouting both beams onto a beam profiling CCD that is placed at the same distance to the focusing lens as the distance from the focusing lens to the end plate of the SIGC. Both beams should be focused to similar sizes, and they also should be detected at the same location on the beam profiler, as shown in Fig. 3-17. When generating high-order harmonics, adjust the delay stage in the 400 nm beam path until the symmetry-breaking field arrives at the XUV source at the same time as the fundamental field, which can be assured by the appearance of even-order harmonics on the X-ray CCD.

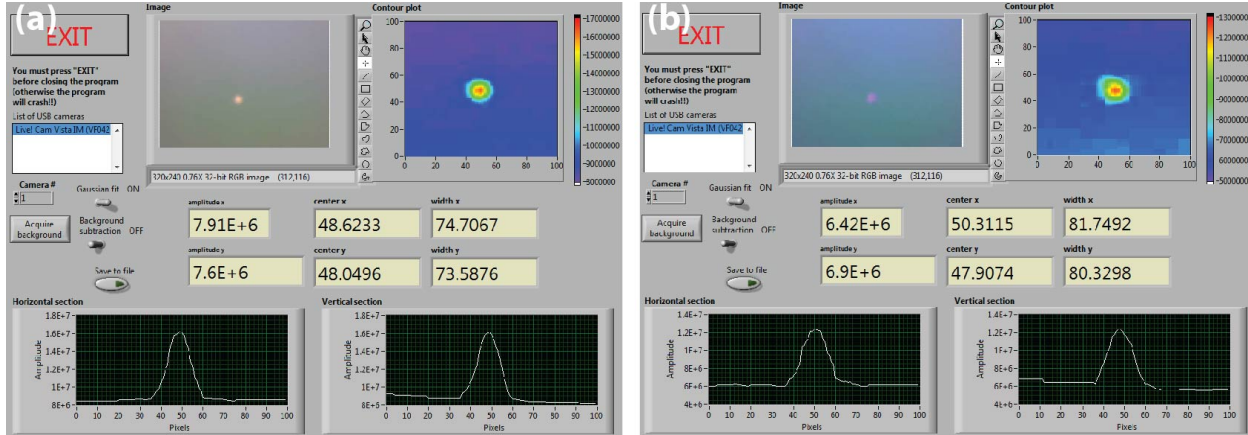


Figure 3-17: Nominal beam profiles of (a) the 800 nm fundamental field and (b) the 400 nm symmetry-breaking field, detected by a CCD beam profiler. Both beams are shown of similar sizes (74 – 80  $\mu\text{m}$  FWHM) and appear on the same location.

In parallel, the pressure readings at all three high vacuum chambers have to be close to the empirical base pressures prior to introducing noble gas medium into the SIGC. The working current and temperature on each individual turbo molecular pump need to be monitored periodically. The X-ray CCD camera should be cooled to -40 °C by a thermalelectric circuit in order to reduce the electronic noise. Making sure all the Al foils are in place to block the infrared fundamental, both gate valves may be opened. If apparent stray light is detected on the X-ray CCD camera, the Al foils need to be checked and replaced. Noble gas mediums (Ar or Ne) can be let into the SIGC at this point, and high-order harmonics should be visible on the X-ray detector. If the pixel location of the Al cut-off edge is clearly out of place, then the incident angle of the grating needs to be adjusted and it might be necessary to redo the X-ray spectrometer calibration as described in Sec. 2.4.4. Every time the regenerative cavity in the amplifier is realigned, a complete realignment is required in order to compensate the beam pointing variation. However in most cases the infrared beam and high-order harmonics can remain consistent and stable for a period of several days.

### 3.5.2 Static XUV Absorption Spectrum

Due to the short penetration length of 30 – 80 eV XUV radiation, the thickness of solid-state samples is usually limited to less than 30 nm. The thin-film and nanomaterial samples are supported on silicon or silica nitride ( $\text{Si}_3\text{N}_4$ ) substrates. To acquire the XUV absorption solely contributed by the sample, the XUV transmitted through a bare substrate is used as the reference beam. The optical density (absorbance) at a specific photon energy is given by the Beer-Lambert law, which can be related to the mass absorption coefficient  $\mu(E)/\rho_m$  (in  $\text{cm}^2/\text{g}$ ) of the sample:

$$OD(E) = -\log_{10} \left[ \frac{I_{\text{sample}}(E)}{I_{\text{substrate}}(E)} \right] = \frac{\mu(E)}{\rho_m} d \quad (3.3)$$

where  $\rho_m$  and  $d$  are the mass density and thickness of the sample, respectively. Experimentally a translation stage moves a sample and a bare substrate alternately into the XUV beam path, and each transmitted XUV spectrum is taken with an  $\sim 3$  second integration time (Fig. 3-18(a)).

Dividing one set of subsequent transmitted spectra would give one static-state XUV absorption spectrum. The XUV absorption spectrum of a thin-film hematite ( $\alpha\text{-Fe}_2\text{O}_3$ ) shown in Fig. 3-18(b) is averaged over 32 sets of such transmitted spectra, and the accompanying error bars are computed at the 95% confidence interval. The sharp absorbance rise at 56 eV indicates the Fe M<sub>2,3</sub>-edge that corresponds to the  $3p \rightarrow 3d$  core level transition. Underneath the resonant absorption edge is a featureless nonresonant absorption that is a contribution due to the direct photoionization of the valence electrons. The M-edge absorption introduces a  $3p^5 3d^{n+1}$  core hole state, which is highly unstable and will decay to a  $3d^{n-1}$  state via Auger process in a few femtoseconds. The final state degeneracy between the M-edge absorption and the direct  $3d$  electron photoionization would cause interference between these two processes, which results in an asymmetric resonant absorption feature (often referred to as a “Fano lineshape”). According to Eq. (3-3), the thickness of a sample can be estimated by comparing the measured optical density and the available database of atomic X-ray mass absorption coefficients,<sup>72</sup> assuming the photoabsorption cross sections are insensitive to the variation of oxidation states. For instance, the spectrum in Fig. 3-18(b) can be approximated to be a 28 nm thick  $\text{Fe}_2\text{O}_3$  layer. It worth noting that the standard deviations from spectral averaging distribute periodically with  $\sim 1.5$  eV spacing; this noise variation is caused by the low-flux regions in the transmitted XUV spectra, which have  $\sim 1.5$  eV energy modulations that result from the interference of an attosecond pulse train of the harmonics. This periodic noisy region becomes less apparent if the XUV continuum level is made high by manipulating the HHG process.

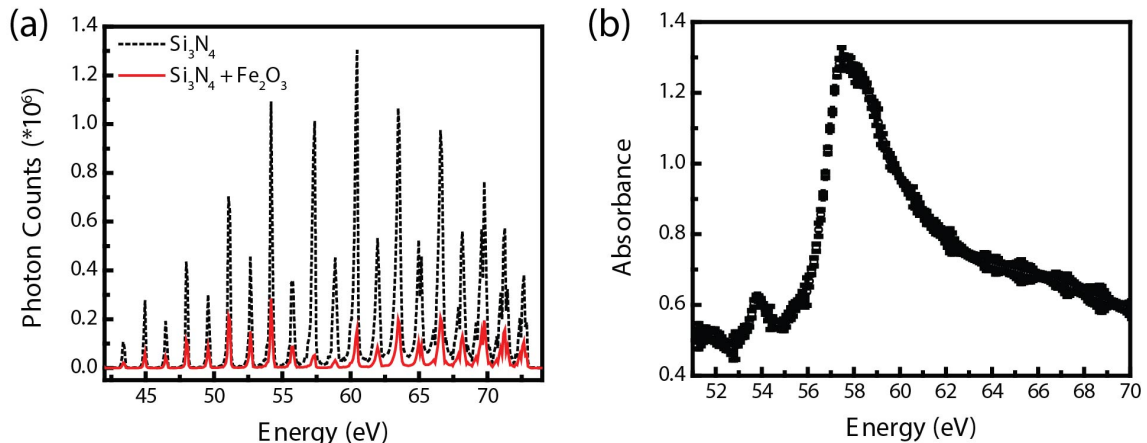


Figure 3-18: (a) The XUV spectra transmitted through a 100 nm bare  $\text{Si}_3\text{N}_4$  substrate (black dotted line) and a  $\text{Fe}_2\text{O}_3$  thin-film supported on a  $\text{Si}_3\text{N}_4$  substrate (red solid line). Each spectrum is collected at a 3-sec integration time. (b) The  $\text{Fe}_2\text{O}_3$  absorption spectrum after averaging 32 sets of transmitted spectra through the sample and the substrate.

### 3.5.3 Transmission Map

In order to minimize the thermal damage caused by the pump beam, the sample is raster scanned during pump-probe experiments. To acquire consistent data from different parts of the sample, however, it is crucial to prepare a sample with spatial homogeneity over a few millimeter scales. While depositing thin-films with an even thickness distribution over a 3 mm  $\times$  3 mm window area is generally possible, a homogeneous dispersion of nanoscale materials (e.g. quantum dots and nanowires) could be a challenging task. The spatial homogeneity of a sample can be visualized by an XUV transmission map measurement: At first a grid is constructed over

a specific substrate area based on the defined boundaries and the spacing between adjacent points, then each location on the grid is moved into the XUV beam path by the 2-D translational stage so that a transmitted XUV spectrum is acquired. The transmission levels at each point are used for constructing a map, which indicates the distribution of sample density in the measured area. Fig. 3-19 shows three transmission maps that are acquired from different samples: the thin-film  $\text{TiO}_2$  sample is prepared by evaporation of metallic titanium under a well-controlled oxygen partial pressure environment, and it shows an excellent spatial homogeneity with a transmission variation less than 10% in a  $3 \times 3 \text{ mm}^2$  area; the  $\text{CoS}_x$  film is prepared on a conductive silicon substrate by an electrodeposition method, and it is clearly more uneven than the  $\text{TiO}_2$  film; lastly,  $\text{Co}_3\text{O}_4$  nanocubes are drop-dispersed on a  $\text{Si}_3\text{N}_4$  substrate with a  $2 \times 2 \text{ mm}^2$  window, and this sample possesses large XUV transmission variations that occur on a length scale as short as 200  $\mu\text{m}$ , suggesting the aggregation of nanocubes in the low-transmission areas.

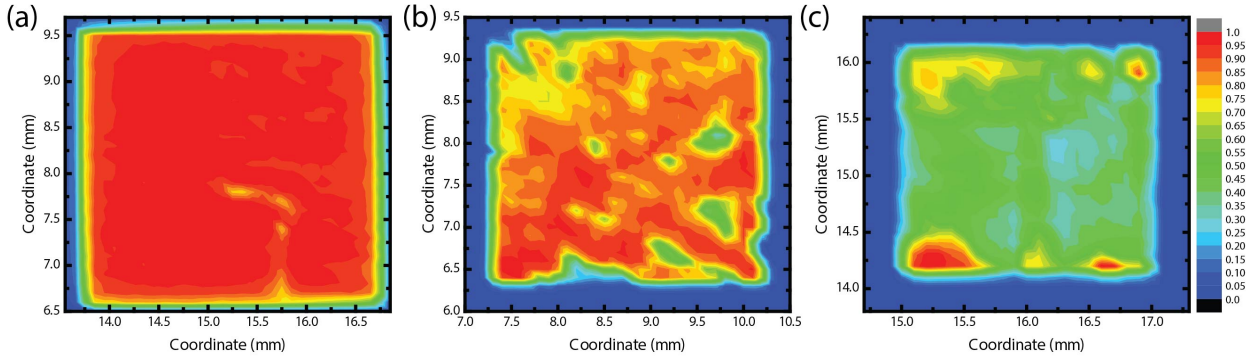


Figure 3-19: XUV transmission maps of (a) a thin-film  $\text{TiO}_2$  on a 250 nm Si substrate, (b) a  $\text{CoS}_x$  thin-film on a 250 nm Si substrate prepared by electrodeposition, and (c) a dispersion of  $\text{Co}_3\text{O}_4$  nanocubes on a 100 nm  $\text{Si}_3\text{N}_4$  substrate.

### 3.5.4 Overlap of Pump and Probe Beams

Both the spatial and the temporal overlaps between visible pump and XUV probe beams at the sample position are crucial for the time-resolved experiments, and therefore require consistent inspection on a daily basis. As has been addressed in Sec. 2.4.3, there is a  $\sim 1^\circ$  crossing angle when the pump and probe beams are recombined at the sample. Mounted together with other solid-state samples is a pinhole with  $\sim 300 \mu\text{m}$  diameter. This pinhole can be used to scan the XUV beam profile *in vacuo*, which is done by acquiring a transmitted XUV spectrum on the X-ray CCD camera at each step of the pinhole scanning (Fig. 3-20). Like the scanning knife-edge technique, the integrated XUV flux should give information about the size and position of the XUV probe beam. A barrier that is placed  $\sim 10 \text{ cm}$  after the sample not only prevents the pump beam from entering the XUV spectrometer, but also plays an important role for spatial overlapping the pump beam to the XUV beam: A CCD webcam detects the pump beam scattering spot on this barrier, and the scattering intensity profile can be used for determining the location and size of the pump beam. If the center of the pump beam deviates from that of the probe beam, then a piezo motor driven mirror mount (AG-M100N, Newport) in the pump beam path can be used for fine adjustments. This procedure should be repeated for both the horizontal and vertical direction, until the location difference between two beams is less than 5  $\mu\text{m}$ . The daily drifting of the pump-probe spatial overlap is less than 40  $\mu\text{m}$ , even when the Ti:Sapphire amplifier is turned off at the end of the day then turned on again the next morning.

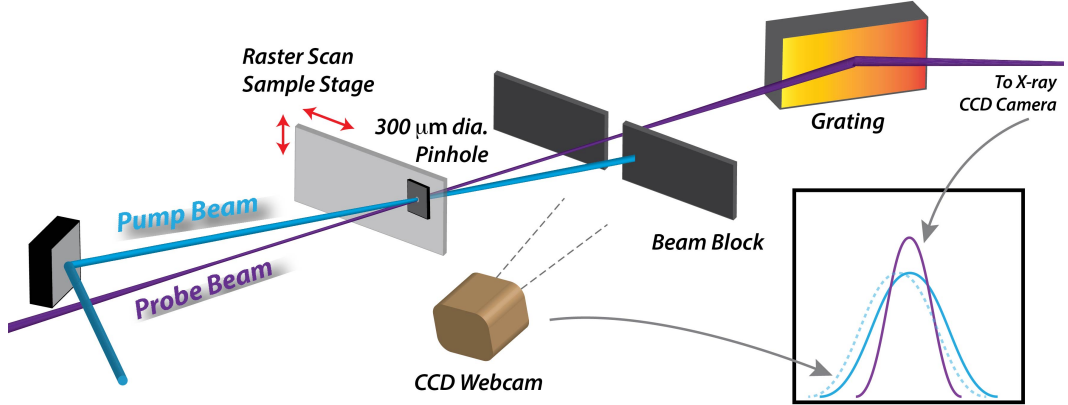


Figure 3-20: Procedure for spatial overlap between the visible pump and the XUV probe beam under a high vacuum condition. A 300  $\mu\text{m}$  diameter pinhole can be scanned across the beam paths along the horizontal and vertical directions. The XUV beam profile is acquired by the integrated flux detected by the X-ray CCD camera, while the pump beam scattering spot on the beam block is recorded as the pump beam profile. The pump beam is aligned toward the fixed XUV beam by a piezo motor driven mirror mount.

The temporal overlap between the pump and probe beams at the sample was first checked with a Si photodiode with 1 ns rise time (DET-10A, ThorLabs) during the instrument construction phase. By monitoring the rising edge of the photodiode response on a 4 GS/sec oscilloscope (LT372, LeCroy), the relative arriving time at the sample can be brought closer into a 10 ps range. Then a 20  $\mu\text{m}$  thick type-I BBO ( $\theta = 44.3^\circ$ ) is used for sum-frequency generation between the 400 nm pump pulses and the 800 nm fundamental pulses, and the cross-correlation trace based on the generated 266 nm intensities is shown in Fig. 3-21(a). For daily operation, the cross-correlation between the high harmonic pulse train and the pump beam is performed on  $\text{Co}_3\text{O}_4$  or  $\text{Fe}_2\text{O}_3$  thin-film samples, in which the transition metal M-edge responds extremely fast to the photoexcitation (Fig. 3-21(b)). The temporal overlap between XUV beam and visible pump beams, often referred as “time zero”, would drift less than 100 fs from day to day, mostly caused by the fluctuation of environment temperature.

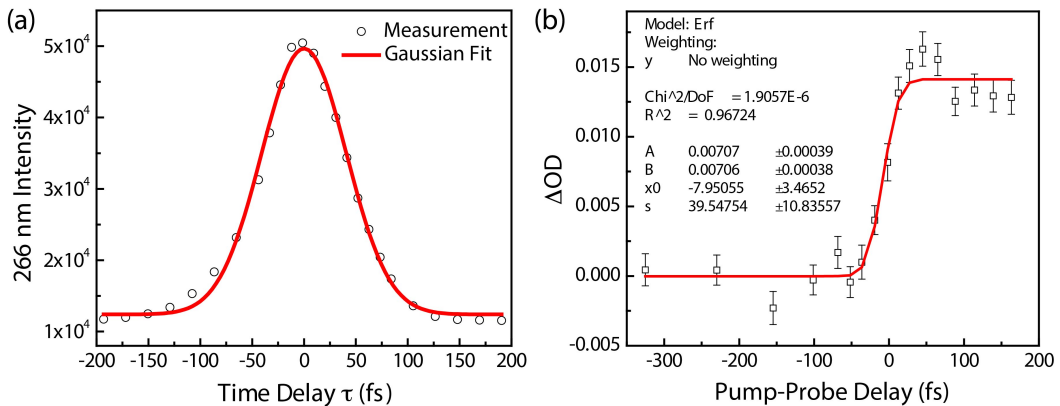


Figure 3-21: (a) Cross-correlation between the 800 nm beam that follows the XUV beam path and the 400 nm pump beam. Wave-mixing is done with a 20  $\mu\text{m}$  thick BBO (type-I,  $\theta = 44.3^\circ$ ). The 266 nm intensity trace is fit with a  $96.2 \pm 2.0$  fs Gaussian function. (b) The Co M-edge response to the 800 nm optical excitation. The signal rise is fit with a  $39.5 \pm 10.8$  fs error function.

### 3.5.5 Transient XUV Absorbance Measurements

In a time-resolved experiment, a transient XUV absorption spectrum is obtained by acquiring a XUV probe spectrum with the pump beam incident on the sample ( $I_{on}(E)$ , “pump on”) and another probe spectrum with the pump beam blocked ( $I_{off}(E)$ , “pump off”). The specific time delay  $\Delta t$  between pump and probe beams is controlled by varying the pump beam path length with a delay stage. The absorbance change  $\Delta OD(E, \Delta t)$  caused by the pump beam can be calculated by the formula

$$\Delta OD(E, \Delta t) = -\log_{10} \left[ \frac{I_{on}(E, \Delta t)}{I_{off}(E, \Delta t)} \right] \quad (3.2)$$

The instrument does not install a monochromator before the sample, instead all the photons energies are transmitted through the sample at once and then dispersed in the XUV spectrometer; therefore the time delay  $\Delta t$  is the only control factor in Eq. (3.2). A time-resolved experiment may measure  $N$  transient XUV absorption spectra at once; each corresponding to a different time delay ( $\Delta t_1, \dots, \Delta t_{N-1}, \Delta t_N$ ). The data acquisition procedure, however, still requires synchronization between different components on the experimental apparatus. A LabVIEW program is written for this purpose, and its function is demonstrated in Fig. 3-22. As has been mentioned earlier, in order to minimize the thermal damage/degradation, each sample is divided into a 2D grid, in which every location is a  $100 \mu\text{m}$  distance away from the nearest neighbors. Each location is used for collecting one set of pump on/off spectra, and then the translational stage would move the next location into the beam path. Meanwhile, the delay stage alters the arrival time  $\Delta t_N$  of the pump beam at the sample. A mechanical shutter that controls the passage of the pump beam is initially closed, and the X-ray CCD is triggered to acquire a pump off XUV transmission spectrum. The LabVIEW program then lets the pump beam pass through the shutter and triggers the X-ray CCD to acquire the pump on spectrum at the same location. The shutter closes right away and the sample is moved to the next location on the raster scan grid, then the same procedure is repeated at another time delay  $\Delta t_{N+1}$ . If the delay stage has reached the last set value  $\Delta t_N$ , it would return to  $\Delta t_1$  to repeat all the set time delay values. Several transient absorbance spectra taken at the same delay  $\Delta t$  are averaged for a better signal-to-noise (S/N) ratio.

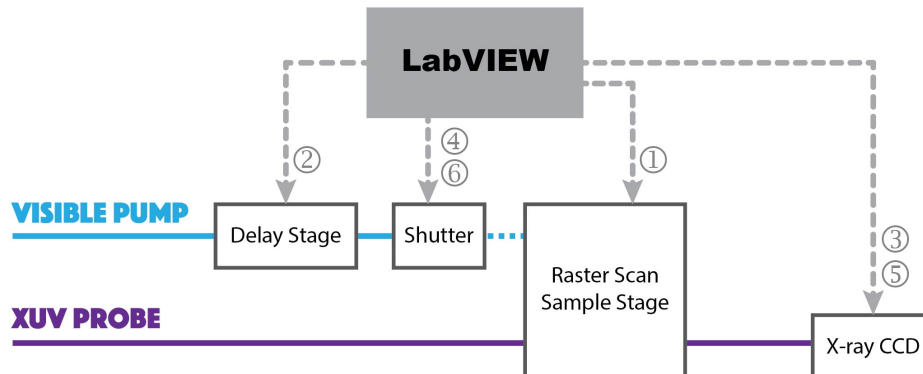


Figure 3-22: The LabVIEW data acquisition program for time-resolved experiments, the circled numbers indicate the sequence of command/trigger for acquiring one set of pump on/off XUV transmission spectra.

It should be noted that the pump beam scattering light would add a background to all the pump on spectra, while the pump off spectra are not affected. Therefore after dividing all the pump on/off spectrum pairs, the acquired transient XUV absorbance signal would contain an artifact. This artifact can be eliminated by using the transient spectrum acquired at a negative time delay, i.e. the pump beam arrives later than the probe beam, as the baseline for all other spectra taken at positive time delays.

The set time delay values can be compared to the actual values recorded by the encoded delay stage. As shown in Fig. 3-23, the actual time delay values exhibit an excellent linear relation to the set values, and the largest difference is no more than 15 fs. However, the deviations from set values do not distribute randomly with respect to the set values: from zero time delay to 300 fs there exists a consistent -10 fs deviation from the set values, while in the 300 – 6000 fs range the deviations are much smaller. The largest deviation occurs on the first set time delay, which can be explained by the relatively long distance that the delay stage needs to travel when returning from the last set time delay. Based on these findings, it is suggested to use the actual time delays, instead of the set values, for the excited-state dynamic studies, especially when the experiment is performed with time steps smaller than 30 fs.

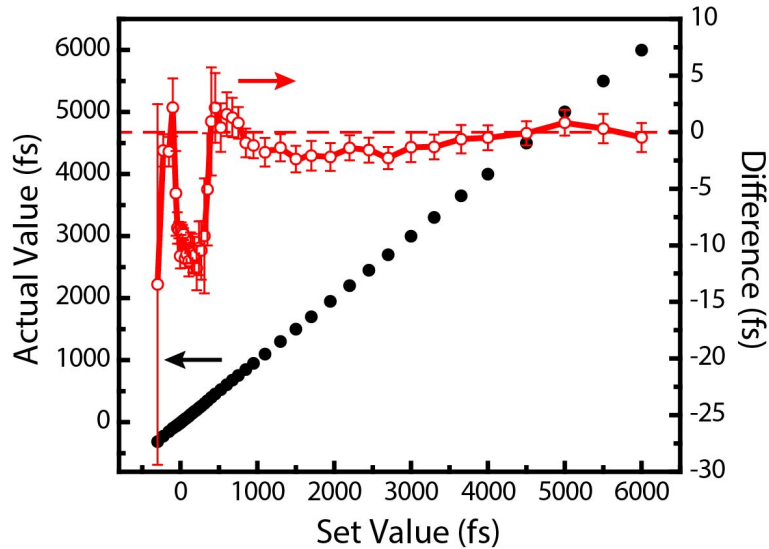


Figure 3-23: Plot of 46 set time delay values (x-coordinate) to the recorded actual values (black dots, y-coordinate). The difference between two values (red line) is averaged over 140 rounds, and the standard deviations are also given in the plot.



# Chapter 4

## Characterization of Photo-Induced Charge Transfer and Hot Carrier Relaxation Pathways in Spinel Cobalt Oxide ( $\text{Co}_3\text{O}_4$ )

A large portion of the content and figures in this chapter are adapted from C.-M. Jiang, L. R. Baker, J. M. Lucas, J. Vura-Weis, A. P. Alivisatos, and S. R. Leone, “Characterization of Photo-Induced Charge Transfer and Hot Carrier Relaxation Pathways in Spinel Cobalt Oxide ( $\text{Co}_3\text{O}_4$ )”, *J. Phys. Chem. C* 2014, 118, 22774–22784. Reproduced with permission.

The identities of photoexcited states in thin-film  $\text{Co}_3\text{O}_4$  and the ultrafast carrier relaxation dynamics of  $\text{Co}_3\text{O}_4$  are investigated with oxidation-state-specific pump-probe femtosecond core level spectroscopy. A thin-film sample is excited near the 2.8 eV optical absorption peak, and the resulting spectral changes at the 58.9 eV  $\text{M}_{2,3}$ -edge of cobalt are probed in transient absorption with femtosecond high order harmonic pulses generated by a Ti:Sapphire laser. The initial transient state shows a significant 2 eV red-shift in the absorption edge compared to the static ground state, which indicates a reduction of the cobalt valence charge. This is confirmed by a charge transfer multiplet spectral simulation, which finds the experimentally observed extreme ultraviolet (XUV) spectrum matches the specific  $\text{O}^{2-}(2p) \rightarrow \text{Co}^{3+}(e_g)$  charge-transfer transition, out of six possible excitation pathways involving  $\text{Co}^{3+}$  and  $\text{Co}^{2+}$  in the mixed valence material. The initial transient state has a power-dependent amplitude decay ( $190 \pm 10$  fs at  $13.2 \text{ mJ/cm}^2$ ) together with a slight red-shift in spectral shape ( $535 \pm 33$  fs), which are ascribed to hot carrier relaxation to the band edge. The faster amplitude decay is possibly due to a decrease of charge carrier density via an Auger mechanism, as the decay rate increases when more excitation fluence is used. This study takes advantage of the oxidation-state-specificity of time-resolved extreme ultraviolet spectroscopy, further establishing the method as a new approach to measure ultrafast charge carrier dynamics in condensed-phase systems.

## 4.1 Introduction

Transition metal oxides have received much attention as photocatalysts and interlayer materials in photovoltaics, especially because of their good earth-abundance, stability, and controllable band gap and charge carrier properties.<sup>79,80</sup> Unlike covalent semiconductor materials like Si, Ge and GaAs, transition metal oxides possess a greater ionic bonding character and a localized electronic structure, thus exhibiting a wide range of important catalytic and semiconductor properties. Not only are the synthetic methods and applications of transition metal oxide-based materials and nanomaterials extensively developed,<sup>81-83</sup> conceptual principles in terms of electronic structure and charge carrier dynamics within these materials have also been studied.<sup>84-87</sup> Understanding these concepts, including *d*-electron behavior, hot carrier relaxation, and interfacial charge transfer, is important for developing highly efficient photovoltaic and photocatalytic devices.

In most transition metal oxides, the *d*-orbitals are partially filled and split between two bands separated by a *d-d* Coulomb repulsion energy  $U$ , such that electron hopping between metal sites requires energy. On the other hand, charge conduction in metal oxides can also occur through electron transfer from the oxygen ligand to the metal cation, which is defined by a charge transfer band gap  $\Delta$ . As a result, in transition metal oxides the conduction band consists mostly of empty metal *d* orbitals, while the valence band has both oxygen  $2p$  and metal *d* orbital characteristics. Whether or not the charge transfer gap  $\Delta$  is larger than the *d-d* repulsion  $U$  defines two different types of semiconductors: Mott-Hubbard ( $U < \Delta$ ) and charge-transfer semiconductor ( $U > \Delta$ ).<sup>4</sup> In the case of transition metal fluorides, a continuous transition from Mott-Hubbard to charge-transfer semiconductor has been observed across the first row transition metals.<sup>88</sup> If the composition is changed from fluorine to oxygen, however, considering the electronegativity difference alone is not sufficient to define the type of semiconductor, because of the larger extent of orbital mixing through interatomic covalent bonding in the oxide compounds.

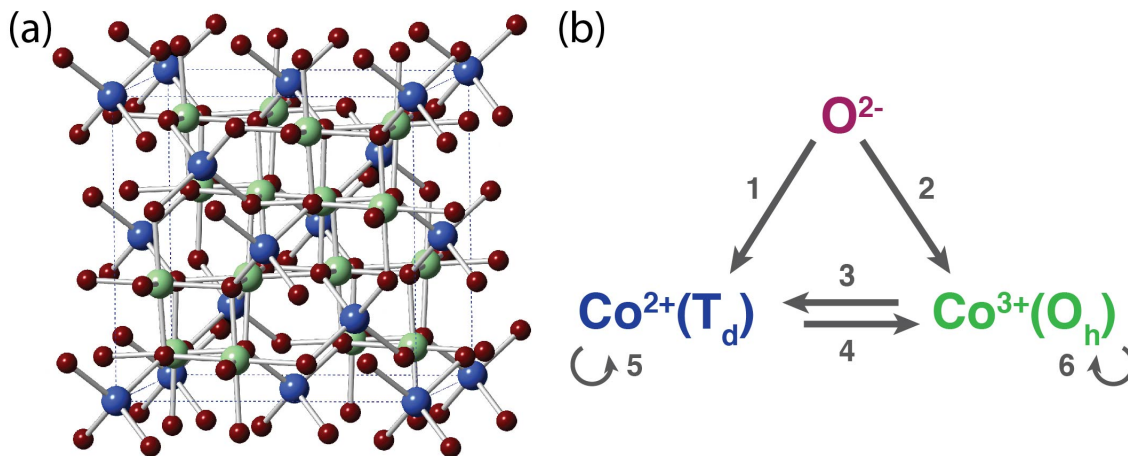


Figure 4-1: (a) Illustration of the crystal structure of spinel  $\text{Co}_3\text{O}_4$ . Red: oxygen *fcc* sublattice. Blue:  $\text{Co}^{2+}$  ions occupying tetrahedral sites. Green:  $\text{Co}^{3+}$  ions occupying octahedral sites. (b) Six possible optical excitation pathways in  $\text{Co}_3\text{O}_4$ , which consists of  $\text{O}^{2-}$  anions and two different cobalt oxidation states ( $\text{Co}^{2+}$  and  $\text{Co}^{3+}$ ). There are two ligand-to-metal-charge-transfer (LMCT) pathways (1 and 2), two metal-to-metal-charge-transfer (MMCT) pathways (3 and 4) and two local *d-d* ligand field excitations (5 and 6).

Among various transition metal oxides, the thermodynamic stability and surface redox reactivity make cobalt oxide ( $\text{Co}_3\text{O}_4$ ) an important catalyst for CO oxidation,<sup>89</sup> Fischer-Tropsch synthesis,<sup>90</sup> cyclohexane dehydrogenation,<sup>91</sup> and the oxygen evolution reaction in water splitting.<sup>92</sup>  $\text{Co}_3\text{O}_4$  doped with other elements (F, Ni or alkali metals) also exhibit enhancements in specific properties.<sup>93-95</sup>  $\text{Co}_3\text{O}_4$  has a spinel structure ( $\text{AB}_2\text{O}_4$ ) in which oxygen ions form a face centered cubic (*fcc*) lattice, and two different cobalt oxidation states,  $\text{Co}^{2+}$  and  $\text{Co}^{3+}$ , respectively, occupy tetrahedral and octahedral symmetry sites with a 1:2 stoichiometric ratio (Fig. 4-1(a)). Because of the presence of two cobalt oxidation states and *d*-electron configurations, the electronic structure of  $\text{Co}_3\text{O}_4$  has even more complexity than other transition metal oxides. Each  $\text{Co}^{2+}$  ion has a high-spin  $^4\text{A}_2$  configuration and three unpaired electrons in  $t_2$  orbitals, while for the  $\text{Co}^{3+}$  ion the *d*-electrons of the low-spin  $^1\text{A}_1$  configuration are all paired in  $t_{2g}$  orbitals. Density functional theory (DFT) calculation<sup>96</sup> has suggested that the conduction band of  $\text{Co}_3\text{O}_4$  is mainly composed of the  $\text{Co}^{2+}$   $t_2$  minority spin orbitals and the  $\text{Co}^{3+}$   $e_g$  orbitals. The valence band has contributions from filled *d* orbitals of both cobalt oxidation states as well as  $2p$  orbitals of the oxygen anion with some extent of hybridization effects between these orbitals.

Considering the composition of spinel  $\text{Co}_3\text{O}_4$ , six possible electronic transitions can occur when absorbing a photon at an energy higher than the band gap (Fig. 4-1(b)): these include two ligand-to-metal-charge-transfer (LMCT) pathways from O- $2p$  to the two types of cobalt cations, two metal-to-metal-charge-transfer (MMCT) transitions between different cobalt oxidation states, and one *d-d* ligand field excitation within each of the  $\text{Co}^{2+}$  and  $\text{Co}^{3+}$  cations. Although the spatial overlap between two *d*-orbitals of separated cobalt cations seems to be small, a MMCT transition can still occur across an oxygen bridge if both *d*-orbitals have significant bonding characters with the same O- $2p$  orbital. High-pressure induced MMCT in  $\text{Co}_3\text{O}_4$  from  $\text{Co}^{2+}$  to  $\text{Co}^{3+}$  has been observed experimentally, transforming the lattice structure from normal spinel to inverse spinel.<sup>97</sup> All the LMCT and MMCT pathways involve cobalt oxidation state changes at one or both lattice sites, while *d-d* excitations only modify the local electronic configuration without affecting the oxidation state of the cobalt ions.

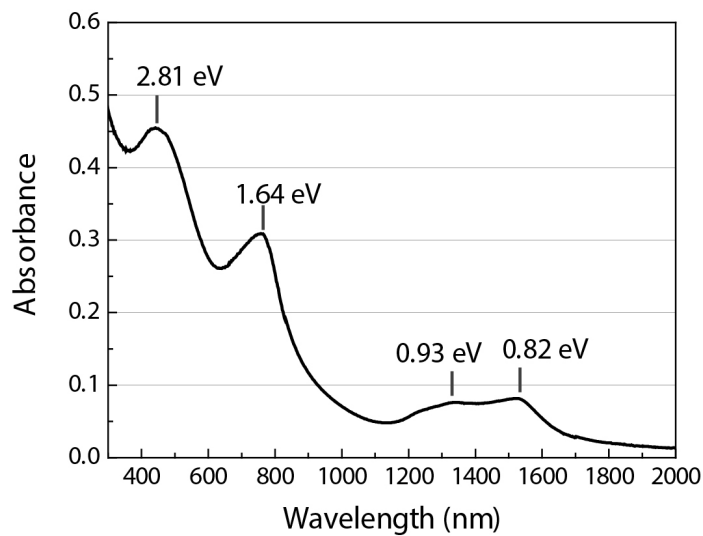


Figure 4-2: UV/Vis absorption spectrum of thin-film  $\text{Co}_3\text{O}_4$  on a quartz substrate prepared by the same procedure as described in the section 4-2.

The visible/infrared absorption spectrum of  $\text{Co}_3\text{O}_4$  (Fig. 4-2) shows four distinguishable peaks at 0.8 eV, 0.9 eV, 1.6 eV and 2.8 eV,<sup>98</sup> however there has been little success in assigning electronic transitions to these absorption peaks. Molecular orbitals in the presence of a ligand field have been constructed for an entire unit cell, and available transitions are compared with the visible/infrared absorption peaks.<sup>99</sup> With this approach the 2.8 eV peak is assigned to the  $\text{O}^{2-}(2p) \rightarrow \text{Co}^{3+}(e_g)$  transition. Experimental interpretation has been made by monitoring the absorption spectrum changes as  $\text{Co}^{2+}$  in tetrahedral sites are gradually substituted by  $\text{Zn}^{2+}$ .<sup>100</sup> That work suggests the broad peak at 2.8 eV actually consists of two transitions, and the lower and higher energy shoulders correspond to  $\text{O}^{2-}(2p) \rightarrow \text{Co}^{2+}(t_2)$  and  $\text{O}^{2-}(2p) \rightarrow \text{Co}^{3+}(e_g)$  charge transfer, respectively. Nevertheless, no direct observation and assignment of photo-excited states of  $\text{Co}_3\text{O}_4$  have been published. Understanding how  $\text{Co}_3\text{O}_4$  interacts with visible photons, including the identity of the initially photo-induced excited state and the subsequent carrier relaxation, can provide insightful explanations for the material's photocatalytic activity.

Time-resolved spectroscopy has been widely used to study ultrafast photophysical or photochemical processes following photon absorption. One common problem when applied to the condensed-phase, however, is that the complexity of the electronic structure makes the experimental excited-state spectrum, from the infrared to UV region, difficult to interpret. Transitions associated with core-levels, usually by probing with X-ray or extreme ultraviolet (XUV) photons, possess unique capabilities to distinguish different elements, oxidation states, local spin states and covalent/ionic bonding characteristics.<sup>23,101,102</sup> Taking cobalt oxide as an example, electronic structure changes occurring near cobalt atoms can be observed via the 58.9 eV cobalt M<sub>2,3</sub>-edge, which is the  $\text{Co } 3p^6 3d^n \rightarrow 3p^5 3d^{n+1}$  dipole transition, and the difference between  $\text{Co}^{2+}$  and  $\text{Co}^{3+}$  can be separated. Moreover, the development of the high harmonic generation (HHG)<sup>44</sup> technique enables conversion of widely available near-infrared 800 nm pulses to extreme ultraviolet pulses with femtoseconds<sup>29,103,104</sup> or even attoseconds<sup>31,105</sup> duration. These short pulses can be utilized as an ideal tool for studying ultrafast photochemical processes in transition-metal-containing condensed-phase systems.

Synchrotron light sources can provide high energy X-ray photons to probe transition metal L-edges, which generally show sharper features than M-edge absorption due to more obvious spin-orbit coupling effects in the n = 2 shell. The energy of photons used to probe L-edges of first-row transition metals (400 – 1200 eV) can also access the K-edge of the oxygen ligand (~540 eV), which provides the opportunity to study the valence charge distribution around both transition metal cations and oxygen ligands at once. However the mass absorption coefficients at the M-edge (~ $10^5 \text{ cm}^2/\text{g}$ ) are larger than at the L-edge (~ $10^4 \text{ cm}^2/\text{g}$ ) by an order of magnitude. This sensitivity makes M-edge absorption in the extreme ultraviolet region especially useful to measure samples at the nanometer scale. Transient X-ray absorption spectroscopy at the L-edge has been applied to investigate the electronic structure of cuprous oxide,<sup>36</sup> photo-induced spin crossover<sup>102</sup> and excited-state molecular and electronic structure changes<sup>30,106,107</sup> in transition metal complexes, and ultrafast spin dynamics in condensed-phase.<sup>108</sup> Coherent optical phonons, ultrafast demagnetization dynamics and the excited-state character of hematite have also been studied by table-top HHG apparatuses.<sup>35,109,110</sup>

This work exploits the elemental and oxidation-state specificity of transient extreme ultraviolet spectroscopy. When pumped at 400 nm, the identity of the  $\text{Co}_3\text{O}_4$  excited-state and the subsequent charge carrier relaxation process are resolved. This research provides evidence that 400 nm excitation induces specifically the  $\text{O}^{2-}(2p) \rightarrow \text{Co}^{3+}(e_g)$  charge transfer transition.

Two sub-ps dynamics timescales are observed after the optical excitation: A  $190 \pm 10$  fs fast lifetime of transient absorbance amplitude decay can be explained as Auger relaxation of extra charge carriers, which is supported by an increased decay rate with higher excitation fluences. An additional  $\sim 300$  meV spectral red-shift that occurs in  $535 \pm 33$  suggests hot carriers undergo relaxation toward the band edge via carrier-phonon scattering.

## 4.2 Experimental Methods

This research aims to study ultrafast charge carrier dynamics of thin-film  $\text{Co}_3\text{O}_4$  following femtosecond 400 nm visible excitation. Changes of electronic structures after excitation are probed by measuring XUV transient absorption differences. The apparatus (Fig. 4-3) consists of an 800 nm Ti:Sapphire laser to generate high order harmonics as the probe and to produce frequency-doubled pulses for the pump excitation, a high vacuum system with high harmonic source, toroidal focusing mirror, and raster scanned sample, and a variable line space grating and X-ray charge coupled device (CCD) camera for spectral detection after the sample.

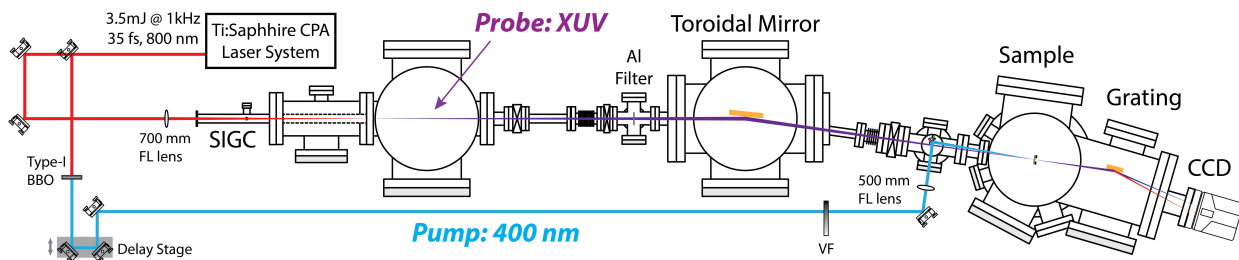


Figure 4-3: Layout of the transient XUV absorption instrument. High harmonics are generated in a semi-infinite gas cell (SIGC) with a two-color laser driver field (1.8 mJ, 40 fs at 800 nm + 20  $\mu\text{J}$ , 60 fs at 400 nm). The neon pressure in the SIGC is 100 Torr ( $1.3 \times 10^4$  Pascals). The residual 800/400 nm driver pulses are blocked by a 0.6  $\mu\text{m}$  Al foil. The 400 nm pump beam is frequency-doubled from 800 nm near-infrared and the pump energy is reduced by a variable neutral density filter (VF). The instrument has to be under high vacuum ( $\sim 10^{-7}$  Torr) beyond the semi-infinite gas cell because air is highly absorptive to XUV photons.

Cobalt oxide thin-film samples are prepared by RF magnetron sputtering of  $\sim 10$  nm cobalt metal on 100-nm  $\text{Si}_3\text{N}_4$  substrates, followed by oxidation in ambient atmosphere in a tube furnace at 500°C for 1 hour and cooling naturally to room temperature. The actual sample thickness is not directly measured, but it is estimated by scaling the resonant  $\text{M}_{2,3}\text{-edge}$  absorption amplitude with the XUV absorption cross-section provided by the CXRO.<sup>72</sup> Four absorption peaks (0.82 eV, 0.93 eV, 1.64 eV and 2.81 eV) appear in the visible/infrared absorption spectra of thin-film  $\text{Co}_3\text{O}_4$  on a quartz substrate prepared by the same procedures (Fig. 4-2), which agree with the literature values.<sup>98</sup> The composition and phase of spinel  $\text{Co}_3\text{O}_4$  are confirmed by selected area electron diffraction (Fig. 4-4). Micro-Raman measurement shows four distinct Raman shift peaks (474, 518, 611 and 679  $\text{cm}^{-1}$ , Fig. 4-5) that match reported signatures of spinel  $\text{Co}_3\text{O}_4$ .<sup>111</sup> Similarly, measurements were also made to confirm that the pump beam does not damage samples after each pump-probe measurement.

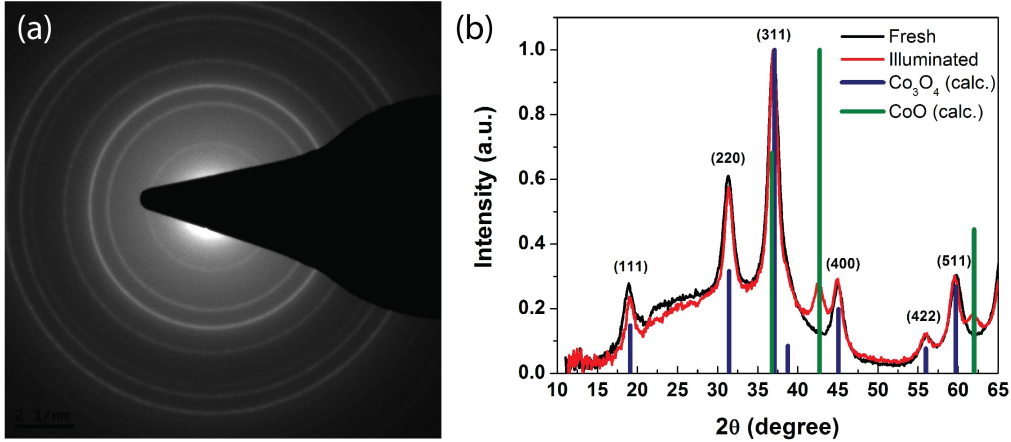


Figure 4-4: (a) Selected area electron diffraction (SAED) pattern of spinel  $\text{Co}_3\text{O}_4$  thin-film. The concentric ring patterns are the result of overlapping of single crystal dot patterns at different crystal orientations. (b) Electron diffractogram of spinel  $\text{Co}_3\text{O}_4$  thin-film measured before and after pump-probe experiment. The broad background underneath the diffraction peaks results from the amorphous  $\text{Si}_3\text{N}_4$  substrate. Red line is the diffractogram taken on a sample illuminated by 2.33 mW 400 nm pump beam for 8 seconds, i.e. four repeated data acquisitions. Less than 10% of  $\text{CoO}$  is formed due to the sample heating effect in vacuum environment by the pump beam.

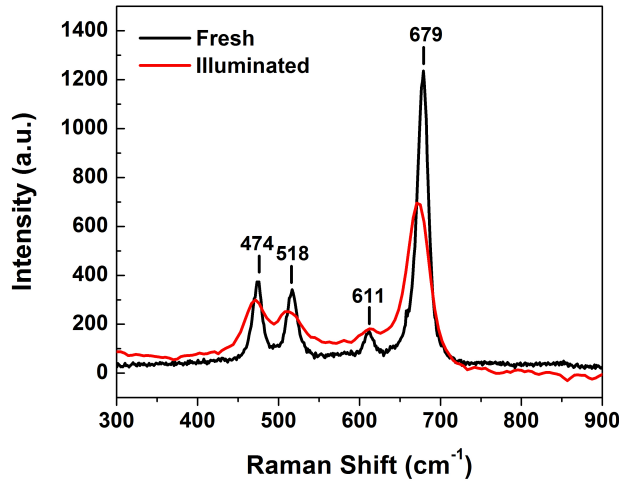


Figure 4-5: Raman spectrum of fresh (black) and illuminated (red) spinel  $\text{Co}_3\text{O}_4$  thin-film measured by micro-Raman technique. The signals are collected for 30 seconds as the sample is excited by 1.28 mW of 527 nm laser within a 5  $\mu\text{m}$  diameter spot.

The Ti:Sapphire chirped pulse amplifier (Spitfire Pro, Spectra Physics) provides 3.5 mJ pulses spectrally centered at 800 nm at a 1 kHz repetition rate. High harmonic generation is accomplished by splitting and focusing  $\sim$ 1.8 mJ of the near-infrared fundamental pulses into a 40 cm long semi-infinite gas cell (SIGC) filled with 100 Torr ( $\sim 1.3 \times 10^4$  Pascals) of neon. The laser peak intensity is  $5.7 \times 10^{14} \text{ W cm}^{-2}$  at the 100  $\mu\text{m}$  diameter focus. About 20  $\mu\text{J}$  of 400 nm light is mixed into the fundamental pulses in order to generate both odd- and even-order harmonics by breaking the electric field symmetry, so that the XUV photons will have more

uniform spectral coverage. The use of a semi-infinite gas cell simplifies the alignment procedure of the high harmonic source and is able to generate extreme ultraviolet pulses with higher efficiency because of its longer interaction region compared to other short pathlength HHG geometries.<sup>59</sup> The generated extreme ultraviolet pulses are used as a probe beam and possess  $\sim 2 \times 10^{-10}$  J energy per pulse. After refocusing by a gold-coated toroidal mirror, the beam size of the XUV probe at the sample location is about 80  $\mu\text{m}$ .

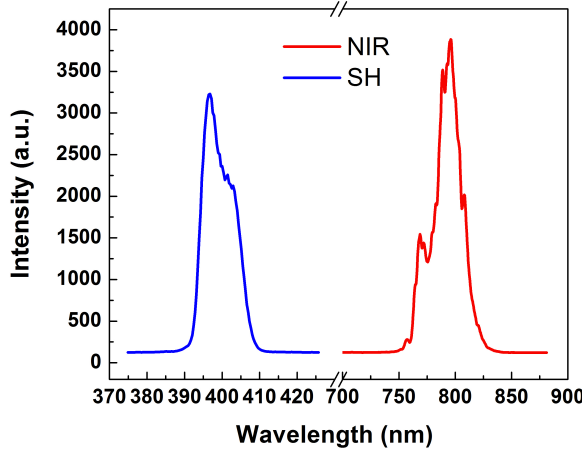


Figure 4-6: Red line: Spectrum of near-infrared (NIR) pulses used for high harmonics generation in a semi-infinite gas cell. Blue line: Second-order harmonics of near-infrared generated by frequency-doubling in a 100  $\mu\text{m}$  thick type-I  $\beta$ -BaB<sub>2</sub>O<sub>4</sub> (BBO). This is used as pump pulses for optical excitation of Co<sub>3</sub>O<sub>4</sub>.

The pump beam is generated by frequency-doubling to 400 nm (FWHM  $\approx 11$  nm, Fig. 4-6) the rest of the split near-infrared pulse energy in a 100  $\mu\text{m}$  thick type-I  $\beta$ -BaB<sub>2</sub>O<sub>4</sub> (BBO) crystal. A variable neutral density filter controls the pump beam power, which is focused to a spot size of 150  $\mu\text{m}$  diameter on the sample and adjusted to an average power between 0.86 to 2.70 mW at 1 kHz for the pump fluence dependence studies. Based on the size of the pump beam and the sample absorbance at 400 nm ( $\sim 0.45$ , refer to Fig. 4-2), this is equivalent to 4.87 to 15.3 mJ/cm<sup>2</sup> fluence and 3 to  $9 \times 10^{21}$  cm<sup>-3</sup> excited charge carrier density. After transmitting through the Co<sub>3</sub>O<sub>4</sub> sample supported by the Si<sub>3</sub>N<sub>4</sub> substrate, the extreme ultraviolet pulses are spectrally dispersed by a variable line-spacing grating onto a CCD camera (PIXIS-400, Princeton Instruments). On one 20  $\mu\text{m} \times 20 \mu\text{m}$  camera pixel, average photon counts are about  $2 \times 10^4$  per second, and the energy range of the spectrometer is from 38 eV to 80 eV with  $\sim 150$  meV spectral resolution. The apparatus combines the spectrometer located after the sample, and the broadband nature of extreme ultraviolet pulses (50-72 eV) generated by HHG, to efficiently record transient spectra at multiple photon energies at once. The temporal resolution of the apparatus is limited by the  $\sim 40$  fs pump beam duration.

Pump-probe traces are taken by varying a delay stage in the pump beam path and a mechanical shutter controlling the pump beam passage. At each pump-probe delay time the differential optical density spectra are obtained by dividing alternating transmitted extreme ultraviolet spectra with pump beam on/off for 2 seconds each. The 3 mm  $\times$  3 mm sample is raster-scanned by 100  $\mu\text{m}$  spatial step sizes between individual pump-probe data acquisition,

such that each transient spectrum is taken at an unused sample spot. Spectra at 500 fs before time-zero (probe beam arrives prior to pump beam) are subtracted from spectra taken at every pump-probe delay in order to eliminate the artifacts of residual scattered light from the pump beam. Transient absorbance spectra at each individual pump-probe delay are averaged over 56 runs. Errors resulting from pump and probe beam fluctuations are less than 1% while the maximum differential absorbance signal is 20%. Electron diffraction shows that less than 10% of CoO is formed after four repeated pump-probe measurements at 2.33 mW average pump power (Fig. 4-4(b)). The heating effect by the pump pulses is believed to cause this sample reduction in high vacuum environment, however the extent of this effect should not alter the acquired XUV transient spectra.

## 4.3 Results and Discussion

### 4.3.1 Static XUV Absorption Spectrum and Fitting Results

Fig. 4-7 shows the resonant absorption edge of a thin-film  $\text{Co}_3\text{O}_4$  sample. The resonant absorption near 60 eV indicates the  $\text{Co } 3p \rightarrow 3d$  transition, which demonstrates the elemental specificity of X-ray spectroscopy. The non-resonant absorption contributions extending from the valence electron ionization at  $\sim 20$  eV have been subtracted from the raw spectrum. By scaling the amplitude of this cobalt M<sub>2,3</sub>-edge with the absorption cross section available on CXRO,<sup>72</sup> the thickness of the sample is approximated to be 22 nanometers. When comparing with the  $\alpha\text{-Fe}_2\text{O}_3$  M-edge absorption,<sup>110</sup>  $\text{Co}_3\text{O}_4$  clearly exhibits a broader feature starting from 58 eV and extending above 70 eV. This is likely due to the existence of both  $\text{Co}^{2+}$  and  $\text{Co}^{3+}$  in the material.

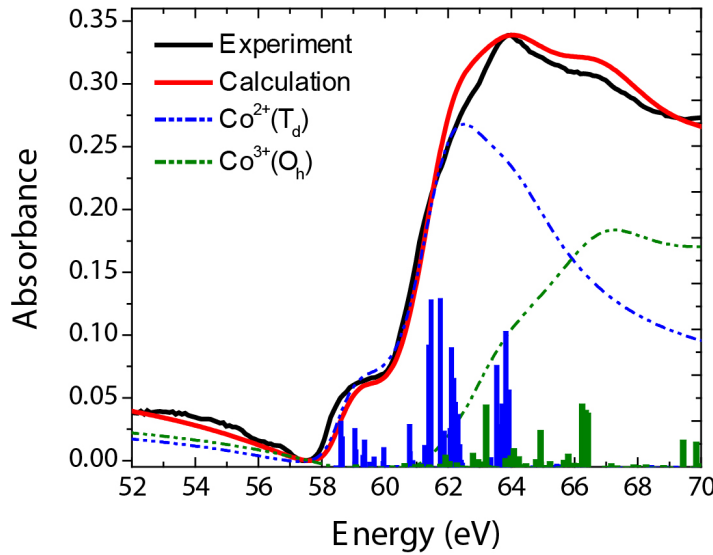


Figure 4-7: Static M-edge absorption spectrum of  $\text{Co}_3\text{O}_4$  in the extreme ultraviolet region. Black line: experimental spectrum. Red line: spectrum calculated by charge transfer multiplet model. Blue sticks and dashed line: tetrahedrally coordinated  $\text{Co}^{2+}$  absorption contribution. Green sticks and dashed line: octahedrally coordinated  $\text{Co}^{3+}$  absorption contribution. The 1:2  $\text{Co}^{2+}/\text{Co}^{3+}$  stoichiometric ratio has been accounted for.

This static absorption spectrum is fitted with the charge transfer multiplet model by using the program CTM4XAS55.<sup>112,113</sup> Calculated Co<sup>2+</sup> and Co<sup>3+</sup> absorptions correspond to  $3d^7(^4A_2) \rightarrow 3p^53d^8$  and  $3d^6(^1A_1) \rightarrow 3p^53d^7$  transitions, respectively, followed by adding up the individual absorptions of Co<sup>2+</sup> and Co<sup>3+</sup> ions with 1:2 stoichiometric ratios. When calculating the multiplet effect resulting from the d-d electrostatic interaction, Slater integrals  $F^2$ ,  $F^4$ ,  $G^1$ , and  $G^3$  are reduced to 60% of the atomic parameters empirically in order to account for the configuration-interaction effect. Based on the actual spinel crystal structure, Co<sup>2+</sup> is given tetrahedral ligand field symmetry in the calculation with a ligand field splitting energy between  $e$  and  $t_2$  orbitals, termed  $10D_q$ , equal to 0.3 eV, while Co<sup>3+</sup> ion is located in a  $10D_q = 1.8$  eV octahedral field. These ligand field parameters, as well as the charge transfer parameter used to account for the orbital mixing between metal ions and surrounding oxygen ligands, are identical to those values used to fit the L-edge absorption spectrum of Co<sub>3</sub>O<sub>4</sub> by Morales et al.<sup>114</sup> The amplitude integral of allowed transitions is then normalized to the number of *d*-electron vacancies (3 and 4 for Co<sup>2+</sup> and Co<sup>3+</sup>, respectively). To give a best match to the experimental data, the calculated stick spectra are broadened by a Lorentzian linewidth  $L_{\min}$  below a certain onset energy  $E_{\text{onset}}$  and an increasing Lorentzian linewidth  $\Gamma = L_{\min} + dL^*(E - E_{\text{onset}})$  above the onset energy. This variable Lorentzian broadening accounts for the term-dependent Auger lifetimes of core-hole excited states, which are generally shorter for higher-energy transitions due to the presence of more decay channels.<sup>115</sup> A Fano lineshape is then applied to the spectra with a Fano parameter  $q$  in order to account for the interference between the  $3p \rightarrow 3d$  transition and the direct ionization of  $3d$  electrons to the continuum. Finally, a 150 meV Gaussian instrumental broadening is applied to the individual spectra before summing up according to the stoichiometric ratio. Calculation parameters used in CTM4XAS55 and the broadening parameters for Co<sup>2+</sup> and Co<sup>3+</sup> are listed in Table 4-1. Considering the stoichiometric ratio and the number of *d*-electron vacancies, Co<sup>3+</sup> should contribute more to the M-edge oscillator strength than Co<sup>2+</sup> although it is not very obvious in Fig. 4-7. This is due to a significant amount of Co<sup>3+</sup> absorption located above the 72 eV aluminum cut-off energy, which is not detectable in the experiment setup.

Electronic Symmetry	Slater Integral <sup>a</sup>	$10D_q$ (eV)	$L_{\min}$ (eV) <sup>b</sup>	$dL^*$ <sup>b</sup>	$E_{\text{onset}}$ (eV) <sup>b</sup>	$q$
Co <sup>2+</sup> ( $T_d$ )	High spin: ${}^4A_2$	0.60	0.3	0.1	0.42	55.8
Co <sup>3+</sup> ( $O_h$ )	Low spin: ${}^1A_1$	0.60	1.9	0.1	0.42	56.3

Table 4-1: Calculation and broadening parameters used for fitting of Co<sub>3</sub>O<sub>4</sub> ground state M-edge absorption spectrum. <sup>a</sup> Ratio relative to atomic parameters. <sup>b</sup> The variable Lorentzian linewidth  $\Gamma$  is approximated by the formula  $\Gamma = L_{\min} + dL^*(E - E_{\text{onset}})$ .

According to the calculation, the pre-edge structure at 58 eV and the rising shoulder of the M-edge absorption at 61 eV are contributions from the tetrahedrally coordinated Co<sup>2+</sup> ions, while absorption of Co<sup>3+</sup> ions in octahedral sites occurs at the 64 eV peak and higher energy region. The offset between Co<sup>2+</sup> and Co<sup>3+</sup> absorptions helps interpret the transient XUV absorbance changes observed in the pump-probe experiment, and it further resolves which of the six band gap transition pathways the 400 nm pump pulse excites.

### 4.3.2 Photo-Induced XUV Absorbance Changes at Cobalt M-edge

When the thin-film  $\text{Co}_3\text{O}_4$  is pumped by  $2.33 \mu\text{J}$  energy of  $400 \text{ nm}$  light, differential absorbance changes, relative to the static spectrum, are obtained, and several of these are shown at several pump-probe temporal delays in Fig. 4-8(a). Immediately after the visible excitation, XUV absorbance has increased in the region from  $59 \text{ eV}$  to  $66 \text{ eV}$  with a main peak at  $62.4 \text{ eV}$ . Meanwhile decreasing XUV absorbance, i.e. bleaching, appears on both sides of the positive absorbance change. From the kinetic traces at various photon energies in Fig. 4-8(b), it can be seen that the amplitude of the transient signal reaches a maximum within  $50 \text{ femtoseconds}$  before starting to decay. The transient signal retains a similar spectral shape during the decay, and eventually it shows no further apparent amplitude decrease out to much longer times. Experiments with pump-probe delays up to  $200 \text{ picoseconds}$  also indicate that the transient XUV absorbance difference barely changes after the first picosecond. The transient absorption spectra are further analyzed by doing global fits with a sequential two-state model ( $A \xrightarrow{k} B$ ) with the Glotaran statistical software package.<sup>116</sup>

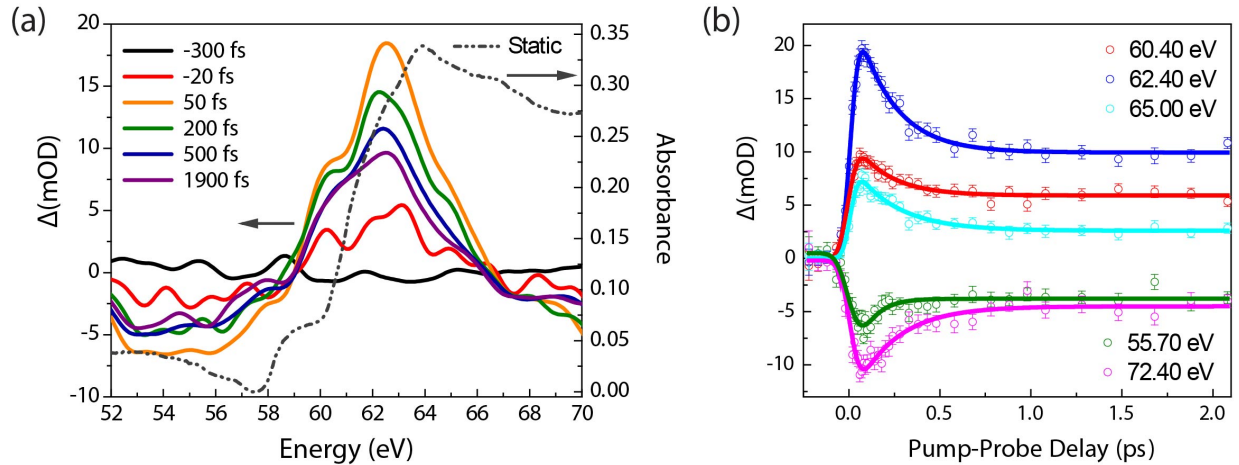


Figure 4-8: (a) Transient extreme ultraviolet (XUV) spectra near the cobalt M-edge. Optical excitation is by  $2.33 \mu\text{J}$  pump energy at  $400 \text{ nm}$  wavelength. Spectra are binned by  $0.1 \text{ eV}$  and smoothed using a  $2.0 \text{ eV}$  running boxcar average. (b) Transient absorbance traces at  $55.7$ ,  $60.4$ ,  $62.4$ ,  $65.0$ , and  $72.4 \text{ eV}$ . Points are experimental data with error bars, and solid lines are fitting results by bi-exponential decay equation with the longer decay component arbitrarily fixed as  $300 \text{ ps}$  since no apparent decay is observed after  $1 \text{ picosecond}$ .

Contour plots of the experimentally obtained data in the first two picoseconds using  $2.33 \mu\text{J}$  pump energy and the global fit results are shown in Fig. 4-9. No characteristic residual signal remains after the fitting procedure. Convolved with a  $45 \text{ fs}$  Gaussian instrumental response function, the fit gives a  $190 \pm 10 \text{ fs}$  decay time constant ( $1/k$ ) from the initial excited state to a second state at this power density. The spectra of the two time-evolved excited states are shown in Fig. 4-10, one immediately induced by the laser pulse and one after the  $190 \text{ fs}$  decay, which lasts for at least  $200 \text{ ps}$ . Both possess very similar spectral shapes: a broad positive peak centered at  $62.4 \text{ eV}$ , with shallow, however broad bleaching on either side. One major difference between the two time-evolved spectra at the two different times is that the initial excited state undergoes a  $\sim 60\%$  decrease in amplitude after transforming to the second and longer-lived state. When

normalizing the two time-evolved excited state spectra, another important experimental observation is that the positive peak in the second time-evolved state has red-shifted by  $\sim 300$  meV, which is especially apparent at the higher energy shoulder.

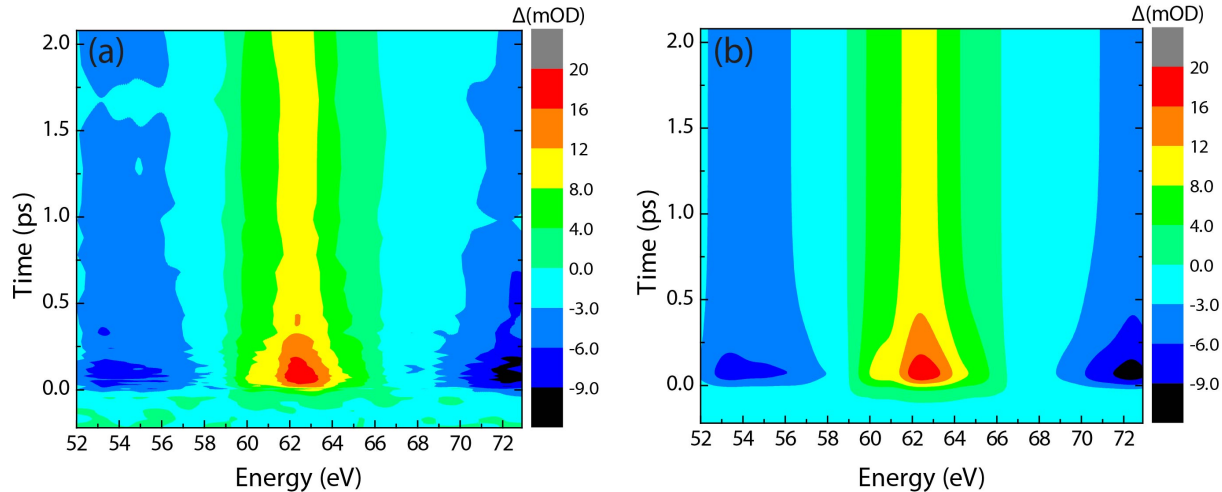


Figure 4-9: (a) Experimental contour plot in the first 2 ps after the pump beam excitation. (b) Reconstructed contour plot from global fit results using a two-component sequential model.

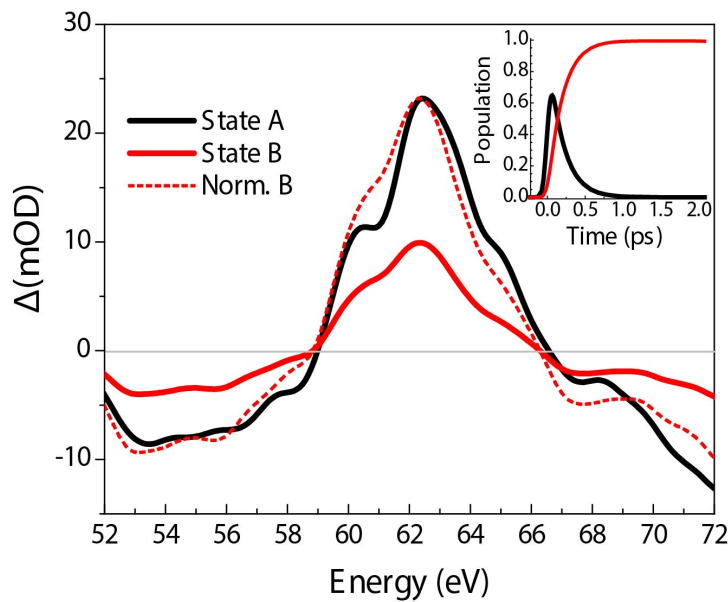


Figure 4-10: Retrieved evolutional spectra by a two-component sequential model global fit. Black solid line: the excited state A immediately after 400 nm photoexcitation. Red solid line: the long-lived state B that the initial excited state A decays into. Red dotted line: state B spectrum after being normalized to the same peak amplitude as state A. Inset: Populations of state A and B versus time. It identifies a  $190 \pm 10$  fs decay time constant ( $1/k$ ) convoluted with a 45 fs Gaussian instrumental response function.

Since the bonding character is very ionic in  $\text{Co}_3\text{O}_4$ , the electron distribution is localized and better described by orbital-like wavefunctions than delocalized energy bands.<sup>96</sup> An optical excitation can thus induce dramatic electron density redistribution at the sub-nanometer scale and changes of atomic oxidation states, which can be viewed as a charge transfer process. When comparing transient XUV spectra with the static  $\text{Co}_3\text{O}_4$  absorption spectrum (Fig. 4-8(a)), it is clear that the positive absorbance change of excited states appears on the rising M-edge, which is mainly of  $\text{Co}^{2+}$  character. This indicates that the 400 nm excitation induces the appearance of extra  $\text{Co}^{2+}$  ions, possibly by the reduction of  $\text{Co}^{3+}$  via either LMCT or MMCT pathways. This hypothesis will be tested by more sophisticated calculations with charge transfer multiplet codes (CTM4XAS55), by comparing the experimental spectrum to simulated spectra of each excitation pathway. The co-existence of two cobalt oxidation states ( $\text{Co}^{2+}$  and  $\text{Co}^{3+}$ ) and the oxygen anion in the spinel  $\text{Co}_3\text{O}_4$  leads to a total number of six excitation pathways as shown in Fig. 4-1(b). The oxidation state and electronic symmetry of cobalt ions in each of the tetrahedral and octahedral sites for these six excited states are listed in Table 4-2. LMCT processes (pathways 1 and 2) and MMCT processes (pathways 3 and 4) change both cobalt oxidation states and the electronic symmetries at one or two lattice sites, while *d-d* excitation pathways (5 and 6) only involve local electronic symmetry changes.

Excitation Pathway <sup>a</sup>	Tetrahedral Site		Octahedral Site		
	Oxidation State	Electronic Symmetry	Oxidation State	Electronic Symmetry	
LMCT	1	1+	$^3\text{T}_1$	3+	$^1\text{A}_1$
	2	2+	$^4\text{A}_2$	2+	$^2\text{E}$
MMCT	3	1+	$^3\text{T}_1$	4+	$^2\text{T}_2$
	4	3+	$^5\text{E}$	2+	$^2\text{E}$
<i>d-d</i> excitation	5	2+	$^4\text{T}_2$	3+	$^1\text{A}_1$
	6	2+	$^4\text{A}_2$	3+	$^1\text{T}_1$
Ground State		2+	$^4\text{A}_2$	3+	$^1\text{A}_1$

Table 4-2: Cobalt oxidation states and electronic symmetries at tetrahedral and octahedral lattice sites at each possible excited states. <sup>a</sup> Numbers indicating excitation pathways can be referred to Figure 4-1(b).

Because of the spin selection rule, electronic symmetries of the two *d-d* excited states are assigned to the lowest excited configurations with the same spin multiplicities on Tanabe-Sugano diagrams.<sup>117</sup> In most cases, electronic symmetries for different cobalt oxidation states can be determined by simply adding (or removing) one electron to (or from) the ground static electronic configurations. Ligand field splitting energies are assumed to be unchanged immediately after the optical excitation, thus tetrahedral sites stay as high-spin and octahedral sites remain as low-spin. For MMCT from  $\text{Co}^{2+}$  to  $\text{Co}^{3+}$  (pathway 4), however, an electron can be removed from either a filled  $\text{Co}^{2+}$  *e* orbital or a half-filled *t*<sub>2</sub> orbital and put into an empty  $\text{Co}^{3+}$  *e* orbital, and the resultant electronic symmetry at the tetrahedral site could be different. Removing an electron

from an  $e$  orbital would oxidize  $\text{Co}^{2+}$  to  $\text{Co}^{3+}$  and leave four unpaired electrons on cobalt (three in  $t_2$  orbitals and one in an  $e$  orbital), just like a typical high-spin tetrahedral  $d^6$  system with the most stable electronic configuration as  ${}^5\text{E}$ . If the electron is alternatively removed from a  $t_2$  orbital, the tetrahedral site would have a triplet  $\text{Co}^{3+}$  cation, which has only two unpaired electrons in each of the other two  $t_2$  orbitals. DFT calculation has shown that the filled minority spin  $e$  states have higher energy than majority spin  $e$  and  $t_2$  states and thus locate closer to the top of the valence band due to the spin exchange interaction.<sup>118</sup> As a result,  ${}^5\text{E}$  electronic symmetry is assigned to the tetrahedrally coordinated  $\text{Co}^{3+}$  ion after the  $\text{Co}^{2+}$ -to- $\text{Co}^{3+}$  MMCT excitation.

Once each of the six possible excited states has been assigned to a set of cobalt oxidation states and electronic symmetries at two different lattice sites, their individual  $3p \rightarrow 3d$  absorption spectra are calculated with charge transfer multiplet codes by using the CTM4XAS55 program. The ground state XUV absorption spectrum is then subtracted from each excited state spectrum in order to be compared with the transient data acquired by pump-probe experiments. The differential spectra between each excited state and ground state are shown in Fig. 4-11. Both LMCT excited states have XUV absorbance enhanced at lower energy and some bleaching at higher energy (Fig. 4-11(a)). This can be explained by the decrease of  $3p$  electron binding energy as the cobalt oxidation number is reduced during the LMCT processes. In the same manner, the  $\text{O}^{2-}(2p) \rightarrow \text{Co}^{2+}(t_2)$  LMCT state is shifted toward lower energy compared to the  $\text{O}^{2-}(2p) \rightarrow \text{Co}^{3+}(e_g)$  LMCT state. The  $\text{Co}^{3+}(t_{2g}) \rightarrow \text{Co}^{2+}(t_2)$  MMCT state has a characteristic bleaching signal at 63 eV with two enhanced absorbance regions on either side (Fig. 4-11(b)), indicating that the  $\text{Co}^{2+}(\text{T}_\text{d})$  absorption is red-shifted as it is reduced to  $\text{Co}^+$  and the  $\text{Co}^{3+}(\text{O}_\text{h})$  absorption becomes blue-shifted as it is oxidized to  $\text{Co}^{4+}$  after the MMCT excitation. As for the  $\text{Co}^{2+}(e) \rightarrow \text{Co}^{3+}(e_g)$  MMCT excited state, it can be viewed as one  $\text{Co}^{2+}$  ion exchanges its lattice symmetry with one  $\text{Co}^{3+}$  ion. Although stoichiometry between  $\text{Co}^{2+}/\text{Co}^{3+}$  remains at 1:2, the different lattice symmetry and spin configuration of the same metal cation can change its XUV absorption. Thus this MMCT to form a  $\text{Co}^{3+}$  state has enhanced absorption from 64 to 68 eV. Although the amplitudes of these calculated differential spectra are somewhat arbitrary, it is clear that both d-d excited states possess only very subtle changes with respect to the ground state. As a result, the amplitudes of differential spectra of the two d-d excited states are much lower (less than 20%) compared to those of LMCT and MMCT states (Fig. 4-11(c)). This is because the cobalt ions in these d-d excited states still retain the same oxidation number and spin multiplicity. An implication is that the XUV absorption spectroscopy technique might not be as sensitive to changes of d-electron configuration compared to changes of oxidation state and spin state.

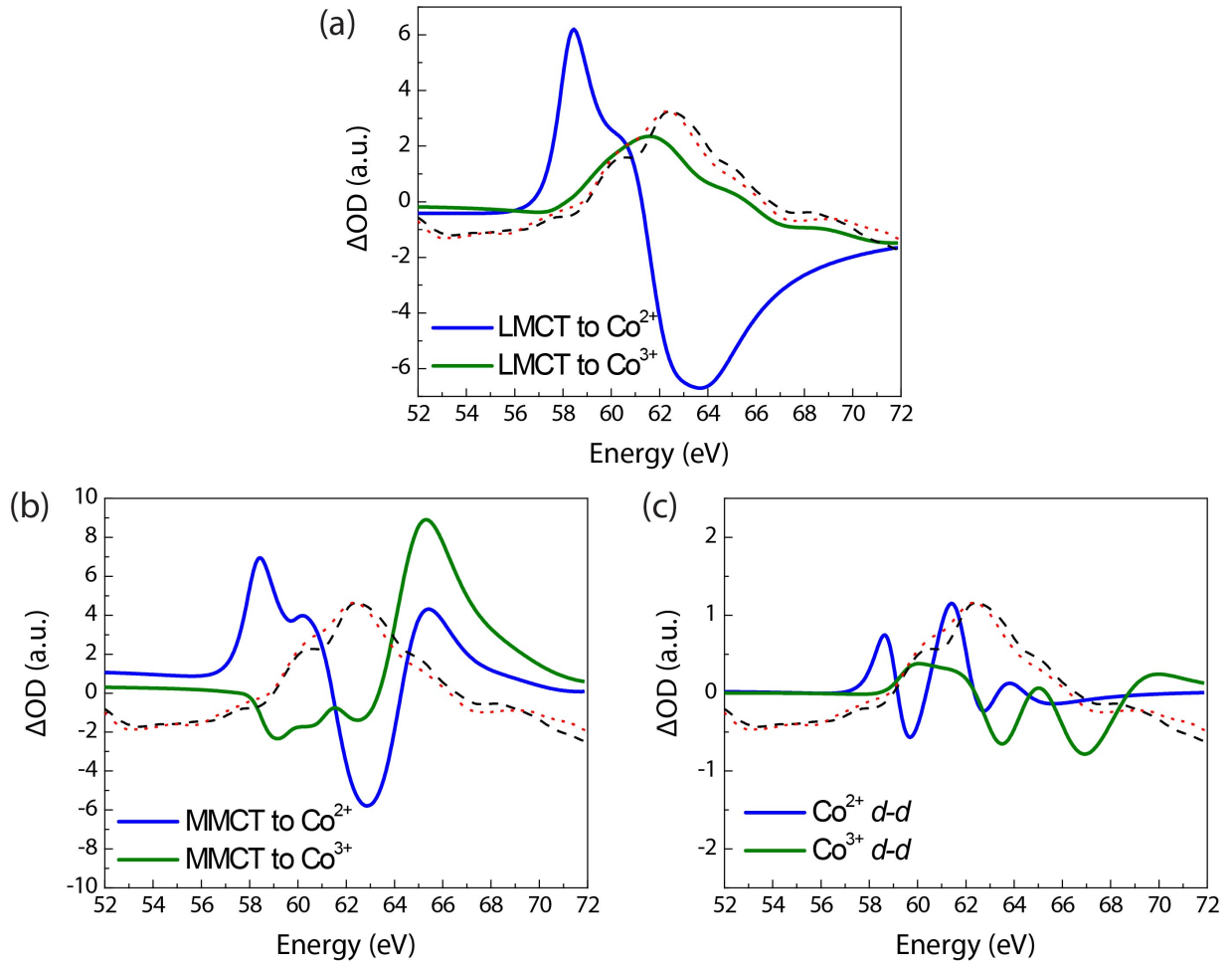


Figure 4-11: Differential XUV absorption spectra between ground state and calculated (a) LMCT excited states, (b) MMCT excited states and (c)  $d-d$  excited states. Spectra in blue lines indicate  $Co^{2+}$  in tetrahedral site receives an electron from oxygen or  $Co^{3+}$ . Spectra in green lines indicate  $Co^{3+}$  in octahedral site receives an electron from oxygen or  $Co^{2+}$ . Experimentally obtained transient spectra of the initial excited state A (black dashed line) and the long-lived state B (red dotted line) have been normalized and overlaid with calculated spectra.

Normalized spectra of the two time-evolved excited states obtained by the global fit of the experimental results are overlapped with these calculated differential spectra, and it can be seen that the  $O^{2-}(2p) \rightarrow Co^{3+}(e_g)$  LMCT state best matches the experimental spectral shape. The enhanced absorbance at 62 eV and bleaching above 66 eV are both well reproduced, although a 500 meV to 1 eV offset might exist between the calculation and experimental data. An excellent match between the calculated spectrum to experimental data is not expected here for two reasons. First, these charge transfer multiplet codes have been widely used to investigate the influence of local lattice symmetry and bonding character to XUV or X-ray absorption of transition metal based material in the ground state. In this study, although oxidation states and electronic symmetries of cobalt ions at each excited state have been carefully assigned, the XUV absorption spectra are still calculated in the same manner as treating ground state spectra. Many phenomena that exist in optically excited states, such as hot electrons and lattice structure

rearrangement, are entirely neglected in the calculation. The interaction between the core-hole and the photogenerated hole in the valence band is also not included. It is possible that once charge transfer happens, the ligand field splitting energy for the reduced/oxidized cobalt ions might have some instantaneous changes that are not considered in the current level of calculation. The second reason that the calculation does not match experimental spectra perfectly is that the calculated spectra at each lattice symmetric site are broadened by the same increasing Lorentzian linewidth formula  $\Gamma = L_{\min} + dL^*(E - E_{\text{onset}})$ , with only the onset energy  $E_{\text{onset}}$  adjusted according to the oxidation states. The fit to the experimental data can be improved if these broadening parameters can be carefully tested and adjusted for each individual excited state. In addition, the reduced absorbance from 52 to 58 eV in the transient XUV absorption spectra cannot be reproduced by the calculation. This low energy bleaching signal might correspond to a change of the non-resonant absorption contribution from the ionization of cobalt 3d valence electrons, but not the  $3p^6 3d^n \rightarrow 3p^5 3d^{n+1}$  core-level transitions.

After calculating differential absorbance spectra of all six possible excited states and comparing them to experimentally obtained results, it seems safe to conclude that 400 nm photoexcitation generates a  $O^{2-} \rightarrow Co^{3+}$  LMCT state in spinel  $Co_3O_4$ . This is in agreement with the previous assignments of the  $Co_3O_4$  band structure obtained theoretically<sup>99</sup> and experimentally,<sup>100</sup> namely that the 2.8 eV absorption peak in the  $Co_3O_4$  UV-Vis spectrum corresponds to the  $O^{2-}(2p) \rightarrow Co^{3+}(e_g)$  transition. By comparing these findings with the current understanding of the catalytic mechanism on spinel cobalt oxide, insightful explanations for the material's catalytic activities can be provided. For example, the  $Co_3O_4$  (110) plane is known to play a crucial role in catalytic oxidation of CO, as demonstrated both theoretically<sup>119,120</sup> and experimentally.<sup>89</sup> Adsorption of CO onto the (110) plane occurs preferably at exposed surface  $Co^{3+}$  cations, and the subsequent abstraction of a neighboring oxygen oxidizes CO to  $CO_2$  while leaving an oxygen vacancy and a partially reduced cobalt ion in the octahedral site. As for the photocatalytic activity for the oxygen evolution half-cell reaction (OER), the  $Co_4O_4$  cubane structures formed by oxygen anions and octahedrally coordinated  $Co^{3+}$  in spinel oxides are suggested to be the active sites for the 4-electron redox process,<sup>121</sup> due to the structural similarity between the  $Co_4O_4$  cubane and the  $CaMn_4O_x$  catalytic core in the natural photosystem II water-oxidizing complex (PSII-WOC). This work identifies that photogenerated holes in the valence band are located near oxygen atoms and might directly be involved in the OER, while electrons are near cobalt ions in octahedral lattice sites. In addition, the oxidative activity of  $Co^{3+}$  cations to be reduced to  $Co^{2+}$  could also assist the redox processes on the nearby oxygen ligands. This study firstly observed and assigned the photoexcited state of  $Co_3O_4$  by pumping the semiconductor material with 400 nm light. Preliminary results acquired by using different wavelengths between 480 and 800 nm to excited  $Co_3O_4$  will be shown in Chapter 5.

#### 4.3.3 Femtosecond Charge Carrier Dynamics in $Co_3O_4$

The two excited states shown in Fig. 4-10 have similar spectral shape; one can thus assume both states possess the same  $O^{2-}(2p) \rightarrow Co^{3+}(e_g)$  charge transfer electronic character. However the amplitude of enhanced absorption decreases by ~60% from the initial excited state to the long-lived state; also a ~300 meV energy red-shift can be observed in the long-lived state. Since the amplitude of observed transient XUV absorbance change is proportional to the product of photogenerated charge carrier density and the transition probability change induced by each excited charge carrier, the rapid 190 fs decay can be associated with a decrease of charge carrier

density near the cobalt atoms assuming the transition probability does not vary greatly. Carrier recombination can occur via both radiative and non-radiative pathways, but the timescale for carrier recombination is expected to be slower, in the nanosecond to microsecond range. Based on the sample absorbance at 400 nm ( $\sim 0.45$ ) and the 2.33  $\mu\text{J}$  pump energy focused to a 150  $\mu\text{m}$  spot size, a very high charge carrier density ( $8 \times 10^{21} \text{ cm}^{-3}$ ) is initially created in the  $\text{Co}_3\text{O}_4$  thin-film. This would be characterized as 0.15 charge carriers per cobalt atom. Coulomb forces among these charge carriers can lead to Auger relaxation by either an ionization or recombination mechanism in order to reduce the charge carrier density and repulsive interactions. A recent *ab initio* study using pseudopotential wave functions predicts that Coulomb mediated Auger processes in spatially confined semiconductors would occur on the time scale of 100 – 500 fs.<sup>122</sup> In colloidal CdSe quantum dots,  $1\text{P}_\text{e} \rightarrow 1\text{S}_\text{e}$  electron relaxation dynamics has been measured with visible transient absorption techniques, and the 100 – 300 fs relaxation is believed to occur through Auger relaxation.<sup>123,124</sup> Although charge carriers in thin-film  $\text{Co}_3\text{O}_4$  are not as spatially confined, an efficient Auger decay channel is still accessible due to the high charge carrier density.

Another possibility for the observed sub-picosecond dynamics is intersystem crossing (ISC) that commonly takes place in transition metal complexes. Although ISC has not been well studied in solid-state metal oxides, this nonadiabatic process can occur with anomalously fast rates (tens to hundreds of femtoseconds) in transition metal complexes in solution following an initial metal-to-ligand-charge-transfer (MLCT) photoexcitation,<sup>102,125,126</sup> and the resulting excited state would have a very long lifetime. For this work, it would suggest the initial  $\text{O}^{2-} \rightarrow \text{Co}^{3+}$  LMCT state undergoes sub-picosecond ISC to a local *d-d* excited state with a different spin multiplicity. However, since the spectral shape remains almost unchanged during the 190 fs decay, it is unlikely that the electronic structure around the cobalt ions has changed dramatically, as it should with ISC. It might be possible that ISC occurs faster than the instrumental response function (45 fs), and all the observed transient XUV absorbance spectra are of the *d-d* excited state character. If this is the case, then the electronic symmetry of *d-d* excited states accessible by ISC is no longer limited to the two options ( $^4\text{T}_2$  for  $\text{Co}^{2+}$  and  $^1\text{T}_1$  for  $\text{Co}^{3+}$ , respectively) listed in Table 4-2. Rather, additional electronic symmetries, such as  $^2\text{E}$  and  $^2\text{T}_1$  (low-spin) for  $\text{Co}^{2+}$ , or  $^3\text{T}_1$  (intermediate-spin) and  $^5\text{T}_2$  (high-spin) for  $\text{Co}^{3+}$ , should also be considered. More sophisticated simulation of the XUV absorption of these states is required, but initial results (Fig. 4-12) do not show that any of these local *d-d* states gives a better fit than the  $\text{O}^{2-} \rightarrow \text{Co}^{3+}$  LMCT state in Fig. 4-11(a). Although the intermediate-spin and high-spin *d-d* excited states of  $\text{Co}^{3+}$  do possess similar enhanced absorption features from 60 to 68 eV (Fig. 4-12(b)), the bleaching signal above 66 eV is not reproduced as well as the simulated  $\text{O}^{2-} \rightarrow \text{Co}^{3+}$  LMCT state. Thus the Auger relaxation is still the most likely explanation for the 190 fs rapid decay observed by the XUV probe.

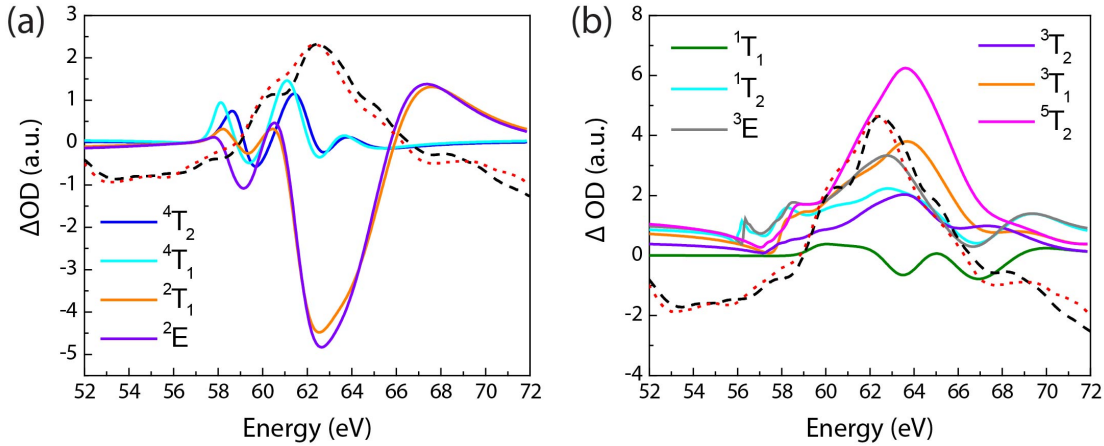


Figure 4-12: (a) The differential XUV absorption spectra between ground state  $\text{Co}^{2+}$  (high-spin,  $^4\text{A}_2$ ) and calculated  $d$ - $d$  excited states, including  $^4\text{T}_2$  (blue),  $^4\text{T}_1$  (cyan),  $^2\text{T}_1$  (orange) and  $^2\text{E}$  (purple). (b) The differential XUV absorption spectra between ground state  $\text{Co}^{3+}$  (low-spin,  $^1\text{A}_1$ ) and calculated  $d$ - $d$  excited states, including  $^1\text{T}_1$  (green),  $^1\text{T}_2$  (cyan),  $^3\text{E}$  (gray),  $^3\text{T}_2$  (purple),  $^3\text{T}_1$  (orange) and  $^5\text{T}_2$  (magenta). Experimentally obtained transient spectra of the initial excited state A (black dashed line) and long-lived state B (red dotted line) have been normalized and overlaid with calculated spectra.

Since the Auger mechanism relies on the interactions between excited charge carriers, one can thus expect the Auger decay rate would increase as more charge carriers are generated by photoexcitation. The pump fluence dependence of the initial decay dynamics is studied by varying the average pump beam energy from 0.86 to 2.70  $\mu\text{J}$  (4.87 to 15.3  $\text{mJ}/\text{cm}^2$  based on a 150  $\mu\text{m}$  diameter focus size). The kinetic traces at 62.4 eV at various pump energies are shown in Fig. 4-13(a). The amplitude of the initial maximum and the plateau at a time after one picosecond both scale with the pump power used, thus the possibility of multiphoton excitation can be excluded. However if higher pump power is used to pump the thin-film  $\text{Co}_3\text{O}_4$  sample, the global fit gives shorter amplitude decay time constants, ranging from 269 fs at 0.86  $\mu\text{J}$  to 165 fs at 2.70  $\mu\text{J}$  (Fig. 4-13(b)). The dependence of the decay rate on pump energy, or excitation density strictly speaking, suggests that the Auger relaxation mechanism is responsible for the observed initial transient signal decay.

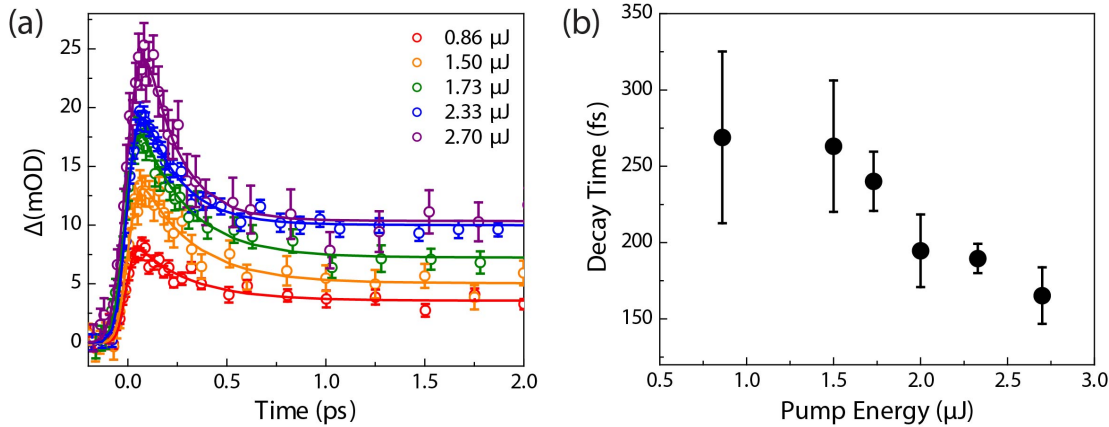


Figure 4-13: (a) Kinetics traces at 62.40 eV (maximum amplitude of the enhanced absorbance) as 400 nm pump beam energy varies from 0.86 to 2.70  $\mu\text{J}$ . (b) Decay time constants by global fit based on a two-component sequential model.

To determine whether the 300 meV spectral shifting is associated with the 150 – 300 fs amplitude decay, all the transient spectra after pump-probe temporal overlap are normalized at the maximum positive amplitude. Processed dynamic traces in Fig. 4-14 confirm that the spectral center of weight does shift to lower energy, as the enhanced XUV absorbance gains are weighted on the lower energy side and lose weight on the higher energy side. This spectral shifting, however, occurs with a  $535 \pm 33$  fs time constant when  $2.33 \mu\text{J}$  pump energy is used, which is slower than the 190 fs amplitude decay at the same pump energy. The same spectral red-shift can still be observed at all pump energies applied, although it is difficult to determine whether the time constant associated with spectral shift also changes, or not, with different pump fluences. Nevertheless, this implies that two different carrier relaxation mechanisms might be occurring within the first 2 picoseconds after 400 nm photoexcitation. While Auger relaxation is most likely responsible for the overall short-lived charge carrier density decay, the most likely explanation for the slower observed spectral changes is relaxation of hot carriers via carrier-phonon interactions.

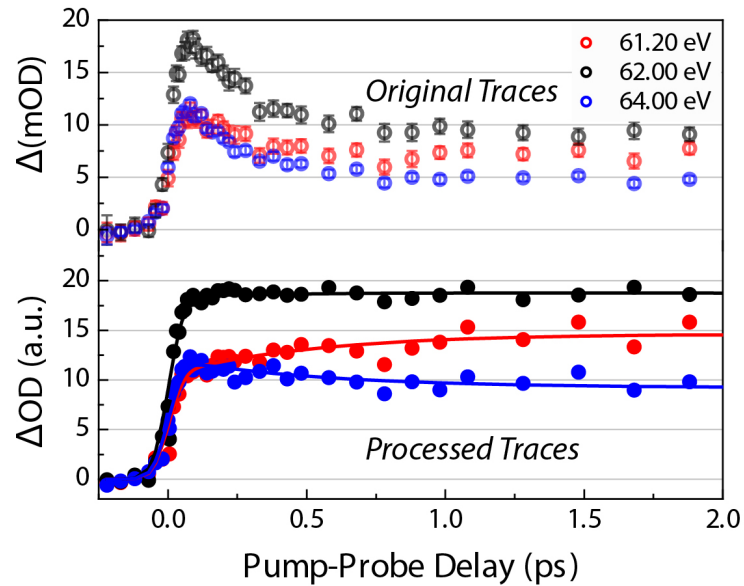


Figure 4-14: Top: Transient absorbance traces at 61.2, 62.0 and 64.0 eV at  $2.33 \mu\text{J}$  400 nm pump energy. Bottom: Processed traces after normalizing the maximum amplitude of every transient spectrum after the pump-probe temporal overlap. Solid lines are fitted by a two-component sequential model global fit with a 535 fs time constant.

The pump photon energy (400 nm, 3.05 eV) is higher than the direct band gap (1.6 eV), thus photogenerated charge carriers would be formed with a significant amount of excess kinetic energy. Instantly after excitation the system is still in a non-thermalized state: the kinetic energy distribution of carriers does not fulfill a Boltzmann distribution, and the carriers are much hotter than the lattice. Relaxation of these “hot” carriers can occur through carrier-carrier scattering or carrier-phonon interactions.<sup>127</sup> Carrier relaxation on the sub-ps timescale has been reported for CdS, another II-VI semiconductor, corresponding to Fröhlich coupling between charge carrier and longitudinal optical (LO) phonons.<sup>128</sup> The 535 fs spectral shift dynamics can thus be associated with the exchange of energy between the charge carriers and the lattice as the carriers undergo relaxation to the band edge. Four fundamental LO phonon frequencies have been

identified for spinel  $\text{Co}_3\text{O}_4$  at 219, 394, 619 and 683  $\text{cm}^{-1}$  (6.57, 11.8, 18.6 and 20.5  $\text{ps}^{-1}$ , respectively),<sup>129</sup> indicating that, during the first 500 fs, charge carriers can effectively dissipate excess energy to the lattice by fast excitation of phonons. The charge carriers being discussed here are not limited to the electrons, but can also be holes in the valence band. The  $\text{O}^{2-}(2p) \rightarrow \text{Co}^{3+}(e_g)$  charge transfer excitation creates electrons near octahedrally coordinated cobalt cations and holes on oxygens. Although the XUV probe is sensitive only to the electronic distribution around cobalt cations, hole relaxation to the top of the valence band can also be the cause of the spectral red-shift. In addition, formation of a bound electron-hole pair after hot carrier relaxation can stabilize the system and modify the XUV absorption cross section. Another possibility is that the 535 fs spectral shift of the excited state corresponds to the trapping of charge carriers on surface defect states, and the lower lattice symmetry of these surface states could affect the XUV transition energies. Nevertheless, the latter case can be ruled out because trapping at surface states requires carrier diffusion and this can happen on a timescale no faster than picoseconds.

## 4.4 Conclusions

In summary, this study utilized femtosecond XUV pulses to study the photoexcited charge transfer process in mixed-valence spinel  $\text{Co}_3\text{O}_4$ , by monitoring absorbance changes at Co M-edge following the optical excitation. Combining transient XUV spectroscopy and charge transfer multiplet calculations, the photoexcited state of thin-film  $\text{Co}_3\text{O}_4$  samples pumped by 400 nm light has been observed and assigned to the  $\text{O}^{2-}(2p) \rightarrow \text{Co}^{3+}(e_g)$  LMCT state. The few-hundred femtosecond Auger relaxation immediately after photoexcitation decreases both the charge carrier density and transient signal amplitude, and the decay rate increases as more charge carriers are generated. A 300 meV spectral red-shift is caused by hot carrier relaxation to the band edge with a  $(535 \text{ fs})^{-1}$  rate constant via carrier-phonon scatterings.



# Chapter 5

## Pump Wavelength Resolved Excited-State Dynamics in Spinel Cobalt Oxide ( $\text{Co}_3\text{O}_4$ )

In this chapter the charge carrier dynamics in thin-films of  $\text{Co}_3\text{O}_4$  are investigated with multiple pump wavelengths in the 400 – 800 nm visible light region. As an extension of Chapter 4, differences in the spectral shape and carrier relaxation times are considered. It has been found that when longer pump wavelengths are used, the transient XUV spectral profile at the Co M-edge has more weight on the higher energy side, although the same  $\text{O}^{2-}(2p) \rightarrow \text{Co}^{3+}(e_g)$  LMCT excited state is still obtained. Broadening of the transient absorption spectra in the first 50 fs is universally observed and attributed to the carrier thermalization process after photoexcitation. Moreover, an intermediate excited state with 0.85 – 2.07 ps lifetime is extracted by a global fit analysis of the transient absorbance data acquired by using longer pump wavelengths.

### 5.1 Experimental Methods

The sample preparation method used in this study is identical to what has been described in Sec. 4.2 and so are the data acquisition procedures used for transient absorption experiments. Besides 400 nm, the  $\text{Co}_3\text{O}_4$  thin-film samples are optically excited by four other wavelengths: 480, 520, 595, and 800 nm. The 800 nm pump beam is directly from the Ti:Sapphire amplifier, while the other three wavelengths are delivered by the TOPAS: in the TOPAS a signal beam at 1180 nm wavelength is produced first, which then undergoes frequency up-conversion to 595 and 480 nm via second-harmonic generation and sum-frequency generation with 800 nm, respectively; the 520 nm wavelength is produced by sum-frequency generation between 800 nm and a 1488 nm signal beam. Fig. 5-1 illustrates how each pump wavelength overlaps with the UV/visible absorption spectrum of  $\text{Co}_3\text{O}_4$ : Both the 480 and 520 nm spectrum (12 and 13 nm FWHM, respectively) lie on the low-energy side of the 2.81 eV absorption peak, which is also the electronic transition directly excited by the 400 nm wavelength (11 nm FWHM). The 800 nm pump wavelength (27 nm FWHM) excites the absorption feature near 1.64 eV, while the 595 nm wavelength (28 nm FWHM) locates between two absorption peaks. To create a similar charge carrier density in the sample, a neutral density filter wheel adjusts the pump pulse energy in the 2.0 – 5.8  $\mu\text{J}$  range based on the extinction coefficient difference at each wavelength.

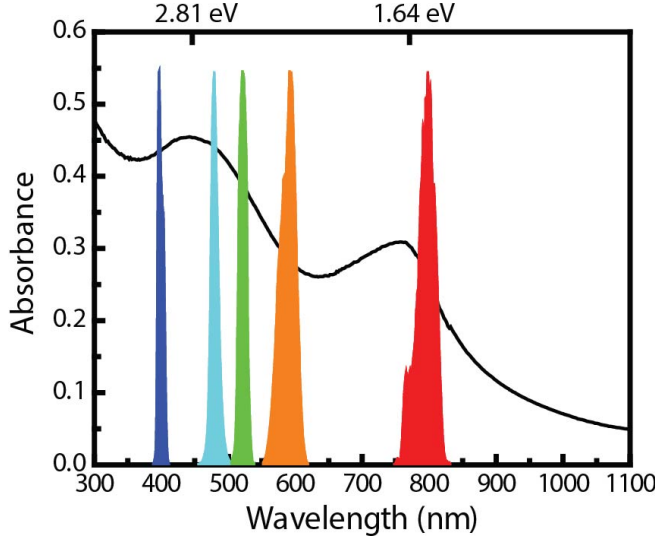


Figure 5-1: UV/visible absorption spectrum of  $\text{Co}_3\text{O}_4$  (black line) and spectral profiles of the pump beam at 400 (blue), 480 (cyan), 520 (green), 595 (orange) and 800 (red) nm wavelengths.

## 5.2 Results and Discussion

The experimentally obtained transient absorbance changes near the Co M-edge are shown in Fig. 5-2. It should be noted that the excited-state spectra are only collected up to 2.8 ps time delay at 480 and 520 nm pump wavelengths, while up to 6 ps delays are measured at the other three wavelengths. Regardless what photon energy is exciting the  $\text{Co}_3\text{O}_4$  sample, a strong enhanced absorption feature in the Co XUV spectrum from 59 to 66 eV always rises within the 40 fs instrumental response function. With careful comparison, nevertheless, a few subtle differences are found among these spectra, as will be discussed in the following sections.

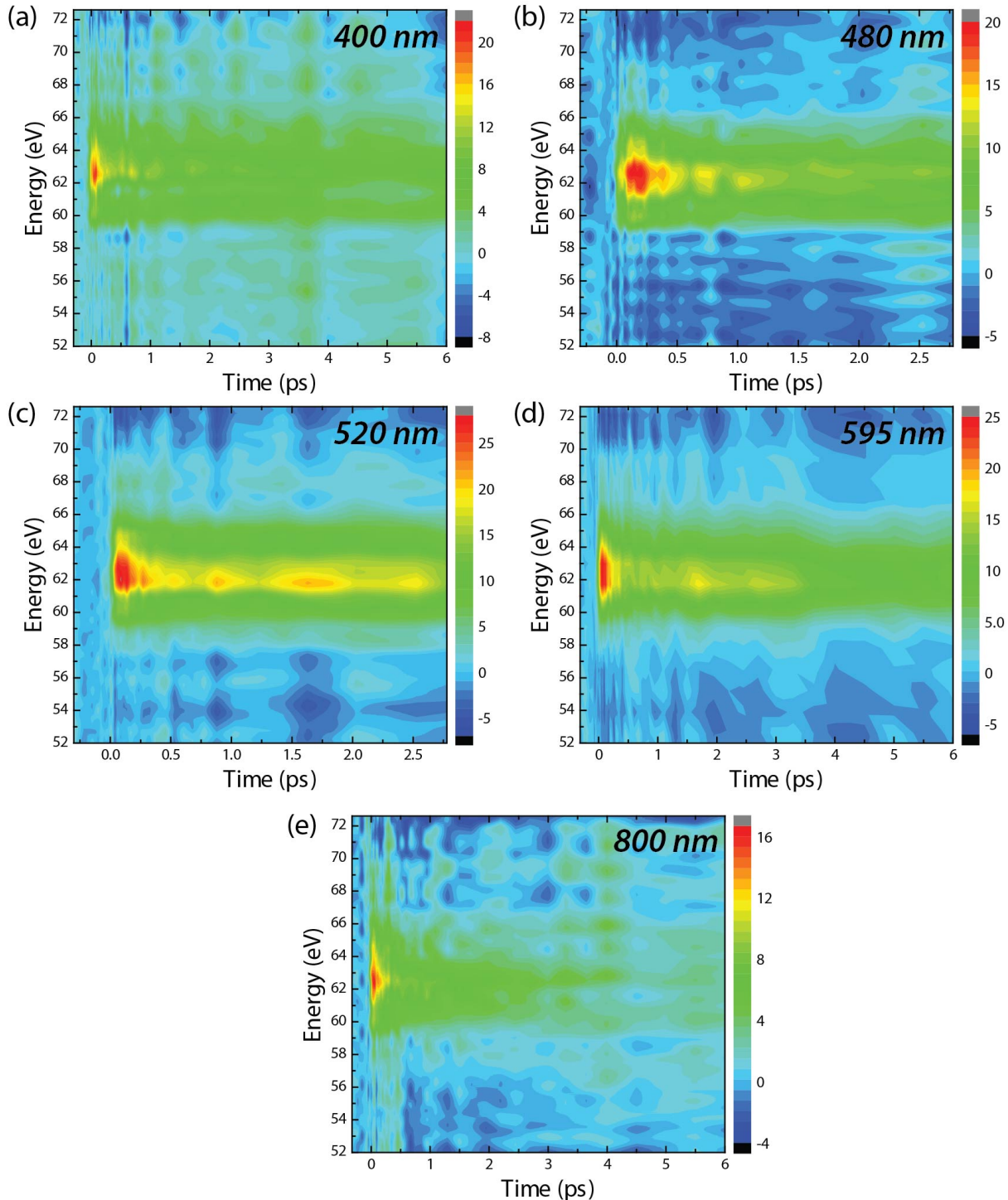


Figure 5-2: Experimental contour plots of transient absorbance signals with respect to the pump-probe time delay (x-axis) and the XUV photon energy (y-axis). Each plot corresponds to a different pump wavelength: (a) 400 nm, (b) 480 nm, (c) 520 nm, (d) 595 nm, and (e) 800 nm.

### 5.2.1 Initial Excited-State Spectra

The transient absorbance spectra acquired immediately after photo-excitation at various wavelengths are shown in Fig. 5-3. Due to the similarity of all the spectra, and based on the assignment previously made in Chapter 4, the experimental observations suggest that the same  $O^{2-}(2p) \rightarrow Co^{3+}(e_g)$  charge-transfer transition is excited in  $Co_3O_4$  at every wavelength. This finding is somewhat surprising because the UV/visible spectrum in Fig. 5-1 consists of at least two different absorption peaks, which have been assigned to distinct electronic transitions by previous studies.<sup>99,100</sup> When compared closely, it can be seen that the amplitude ratio between both sides of the main signal exhibits a systematic change with respect to the pump wavelength: With 400 nm excitation, the shoulder-like structures at 60 and 65 eV are of the same intensity, however the enhanced absorption feature at 65 eV becomes more pronounced when longer pump wavelengths are used.

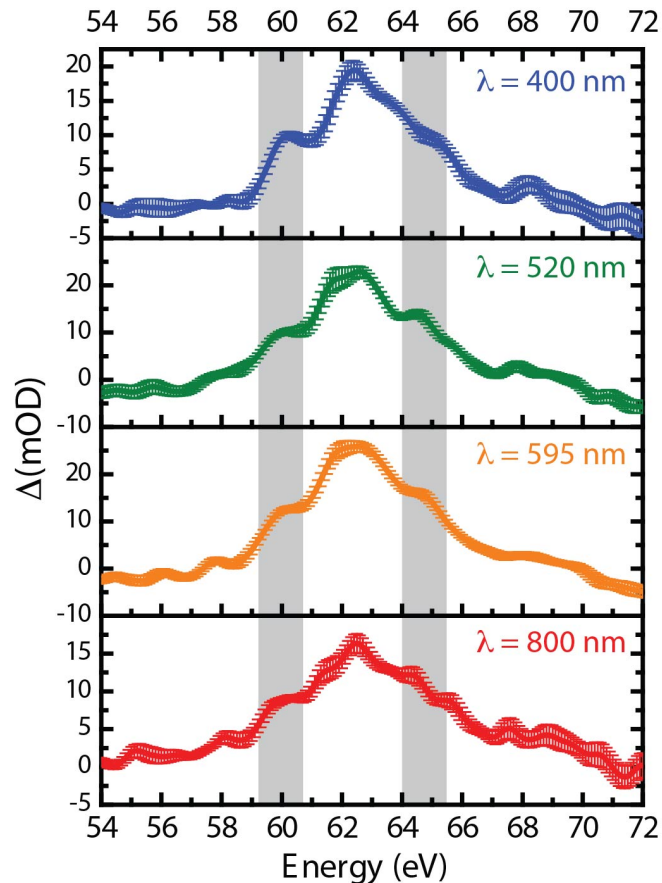


Figure 5-3: Transient absorbance spectra of the initial excited states created by optical excitations at various wavelengths.

Of the six possible optical excitation pathways listed in Table 4-2, the  $O^{2-}(2p) \rightarrow Co^{2+}(t_2)$  LMCT state is predicted to increase absorbance between 57 and 61 eV by the charge transfer multiplet calculation, while the  $Co^{2+}(e) \rightarrow Co^{3+}(e_g)$  MMCT excited state gives an enhanced absorption feature at 65 eV (Fig. 4-11(a) and (b)). Therefore two explanations are possible for

the observed spectral difference in these initial excited states: In the first scenario, the  $\text{Co}_3\text{O}_4$  band edge absorption at 1.64 eV could also be mainly of  $\text{O}^{2-}(2p) \rightarrow \text{Co}^{3+}(e_g)$  LMCT character. The higher energy levels in the conduction band, however, can possess more contribution from the  $\text{Co}^{2+} t_2$  minority spin orbitals, as has been suggested by density functional theory (DFT) calculation using the GGA + U approximation.<sup>96</sup> By utilizing pump pulses with shorter wavelengths, electrons are also excited from the oxygen  $2p$  level into the empty  $\text{Co}^{2+} 3d$  orbitals via the higher conduction band. When probing the  $\text{Co } 3p \rightarrow 3d$  core level transition, a higher amplitude at the 60 eV absorption feature is expected in the measured differential XUV absorption spectrum, because the excited electrons are shared between the  $\text{Co}^{3+}$  and  $\text{Co}^{2+}$  cations.

In the alternative explanation, it could also be that the 2.81 eV peak in the UV/visible absorption spectrum corresponds to the  $\text{O}^{2-}(2p) \rightarrow \text{Co}^{3+}(e_g)$  LMCT excitation, and the top of the valence band has more contribution from the  $\text{Co}^{2+} e$  orbital via hybridization between  $\text{Co}^{2+}$  and O. Therefore when the pump wavelength is varied from 400 nm to longer wavelength, the electronic transition starts to mix in some  $\text{Co}^{2+}(e) \rightarrow \text{Co}^{3+}(e_g)$  MMCT character, which can explain the higher enhanced absorption amplitude at 65 eV. Considering both mechanisms, the almost identical transient XUV absorption spectra at every pump wavelength indicates the existence of significant orbital hybridizations in both the valence and conduction bands, such that the optical excitation exhibits a slowly and smoothly varying interchange between the six possible excitation pathways, rather than an abrupt transition when different absorption peaks are excited.

### 5.2.2 Effect of Carrier Thermalization

Regardless of the wavelength used to excite the  $\text{Co}_3\text{O}_4$  sample, a fast spectral broadening can be observed in the first 50 fs, as shown in Fig. 5-4. The initial response at the Co M-edge always exhibits several distinguishable peaks, however after 50 fs these peaks have broadened and merged into a single peak with shoulder-like structures. Since the duration of the pump pulses ranges from 40 to 60 fs in this study, the details of this dynamic cannot be completely resolved with the current temporal resolution. Nevertheless, this extremely fast linewidth modification of the core level absorption could be an indication of a carrier thermalization process: The energy distribution in an ensemble of electrons and holes does not follow Fermi-Dirac statistics immediately after photoexcitation, however a quasi-equilibrium state can be achieved by energy exchange between carriers through scattering events, which can be complete in less than 100 fs.

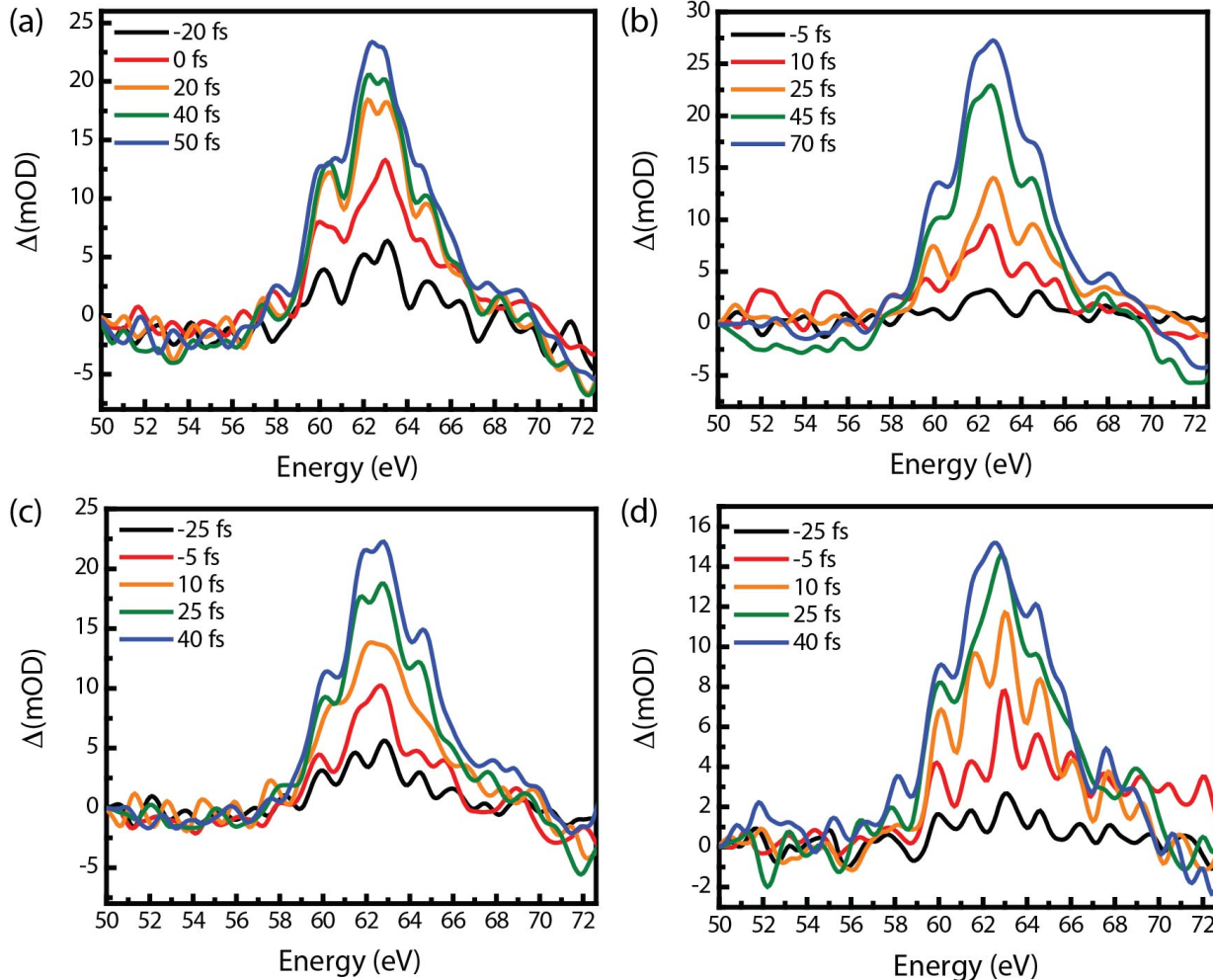


Figure 5-4: Transient absorbance changes at early pump-probe delays using (a) 400 nm, (b) 520 nm, (c) 595 nm, and (d) 800 nm as the pump wavelength.

### 5.2.3 Difference in Excited-State Dynamics

A major difference found in this wavelength-resolved study is the decay behavior of the initially created excited state. As stated in Chapter 4, with 400 nm excitation the initial excited state undergoes a  $190 \pm 10$  fs decay to  $\sim 40\%$  of the maximum amplitude then stays unchanged over the next 2 ps.<sup>130</sup> At 400 nm excitation, a complementary study has found the long-lived excited state decays back to the ground state with a  $1.9 \pm 0.3$  ns time scale.<sup>73</sup> At longer pump wavelengths, however, the decay of this long-lived state becomes faster, which is also apparent in Fig. 5-2. When the  $\text{Co}_3\text{O}_4$  sample is pumped by 800 nm, it can be clearly seen that the decay is almost complete at 6 ps after the initial excitation. The difference of the decay behavior can be better visualized by comparing the energy lineouts at 62.4 eV, as shown in Fig. 5-5. The amplitude decay starts to level off after 500 fs at 400 nm pump wavelength, but continues decaying if 800 nm pump beam is used. At 595 nm pump wavelength, the lineout exhibits an increasing amplitude from 0.5 to 2 ps then starts to decay again.

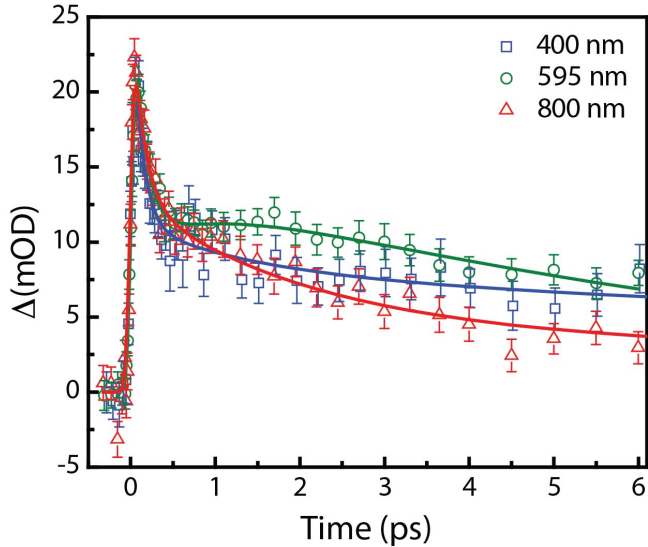


Figure 5-5: Comparison of transient absorbance traces at 62.4 eV using three different pump wavelengths.

A global fit analysis<sup>116</sup> is used to model and reproduce the transient absorbance contour plots in Fig. 5-2, and the retrieved time constants (assuming a sequential kinetic model) are summarized in Table 5-1. Essentially at every pump wavelength the initial excited state undergoes an amplitude decay that is faster than 200 fs, and a long-lived state can be found with a lifetime longer than 10 ps. At pump wavelengths longer than 520 nm, however, it becomes necessary to add an intermediate state into the kinetic model in order to obtain a good fitting result. It is also this intermediate excited state, which has a lifetime ranging from 0.85 to 2.07 ps, that accounts for the faster observed decay when longer pump wavelengths are used.

Pump Wavelength (nm)	Number of Components	$\tau_1$	$\tau_2$	$\tau_3^a$
400	2	$128 \pm 20$ fs	--	$> 19$ ps
480 <sup>b</sup>	2	$362 \pm 90$ fs	--	$> 50$ ps
520 <sup>b</sup>	3	$130 \pm 31$ fs	$1.77 \pm 1.23$ ps	$> 4$ ps
595	3	$147 \pm 29$ fs	$0.85 \pm 0.12$ ps	$8.15 \pm 0.47$ ps
800	3	$139 \pm 23$ fs	$2.07 \pm 0.25$ ps	$> 24$ ps

Table 5-1: Result of the global fit analysis for the transient absorption traces acquired with 400, 595, and 800 nm pump wavelengths. <sup>a</sup> Since the longest pump-probe time delay is usually much shorter than the fitting results, the values are only set as the lower limit of the lifetime. <sup>b</sup> Only up to 2.8 ps pump-probe time delay have been measured.

Fig. 5-6 shows the spectral evolution for a sequential three-component kinetic model for 520, 595, and 800 nm pump wavelengths. The intensity ratio between the initial and intermediate excited states stays close to 0.4, similar to the value obtained at 400 nm pump wavelength using a two-component sequential model. At 520 and 595 nm pump wavelengths, nevertheless, a third spectral component retrieved by the global fit has higher intensity than the intermediate excited

state (Fig. 5-6(a) and (b)). These fitting results correlate well with the energy lineouts shown in Fig. 5-5, apart from the fact that when the 595 nm pump wavelength is used, an increasing spectral intensity at 62.4 eV is observed after 500 fs.

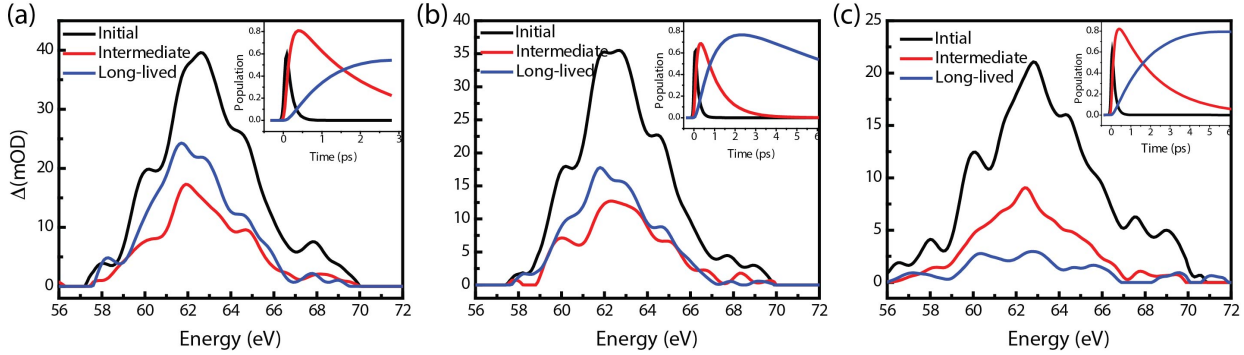


Figure 5-6: Retrieved spectra evolution assuming a sequential three-component model global fit at (a) 520 nm, (b) 595 nm, and (c) 800 nm pump wavelengths. The black lines are the initial excited states created by the pump pulses. The red lines are the intermediate state, and the blue lines are the spectra of the long-lived components. Insets: population evolution curves for the three spectral components.

### 5.3 Conclusions

It has been demonstrated that when thin-film  $\text{Co}_3\text{O}_4$  is photo-excited by visible wavelengths between 400 and 800 nm, a similar enhanced absorbance feature from 59 to 66 eV is obtained by transient XUV absorption spectroscopy. The results indicate that the excited states have the same  $\text{O}^{2-}(2p) \rightarrow \text{Co}^{3+}(e_g)$  LMCT character. This deviates from the previous hypothesis that the 1.64 and 2.81 eV peaks in the UV/visible absorption spectrum of  $\text{Co}_3\text{O}_4$  correspond to two distinct electronic transitions. The enhanced absorption feature at 65 eV does gain intensity when longer pump wavelengths are used, suggesting possible hybridization in both the valence and conduction bands. It is either that the top of the valence band consists of more  $\text{Co}^{2+} e$  orbital character, or higher unoccupied levels in the conduction band are more distributed between  $\text{Co}^{3+}$  to  $\text{Co}^{2+}$  cations. The transient XUV absorbance spectra exhibit very fast broadening that is completed in 50 fs, which could be an indicator of carrier thermalization dynamics. Lastly, an intermediate excited state can be found by global fitting if the pump wavelength is longer than 520 nm.

# Chapter 6

## Observing Photo-Induced Electron Transfer Dynamics in a Type II Si/TiO<sub>2</sub> Heterojunction

The electron transfer process in a type II Si/TiO<sub>2</sub> heterojunction is studied by means of transient XUV absorbance spectroscopy. The TiO<sub>2</sub> film is prepared with a large number of oxygen vacancies by not fully oxidizing the deposited Ti film. This works as a *n*-type semiconductor and forms a *p-n* junction with the *p*-type Si(100) substrate. Optical excitation using 520 nm wavelength initially creates excited carriers in the Si, and electron transfer across the *p-n* junction to the TiO<sub>2</sub> conduction band is monitored at the Ti  $3p \rightarrow 3d$  absorption edge at 32 – 50 eV. In preliminary results, an XUV absorption depletion near the conduction band edge indicates a possible electron transfer from Si to TiO<sub>2</sub>, which occurs in a  $254 \pm 95$  fs time scale. In addition, an enhanced absorption feature at  $\sim 1 - 2$  eV below the conduction band edge appears instantaneously with the visible light excitation, which is attributed to a photodepletion of the oxygen defect states in TiO<sub>2</sub>. Photoelectron emission spectra are also measured on similar Ti films that are evaporated at various background oxygen pressures, and a mid-gap state  $\sim 1$  eV below the Fermi level is found on non-fully oxidized Ti films. This study utilizes the advantageous element specificity of the core level transition, and applies the method of transient XUV absorbance spectroscopy to a semiconductor heterostructure.

### 6.1 Introduction

In semiconductor materials, the energetically forbidden region between the highest occupied band (“valence band”) and the lowest empty band (“conduction band”) can be overcome by the energy of a visible photon, and thus band-to-band excitations can be achieved via optical absorption. It is this ability to interact with light that makes semiconductors of tremendous interest in both fundamental research and device applications. The earth-abundant first-row transition metal oxides (TMOs) have become promising candidates for solar energy conversion, such as for photoelectrodes and photocatalysts.<sup>13,80,131–133</sup> Titanium dioxide (TiO<sub>2</sub>) not only exhibits excellent electric conductivity and photoactivity, it also possesses excellent chemical and mechanical stabilities. Various photocatalytic applications of TiO<sub>2</sub> including water splitting and degradation of hazardous organic pollutants<sup>134–136</sup> have been extensively investigated over the past few decades. However, the large intrinsic band gap of TiO<sub>2</sub> (3.2 and 3.0 eV for the anatase and rutile phases, respectively) only matches UV wavelengths, which accounts for less than 5% of the solar spectrum, for effectively generating photoexcited charge carriers. Advances in the synthesis of complex TiO<sub>2</sub>-based nanomaterials allow the optical band

gap and photoactivity to be tailored, by either adding dopants,<sup>83,137,138</sup> forming ternary oxides,<sup>139</sup> or controlling the oxidation state and crystal phase.<sup>79,140</sup> In addition, photoelectrochemical performance can be enhanced by coupling TiO<sub>2</sub> to another semiconductor with a narrower band gap, assuming the charge carriers generated in the narrow band gap material by visible light absorption can effectively migrate to TiO<sub>2</sub>. This assisted charge carrier harvesting in TiO<sub>2</sub> has been demonstrated by incorporating *p*-type silicon,<sup>141–143</sup> spinel cobalt oxide (Co<sub>3</sub>O<sub>4</sub>),<sup>144</sup> and CdSe quantum dots.<sup>145</sup> In this chapter, the electron transfer dynamics in a type II heterojunction system formed by *p*-Si and *n*-TiO<sub>2</sub> is directly probed by transient XUV absorption spectroscopy, which is capable of providing element-specific information on the charge carrier distribution. The *p*-Si part is selectively excited with 520 nm light, and the rate of electron transfer from silicon to the TiO<sub>2</sub> conduction band is measured by probing the depletion of the Ti 3p-to-3d core level absorption.

### 6.1.1 Semiconductor Doping

Two most common and well-studied crystal phases of TiO<sub>2</sub> are rutile (space group: *P4<sub>2</sub>/mnm*) and anatase (space group: *I4<sub>1</sub>/amd*), respectively.<sup>146</sup> In both phases the Ti<sup>4+</sup> cations are 6-fold coordinated and located in lattice sites with the D<sub>4h</sub> symmetry. One major difference between the two phases is the distortion inside the [TiO<sub>6</sub>] octahedron: the average distance between Ti<sup>4+</sup> cations is slightly larger in rutile, which therefore makes rutile the more thermodynamically stable phase. The anatase phase is dynamically stable, i.e. it does not transform to rutile unless heated above 700 °C, and it is often obtained when the synthesized TiO<sub>2</sub> material is of nanoscale size in at least one dimension. Given the *d*<sup>0</sup>-configuration of the Ti<sup>4+</sup> cations, the calculated band structure of TiO<sub>2</sub> predicts it to be a charge-transfer semiconductor, i.e. the valence band mainly consists of the O 2p levels, while the conduction band minimum is dominated by the Ti 3d states.<sup>147</sup>

Carrier concentration in a semiconductor can be increased and controlled by addition of donor or acceptor dopants in the case of *n*-type and *p*-type semiconductors, respectively. As illustrated in Fig. 6-1, the extra charge carriers are introduced by the dopant energy levels in the originally forbidden band gap; the presence of acceptor or donor levels allows more carriers to be easily excited via thermal energy fluctuations. The electrical resistivity  $\rho$  of a doped semiconductor is given as

$$\rho = \frac{1}{\sigma} = \frac{1}{en\mu} \quad (6.1)$$

where  $\sigma$  is the conductivity,  $e$  is the charge of an electron,  $n$  is the majority carrier concentration, and  $\mu$  is the carrier mobility that is proportional to the average carrier scattering time  $\bar{\tau}$ :

$$\mu \approx \frac{e}{m^*} \bar{\tau} \quad (6.2)$$

where  $m^*$  is the effective mass of charge carrier (electron or hole). Adding a dopant not only increases the carrier concentration, but meanwhile also raises the scattering probability of the carriers with the dopant sites; therefore the resistivity is determined by both the dopant element and the doping concentration. For example, the Si(100) substrates used in this study are *p*-type doped by boron atoms and have 10 – 20 Ohm-cm resistivity, which is equivalent to  $7.0 \times 10^{14}$  –  $1.3 \times 10^{15}$  cm<sup>-3</sup> doping concentration.

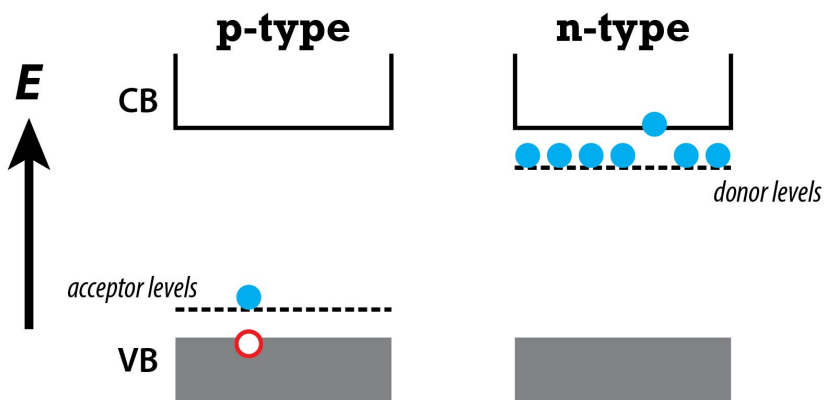


Figure 6-1: Dopant in a semiconductor alters charge carrier concentration by introducing new energy levels in the band gap. (left) Empty acceptor levels close to the valence band maximum increase hole concentration in a *p*-type semiconductor. (right) In a *n*-type semiconductor, donor levels right below the conduction band minimum contribute extra electrons that can be thermally excited to the conduction band.

Even without any doping,  $\text{TiO}_2$  is usually categorized as a *n*-type semiconductor because of the intrinsic defects existing in the lattice. This “*self-doping*” effect of  $\text{TiO}_2$  results from two types of stoichiometric imbalance: oxygen vacancies  $V_O$  and titanium interstitials  $Ti_{int}$ . As shown in Fig. 6-2, the three Ti ions that were supposed to form bonding with the oxygen in the vacant site are undercoordinated and partially reduced. Computational studies<sup>148–150</sup> have suggested that the two extra electrons associated with  $V_O$  are partially localized on one or more vacancy-neighboring Ti sites and may delocalize further to the nearest 6-fold coordinated Ti cations. The electrical resistivity of  $\text{TiO}_2$  sensitively decreases in response to increasing numbers of oxygen vacancies, which makes  $\text{TiO}_2$  an useful candidate as an oxygen sensor.<sup>151</sup>

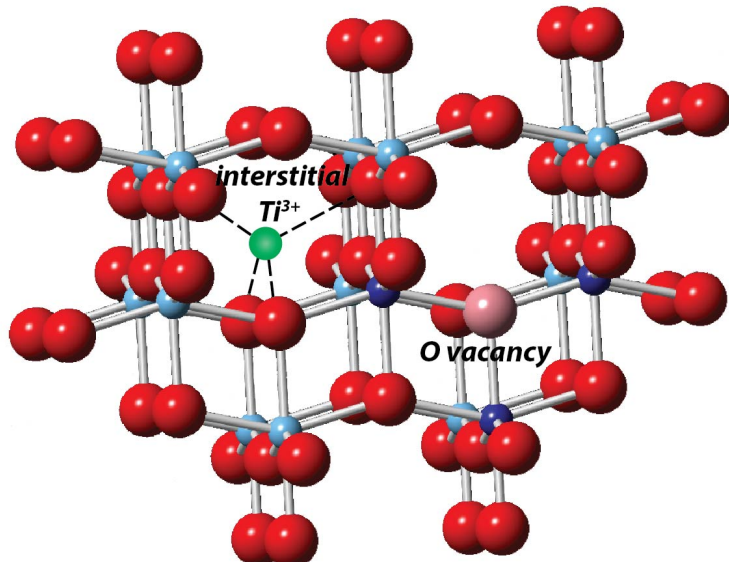


Figure 6-2: In an anatase  $\text{TiO}_2$  crystal, each  $\text{Ti}^{4+}$  ion (blue) is 6-fold coordinated while each  $\text{O}^{2-}$  ion (red) is 3-fold coordinated. An oxygen vacancy (pink) would make the three surrounding Ti ions (dark blue) partially reduced. In addition, extra  $\text{Ti}^{3+}$  ions can diffuse into interstitial sites.

It has also been discovered that when  $\text{TiO}_2$  is annealed at a high temperature,  $\text{Ti}^{4+}$  ions on the surface layer are reduced and may diffuse into the bulk,<sup>152</sup> occupying the interstitial sites of the lattice; the oxidation state of these  $\text{Ti}_{int}$  species varies from 0 to +4, so that they may act as shallow electron donors. The presence of reduced  $\text{Ti}^{3+}$  ions in bulk  $\text{TiO}_2$ , due to either  $V_O$  or  $\text{Ti}_{int}$ , has been confirmed by electron paramagnetic resonance (EPR) experiments<sup>153</sup> and the binding energy shift on the Ti 3p core level.<sup>154</sup> In terms of the UV/Vis absorption spectrum,  $\text{TiO}_2$  that is prepared with intrinsic defects exhibits non-zero absorption below the 3.0 – 3.2 eV band gap.<sup>155</sup> Theoretical studies have found new mid-gap states that are associated with the  $V_O$  and  $\text{Ti}_{int}$  defects with energy distributions ranging from 0.3 – 1.5 eV below the conduction band minimum;<sup>148,149</sup> The new absorption can either be a localized Ti  $d$ - $d$  excitation or an optical transition from a localized defect state to the delocalized conduction band.

The  $\text{TiO}_2$  thin-films that are investigated in this work are prepared by titanium metal evaporation under a background oxygen pressure, where oxygen vacancies can be created by purposely reducing the  $\text{O}_2$  pressure. Valence electron photoemission spectroscopy are used to characterize the defect states in  $\text{TiO}_2$ , and a mid-gap state about 1.0 eV below the Fermi energy is observed if the  $\text{TiO}_2$  is not fully oxidized.

### 6.1.2 Heterojunction

A semiconductor heterojunction is formed at the interface of two crystalline semiconductors that have unequal band gaps. Depending on the alignment of the valence bands and conduction bands of two semiconductors, a heterojunction can be categorized into three classes (Fig. 6-3): (1) Type I heterojunction is defined for as a straddling gap, for which the wider band gap material has its conduction band higher and its valence band lower than that of the narrower band gap material; (2) Type II heterojunction has staggered band gaps, i.e. both the conduction and valence bands of one material are higher in energy compared to their analogues in the other material; (3) If the valence band maximum of one material is energetically higher than the conduction band minimum of the other material, it is defined as a type III heterojunction.

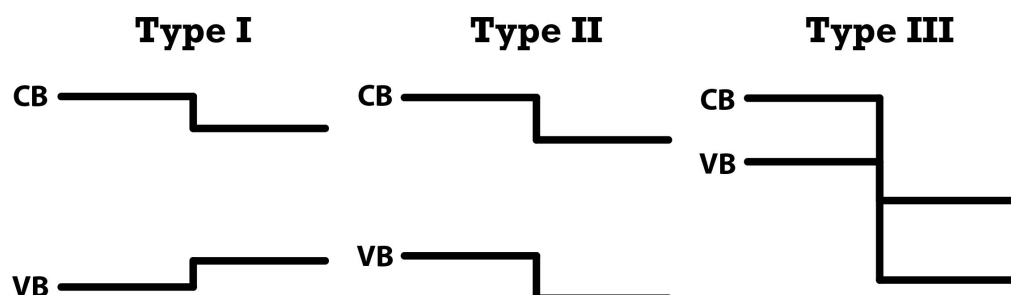


Figure 6-3: Energy band alignments for each type of semiconductor heterojunction.

When a  $p$ -type semiconductor is brought in direct contact with a  $n$ -type semiconductor, as in this study where the  $p$ -Si is covered by a layer of  $n$ - $\text{TiO}_2$ , charge carriers near the  $p$ - $n$  junction would move around to establish a new thermodynamic equilibrium. As denoted in Fig. 6-4(a), the energy bands of two materials are aligned with respect to the same vacuum level, i.e. the

energy of the conduction band minimum  $E_c$  is determined by the electron affinity  $\chi$ ; therefore the conduction band offset  $\Delta E_c$  can be written as:

$$\Delta E_c = E_{c2} - E_{c1} = \chi_1 - \chi_2 \quad (6.3)$$

While the valence band offset is given by

$$\Delta E_v = (-\chi_2 - E_{g2}) - (-\chi_1 - E_{g1}) = \Delta E_c - \Delta E_g \quad (6.4)$$

And the built-in voltage  $V_{bi}$  is defined by the difference of the Fermi levels of the *p*-type and the *n*-type semiconductors.

$$eV_{bi} = E_{F,2} - E_{F,1} = \Delta E_c + k_B T \ln \frac{n_{e,2} N_{c,1}}{n_{e,1} N_{c,2}} \quad (6.5)$$

where  $n_e$  is the electron concentration, and  $N_c$  is the effective density of states in the conduction band.

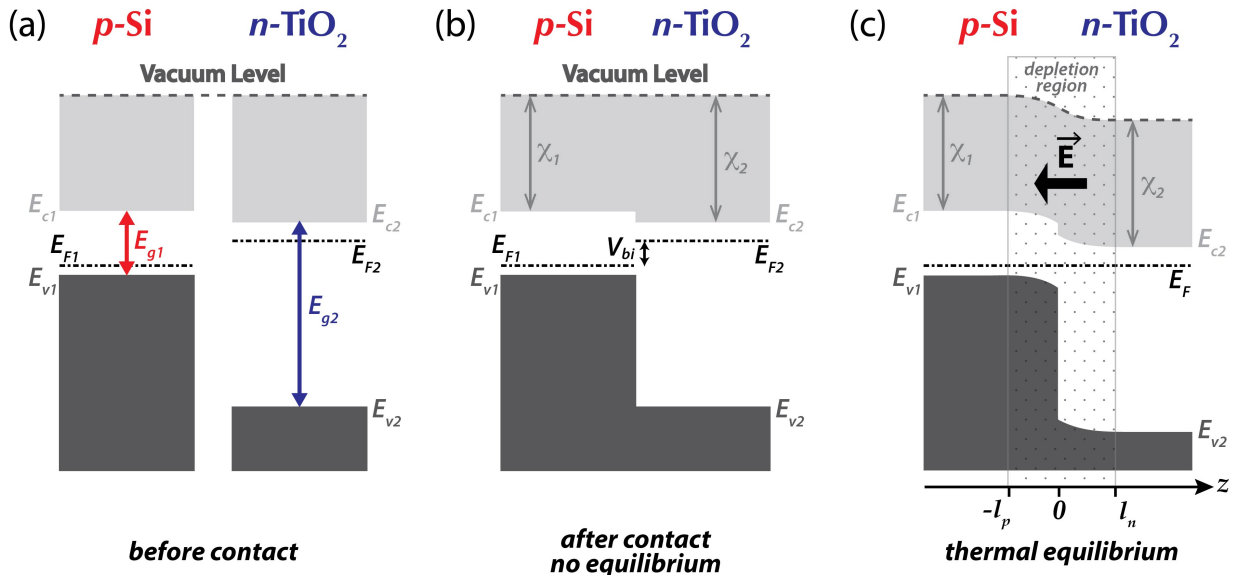


Figure 6-4: Band diagram of the *p*-Si/*n*-TiO<sub>2</sub> heterojunction. (a) Each semiconductor has a characteristic Fermi energy  $E_F$  and a band gap  $E_g$  separating the conduction band minimum  $E_c$  and the valence band maximum  $E_v$ . (b) Energy bands of two semiconductors are aligned with respect to the same vacuum level, which has energy  $\chi$  above  $E_c$ . Note that the charge carriers are not at a thermal equilibrium yet. (c) Charge carrier diffusion causes the band bending and the depletion region near the *p*-*n* junction. An electric field is also induced by the charged regions near the interface.

The band alignment of *p*-Si/*n*-TiO<sub>2</sub> forms a type II heterojunction, however the Fermi energy still exhibits discontinuity at the interface, indicating the thermodynamic equilibrium of charge carriers has yet to be achieved. Electrons would diffuse from the *n*-side, where the electron concentration is high, into the *p*-side of the junction; similarly, holes would diffuse from the *p*-side into the *n*-side. As both types of charge carriers diffuse in opposite directions, net negative and positive charge densities are built up in the *p*-side and *n*-side, respectively, and the

resulting electric field slows the carrier diffusion. At thermal equilibrium, the carrier drift caused by the electric field in the charged regions exactly cancels out the carrier diffusion components, and the Fermi level is constant throughout the system. A depletion region is formed near the *p-n* junction, where the charge carrier density is much lower than that in the bulk semiconductors. The “bending” of valence and conduction bands in the depletion region can be obtained via solving Poisson’s equation:

$$\frac{d^2\phi(z)}{dz^2} = -\frac{e}{\epsilon_s} [n_h(z) - n_e(z) + N_D - N_A] \quad (6.6)$$

where  $z$  is the direction perpendicular to the *p-n* junction,  $\epsilon_s$  is the electric permittivity,  $N_D$  and  $N_A$  are the doping concentrations of donor and acceptor, respectively. It should be noted that in Eq. (6.6) the carrier concentrations  $n_h(z)$  and  $n_e(z)$  also have dependences on the potential ( $\phi(z)$ ). Under the depletion approximation, which states that the electric field only exists in the depletion region ( $-l_p \leq z \leq l_n$ ) and the free carrier charge can be ignored in the depletion region, solving Eq. (6.6) gives the modified conduction band edge energies as:

$$\phi(z) = \begin{cases} -\frac{eN_D}{2\epsilon_s}(z - l_n)^2 + E_{c2} & \text{for } 0 \leq z \leq l_n \\ \frac{eN_A}{2\epsilon_s}(z + l_p)^2 + E_{c1} & \text{for } -l_p \leq z \leq 0 \end{cases} \quad (6.7)$$

In a similar manner, the parabolic-like bending in the valence band maximum can also be described by solving Eq. (6.6). The width of the depletion region in both semiconductors is given as:

$$l_p = \sqrt{\frac{2\epsilon_s N_D V_{bi}}{e^2 N_A (N_A + N_D)}} \quad (6.8)$$

$$l_n = \sqrt{\frac{2\epsilon_s N_A V_{bi}}{e^2 N_D (N_A + N_D)}} \quad (6.9)$$

The result therefore depends on the relative doping concentrations between donor and acceptor, and the depletion region might exhibit asymmetric depths from the *p-n* junction into both semiconductors.

## 6.2 Experimental Methods

### 6.2.1 Sample Preparation and Characterization

For the transient XUV absorption studies, TiO<sub>2</sub> thin-films are prepared on 200 nm thick, 3 × 3 mm<sup>2</sup> single crystal (100) silicon membranes that are supported on 500 μm thick, 7.5 × 7.5 mm<sup>2</sup> silicon frames (SQ7300D, Norcada). All the sample preparation procedures are carried out in an ultra-high vacuum chamber with a base pressure lower than 2 × 10<sup>-10</sup> Torr (2.7 × 10<sup>-8</sup> Pascal). A tungsten filament first heats up each Si membrane above 360 °C for 5 minutes in

order to desorb water molecules from the surface, then an Ar sputter gun is used to remove the surface oxide layer that is formed via silicon oxidation under atmosphere (Fig. 6-5). During the sputtering process, the surface of the Si membrane is bombarded by about  $2 \mu\text{A}$  of  $\text{Ar}^+$  ions at a kinetic energy of 300 eV for one hour.

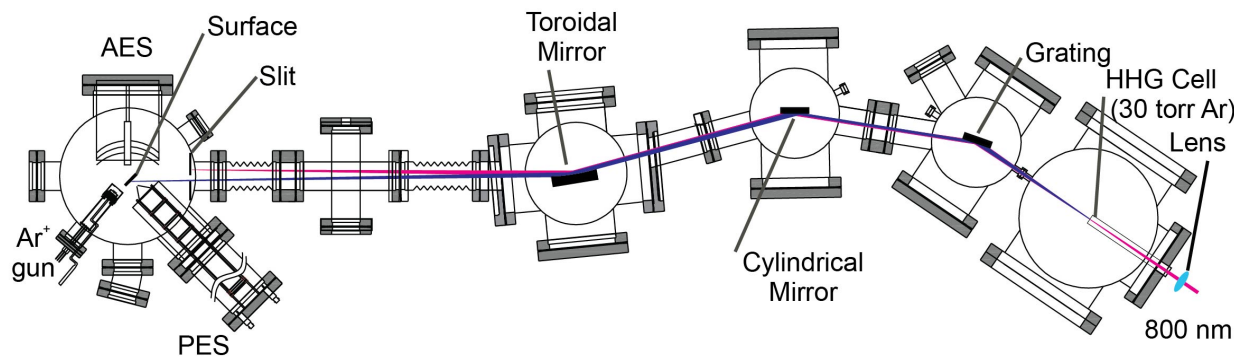


Figure 6-5: Schematic of the experimental setup used for sample preparation and characterization. The chamber on the left is responsible for cleaning of Si (100) substrate, evaporation of Ti and generation of  $\text{TiO}_2$ , and Auger electron spectroscopy (AES). Optical layout on the right denotes where the Ar high harmonic emission is generated, energetically dispersed, and then refocused into the sample chamber for valence photoemission spectroscopy (PES) studies. Courtesy of Dr. Mihai E. Vaida.

The cleanliness of the Si substrate is verified by Auger electron spectroscopy (AES): as shown in Fig. 6-6(a), the oxygen and carbon signals are negligible in the as-prepared clean Si(100) surface after  $\text{Ar}^+$ -sputtering treatment. Titanium metal is then evaporated onto the Si substrate with  $\sim 1 \times 10^{-9}$  Torr oxygen pressure in the chamber. Considering the Auger electrons from Si are less likely to escape the surface when a thicker Ti/TiO<sub>2</sub> layer is deposited, the Ti/Si signal ratio in an Auger electron spectrum can be used for calibration of the evaporation rate. The same methodology has been previously applied to the  $\text{TiO}_2$  film growth on Mo substrates.<sup>156</sup> In Fig. 6-6(b), a change of increasing slope of the Ti/Si peak ratio indicates the presence of the second Ti monolayer on the Si(100) substrate, which means it takes about 170 seconds to deposit a monolayer (ML) of Ti atoms. Based on the 4-hour evaporation time used for preparing samples, the sample thickness is estimated to be about 85 ML (or  $\sim 32$  nm), which agrees well with the measured optical absorbance at the Ti M-edge (Fig. 6-7). Lattice mismatch between Si ( $a = 0.3903$  nm) and the anatase phase of  $\text{TiO}_2$  ( $a = 0.3780$  nm,  $c = 0.9628$  nm) is about 3%, therefore the lattice strain near the *p-n* junction is not expected to be too large.

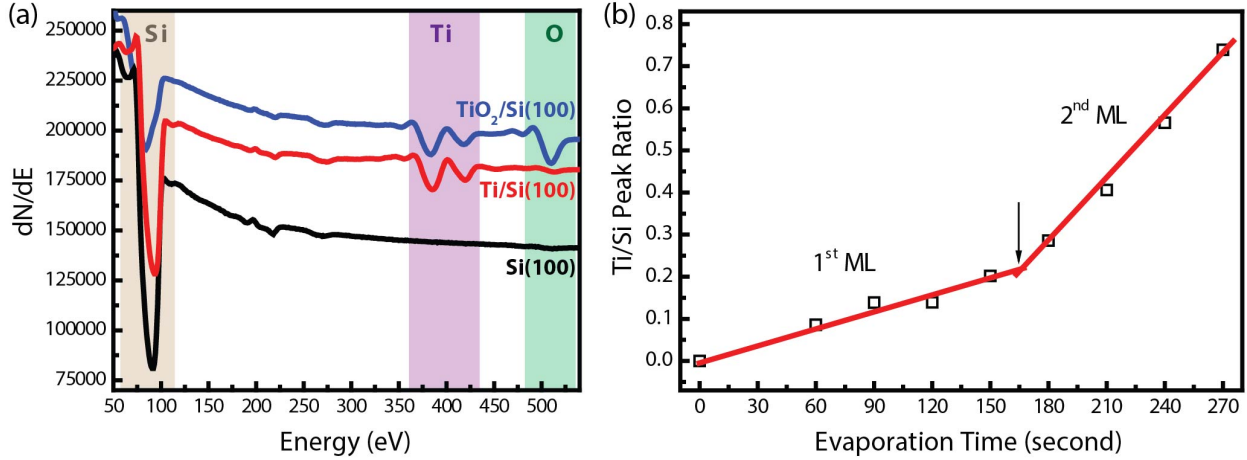


Figure 6-6: (a) Auger electron spectrum of the as-prepared clean Si(100) surface (black line), and the spectra taken after deposition of metallic Ti metal (red line) or an oxidized TiO<sub>2</sub> thin-film (blue line). The carbon signal near 200 eV is negligible in all three spectra. (b) Ti/Si Auger electron signal ratio with respect to the Ti evaporation time.

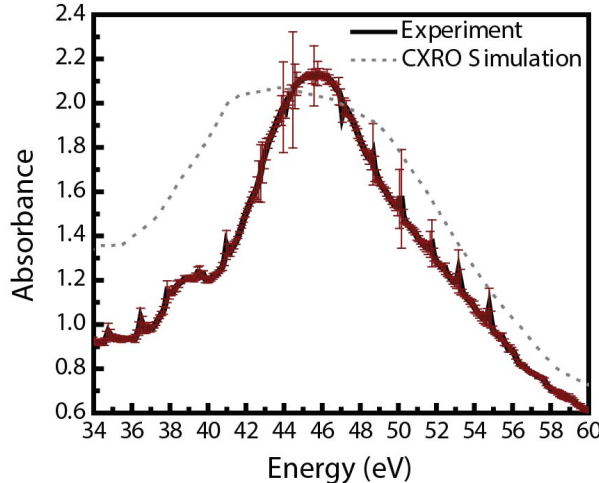


Figure 6-7: Static XUV absorption spectrum of a *n*-TiO<sub>2</sub> film prepared on a *p*-Si(100) substrate. The grey dotted line shows the simulated absorption of a 35 nm thick TiO<sub>2</sub> based on CXRO database.

### 6.2.2 Valence Photoemission

In the same ultra-high vacuum chamber that the TiO<sub>2</sub> thin-films are prepared in, photoemission spectroscopy is used for probing the mid-gap levels associated with the oxygen vacancies. Each sample is prepared at a different oxygen partial pressure, and every sample contains 5ML Ti by the same evaporation parameters. The experimental apparatus is shown in Fig. 6-5: about 1.4 mJ, 30 fs pulses at 800 nm wavelength provided by a Ti:Sapphire amplifier (Dragon, KMLabs) are focused into a semi-infinite gas cell filled with 30 Torr ( $4.0 \times 10^3$  Pascal) Ar for high-order harmonic generation. An XUV monochromator that consists of a plane diffraction grating, a cylindrical mirror, and a toroidal mirror selects the 27<sup>th</sup>-order Ar harmonic emission ( $E_{ph} = 40.8$  eV) to ionize the valence electrons from the sample at a 45° incidence

angle. The sample surface is positioned 5 mm away from the photoelectron spectrometer (PES) entrance with the surface normal parallel to the PES axis. Typically a 5-10 V bias is applied to the sample surface in order to prevent cutting off the low energy electrons due to the work function difference between the sample and the PES. The PES consists of a home built time-of-flight tube that is 1-meter long and double-walled with mu-metal, and a microchannel-plate amplifier for photoelectron detection.

### 6.2.3 Transient XUV Absorbance at the Ti $M_{2,3}$ -edge

The detailed design of the transient XUV absorption apparatus has been discussed extensively in Chapter 2, therefore only a simplified version of the apparatus is shown in Fig. 6-8: the 35 fs infrared pulses with  $\sim 1.8$  mJ energy at 800 nm center wavelength are focused into the semi-infinite gas cell that is filled with 25 Torr ( $3.3 \times 10^3$  Pascal) Ar as the HHG medium. A 400 nm symmetry-breaking field used in the HHG process generates both odd- and even-order harmonics, and the resulting Ar harmonic spectrum provides photon energy coverage of 30 – 50 eV. After removing the residual 800 nm beam with a 0.6  $\mu\text{m}$  Al foil, the XUV beam is refocused onto the sample as the probe beam for time-resolved experiments. The transmitted XUV is then energetically dispersed in the XUV spectrometer and detected by an X-ray CCD camera.

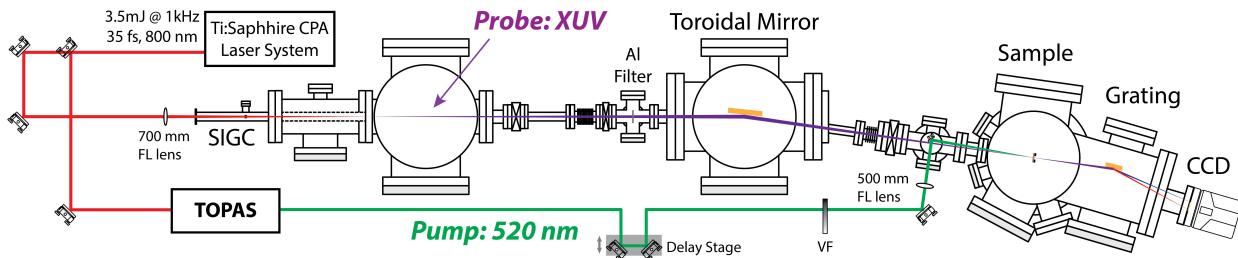


Figure 6-8: Experimental configuration for the 520 nm-pump/XUV-probe measurement of the Si/TiO<sub>2</sub> heterojunction.

Another 800 nm infrared beam of 1.4 mJ pulse energy is used for pumping an optical parametric amplifier (TOPAS-Prime, Light Conversion) that produces a signal beam output at 1488.13 nm. Sum frequency generation between the signal beam and the residual 800 nm gives  $\sim 80$   $\mu\text{J}$  of 520 nm light (9 nm/10.3 THz FWHM) with  $\sim 60$  fs pulse duration (Fig. 6-9). The pulse energy of the 520 nm pump beam and its temporal delay with respect to the XUV probe beam are controlled by a variable neutral density filter and a piezo motor driven stage, respectively. The pump beam is focused by a 500 mm focal length spherical focusing lens to a 120  $\mu\text{m}$  diameter (FWHM) spot size, which is slightly larger than the 100  $\mu\text{m}$  size of the Ar high harmonic emissions.

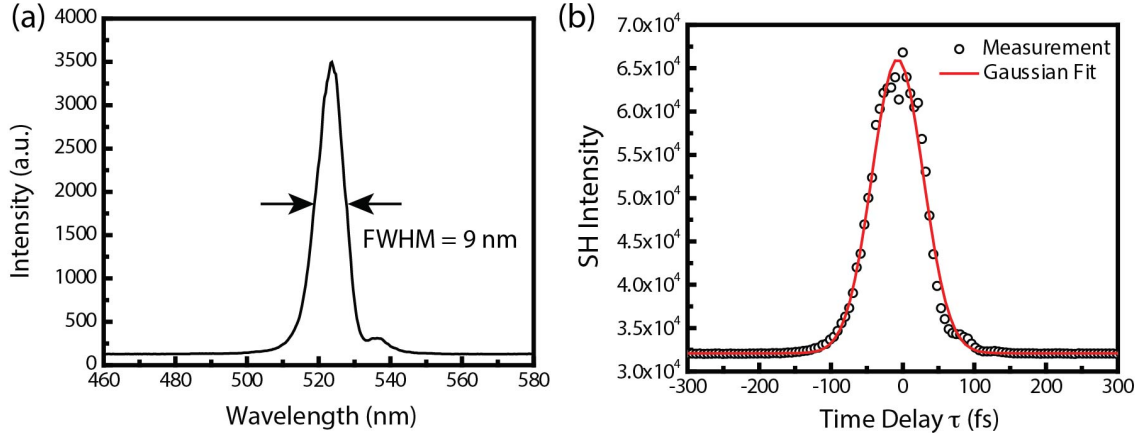


Figure 6-9: (a) Energy spectrum of the 520 nm pump pulses. The spectral bandwidth is 9 nm / 10.3 THz. (b) Intensity autocorrelation trace of the pump pulses by a 50  $\mu\text{m}$  thick BBO (type I,  $\theta = 48^\circ$ ). The Gaussian fit gives  $59.8 \pm 0.7$  fs pulse duration.

Static absorption spectra are taken by dividing one pair of transmitted XUV spectra, that is each going through a  $\text{TiO}_2/\text{Si}$  sample and a bare Si membrane substrate, respectively. A total 32 sets of such spectrum are averaged for obtaining the spectrum shown in Fig. 6-7, with the accompanying error bars computed at 95% confidence interval. By scaling the amplitude of the resonant Ti  $M_{2,3}$ -edge absorption at 46 eV with the XUV absorption cross-section provided by the CXRO,<sup>72</sup> the thickness of the  $\text{TiO}_2$  film is approximated to be 35 nm, which is very close to the estimated value (32 nm) according to the Ti evaporation time. Time-resolved experiments are done at 3.7  $\mu\text{J}$  pump pulse energy, and at each pump-probe delay the differential optical density spectra are obtained by dividing alternating transmitted XUV spectra with pump beam on/off for 100 milliseconds each. A total of 280 differential optical density spectra are averaged at each temporal delay.

## 6.3 Results and Discussion

### 6.3.1 Alignment of Energy Bands

Photoemission spectra of 5ML Ti films at different oxidation extents are shown in Fig. 6-10 as well as the photoemission spectrum of the bare Si(100) substrate. The Fermi level of the metallic Ti layers prepared on Si(100), which is experimentally observed as the photoemission onset, is defined as the zero binding energy. When oxygen is let into the preparation chamber during Ti evaporation, even at a partial pressure as low as  $1 \times 10^{-9}$  Torr, a prominent photoemission feature appears and extends from 4 to 9 eV binding energy. This peak is attributed to the  $O\ 2p$  energy level, which has a major contribution to the valence band of  $\text{TiO}_2$ .<sup>157</sup> It should be noted that the  $\text{TiO}_2$  valence band maximum, which is determined by the onset of its photoemission, lies between 3.5 to 3.7 eV. This means the band gap of the prepared  $\text{TiO}_2$  layer is larger than the reported values (3.0 and 3.2 eV for rutile and anatase phases, respectively), assuming the Fermi level of the  $n$ -type  $\text{TiO}_2$  is near the conduction band minimum. This discrepancy may be explained by two aspects: Since only 5 ML of Ti are evaporated onto the Si(100) substrate, it is possible that the lattice strain near the interface slightly modifies the

electronic structure and thus expands the band gap. Alternatively, the Fermi levels of the oxidized Ti films might be shifted to lower energy than that of the metallic Ti layers. Therefore when the Fermi level of the metallic Ti is defined as the zero binding energy, the valence band maximum of the  $\text{TiO}_2$  that is measured by photoemission would appear at a higher binding energy.

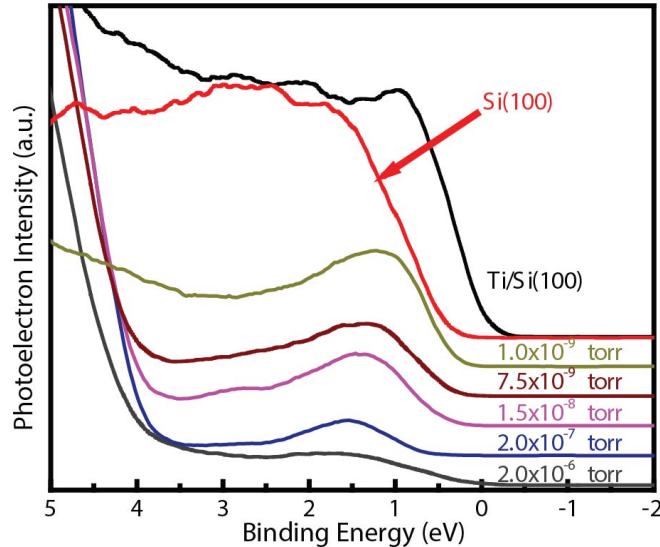


Figure 6-10: Photoemission spectra of 5 ML Ti evaporated on Si(100) substrates at different oxygen partial pressures. The 27<sup>th</sup>-order Ar harmonic emission ( $E_{ph} = 40.8$  eV) is used to ionize the electrons in the valence levels.

Besides the ionization of the  $O\ 2p$  levels, an additional feature is found in the photoemission spectra if the background  $\text{O}_2$  pressure during the Ti evaporation is lower than  $2 \times 10^{-6}$  Torr. This new energy level first appears at  $\sim 1$  eV binding energy at  $1 \times 10^{-9}$  Torr  $\text{O}_2$  pressure, and shifts to higher binding energy while decreasing in amplitude as the  $\text{O}_2$  pressure is increased, and eventually disappears if the  $\text{TiO}_2$  film is fully oxidized. The dependence on the background  $\text{O}_2$  pressure of this new energy level, together with the 1.0 – 1.5 eV energy below the Fermi level, suggests that it comes from the partially reduced Ti cations near the oxygen vacancies in the  $\text{TiO}_2$  lattice.

The photoemission spectrum taken on a Si(100) substrate shows the valence band maximum is about 0.4 eV lower than the metallic Ti Fermi level. Based on the aforementioned results and the band gaps of each semiconductor, the energy band alignment of the  $p$ -Si/ $n$ - $\text{TiO}_2$  heterostructure is summarized in Fig. 6-11. In this type II  $p$ - $n$  heterojunction, the 520 nm pump wavelength would excite only the bulk Si but not the wider band gap  $\text{TiO}_2$ , and the electron transfer from Si to  $\text{TiO}_2$  in the conduction bands is energetically favorable. An XUV beam is used to probe the core level absorption from the localized Ti  $3p$  level to the delocalized empty levels of Ti  $3d$  character in the conduction band. This core level absorption would not be affected by the excited carrier population on the Si part of the heterojunction due to the elemental specificity; however once electrons move into the  $\text{TiO}_2$  conduction band a decrease in the Ti  $3p \rightarrow 3d$  absorption cross section is expected, because the empty density of states in the conduction band would be reduced. Therefore the electron transfer rate from Si to  $\text{TiO}_2$  following the 520 nm optical excitation can be measured by monitoring the depletion of the Ti M-edge absorption.

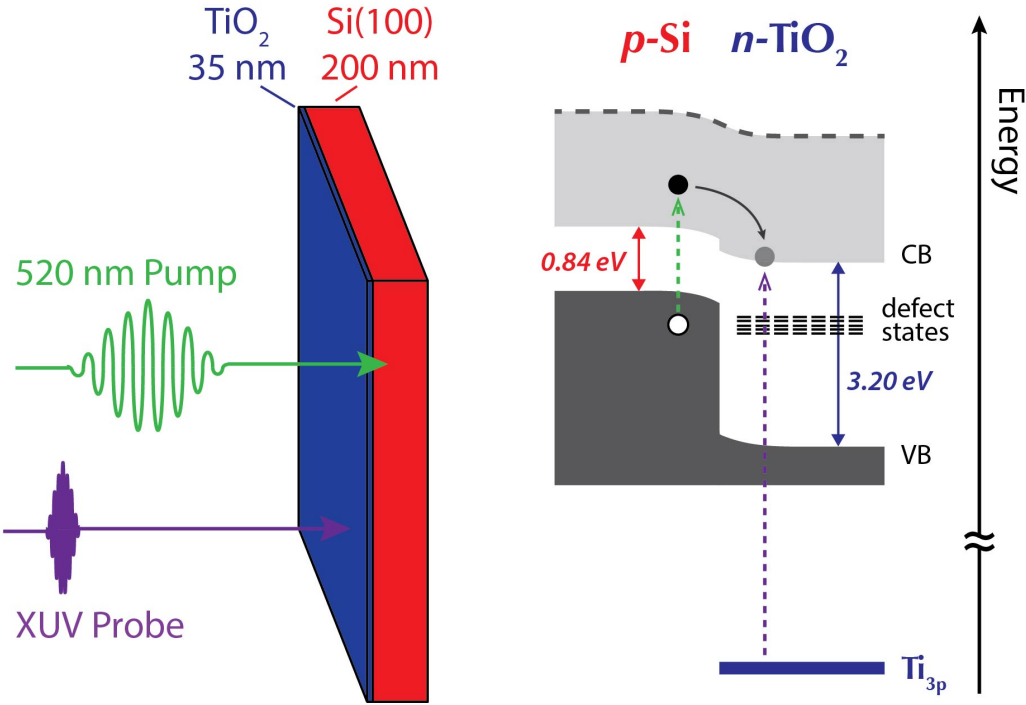


Figure 6-11: Schematic of the pump-probe experiment on the Si/TiO<sub>2</sub> system and the relevant band diagram. Energy band alignment between two semiconductor forms a type II heterojunction, and additional defect states caused by the oxygen vacancies are  $\sim 1.0$  eV below the TiO<sub>2</sub> conduction band.

### 6.3.2 Electron Transfer from *p*-Si to *n*-TiO<sub>2</sub>

The differential XUV absorbance spectra in response to the 520 nm excitation of the *p*-Si/*n*-TiO<sub>2</sub> heterojunction are shown in Fig. 6-12, and several noticeable changes are observed: First, a feature with positive optical density change ( $\Delta\text{OD} > 0$ ) between 34 and 36 eV appears immediately after the photo-excitation. This enhanced absorbance signal shows a fast decay in the first 300 fs, but remains prominent until 4 ps after the excitation. When compared with the static TiO<sub>2</sub> XUV absorption spectrum (Fig. 6-7), which has the Ti M-edge onset at 37 eV, the transition energy for the new absorption is about 1–2 eV lower. The combination of the fast response to the photo-excitation, and the lower transition energy, strongly suggests the XUV absorbance change in the 34 – 36 eV region results from the direct excitation of the TiO<sub>2</sub> oxygen vacancy defect states into the conduction band: Although the band gap of bulk TiO<sub>2</sub> (3.0 – 3.2 eV) is too large to be excited with a photon with 520 nm wavelength (2.38 eV), there still exist some mid-gap states introduced by reduced Ti cations and oxygen vacancies that have been verified by both computational studies and valence photoemission experiments. The energy difference between the localized defect states with the conduction band allows excitation via one-photon absorption, and by doing so it opens up a new core level absorption pathway from the Ti 3p level to the now depleted defect states. The  $75 \pm 37$  fs exponential decay of this feature (Fig. 6-13(a)) can be related to two possible relaxation channels: (1) Recombination of the excited electron in the TiO<sub>2</sub> conduction band back to the defect states, which can explain the observed amplitude decay. (2) A lattice relaxation following a positive charge that is created on/near the defect location; this could mean the formation of a polaron or a lattice deformation around the defect, in order to stabilize the extra Coulomb interaction with the positive charge.

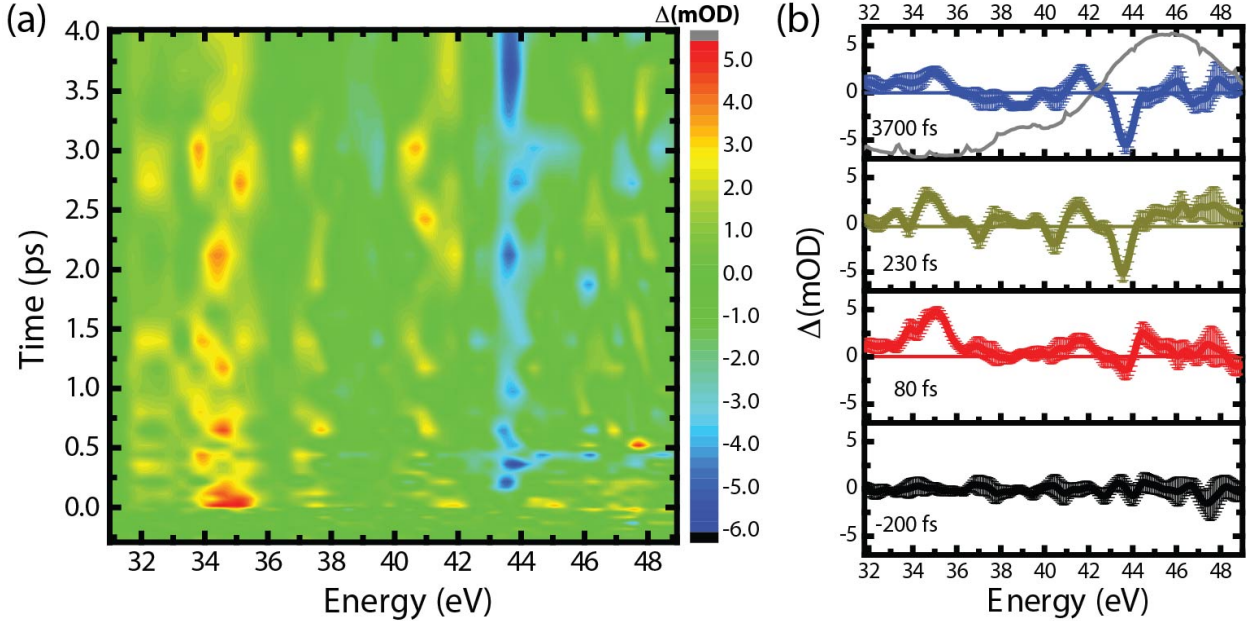


Figure 6-12: (a) Contour plot of the XUV absorbance change  $\Delta\text{mOD}$  between 31 – 49 eV energy region (x-axis) with respect to the pump-probe time delay (y-axis). (b) Transient absorbance spectra measured on the Si/TiO<sub>2</sub> heterostructure at different times after the 520 nm photo-excitation. In the top panel, the static XUV absorption spectrum of TiO<sub>2</sub> is overlaid for comparison.

At about 200 fs after the photo-excitation, a negative optical density change ( $\Delta\text{OD} < 0$ ) starts to appear at 43.6 eV. The growing time constant of this feature ( $54 \pm 38$  fs) is comparable to the decay rate of the Ti 3p-to-defect absorption at 34 – 36 eV, therefore it can be attributed to the relaxed excited state at the defect locations. However, the possibility that an electron transfer from Si to TiO<sub>2</sub> causes this absorbance decrease cannot be entirely ruled out. These extra electrons from the excited Si would occupy certain energy levels in the TiO<sub>2</sub> conduction band and therefore prohibit the absorption from the Ti 3p core level into the 3d-like conduction band. In order to clarify the exact cause of the decreased absorbance at 43.6 eV, a future control experiment will be done on a same n-TiO<sub>2</sub> film deposited on a Si<sub>3</sub>N<sub>4</sub> substrate, which has an even wider band gap (5 eV) than TiO<sub>2</sub>. As the electron transfer pathway across the heterostructure is no longer accessible, the decreased absorbance feature at 43.6 eV should vanish if it were caused by the filling of electrons into the conduction band.

In addition to the aforementioned excited-state changes, a shallower and slower decreasing optical density feature is found between 38 and 40 eV. Immediately after the photo-excitation a weak but fast absorbance increase is initially observed, possibly correlated to the defect state responses at lower energy, however soon it turns into a negative absorbance change with a  $254 \pm 95$  fs time constant (Fig. 6-13(b)). Since this depletion occurs in the energy range close to the Ti M-edge absorption onset of TiO<sub>2</sub>, it possibly reflects that the bottom of the conduction band is filled by the electrons migrating from the *p*-type Si.

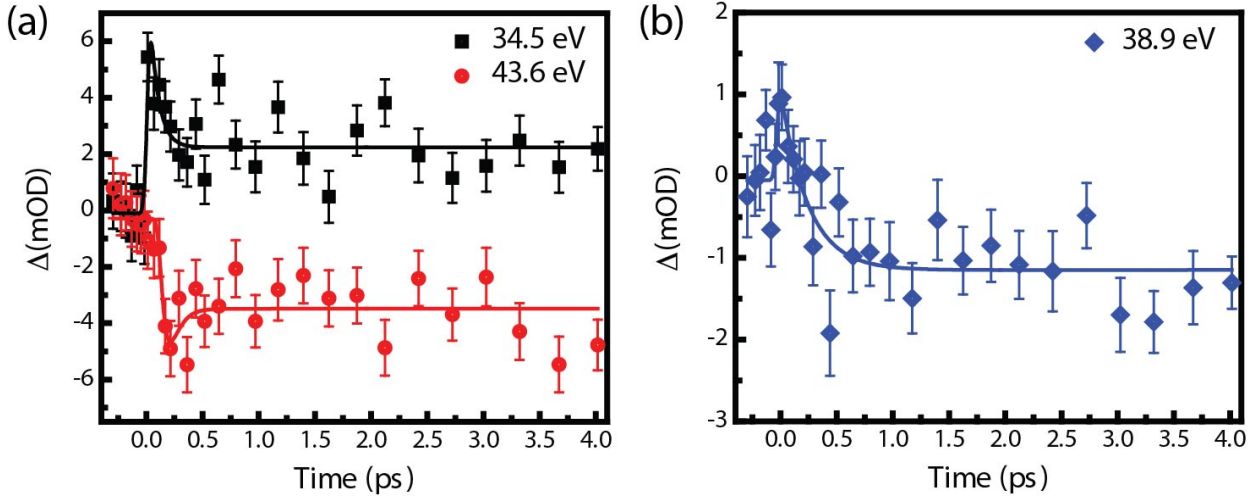


Figure 6-13: (a) Transient absorbance traces at 34.5 (black) and 43.6 eV (red). The fit curve for 34.5 eV is a 60 fs wide Gaussian instrument response function convoluted with a  $75 \pm 37$  fs exponential decay. The fit curve for 43.6 eV is a  $54 \pm 38$  fs exponential rise convoluted with a  $79 \pm 32$  fs exponential decay. (b) Transient absorbance trace at 38.9 eV, fit by the instrument response function and an exponential raise with  $254 \pm 95$  fs time constant.

It should be noted that if the TiO<sub>2</sub> film is deposited at a higher oxygen background pressure, i.e. the number of oxygen vacancy sites is reduced, the transient absorbance changes at 34 – 36 eV and at 43.6 eV are not observed even at higher pump pulse energies. This also justifies that these changes are highly correlated to the defect states. Nevertheless, the slow-growing depletion feature at 39 eV is also very weak in the fully oxidized TiO<sub>2</sub> film. It cannot be ruled out that the density of defect states in the TiO<sub>2</sub> film, which is equivalent to the doping concentration, has a strong effect on the band-alignment near the *p-n* junction. Further investigations will require careful control and characterization of the doping level of the *n*-type TiO<sub>2</sub>, as well as the correlation between the doping concentration and the electron transfer rate.

## 6.4 Conclusions and Perspectives

In summary, the ultrafast charge carrier dynamics in the *p*-Si/*n*-TiO<sub>2</sub> heterostructure has been studied by means of transient XUV absorbance measurement. Extra care is taken during the sample preparation to have a clean and well-controlled interface between two semiconductors. Instantaneous XUV absorbance changes in response to the 520 nm light illumination are due to the direct excitation from the Ti ions around the defect sites to the delocalized conduction band. In addition, a  $\sim 250$  fs depletion at the onset of the Ti M-edge absorption could relate the electron transfer across the *p-n* junction.

In order to further clarify the heterojunction band diagram in Fig. 6.11, several additional measurements need be carried out. First, when determining the energy of the valence band maximum, the Fermi level of the oxidized Ti films must be carefully assigned. The referencing to the Fermi level of the metallic Ti layers, as is done in this study, might not be the most rigorous method. It would be helpful to have a separate metal substrate available, so that the photoemission spectra can be calibrated. Once the valence band offset  $\Delta E_v$  is determined, the exact band gaps of the two semiconductors are required to calculate the conduction band offset

$\Delta E_c$ . This can be achieved by measuring the optical absorption spectrum of the two semiconductors separately. The anatase and rutile phases of TiO<sub>2</sub> would have different band gaps; the phase of the prepared TiO<sub>2</sub> film can be verified via Raman spectroscopy. Moreover, it has been reported that the anatase-to-rutile phase transition in TiO<sub>2</sub> nanoparticles can occur upon visible light irradiation in a vacuum environment,<sup>158</sup> therefore the same Raman spectroscopy can be used to check if the TiO<sub>2</sub> structure has been changed during the pump-probe experiment.

In terms of the acquisition of the transient XUV absorbance spectra, the XUV flux fluctuation causes a higher noise level when Ar harmonics are used instead of Ne harmonics. This is due to the fact that the spacing between adjacent harmonic orders becomes wider at the low energy side of the XUV spectrometer, where the experiments on Ti have to be performed. Therefore in the raw transmitted Ar harmonic spectra there would be more low-flux regions even in the presence of the even-order harmonics. In the current study, the number of pump-probe time delays that are measured is slightly reduced for the purpose of longer data averaging, therefore the kinetic traces in Fig. 6-13 are fitted by time constants accompanied with large errors. As has been demonstrated in Chapter 3, efforts should be made for producing a more optimal Ar harmonic spectrum as the probe beam, such that the data acquisition can be more efficient.



# Chapter 7

## Outlook and Conclusion

The main focus of this dissertation is to apply a transient XUV absorption technique to study charge carrier dynamics in condensed phase systems, especially transition metal oxides. When this project was initiated in late 2009, almost all the existing high-order harmonic spectroscopic studies were still limited to the interaction between a strong laser electric field and an atom or a small molecule (at that time even this was a rare case). There have been numerous challenges during attempt to make the leap into solid-state systems. After nearly six years, it is encouraging to witness how far this research field has advanced. Tremendous breakthroughs have been made not only in this work or in the Leone group, but also in other relevant research groups located worldwide, in terms of using femtosecond and attosecond XUV techniques for investigating solid-state electron dynamics.

Experimentally one of the biggest challenges is to find suitable samples; this can be addressed from two aspects: First, not every element exhibits measurable absorption edges in the XUV photon energy range. Some commonly studied II-VI or III-V group semiconductors, such as CdSe, ZnS, or GaAs, do not show sharp resonant absorption features in transmissive XAS even though their core level binding energies fulfill the requirement. Second, attenuating lengths of XUV radiation are much shorter than that of soft and hard X-rays, which means the samples have to be prepared with small optical path lengths (< 30 nm). Technically there are various deposition methods for preparing thin-films with such a thickness requirement, however the delicacy and surface properties of the  $\text{Si}_3\text{N}_4$  substrate add some extra constraints to these methods. Moreover, 0D or 1D nanomaterials would need to form a close-packed dispersion on the substrate, which is another practical challenge. Combining these factors, it explains why thin-films of transition metal oxides were chosen as the prototype system to be investigated by the transient XUV absorption technique. Not only do these transition metal elements exhibit strong and sharp  $3p \rightarrow 3d$  absorption structures, but homogeneous films can also be easily obtained via sputtering or atomic layer deposition methods. Now that some initial successes have been achieved on these oxide compounds, and a robust methodology has been established, it would be worth investing more effort to expand the group of accessible materials. This can be done by either extending the high harmonic spectrum to higher photon energies, so that more elements can be studied, or by optimizing the instrument performance, so that weaker absorption features can be resolved.

Regarding the interpretation of the measured XAS spectra of either static or excited states, a better modeling of the spectra is still desired. Considering the core level absorption events that move a core electron to the empty states in the conduction band, the core levels can be generally treated as localized with significant atomic character, however an ambiguity appears when describing the electronic structures of valence and conduction bands. The charge transfer multiplet theory, which is used to model the excited-state M-edge absorption spectra in Chapter

4, views each transition metal cation as a small cluster coordinated by anionic ligands. In other words, the X-ray absorption spectrum is largely determined by the local configuration of  $3d$  electrons, with some sort of perturbation from the solid-state effects. Alternatively, from the viewpoint of a delocalized energy band theory, the electronic transition probability via photon absorption depends more on the distribution of empty densities of states. If one transient spectrum exhibits enhanced absorbance below the static absorption edge, it would be interpreted by the charge multiplet theory as the reduction of the metal cation, but the energy band theory would explain the transient spectrum via the created electron vacancies in the valence band. One may perceive that band theory is better suited for describing metals and covalent semiconductors, while the charge transfer multiplet theory would include the interaction between  $d$  electrons in ionic transition metal oxide compounds. Nonetheless the actual electronic structure might lie in between these two extremes, and seeking theoretical collaboration for higher-level XAS calculations would be beneficial to the experimental part of the research.

Early accomplishments of this study are mostly on resolving the carrier dynamics in single-component semiconductor systems, such as the excitation pathways and carrier relaxation processes in  $\text{Fe}_2\text{O}_3$  and  $\text{Co}_3\text{O}_4$  thin-films. Recently the capability of transient XUV absorption spectroscopy is expanded to more complicated heterojunction systems, taking advantage of the elemental specificity of the core level transitions. It would be an interesting modification if a bias voltage can be applied and controlled across the semiconductor heterojunction during a pump-probe measurement, such that the experimental conditions resemble what used in actual photoelectrochemical cells. Among other potential investigation targets, electron and hole injection dynamics from molecular light absorbers attached on the sample surface to the bulk semiconductor are also of scientific interest. Not only do these processes have numerous practical applications, but more insight into core level absorption can also be gained through related studies. For example, since Ti atom in  $\text{TiO}_2$  has a  $d^0$  configuration, the band gap excitation should be purely of O-to-Ti charge transfer character. The local electronic configuration changes around Ti atoms can be probed by monitoring the  $3p \rightarrow 3d$  absorption edge, but it is difficult to know how the presence of holes in the valence band affect the core level absorption of Ti. If the electrons are injected into the empty conduction band from light-absorbing molecules, e.g. the  $\text{Ru}(\text{dcbpy})_2(\text{NCS})_2$  ( $\text{RuN3}$ ) complex that is widely used in dye-sensitized solar cells (DSSCs), modifications to the XUV absorption spectra by the holes are therefore eliminated.

To sum up, a reliable femtosecond XUV light source has been constructed and utilized for probing the core level transitions of several transition metal oxides. Optical excitation pathways in these semiconductors have been assigned by means of the XUV absorption spectroscopy with the assistance of charge transfer multiplet theory. Various charge carrier relaxation dynamics, including carrier-carrier and carrier-phonon scattering, are observed in the time-resolved experimental results. Electron transfer processes across a semiconductor heterojunction are also observed by the elemental specificity of the developed technique. Combining these findings, transient XUV absorption spectroscopy is proven to be a promising tool for studying electron dynamics in condensed phase materials, and deeper insights into yet more complex systems will continue to be gained in the future.

# Appendix A

## Excited-State Dynamics of Iron Pyrite

Iron pyrite ( $\text{FeS}_2$ ) is an earth abundant material that has become a promising candidate for solar cell applications.  $\text{FeS}_2$  not only possesses a low band gap ( $E_g \sim 0.95$  eV) and a strong extinction coefficient ( $\alpha > 10^5 \text{ cm}^{-1}$  for  $\lambda < 700$  nm), the long diffusion length of minority carriers ( $> 100$  nm) also makes it an ideal photovoltaic material. However, solar cells that are made of  $\text{FeS}_2$  have an abnormally low open-circuit voltage ( $V_{\text{OC}}$ ), which hampers the solar energy conversion efficiency.<sup>159</sup> Better knowledge of the  $\text{FeS}_2$  band structure and the charge carrier relaxation pathways would be beneficial to the development of pyrite-based devices. Iron pyrite crystallizes in a NaCl-like structure (space group  $Pa3$ ), in which the  $\text{Fe}^{2+}$  cations form a *fcc* lattice and the centroid of the  $\text{S}_2^{2-}$  dimer anions occupy the  $\text{Cl}^-$  sites in the rocksalt structure. Each Fe atom is coordinated by six S atoms that form an octahedron, while each S atom is tetrahedrally coordinated by one S atom and three Fe atoms. The approximately  $O_h$  crystal symmetry reduces the Fe *d* degeneracy into 2  $e_g$  orbitals and 3  $t_{2g}$  orbitals at a low-spin ( $t_{2g})^6(e_g)^0$  configuration. Computational studies have found that the top of the valence band is dominated by the filled Fe  $t_{2g}$  orbitals, and the S  $3p$  orbitals have a wide spread deeper in the valence band (Fig. A-1).<sup>160,161</sup> The Fe  $e_g$  orbitals, on the other hand, strongly hybridize with the  $pp\sigma^*$  anti-bonding orbital of the  $\text{S}_2^{2-}$  dimer at the bottom of the conduction band.

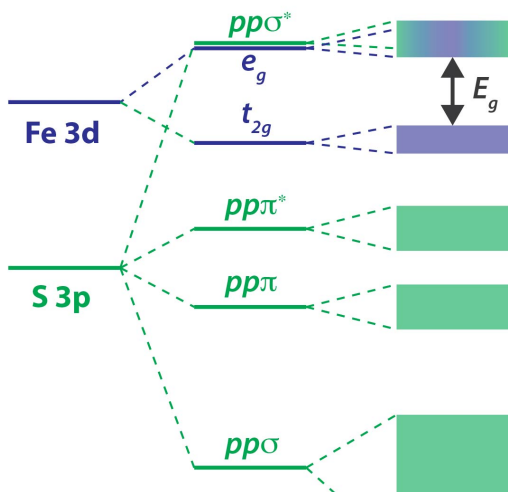


Figure A-1: Simplified band structure of  $\text{FeS}_2$ . The Fe  $3d$  orbitals are split into  $e_g$  and  $t_{2g}$  levels by the local  $O_h$  symmetry, and the S  $3p$  orbitals in the  $\text{S}_2^{2-}$  dimer form bonding and anti-bonding orbitals. The conduction band of  $\text{FeS}_2$  is strongly hybridized between the Fe  $e_g$  and S  $3p$  orbitals, while the top of the valence band is contributed solely by the Fe  $t_{2g}$  orbitals.

In the present study, the  $\text{FeS}_2$  samples are prepared by Matt Lucas in the Alivisatos group. First an  $\sim 10$  nm metallic Fe layer is sputtered onto the 100 nm  $\text{Si}_3\text{N}_4$  substrate and then transformed to  $\text{FeS}_2$  via vapor sulfurization. The static XUV absorption spectrum is shown in Fig. A-2, in which the  $\text{Fe } 3p \rightarrow 3d$  transition energy is slightly higher than that of the hematite ( $\alpha\text{-Fe}_2\text{O}_3$ ).  $\text{FeS}_2$  also exhibits a higher absorption cross section above 60 eV, indicating strong hybridization between the Fe  $e_g$  and S  $p\sigma^*$  orbitals.

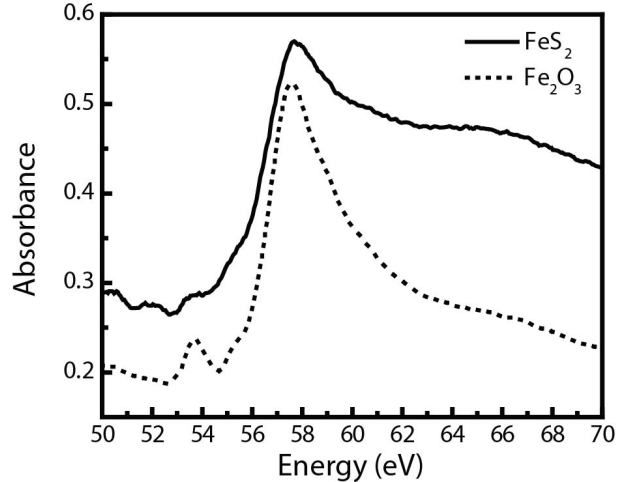


Figure A-2: Static XUV absorption spectrum of  $\text{FeS}_2$  and  $\text{Fe}_2\text{O}_3$  at the Fe M-edge.

Time-resolved experiments are carried out using 800 nm as the pump wavelength. About 1.2  $\mu\text{J}$  of pump energy excites the valence band electrons across the band gap, and the induced XUV absorbance changes are shown in Fig. A-3: Immediately after photoexcitation an enhanced absorbance feature appear between 52 and 60 eV, and a bleaching signal is observed above 64 eV. The amplitudes of both the enhanced absorbance and the bleaching signal undergo fast decays in the first 300 fs then stay unchanged up to 2.5 ps after the pump excitation.

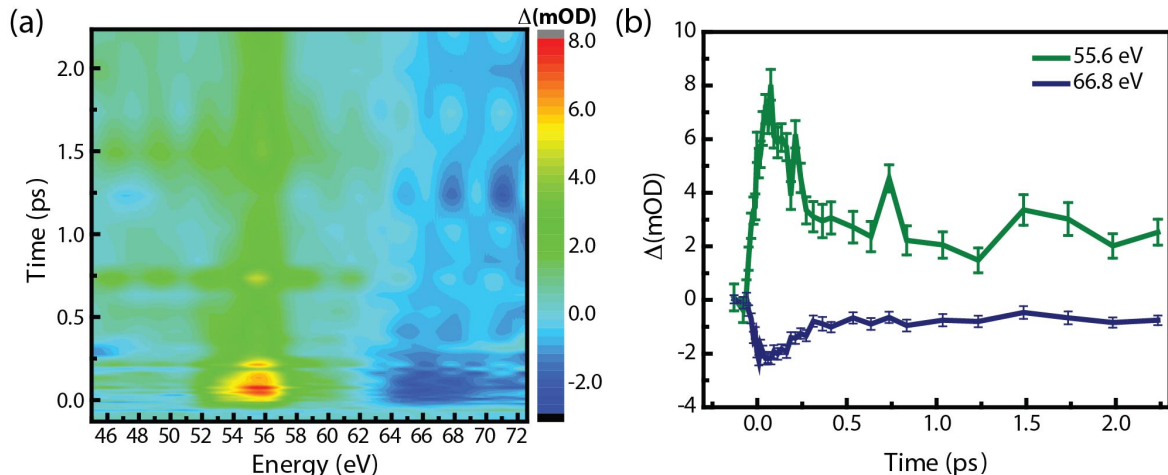


Figure A-3: (a) Contour plot of the excited-state XUV absorbance changes after the 800 nm excitation with respect to pump-probe time delays. (b) Lineouts at 55.6 and 66.8 eV show, respectively, an enhanced absorbance and a bleaching signal; both appear faster than the 40 fs instrument response function. A  $118 \pm 28$  fs exponential decay leads to a long-lived state.

A global fit analysis to the data shown in Fig. A-3(a) gives a sequential two-state model ( $A \xrightarrow{k} B$ ) with a  $118 \pm 28$  fs decay time constant ( $1/k$ ). The characteristic transient spectra of both the initial excited state A and the long-lived state B have qualitatively similar spectral features, but with  $\sim 70\%$  difference in signal amplitude (Fig. A-4).

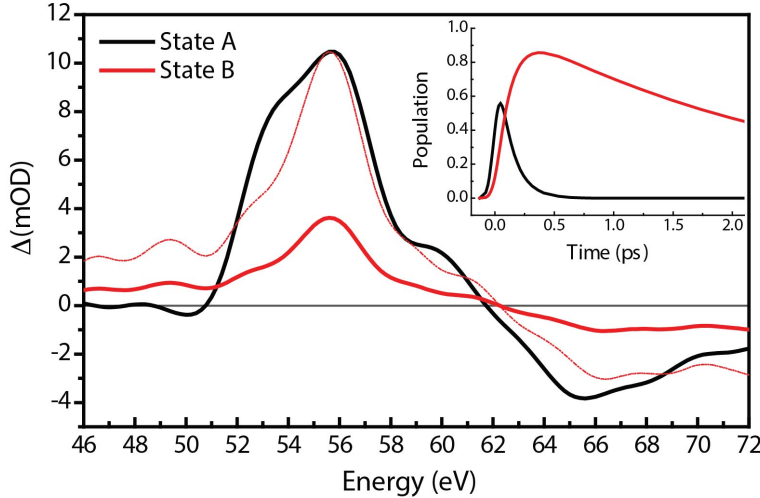


Figure A-4: Retrieved spectral evolution by a two-component sequential model global fit. Black solid line is the transient absorption spectrum of the initially created excited state A, which then undergoes a  $118 \pm 28$  fs decay into state B (red solid line). The thin red line in the state B spectrum normalized at the same maximum amplitude as state A. Inset: Population of state A and B at different pump-probe time delays.

It should be noted that the pump pulses easily damaged the FeS<sub>2</sub> thin-films. Initially the time-resolved measurements were done at the 400 nm pump wavelength; even when the sample is raster scanned during the data acquisition and each location is only illuminated by the pump beam for 1.5 second, significant XUV transmission changes are noticed. Inspection of the sample afterward found the dark color of the as-prepared FeS<sub>2</sub> turns almost transparent, and a clear sample damage pattern that matches the raster grid is observed with an optical microscope (Fig. A-5(a)). In addition, the static absorption spectrum of FeS<sub>2</sub> exhibits an  $\sim 1.5$  eV red shift after a pump-probe experiment (Fig. A-5(b)), manifesting the extent of sample damage and possibly the reduction of Fe cations. When the 800 nm wavelength is used instead as the pump beam, degradation of FeS<sub>2</sub> occurs at a slower rate, i.e. each spot can be illuminated for 8 seconds before the bleaching of sample color is visible. Since the 400 nm wavelength ( $E_{ph} \sim 3.0$  eV) is much larger than the FeS<sub>2</sub> band gap, electrons can be excited from deeper in the valence band to higher in the conduction band. Based on the band structure of FeS<sub>2</sub>, the electronic transition from the S<sub>2</sub><sup>2-</sup> bonding orbital into an anti-bonding orbital may be excited by a high-energy photon. Therefore the observed sample degradation could be related to the breaking of S-S chemical bonds, although this hypothesis needs to be supported by more rigorous sample characterization procedures. Interpretation of the transient spectra in Fig. A-4 and the associated dynamics have not been completed when this dissertation is written.

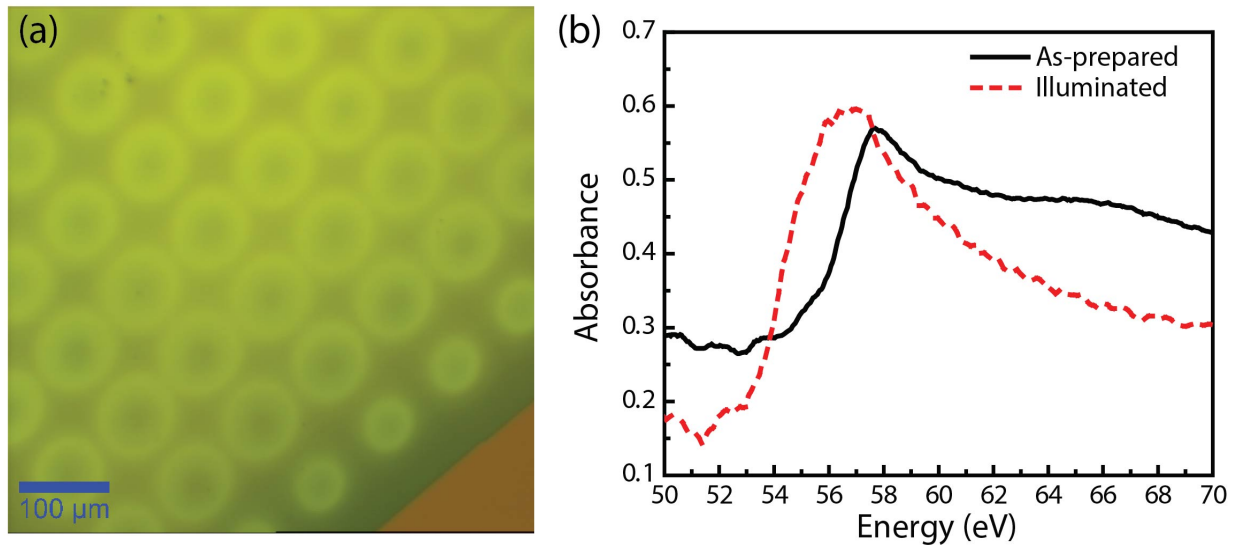


Figure A-5: (a) The optical microscope image shows damaged spots on a  $\text{FeS}_2$  thin-film after illumination by a 400 nm pump beam. Spacing between adjacent spots matches the  $100\ \mu\text{m}$  step size used for the raster scan. (b) Change of static  $\text{FeS}_2$  XUV absorption spectrum after 400 nm illumination.

## Appendix B

# Pump-Probe Measurement on Fe<sub>2</sub>O<sub>3</sub> Nanoparticles

The first attempt at studying semiconductor nanoparticles on the existing experimental apparatus was carried out in October 2012. Five monolayers of Fe<sub>2</sub>O<sub>3</sub> nanoparticles of  $\sim 6$  nm size is prepared on a  $3 \times 3$  mm<sup>2</sup> 100  $\mu\text{m}$  thick Si<sub>3</sub>N<sub>4</sub> substrate by a Langmuir-Blodgett deposition. The static XUV absorption spectrum of this nanoparticle assembly is shown in Fig. B-1. The absorption features and the peak positions of the Fe<sub>2</sub>O<sub>3</sub> nanoparticles are very close to what is measured for Fe<sub>2</sub>O<sub>3</sub> thin-films.<sup>110</sup> When the amplitudes of the Fe M-edge are normalized, however, it can be seen that the Fe<sub>2</sub>O<sub>3</sub> nanoparticle sample has a higher non-resonant absorption contribution than the thin-film Fe<sub>2</sub>O<sub>3</sub>. This additional non-resonant absorbance can be attributed to the carbon atoms of the oleic acid ligands that are used for passivating the nanoparticle surfaces.

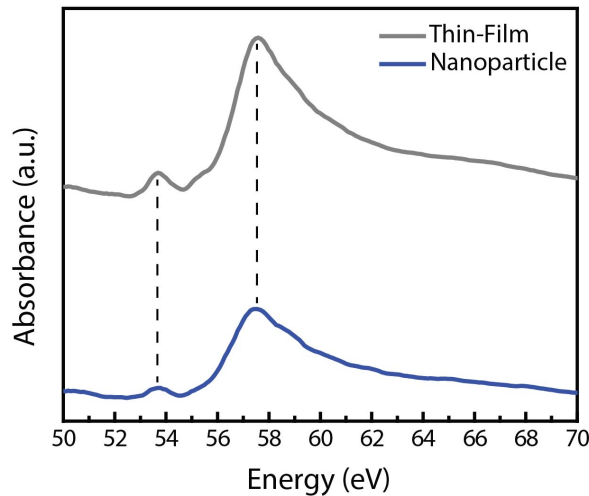


Figure B-1: Static XUV absorption spectra at the Fe M-edge of thin-film Fe<sub>2</sub>O<sub>3</sub> (grey line) and Fe<sub>2</sub>O<sub>3</sub> nanoparticles (blue line), respectively.

The pump-probe experiment used 400 nm as the optical excitation wavelength, and the 3.0  $\mu\text{J}$  pump pulse energy is identical to what is used when studying the excited-state dynamics in a Fe<sub>2</sub>O<sub>3</sub> thin-film.<sup>110</sup> As shown in Fig. B-2(a), transient XUV absorbance changes near the Fe M-edge are distinguishable from the noise level. The spectral features are qualitatively similar to what are observed on thin-film Fe<sub>2</sub>O<sub>3</sub>: an enhanced absorption feature at 54 – 56 eV appears together with a bleaching signal at 57.5 eV. This suggests that the optical excitation of Fe<sub>2</sub>O<sub>3</sub> nanoparticles also follows the ligand-to-metal charge transfer ( $\text{O}^{2-} 2p \rightarrow \text{Fe}^{3+} 3d$ ) pathway.

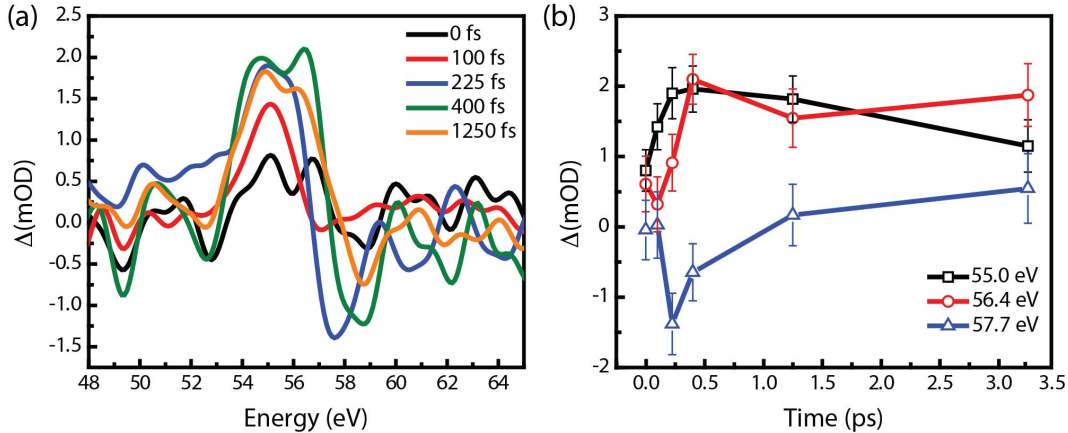


Figure B-2: (a) Transient XUV absorption spectra of  $\text{Fe}_2\text{O}_3$  nanoparticles after the 400 nm photo-excitation. (b) Kinetic traces at 55.0, 56.4, and 57.7 eV.

Despite demonstrating that collecting transient absorbance data from a close-packed nanoparticle assembly is feasible, the observed signal-to-noise (S/N) level is lower than what is achieved in the thin-film  $\text{Fe}_2\text{O}_3$ . Fig. B-3 compares the excited-state absorbance changes on the two types of  $\text{Fe}_2\text{O}_3$  sample at 100 fs following the optical excitation, and it can be seen that even at the same pump energy ( $3.0 \mu\text{J}$ ) used for optical excitation, the signal amplitude of the thin-film is about three times higher than that of nanoparticles. This can be attributed to the difference in the Fe atomic density, which is expected to be higher in the bulk-like thin-film samples. From this preliminary study, it has been learned that transient XUV spectroscopy can be applied to nanoscale materials; however the sample homogeneity needs to be carefully controlled and improvements to signal to noise are desirable. The organic ligands that are used for passivating the nanoparticles have a significant non-resonant absorption contribution. Therefore at the same XUV transmission level, the density of transition metal atoms would be lower in the nanoparticle sample, so also will be the measured amplitude of the transient absorbance changes.

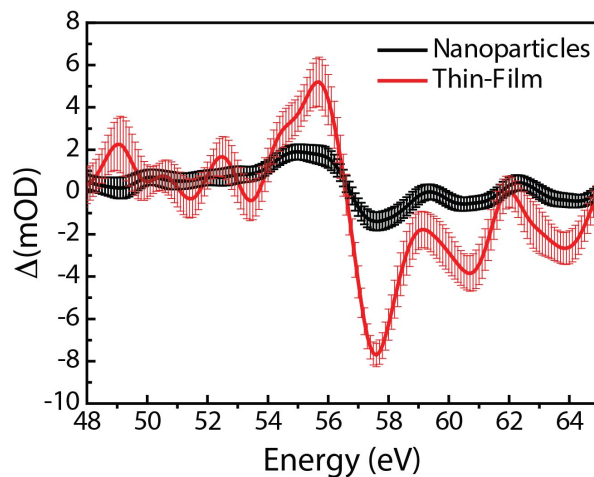


Figure B-3: Transient XUV absorbance spectra obtained 100 fs after 3.0  $\mu\text{J}$  400 nm photoexcitation. The spectrum measured from a thin-film sample (red) has three times signal amplitude when compared to the nanoparticle assembly.

# Appendix C

## Pump-Probe Measurement on $\text{Co}_3\text{O}_4$ Nanocubes

In this study,  $\text{Co}_3\text{O}_4$  nanocubes of 5 nm average size are prepared by collaborators in Yang's group. The nanocubes are drop-cast onto a 100 nm  $\text{Si}_3\text{N}_4$  substrate, and the spatial homogeneity of the sample is inspected by means of XUV transmission mapping that has been described in Chapter 3. Fig. C-1(a) shows that the XUV transmission is generally higher on the edges of the substrate, which means the nanocube sample density is lower compared to the central region of the substrate. Static absorption spectra taken at five different locations are compared with a 17 nm  $\text{Co}_3\text{O}_4$  thin-film in Fig. C-1(b). Although the  $\text{Co } 3p \rightarrow 3d$  absorption peak at 63 eV are present in every spectra, in the high transmission region (location f and g) both the resonant and non-resonant absorption levels are lower than that in the high sample density region (location c, d, and e). Raman spectroscopy is used to characterize the composition of the nanoparticles. The four distinct Raman shift peaks ( $478, 530, 616$ , and  $680 \text{ cm}^{-1}$ ) match the reported values of spinel cobalt oxide ( $\text{Co}^3\text{O}_4^{111}$ ) and are slightly blueshifted compared to the thin-film sample (Fig. C-2). The sharper Raman shift peaks exhibited by the nanocube  $\text{Co}_3\text{O}_4$  also indicate the crystallinity is higher than that of  $\text{Co}_3\text{O}_4$  thin-film.

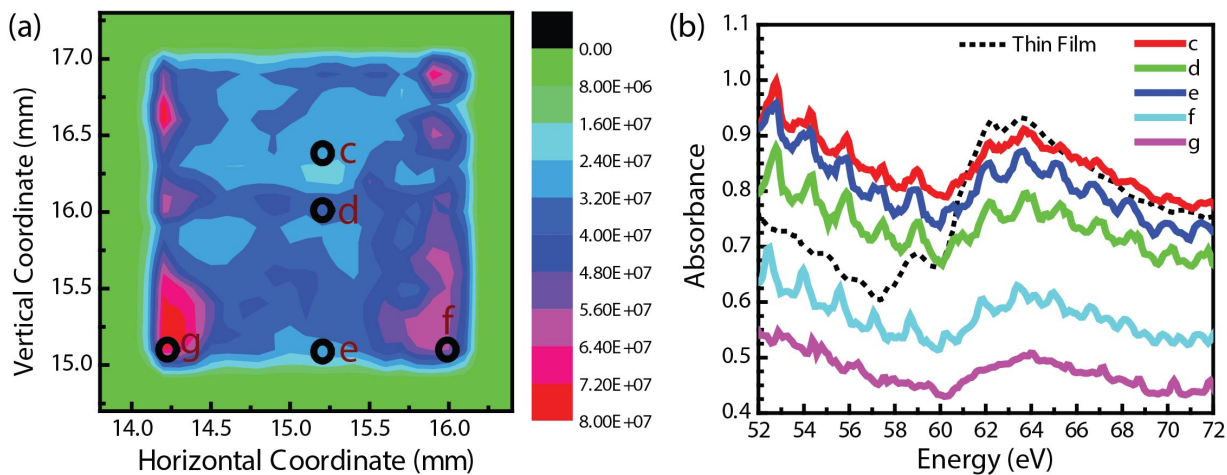


Figure C-1: (a) XUV transmission map of a  $2 \times 2 \text{ mm}^2$   $\text{Si}_3\text{N}_4$  substrate that is drop-cast with 5 nm  $\text{Co}_3\text{O}_4$  nanocubes. The static absorption spectra at the Co M-edge taken at locations c-f are compared in (b).

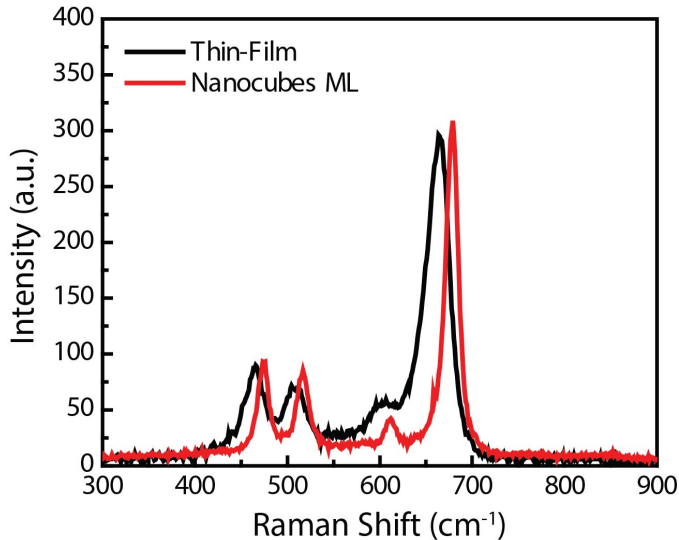


Figure C-2: Raman spectra of thin-film and nanocube  $\text{Co}_3\text{O}_4$ , taken with 1.28 mW of 528 nm excitation in a 5  $\mu\text{m}$  diameter spot.

Optical excitation of the  $\text{Co}_3\text{O}_4$  nanocube monodispersion used the 400 nm wavelength and 3.8  $\mu\text{J}$  pulse energy, and transient features that are distinct from the XUV absorbance changes on thin-films are obtained (Fig. C-3(a)). As has been shown in Chapter 4, excited states of thin-film  $\text{Co}_3\text{O}_4$  exhibit a strong enhanced absorption centered at 62.4 eV. On the nanocube sample, however, a fast growing positive absorbance increase appears at 58.5 eV right after the optical excitation. At the same time, a shallow depletion region can be seen in the energy region above 61 eV. Initially it was conceived that a different excited state is created in the nanoscale  $\text{Co}_3\text{O}_4$ , however after careful inspection the new transient XUV absorption signal was attributed to sample degradation. The transmission map of the sample was measured again after a pump-probe experiment. As shown in Fig. C-3(c), the inhomogeneous pattern of the sample remains similar after a pump-probe scan, however the overall XUV transmission level has increased for about 4 times. The static absorption spectra not only exhibits a much lower non-resonant absorption level (Fig. C-3(d)), but the Co M-edge absorption peak has shifted by  $\sim 2$  eV to lower energy. Since these dramatic sample composition changes occur during the pump-probe measurement, the obtained transient XUV spectra should be interpreted as a sample degradation process rather than a distinct excited state. Especially since the static absorption shows an energy redshift after sample degradation, the transient spectra in Fig. C-3(a) can be explained as the XUV absorbance difference before and after the degradation.

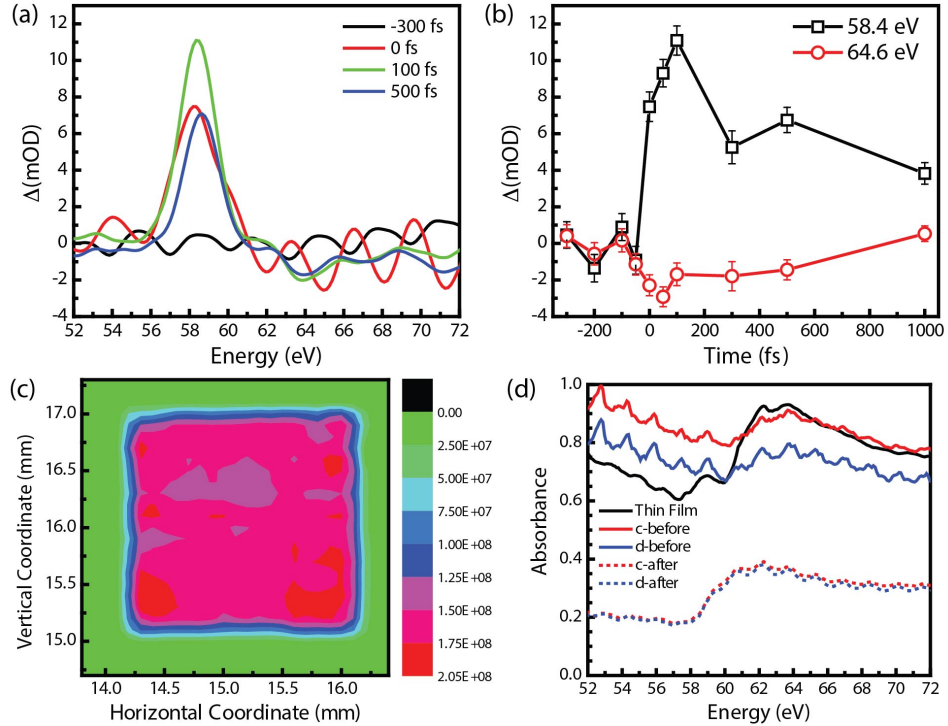


Figure C-3: (a) Transient XUV absorption spectra of  $\text{Co}_3\text{O}_4$  nanocubes with 400 nm optical excitation. (b) Transient absorbance traces at 58.4 and 64.6 eV. (c) Transmission map of the same sample as in Fig. C-1(a), but taken after the pump-probe experiment. (d) Static XUV absorption spectra at location c and d labeled in Fig. C-1(a), after the pump-probe experiment the non-resonant absorption level exhibit a significant drop with the Co M-edge redshifted by  $\sim 2$  eV.

Based on observations of the lower non-resonant absorption level, and the redshifting of the Co absorption edge, a sample degradation mechanism is proposed as in Fig. C-4: The pump pulses would heat up the illuminated sample area, so that the organic ligands surrounding the nanocubes are oxidized. In a vacuum chamber, oxidation of these organic ligands would require the extraction of oxygen from the nanocube surfaces. As a result, the Co cations in the nanocubes are reduced to a lower oxidation state, reflected by the dramatic redshift of the M-edge absorption. The decrease of the non-resonant absorption contribution can be explained by the reduced densities of both C and O atoms in the nanocube sample.

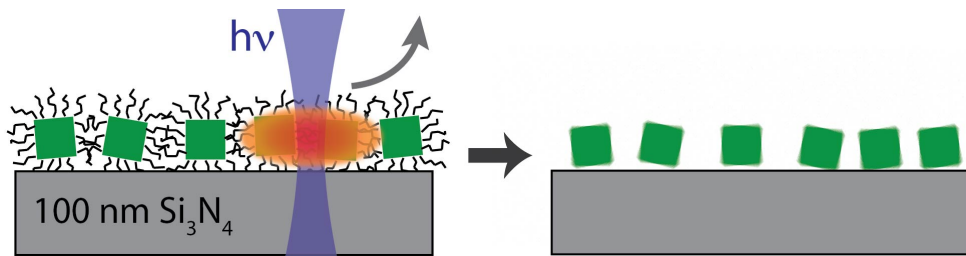


Figure C-4: Schematic of the proposed  $\text{Co}_3\text{O}_4$  degrading mechanism under light illumination. The pump pulses heat up the sample and facilitate the oxidation of the organic ligands surrounding the nanocubes. Since this process happens in a vacuum environment, Co atoms are reduced to lower oxidation states.



# Bibliography

- (1) Ashcroft, N. W.; Mermin, N. D. *Solid State Physics*; Brooks/Cole, Cengage Learning, 1976.
- (2) Tasaki, H. The Hubbard Model: Introduction and Selected Rigorous Results. *J. Phys. Condens. Matter* **1995**, *10* (20), 34.
- (3) Yamada, A. Magnetic Properties and Mott Transition in the Hubbard Model on the Anisotropic Triangular Lattice. *Phys. Rev. B* **2014**, *89* (19), 10.
- (4) Zaanen, J.; Sawatzky, G. A.; Allen, J. W. Band Gaps and Electronic Structure of Transition-Metal Compounds. *Phys. Rev. Lett.* **1985**, *55* (4), 418–421.
- (5) Bigot, J. Y.; Portella, M. T.; Schoenlein, R. W.; Cunningham, J. E.; Shank, C. V. Two-Dimensional Carrier-Carrier Screening in a Quantum Well. *Phys. Rev. Lett.* **1991**, *67* (5), 636–639.
- (6) Shah, J. *Ultrafast Spectroscopy of Semiconductors and Semiconductor Nanostructures*; Springer-Verlag Berlin Heidelberg, 1999.
- (7) Devreese, J. T. *Polarons*, 3rd ed.; Wiley-VCH: Weinheim, 2005.
- (8) Sagar, D.; Cooney, R.; Sewall, S.; Dias, E.; Barsan, M.; Butler, I.; Kambhampati, P. Size Dependent, State-Resolved Studies of Exciton-Phonon Couplings in Strongly Confined Semiconductor Quantum Dots. *Phys. Rev. B* **2008**, *77* (23), 235321.
- (9) Dimitrov, S. D.; Dooley, C. J.; Trifonov, A. A.; Fiebig, T. Femtosecond Probing of Optical Phonon Dynamics in Quantum-Confining CdTe Nanocrystals. *J. Phys. Chem. C* **2009**, *113* (10), 4198–4201.
- (10) Smieja, J. M.; Benson, E. E.; Kumar, B.; Grice, K. A.; Seu, C. S.; Miller, A. J. M.; Mayer, J. M.; Kubiak, C. P. Kinetic and Structural Studies, Origins of Selectivity, and Interfacial Charge Transfer in the Artificial Photosynthesis of CO. *Proc. Natl. Acad. Sci.* **2012**, *109* (39), 15646–15650.
- (11) Prezhdo, O. V.; Duncan, W. R.; Prezhdo, V. V. Photoinduced Electron Dynamics at the Chromophore–semiconductor Interface: A Time-Domain *ab Initio* Perspective. *Prog. Surf. Sci.* **2009**, *84* (1-2), 30–68.
- (12) Adams, D. M.; Brus, L.; Chidsey, C. E. D.; Creager, S.; Creutz, C.; Kagan, C. R.; Kamat, P. V.; Lieberman, M.; Lindsay, S.; Marcus, R. A.; et al. Charge Transfer on the Nanoscale: Current Status. *J. Phys. Chem. B* **2003**, *107* (28), 6668–6697.

- (13) Kudo, A.; Miseki, Y. Heterogeneous Photocatalyst Materials for Water Splitting. *Chem. Soc. Rev.* **2009**, *38* (1), 253.
- (14) Buchalska, M.; Kuncewicz, J.; Świetek, E.; Łabuz, P.; Baran, T.; Stochel, G.; Macyk, W. Photoinduced Hole Injection in Semiconductor-Coordination Compound Systems. *Coord. Chem. Rev.* **2013**, *257* (3-4), 767–775.
- (15) Marcus, R. A.; Sutin, N. Electron Transfers in Chemistry and Biology. *Biochim. Biophys. Acta - Rev. Bioenerg.* **1985**, *811* (3), 265–322.
- (16) Anderson, N. A.; Lian, T. Q. Ultrafast Electron Transfer at the Molecule-Semiconductor Nanoparticle Interface. *Annu. Rev. Phys. Chem.* **2005**, *56*, 491–519.
- (17) Gao, Y. Q.; Georgievskii, Y.; Marcus, R. A. On the Theory of Electron Transfer Reactions at Semiconductor Electrode/liquid Interfaces. *J. Chem. Phys.* **2000**, *112*, 3358.
- (18) Fork, R. L.; Greene, B. I.; Shank, C. V. Generation of Optical Pulses Shorter than 0.1 Psec by Colliding Pulse Mode Locking. *Appl. Phys. Lett.* **1981**, *38* (9), 671–672.
- (19) Dantus, M.; Bowman, R. M.; Zewail, A. H. Femtosecond Laser Observations of Molecular Vibration and Rotation. *Nature* **1990**, *343* (6260), 737–739.
- (20) Ward, M. D. Photo-Induced Electron and Energy Transfer in Non-Covalently Bonded Supramolecular Assemblies. *Chem. Soc. Rev.* **1997**, *26* (5), 365.
- (21) Bardeen, C. J.; Wang, Q.; Shank, C. V. Selective Excitation of Vibrational Wave Packet Motion Using Chirped Pulses. *Phys. Rev. Lett.* **1995**, *75* (19), 3410–3413.
- (22) Serpone, N.; Lawless, D.; Khairutdinov, R.; Pelizzetti, E. Subnanosecond Relaxation Dynamics in TiO<sub>2</sub> Colloidal Sols (Particle Sizes R<sub>p</sub> = 1.0-13.4nm). Relevance to Heterogenous Photocatalysis. *J. Phys. Chem.* **1995**, *99* (45), 16655–16661.
- (23) Qiao, R.; Chin, T.; Harris, S. J.; Yan, S.; Yang, W. Spectroscopic Fingerprints of Valence and Spin States in Manganese Oxides and Fluorides. *Curr. Appl. Phys.* **2013**, *13* (3), 544–548.
- (24) Huse, N.; Kim, T. K.; Jamula, L.; McCusker, J. K.; de Groot, F. M. F.; Schoenlein, R. W. Photo-Induced Spin-State Conversion in Solvated Transition Metal Complexes Probed via Time-Resolved Soft X-Ray Spectroscopy. *J. Am. Chem. Soc.* **2010**, *132* (19), 6809–6816.
- (25) Schoenlein, R. W. Generation of Femtosecond Pulses of Synchrotron Radiation. *Science* (80-. ). **2000**, *287* (5461), 2237–2240.
- (26) De Groot, F. M. F.; Kotani, A. *Core Level Spectroscopy of Solids*; 2008.

- (27) Henke, B. L.; Gullikson, E. M.; Davis, J. C. X-Ray Interactions: Photoabsorption, Scattering, Transmission, and Reflection at  $E = 50\text{--}30,000$  eV,  $Z = 1\text{--}92$ . *At. Data Nucl. Data Tables* **1993**, *54* (2), 181–342.
- (28) Attwood, D. *Soft X-Rays and Extreme Ultraviolet Radiation: Principles and Applications*; Cambridge University Press: Cambridge, 2007.
- (29) Loh, Z.; Leone, S. R. Capturing Ultrafast Quantum Dynamics with Femtosecond and Attosecond X-Ray Core-Level Absorption Spectroscopy. *J. Phys. Chem. Lett.* **2013**, *4* (2), 292–302.
- (30) Lima, F. A.; Milne, C. J.; Amarasinghe, D. C. V.; Rittmann-Frank, M. H.; van der Veen, R. M.; Reinhard, M.; Pham, V.-T.; Karlsson, S.; Johnson, S. L.; Grolimund, D.; et al. A High-Repetition Rate Scheme for Synchrotron-Based Picosecond Laser Pump/x-Ray Probe Experiments on Chemical and Biological Systems in Solution. *Rev. Sci. Instrum.* **2011**, *82* (6), 063111.
- (31) Goulielmakis, E.; Loh, Z.-H.; Wirth, A.; Santra, R.; Rohringer, N.; Yakovlev, V. S.; Zherebtsov, S.; Pfeifer, T.; Azzeer, A. M.; Kling, M. F.; et al. Real-Time Observation of Valence Electron Motion. *Nature* **2010**, *466* (7307), 739–743.
- (32) Papadogiannis, N. A.; Nikolopoulos, L. A.; Charalambidis, D.; Tsakiris, G. D.; Tzallas, P.; Witte, K. Two-Photon Ionization of He through a Superposition of Higher Harmonics. *Phys. Rev. Lett.* **2003**, *90*, 133902.
- (33) Rousse, A.; Rischel, C.; Fourmaux, S.; Uschmann, I.; Sebban, S.; Grillon, G.; Balcou, P.; Förster, E.; Geindre, J. P.; Audebert, P.; et al. Non-Thermal Melting in Semiconductors Measured at Femtosecond Resolution. *Nature* **2001**, *410*, 65.
- (34) Cavalleri, A.; Schoenlein, R. W. Femtosecond X-Rays and Structural Dynamics in Condensed Matter. *Ultrafast Dyn. Process. Semicond.* **2004**, *92*, 309–337.
- (35) Papalazarou, E.; Boschetto, D.; Gautier, J.; Garl, T.; Valentin, C.; Rey, G.; Zeitoun, P.; Rousse, A.; Balcou, P.; Marsi, M. Probing Coherently Excited Optical Phonons by Extreme Ultraviolet Radiation with Femtosecond Time Resolution. *Appl. Phys. Lett.* **2008**, *93* (4), 41114.
- (36) Hillyard, P. W.; Kuchibhatla, S. V. N. T.; Glover, T. E.; Hertlein, M. P.; Huse, N.; Nachimuthu, P.; Saraf, L. V.; Thevuthasan, S.; Gaffney, K. J. Atomic Resolution Mapping of the Excited-State Electronic Structure of  $\text{Cu}_2\text{O}$  with Time-Resolved X-Ray Absorption Spectroscopy. *Phys. Rev. B* **2009**, *80* (12), 125210.
- (37) Schultze, M.; Ramasesha, K.; Pemmaraju, C. D.; Sato, S. A.; Whitmore, D.; Gandman, A.; Prell, J. S.; Borja, L. J.; Prendergast, D.; Yabana, K.; et al. Attosecond Band-Gap Dynamics in Silicon. *Science (80- )* **2014**, *346* (6215), 1348–1352.

- (38) Adams, B. W.; Rose-Petrucci, C.; Jiao, Y. Picosecond-Resolved X-Ray Absorption Spectroscopy at Low Signal Contrast Using a Hard X-Ray Streak Camera. *J. Synchrotron Radiat.* **2015**, *22* (4), 1022–1029.
- (39) Franken, P. A.; Hill, A. E.; Peters, C. W.; Weinreich, G. Generation of Optical Harmonics. *Phys. Rev. Lett.* **1961**, *7* (4), 118–119.
- (40) McPherson, A.; Gibson, G.; Jara, H.; Johann, U.; Luk, T. S.; McIntyre, I. A.; Boyer, K.; Rhodes, C. K. Studies of Multiphoton Production of Vacuum-Ultraviolet Radiation in the Rare Gases. *J. Opt. Soc. Am. B* **1987**, *4* (4), 595.
- (41) Shafir, D.; Mairesse, Y.; Villeneuve, D. M.; Corkum, P. B.; Dudovich, N. Atomic Wavefunctions Probed through Strong-Field Light–matter Interaction. *Nat. Phys.* **2009**, *5* (6), 412–416.
- (42) Wörner, H.; Bertrand, J.; Fabre, B.; Higuet, J.; Ruf, H.; Dubrouil, A.; Patchkovskii, S.; Spanner, M.; Mairesse, Y.; Blanchet, V.; et al. Conical Intersection Dynamics in NO<sub>2</sub> Probed by Homodyne High-Harmonic Spectroscopy. *Science (80-. ).* **2011**, *334* (6053), 208–212.
- (43) Wörner, H. J.; Bertrand, J. B.; Corkum, P. B.; Villeneuve, D. M. High-Harmonic Homodyne Detection of the Ultrafast Dissociation of Br<sub>2</sub> Molecules. *Phys. Rev. Lett.* **2010**, *105* (10), 103002.
- (44) Corkum, P. B. Plasma Perspective on Strong Field Multiphoton Ionization. *Phys. Rev. Lett.* **1993**, *71* (13), 1994–1997.
- (45) Ammosov, M. V.; Delone, N. B.; Krainov, V. P. Tunnel Ionization of Complex Atoms and of Atomic Ions in an Alternating Electromagnetic Field. *Sov. Phys. JETP* **1986**, *64* (December 1986), 1191–1194.
- (46) Winterfeldt, C.; Spielmann, C.; Gerber, G. Colloquium: Optimal Control of High-Harmonic Generation. *Rev. Mod. Phys.* **2008**, *80* (1), 117–140.
- (47) Lewenstein, M.; Balcou, P.; Ivanov, M. Y.; L’Huillier, A.; Corkum, P. B. Theory of High-Harmonic Generation by Low-Frequency Laser Fields. *Phys. Rev. A* **1994**, *49* (3), 2117–2132.
- (48) Bellini, M.; Lyngå, C.; Tozzi, A.; Gaarde, M. B.; Hänsch, T. W.; L’Huillier, A.; Wahlström, C.-G. Temporal Coherence of Ultrashort High-Order Harmonic Pulses. *Phys. Rev. Lett.* **1998**, *81* (2), 297–300.
- (49) Zaïr, A.; Holler, M.; Guandalini, A.; Schapper, F.; Biegert, J.; Gallmann, L.; Keller, U.; Wyatt, a. S.; Monmayrant, A.; Walmsley, I. a.; et al. Quantum Path Interferences in High-Order Harmonic Generation. *Phys. Rev. Lett.* **2008**, *100* (14), 143902.

- (50) Chen, M. C.; Arpin, P.; Popmintchev, T.; Gerrity, M.; Zhang, B.; Seaberg, M.; Popmintchev, D.; Murnane, M. M.; Kapteyn, H. C. Bright, Coherent, Ultrafast Soft X-Ray Harmonics Spanning the Water Window from a Tabletop Light Source. *Phys. Rev. Lett.* **2010**, *105* (17), 1–4.
- (51) Balcou, P.; L’Huillier, A. Phase-Matching Effects in Strong-Field Harmonic Generation. *Phys. Rev. A* **1993**, *47* (2), 1447–1459.
- (52) Van Dao, L.; Teichmann, S.; Davis, J.; Hannaford, P. Generation of High Flux, Highly Coherent Extreme Ultraviolet Radiation in a Gas Cell. *J. Appl. Phys.* **2008**, *104* (2), 23105.
- (53) Constant, E.; Garzella, D.; Breger, P.; Mevel, E.; Dorrer, C.; Le Blanc, C.; Salin, F.; Agostini, P. Optimizing High Harmonic Generation in Absorbing Gases: Model and Experiment. *Phys. Rev. Lett.* **1999**, *82* (8), 1668–1671.
- (54) Kim, J.-H.; Shin, H. J.; Lee, D. G.; Nam, C. H. Enhanced Spectral Resolution of High-Order Harmonics by the Coherent Sum of Dipole Spectra. *Phys. Rev. A* **2000**, *62* (5), 055402.
- (55) Takahashi, E.; Nabekawa, Y.; Otsuka, T.; Obara, M.; Midorikawa, K. Generation of Highly Coherent Submicrojoule Soft X Rays by High-Order Harmonics. *Phys. Rev. A* **2002**, *66* (2), 1–4.
- (56) Popmintchev, T.; Chen, M.-C.; Arpin, P.; Murnane, M. M.; Kapteyn, H. C. The Attosecond Nonlinear Optics of Bright Coherent X-Ray Generation. *Nat. Photonics* **2010**, *4* (12), 822–832.
- (57) Peatross, J.; Miller, J.; Smith, K.; Rhynard, S.; Pratt, B. Phase Matching of High-Order Harmonic Generation in Helium- and Neon-Filled Gas Cells. *J. Mod. Opt.* **2004**, *51*, 2675.
- (58) Hauri, C. P.; Kornelis, W.; Helbing, F. W.; Heinrich, A.; Couairon, A.; Mysyrowicz, A.; Biegert, J.; Keller, U. Generation of Intense, Carrier-Envelope Phase-Locked Few-Cycle Laser Pulses through Filamentation. *Appl. Phys. B* **2004**, *79* (6), 673–677.
- (59) Brichta, J.-P.; Wong, M. C. H.; Bertrand, J. B.; Bandulet, H.-C.; Rayner, D. M.; Bhardwaj, V. R. Comparison and Real-Time Monitoring of High-Order Harmonic Generation in Different Sources. *Phys. Rev. A* **2009**, *79* (3), 33404.
- (60) Sutherland, J. R.; Christensen, E. I.; Powers, N. D.; Rhynard, S. E.; Painter, J. C.; Peatross, J. High Harmonic Generation in a Semi-Infinite Gas Cell. *Opt. Express* **2004**, *12*, 4430.
- (61) Wahlström, C.-G.; Larsson, J.; Persson, A.; Starczewski, T.; Svanberg, S.; Salières, P.; Balcou, P.; L’Huillier, A. High-Order Harmonic Generation in Rare Gases with an Intense Short-Pulse Laser. *Phys. Rev. A* **1993**, *48* (6), 4709–4720.

- (62) Teichmann, S.; Hannaford, P.; Van Dao, L. Phase-Matched Emission of Few High-Harmonic Orders from a Helium Gas Cell. *Appl. Phys. Lett.* **2009**, *94* (17), 171111.
- (63) Steingrube, D.; Vockerodt, T.; Schulz, E.; Morgner, U.; Kovačev, M. Phase Matching of High-Order Harmonics in a Semi-Infinite Gas Cell. *Phys. Rev. A* **2009**, *80* (4), 43819.
- (64) Steingrube, D. S.; Schulz, E.; Binhammer, T.; Vockerodt, T.; Morgner, U.; Kovacev, M. Generation of High-Order Harmonics with Ultra-Short Pulses from Filamentation. *Opt. Express* **2009**, *17*, 16177.
- (65) Dao, L. V.; Hall, C.; Vu, H. L.; Dinh, K. B.; Balaur, E.; Hannaford, P.; Smith, T. A. Phase-Matched Generation of Highly Coherent Radiation in Water Window Region. *Appl. Opt.* **2012**, *51* (18), 4240.
- (66) Chini, M.; Zhao, K.; Chang, Z. The Generation, Characterization and Applications of Broadband Isolated Attosecond Pulses. *Nat. Photonics* **2014**, *8* (3), 178–186.
- (67) He, X.; Dahlström, J. M.; Rakowski, R.; Heyl, C. M.; Persson, A.; Mauritsson, J.; L’Huillier, A. Interference Effects in Two-Color High-Order Harmonic Generation. *Phys. Rev. A* **2010**, *82* (3), 033410.
- (68) Misoguti, L.; Christov, I. P.; Backus, S.; Murnane, M. M.; Kapteyn, H. C. Nonlinear Wave-Mixing Processes in the Extreme Ultraviolet. *Phys. Rev. A* **2005**, *72* (6), 063803.
- (69) Kfir, O.; Grychtol, P.; Turgut, E.; Knut, R.; Zusin, D.; Popmintchev, D.; Popmintchev, T.; Nembach, H.; Shaw, J. M.; Fleischer, A.; et al. Generation of Bright Phase-Matched Circularly-Polarized Extreme Ultraviolet High Harmonics. *Nat. Photonics* **2014**, *9* (2), 99–105.
- (70) Trebino, R.; DeLong, K. W.; Fittinghoff, D. N.; Sweetser, J. N.; Krumbügel, M. A.; Richman, B. A.; Kane, D. J. Measuring Ultrashort Laser Pulses in the Time-Frequency Domain Using Frequency-Resolved Optical Gating. *Rev. Sci. Instrum.* **1997**, *68* (9), 3277.
- (71) Cerullo, G.; de Silvestri, S. Ultrafast Optical Parametric Amplifiers. *Rev. Sci. Instrum.* **2003**, *74*, 1.
- (72) <http://www.cxro.lbl.gov/>.
- (73) Baker, L. R.; Jiang, C.; Kelly, S. T.; Lucas, J. M.; Vura-Weis, J.; Gilles, M. K.; Alivisatos, A. P.; Leone, S. R. Charge Carrier Dynamics of Photoexcited  $\text{Co}_3\text{O}_4$  in Methanol: Extending High Harmonic Transient Absorption Spectroscopy to Liquid Environments. *Nano Lett.* **2014**, *14* (10), 5883–5890.
- (74) Kita, T.; Harada, T.; Nakano, N.; Kuroda, H. Mechanically Ruled Aberration-Corrected Concave Gratings for a Flat-Field Grazing-Incidence Spectrograph. *Appl. Opt.* **1983**, *22*, 512.

- (75) Ederer, D. L.; Manalis, M. Photoabsorption of the 4d Electrons in Xenon. *J. Opt. Soc. Am.* **1975**, *65*, 634.
- (76) Samson, J. A. R.; Stolte, W. C. Precision Measurements of the Total Photoionization Cross-Sections of He, Ne, Ar, Kr, and Xe. *J. Electron Spectros. Relat. Phenomena* **2002**, *123* (2-3), 265–276.
- (77) Loh, Z.-H.; Khalil, M.; Correa, R. E.; Leone, S. R. A Tabletop Femtosecond Time-Resolved Soft X-Ray Transient Absorption Spectrometer. *Rev. Sci. Instrum.* **2008**, *79* (7), 073101.
- (78) Wörner, H. J.; Niikura, H.; Bertrand, J. B.; Corkum, P. B.; Villeneuve, D. M. Observation of Electronic Structure Minima in High-Harmonic Generation. *Phys. Rev. Lett.* **2009**, *102* (10), 1–4.
- (79) Goodenough, J. B. Perspective on Engineering Transition-Metal Oxides. *Chem. Mater.* **2014**, *26* (1), 820–829.
- (80) Toroker, M. C.; Carter, E. A. Transition Metal Oxide Alloys as Potential Solar Energy Conversion Materials. *J. Mater. Chem. A* **2013**, *1* (7), 2474–2484.
- (81) Poizot, P.; Laruelle, S.; Grugeon, S.; Dupont, L.; Tarascon, J. M. Nano-Sized Transition-Metal Oxides as Negative-Electrode Materials for Lithium-Ion Batteries. *Nature* **2000**, *407* (6803), 496–499.
- (82) Rockenberger, J.; Scher, E. C.; Alivisatos, A. P. A New Nonhydrolytic Single-Precursor Approach to Surfactant-Capped Nanocrystals of Transition Metal Oxides. *J. Am. Chem. Soc.* **1999**, *121* (49), 11595–11596.
- (83) Liu, B.; Chen, H. M.; Liu, C.; Andrews, S. C.; Hahn, C.; Yang, P. Large-Scale Synthesis of Transition-Metal-Doped TiO<sub>2</sub> Nanowires with Controllable Overpotential. *J. Am. Chem. Soc.* **2013**, *135* (27), 9995–9998.
- (84) Wall, S.; Foglia, L.; Wegkamp, D.; Appavoo, K.; Nag, J.; Haglund, R. F.; Stähler, J.; Wolf, M. Tracking the Evolution of Electronic and Structural Properties of VO<sub>2</sub> during the Ultrafast Photoinduced Insulator-Metal Transition. *Phys. Rev. B* **2013**, *87* (11), 115126.
- (85) Němec, H.; Rochford, J.; Taratula, O.; Galoppini, E.; Kužel, P.; Polívka, T.; Yartsev, A.; Sundström, V. Influence of the Electron-Cation Interaction on Electron Mobility in Dye-Sensitized ZnO and TiO<sub>2</sub> Nanocrystals: A Study Using Ultrafast Terahertz Spectroscopy. *Phys. Rev. Lett.* **2010**, *104* (19), 197401.
- (86) Thimsen, E.; Biswas, S.; Lo, C. S.; Biswas, P. Predicting the Band Structure of Mixed Transition Metal Oxides: Theory and Experiment. *J. Phys. Chem. C* **2009**, *113* (5), 2014–2021.

- (87) Pastore, M.; De Angelis, F. Computational Modelling of TiO<sub>2</sub> Surfaces Sensitized by Organic Dyes with Different Anchoring Groups: Adsorption Modes, Electronic Structure and Implication for Electron Injection/recombination. *Phys. Chem. Chem. Phys.* **2012**, *14* (2), 920–928.
- (88) Olalde-Velasco, P.; Jiménez-Mier, J.; Denlinger, J. D.; Hussain, Z.; Yang, W. L. Direct Probe of Mott-Hubbard to Charge-Transfer Insulator Transition and Electronic Structure Evolution in Transition-Metal Systems. *Phys. Rev. B* **2011**, *83* (24), 241102.
- (89) Xie, X.; Li, Y.; Liu, Z.-Q.; Haruta, M.; Shen, W. Low-Temperature Oxidation of CO Catalysed by Co<sub>3</sub>O<sub>4</sub> Nanorods. *Nature* **2009**, *458* (7239), 746–749.
- (90) Park, J.-Y.; Lee, Y.-J.; Karandikar, P. R.; Jun, K.-W.; Ha, K.-S.; Park, H.-G. Fischer-Tropsch Catalysts Deposited with Size-Controlled Co<sub>3</sub>O<sub>4</sub> Nanocrystals: Effect of Co Particle Size on Catalytic Activity and Stability. *Appl. Catal. A Gen.* **2012**, *411-412*, 15–23.
- (91) Tyo, E. C.; Yin, C.; Di Vece, M.; Qian, Q.; Kwon, G.; Lee, S.; Lee, B.; DeBartolo, J. E.; Seifert, S.; Winans, R. E.; et al. Oxidative Dehydrogenation of Cyclohexane on Cobalt Oxide (Co<sub>3</sub>O<sub>4</sub>) Nanoparticles: The Effect of Particle Size on Activity and Selectivity. *ACS Catal.* **2012**, *2* (11), 2409–2423.
- (92) Jiao, F.; Frei, H. Nanostructured Cobalt Oxide Clusters in Mesoporous Silica as Efficient Oxygen-Evolving Catalysts. *Angew. Chem. Int. Ed. Engl.* **2009**, *48* (10), 1841–1844.
- (93) Gasparotto, A.; Barreca, D.; Bekermann, D.; Devi, A.; Fischer, R. A.; Fornasiero, P.; Gombac, V.; Lebedev, O. I.; Maccato, C.; Montini, T.; et al. F-Doped Co<sub>3</sub>O<sub>4</sub> Photocatalysts for Sustainable H<sub>2</sub> Generation from Water/Ethanol. *J. Am. Chem. Soc.* **2011**, *133* (48), 19362–19365.
- (94) Zou, X.; Su, J.; Silva, R.; Goswami, A.; Sathe, B. R.; Asefa, T. Efficient Oxygen Evolution Reaction Catalyzed by Low-Density Ni-Doped Co<sub>3</sub>O<sub>4</sub> Nanomaterials Derived from Metal-Embedded Graphitic C<sub>3</sub>N<sub>4</sub>. *Chem. Commun.* **2013**, *49* (68), 7522–7524.
- (95) Haneda, M.; Kintaichi, Y.; Bion, N.; Hamada, H. Alkali Metal-Doped Cobalt Oxide Catalysts for NO Decomposition. *Appl. Catal. B Environ.* **2003**, *46* (3), 473–482.
- (96) Chen, J.; Wu, X.; Selloni, A. Electronic Structure and Bonding Properties of Cobalt Oxide in the Spinel Structure. *Phys. Rev. B* **2011**, *83* (24), 245204.
- (97) Bai, L.; Pravica, M.; Zhao, Y.; Park, C.; Meng, Y.; Sinogeikin, S. V; Shen, G. Charge Transfer in Spinel Co<sub>3</sub>O<sub>4</sub> at High Pressures. *J. Phys. Condens. Matter* **2012**, *24* (43), 435401.

- (98) Ruzakowski Athey, P.; Urban III, F. K.; Tabet, M. F.; McGahan, W. A. Optical Properties of Cobalt Oxide Films Deposited by Spray Pyrolysis. *J. Vac. Sci. Technol. A* **1996**, *14*, 685–692.
- (99) Miedzinska, K. M. E.; Hollebone, B. R.; Cook, J. G. An Assignment of the Optical Absorption Spectrum of Mixed Valence  $\text{Co}_3\text{O}_4$  Spinel Films. *J. Phys. Chem. Solids* **1987**, *48* (7), 649–656.
- (100) Kim, K. J.; Park, Y. R. Optical Investigation of Charge-Transfer Transitions in Spinel  $\text{Co}_3\text{O}_4$ . *Solid State Commun.* **2003**, *127* (1), 25–28.
- (101) Van der Laan, G. M<sub>2,3</sub> Absorption Spectroscopy of 3d Transition-Metal Compounds. *J. Phys. Condens. Matter* **1991**, *3* (38), 7443–7454.
- (102) Huse, N.; Cho, H.; Hong, K.; Jamula, L.; de Groot, F. M. F.; Kim, T. K.; McCusker, J. K.; Schoenlein, R. W. Femtosecond Soft X-Ray Spectroscopy of Solvated Transition-Metal Complexes: Deciphering the Interplay of Electronic and Structural Dynamics. *J. Phys. Chem. Lett.* **2011**, *2* (8), 880–884.
- (103) Hosler, E. R.; Leone, S. R. Characterization of Vibrational Wave Packets by Core-Level High-Harmonic Transient Absorption Spectroscopy. *Phys. Rev. A* **2013**, *88* (2), 023420.
- (104) Lin, M.-F.; Neumark, D. M.; Gessner, O.; Leone, S. R. Ionization and Dissociation Dynamics of Vinyl Bromide Probed by Femtosecond Extreme Ultraviolet Transient Absorption Spectroscopy. *J. Chem. Phys.* **2014**, *140* (6), 064311.
- (105) Schultze, M.; Bothschafter, E. M.; Sommer, A.; Holzner, S.; Schweinberger, W.; Fiess, M.; Hofstetter, M.; Kienberger, R.; Apalkov, V.; Yakovlev, V. S.; et al. Controlling Dielectrics with the Electric Field of Light. *Nature* **2013**, *493* (7430), 75–78.
- (106) Chen, L. X.; Zhang, X.; Lockard, J. V.; Stickrath, A. B.; Attenkofer, K.; Jennings, G.; Liu, D.-J. Excited-State Molecular Structures Captured by X-Ray Transient Absorption Spectroscopy: A Decade and beyond. *Acta Crystallogr. Sect. A* **2010**, *66*, 240–251.
- (107) Canton, S. E.; Zhang, X.; Zhang, J.; van Driel, T. B.; Kjaer, K. S.; Haldrup, K.; Chabera, P.; Harlang, T.; Suarez-Alcantara, K.; Liu, Y.; et al. Toward Highlighting the Ultrafast Electron Transfer Dynamics at the Optically Dark Sites of Photocatalysts. *J. Phys. Chem. Lett.* **2013**, *4* (11), 1972–1976.
- (108) Boeglin, C.; Beaurepaire, E.; Halté, V.; López-Flores, V.; Stamm, C.; Pontius, N.; Dürr, H. A.; Bigot, J.-Y. Distinguishing the Ultrafast Dynamics of Spin and Orbital Moments in Solids. *Nature* **2010**, *465* (7297), 458–461.
- (109) Turgut, E.; La-o-vorakiat, C.; Shaw, J. M.; Grychtol, P.; Nembach, H. T.; Rudolf, D.; Adam, R.; Aeschlimann, M.; Schneider, C. M.; Silva, T. J.; et al. Controlling the

Competition between Optically Induced Ultrafast Spin-Flip Scattering and Spin Transport in Magnetic Multilayers. *Phys. Rev. Lett.* **2013**, *110* (19), 197201.

- (110) Vura-Weis, J.; Jiang, C.-M.; Liu, C.; Gao, H.; Lucas, J. M.; de Groot, F. M. F.; Yang, P.; Alivisatos, A. P.; Leone, S. R. Femtosecond M<sub>2,3</sub>-Edge Spectroscopy of Transition-Metal Oxides: Photoinduced Oxidation State Change in A-Fe<sub>2</sub>O<sub>3</sub>. *J. Phys. Chem. Lett.* **2013**, *4* (21), 3667–3671.
- (111) Tang, C.-W.; Wang, C.-B.; Chien, S.-H. Characterization of Cobalt Oxides Studied by FT-IR, Raman, TPR and TG-MS. *Thermochim. Acta* **2008**, *473* (1-2), 68–73.
- (112) Stavitski, E.; de Groot, F. M. F. The CTM4XAS Program for EELS and XAS Spectral Shape Analysis of Transition Metal L Edges. *Micron* **2010**, *41* (7), 687–694.
- (113) Ikeno, H.; de Groot, F. M. F.; Stavitski, E.; Tanaka, I. Multiplet Calculations of L<sub>2,3</sub> X-Ray Absorption near-Edge Structures for 3d Transition-Metal Compounds. *J. Phys. Condens. Matter* **2009**, *21* (10), 104208.
- (114) Morales, F.; de Groot, F. M. F.; Glatzel, P.; Kleimenov, E.; Bluhm, H.; Hävecker, M.; Knop-Gericke, A.; Weckhuysen, B. M. In Situ X-Ray Absorption of Co/Mn/TiO<sub>2</sub> Catalysts for Fischer–Tropsch Synthesis. *J. Phys. Chem. B* **2004**, *108* (41), 16201–16207.
- (115) Taguchi, M.; Uozumi, T.; Kotani, A. Theory of X-Ray Photoemission and X-Ray Emission Spectra in Mn Compounds. *J. Phys. Soc. Japan* **1997**, *66* (1), 247–256.
- (116) Valero-Mora, P. M.; Ledesma, R. D. Graphical User Interfaces for R. *J. Stat. Softw.* **2012**, *49* (1), 1–8.
- (117) Tanabe, Y.; Sugano, S. On the Absorption Spectra of Complex Ions II. *J. Phys. Soc. Japan* **1954**, *9* (5), 766–779.
- (118) Walsh, A.; Wei, S.-H.; Yan, Y.; Al-Jassim, M. M.; Turner, J. A.; Woodhouse, M.; Parkinson, B. A. Structural, Magnetic, and Electronic Properties of the Co-Fe-Al Oxide Spinel System: Density-Functional Theory Calculations. *Phys. Rev. B* **2007**, *76* (16), 165119.
- (119) Broqvist, P.; Panas, I.; Persson, H. A DFT Study on CO Oxidation over Co<sub>3</sub>O<sub>4</sub>. *J. Catal.* **2002**, *210* (1), 198–206.
- (120) Jiang, D.; Dai, S. The Role of Low-Coordinate Oxygen on Co<sub>3</sub>O<sub>4</sub>(110) in Catalytic CO Oxidation. *Phys. Chem. Chem. Phys.* **2011**, *13* (3), 978–984.
- (121) Gardner, G. P.; Go, Y. B.; Robinson, D. M.; Smith, P. F.; Hadermann, J.; Abakumov, A.; Greenblatt, M.; Dismukes, G. C. Structural Requirements in Lithium Cobalt Oxides for the Catalytic Oxidation of Water. *Angew. Chem. Int. Ed. Engl.* **2012**, *51* (7), 1616–1619.

- (122) Wang, L.-W.; Califano, M.; Zunger, A.; Franceschetti, A. Pseudopotential Theory of Auger Processes in CdSe Quantum Dots. *Phys. Rev. Lett.* **2003**, *91* (5), 056404.
- (123) Klimov, V. I.; McBranch, D. W. Femtosecond 1P-to-1S Electron Relaxation in Strongly Confined Semiconductor Nanocrystals. *Phys. Rev. Lett.* **1998**, *80*, 4028–4031.
- (124) Cooney, R. R.; Sewall, S. L.; Dias, E. A.; Sagar, D. M.; Anderson, K. E. H.; Kambhampati, P. Unified Picture of Electron and Hole Relaxation Pathways in Semiconductor Quantum Dots. *Phys. Rev. B* **2007**, *75* (24), 245311.
- (125) Gawelda, W.; Cannizzo, A.; Pham, V.-T.; van Mourik, F.; Bressler, C.; Chergui, M. Ultrafast Nonadiabatic Dynamics of  $[\text{Fe}^{\text{II}}(\text{bpy})_3]^{2+}$  in Solution. *J. Am. Chem. Soc.* **2007**, *129* (26), 8199–8206.
- (126) Chou, P.-T.; Chi, Y.; Chung, M.-W.; Lin, C.-C. Harvesting Luminescence via Harnessing the Photophysical Properties of Transition Metal Complexes. *Coord. Chem. Rev.* **2011**, *255* (21-22), 2653–2665.
- (127) Klimov, V. I. Optical Nonlinearities and Ultrafast Carrier Dynamics in Semiconductor Nanocrystals. *J. Phys. Chem. B* **2000**, *104* (26), 6112–6123.
- (128) Klimov, V.; Haring Bolivar, P.; Kurz, H. Hot-Phonon Effects in Femtosecond Luminescence Spectra of Electron-Hole Plasmas in CdS. *Phys. Rev. B* **1995**, *52* (7), 4728–4731.
- (129) Lenglet, M.; Lefez, B. Infrared Optical Properties of Cobalt (II) Spinels. *Solid State Commun.* **1996**, *98* (8), 689–694.
- (130) Jiang, C.; Baker, L. R.; Lucas, J. M.; Vura-Weis, J.; Alivisatos, A. P.; Leone, S. R. Characterization of Photo-Induced Charge Transfer and Hot Carrier Relaxation Pathways in Spinel Cobalt Oxide ( $\text{Co}_3\text{O}_4$ ). *J. Phys. Chem. C* **2014**, *118* (39), 22774–22784.
- (131) Seabold, J. A.; Neale, N. R. All First Row Transition Metal Oxide Photoanode for Water Splitting Based on  $\text{Cu}_3\text{V}_2\text{O}_8$ . *Chem. Mater.* **2015**, *27* (3), 1005–1013.
- (132) Tada, H.; Jin, Q.; Iwaszuk, A.; Nolan, M. Molecular-Scale Transition Metal Oxide Nanocluster Surface-Modified Titanium Dioxide as Solar-Activated Environmental Catalysts. *J. Phys. Chem. C* **2014**, *118* (23), 12077–12086.
- (133) Yuan, C.; Wu, H. Bin; Xie, Y.; Lou, X. W. Mixed Transition-Metal Oxides: Design, Synthesis, and Energy-Related Applications. *Angew. Chemie - Int. Ed.* **2014**, *53* (6), 1488–1504.
- (134) Hoffmann, M. R.; Martin, S. T.; Choi, W.; Bahnamann, D. W. Environmental Applications of Semiconductor Photocatalysis. *Chem. Rev.* **1995**, *95* (1), 69–96.

- (135) Carp, O.; Huisman, C. L.; Reller, a. Photoinduced Reactivity of Titanium Dioxide. *Prog. Solid State Chem.* **2004**, *32* (1-2), 33–177.
- (136) Nakata, K.; Fujishima, A. TiO<sub>2</sub> Photocatalysis: Design and Applications. *J. Photochem. Photobiol. C Photochem. Rev.* **2012**, *13* (3), 169–189.
- (137) Pereira, A. L. J.; Gracia, L.; Beltran, A.; Lisboa-Filho, P. N.; da Silva, J. H. D.; Andres, J. Structural and Electronic Effects of Incorporating Mn in TiO<sub>2</sub> Films Grown by Sputtering: Anatase versus Rutile. *J. Phys. Chem. C* **2012**, *116* (15), 8753–8762.
- (138) Mangham, A. N.; Govind, N.; Bowden, M. E.; Shutthanandan, V.; Joly, A. G.; Henderson, M. A.; Chambers, S. A. Photochemical Properties, Composition, and Structure in Molecular Beam Epitaxy Grown Fe “Doped” and (Fe,N) Codoped Rutile TiO<sub>2</sub>(110). *J. Phys. Chem. C* **2011**, *115* (31), 15416–15424.
- (139) Mcleod, J.; Green, R.; Kurmaev, E.; Kumada, N.; Belik, A.; Moewes, A. Band-Gap Engineering in TiO<sub>2</sub>-Based Ternary Oxides. *Phys. Rev. B* **2012**, *85* (19), 195201.
- (140) Su, R.; Bechstein, R.; Sø, L.; Vang, R. T.; Sillassen, M.; Esbjörnsson, B.; Palmqvist, A.; Besenbacher, F. How the Anatase-to-Rutile Ratio Influences the Photoreactivity of TiO<sub>2</sub>. *J. Phys. Chem. C* **2011**, *115* (49), 24287–24292.
- (141) Scheuermann, A. G.; Prange, J. D.; Gunji, M.; Chidsey, C. E. D.; McIntyre, P. C. Effects of Catalyst Material and Atomic Layer Deposited TiO<sub>2</sub> Oxide Thickness on the Water Oxidation Performance of Metal–insulator–silicon Anodes. *Energy Environ. Sci.* **2013**, *6* (8), 2487.
- (142) Yu, H.; Chen, S.; Quan, X.; Zhao, H.; Zhang, Y. Silicon nanowire/TiO<sub>2</sub> Heterojunction Arrays for Effective Photoelectrocatalysis under Simulated Solar Light Irradiation. *Appl. Catal. B Environ.* **2009**, *90* (1-2), 242–248.
- (143) Chang, Y.-H.; Liu, C.-M.; Tseng, Y.-C.; Chen, C.; Chen, C.-C.; Cheng, H.-E. Direct Probe of Heterojunction Effects upon Photoconductive Properties of TiO<sub>2</sub> Nanotubes Fabricated by Atomic Layer Deposition. *Nanotechnology* **2010**, *21* (22), 225602.
- (144) Huang, B.; Yang, W.; Wen, Y.; Shan, B.; Chen, R. Co<sub>3</sub>O<sub>4</sub> -Modified TiO<sub>2</sub> Nanotube Arrays via Atomic Layer Deposition for Improved Visible-Light Photoelectrochemical Performance. *ACS Appl. Mater. Interfaces* **2015**, *7* (1), 422–431.
- (145) Kongkanand, A.; Tvrdy, K.; Takechi, K.; Kuno, M.; Kamat, P. V. Quantum Dot Solar Cells. Tuning Photoresponse through Size and Shape Control of CdSe-TiO<sub>2</sub> Architecture. *J. Am. Chem. Soc.* **2008**, *130* (12), 4007–4015.
- (146) Zhu, T.; Gao, S.-P. The Stability, Electronic Structure, and Optical Property of TiO<sub>2</sub> Polymorphs. *J. Phys. Chem. C* **2014**, *118* (21), 11385–11396.

- (147) Scanlon, D. O.; Dunnill, C. W.; Buckeridge, J.; Shevlin, S. A.; Logsdail, A. J.; Woodley, S. M.; Catlow, C. R. a; Powell, M. J.; Palgrave, R. G.; Parkin, I. P.; et al. Band Alignment of Rutile and Anatase TiO<sub>2</sub>. *Nat. Mater.* **2013**, *12* (9), 798–801.
- (148) Di Valentin, C.; Pacchioni, G.; Selloni, A. Reduced and N-Type Doped TiO<sub>2</sub>: Nature of Ti<sup>3+</sup> Species. *J. Phys. Chem. C* **2009**, *113* (48), 20543–20552.
- (149) Morgan, B. J.; Watson, G. W. Intrinsic N-Type Defect Formation in TiO<sub>2</sub>: A Comparison of Rutile and Anatase from GGA+U Calculations. *J. Phys. Chem. C* **2010**, *114* (5), 2321–2328.
- (150) Janotti, A.; Varley, J. B.; Rinke, P.; Umezawa, N.; Kresse, G.; Van de Walle, C. G. Hybrid Functional Studies of the Oxygen Vacancy in TiO<sub>2</sub>. *Phys. Rev. B* **2010**, *81* (8), 085212.
- (151) Ramamoorthy, R.; Dutta, P. K.; Akbar, S. A. Oxygen Sensors: Materials, Methods, Designs and Applications. *J. Mater. Sci.* **2003**, *38* (21), 4271–4282.
- (152) Henderson, M. A. A Surface Perspective on Self-Diffusion in Rutile TiO<sub>2</sub>. *Surf. Sci.* **1999**, *419* (2-3), 174–187.
- (153) Zuo, F.; Wang, L.; Wu, T.; Zhang, Z.; Borchardt, D.; Feng, P. Self-Doped Ti<sup>3+</sup> Enhanced Photocatalyst for Hydrogen Production under Visible Light. *J. Am. Chem. Soc.* **2010**, *132* (34), 11856–11857.
- (154) Nerlov, J.; Christensen, S. V.; Weichel, S.; Pedersen, E. H.; Møller, P. J. A Photoemission Study of the Coadsorption of CO<sub>2</sub> and Na on TiO<sub>2</sub>(110)-(1 × 1) and -(1 × 2) Surfaces: Adsorption Geometry and Reactivity. *Surf. Sci.* **1997**, *371* (2-3), 321–336.
- (155) Nakamura, I.; Negishi, N.; Kutsuna, S.; Ihara, T.; Sugihara, S.; Takeuchi, K. Role of Oxygen Vacancy in the Plasma-Treated TiO<sub>2</sub> Photocatalyst with Visible Light Activity for NO Removal. *J. Mol. Catal. A Chem.* **2000**, *161* (1-2), 205–212.
- (156) Kumar, D.; Chen, M. S.; Goodman, D. W. Characterization of Ultra-Thin TiO<sub>2</sub> Films Grown on Mo(112). *Thin Solid Films* **2006**, *515* (4), 1475–1479.
- (157) Tao, J.; Luttrell, T.; Batzill, M. A Two-Dimensional Phase of TiO<sub>2</sub> with a Reduced Bandgap. *Nat. Chem.* **2011**, *3* (4), 296–300.
- (158) Ricci, P. C.; Carbonaro, C. M.; Stagi, L.; Salis, M.; Casu, A.; Enzo, S.; Delogu, F. Anatase-to-Rutile Phase Transition in TiO<sub>2</sub> Nanoparticles Irradiated by Visible Light. *J. Phys. Chem. C* **2013**, *117* (15), 7850–7857.
- (159) Ennaoui, A.; Tributsch, H. Energetic Characterization of the Photoactive FeS<sub>2</sub> (pyrite) Interface. *Sol. Energy Mater.* **1986**, *14* (6), 461–474.

- (160) Antonov, V. N.; Germash, L. P.; Shpak, a. P.; Yaresko, a. N. Electronic Structure, Optical and X-Ray Emission Spectra in FeS<sub>2</sub>. *Phys. status solidi* **2009**, *246* (2), 411–416.
- (161) Hu, J.; Zhang, Y.; Law, M.; Wu, R. Increasing the Band Gap of Iron Pyrite by Alloying with Oxygen. *J. Am. Chem. Soc.* **2012**, *134* (32), 13216–13219.